The Exclusive Production of ρ^0 Mesons in Polarized Muon–Nucleon Scattering

within the SMC Experiment at CERN

Dissertation
zur Erlangung der Doktorgrades
der Fakultät für Physik
der Universität Bielefeld

vorgelegt von
Angèle Tripet
aus Neuchâtel, Schweiz

Bielefeld
2002

Gutachter der Dissertation: _____

_____

Datum der Disputation:

Everyone can acquire knowledge,
but the art of thinking is the rarest gift of Nature.

Frederick the Great

A mes parents, Anne-Marie et Jean-Pierre,
à Alessandro
et à Claudine.

Contents

List of Figures

List of Tables

Vita

October 21, 1970	Born in Neuchâtel, Switzerland
	Nationality: swiss
	Place of origin: Chézard-Saint-Martin (Neuchâtel)
1976-1981	Primary school in Hauterive (Neuchâtel)
1981-1985	Secondary school in Neuchâtel
1985-1988	Gymnase Cantonal of Neuchâtel
	(presently named Lycée Denis-de-Rougemont)
30.06.1988	**Maturité fédérale of type B (latin-english)**
1988-1994	University of Neuchâtel
September 1991	Summer Student at PSI (Paul Scherrer Institut, Villigen, Switzerland)
11.10.1994	**Diploma thesis in Physics**
1994-1995	research assistant for NIKHEF-H (Amsterdam, NL)
	combined with a stay at CERN (Geneva, Switzerland)
1995-1996	research assistant for the University of München (Germany)
	combined with a stay at CERN (Geneva, Switzerland)
March 1996	Start of the Ph.D. thesis at the University of Bielefeld (Germany)
	combined with a stay at CERN (Geneva, Switzerland)
August 2000	Zuoz Summer School organized by PSI (Paul Scherrer Institut,
	Villigen, Switzerland)

Publications

A. Tadsen, D. Gerber, A. Paić, A. Tripet, D. Twerenbold, J.-L. Vuilleumier, A prototype for the microwave-enhanced bolometer, Nucl. Instr. Meth. A **391** (1997) 310.

COMPASS: G. Baum *et al.*, A Proposal for a COmmon Muon and Proton Apparatus for Structure and Spectroscopy, CERN/SPSLC 96-14, SPSLC/P297, 1 March 1996.

SMC: D. Adams *et al.*, The Spin-Dependent Structure Function $g_1(x)$ of the Deuteron from Polarized Deep-Inelastic Muon Scattering, Phys. Lett. B **396** (1997) 338.

SMC: B. Adeva *et al.*, The Spin-Dependent Structure Function $g_1(x)$ of the Proton from Polarized Deep-Inelastic Muon Scattering, Phys. Lett. B **412** (1997) 414.

SMC: C. Dulya *et al.*, A line-Shape Analysis for Spin-1 NMR Signals, Nucl. Instr. Meth. A **398** (1997) 109.

SMC: B. Adeva *et al.*, Measurement of Proton and Nitrogen Polarization in Ammonia and a Test of Equal Spin Temperature, Nucl. Instr. Meth. A **419** (1998) 60.

SMC: B. Adeva *et al.*, Polarised Quark Distributions in the Nucleon from Semi-inclusive Spin Asymmetries, Phys. Lett. B **420** (1998) 180.

SMC: B. Adeva *et al.*, Spin Asymmetries A_1 and Structure Functions g_1 of the Proton and Deuteron from Polarized High Energy Muon Scattering, Phys. Rev. D **58** (1998) 112001.

SMC: B. Adeva *et al.*, A Next to Leading Order QCD Analysis of the Spin Structure Function g_1, Phys. Rev. D **58** (1998) 112002.

SMC: D. Adams *et al.*, A large streamer chamber muon tracking detector in a high-flux fixed-target application, Nucl. Instr. Meth. A **435** (1999) 354.

SMC: B. Adeva *et al.*, The Polarized Double Cell Target of the SMC, Nucl. Instr. Meth. A **437** (1999) 23.

SMC: B. Adeva *et al.*, Spin Asymmetries A_1 of the Proton and the Deuteron in the Low x and Low Q^2 Region from Polarized High Energy Muon Scattering, Phys. Rev. D **60** (1999) 072004.

A. Tripet for the Spin Muon Collaboration, Exclusive ρ^0 Production in Polarized DIS at SMC, in *Proceedings of the* 7^{th} *International Workshop on Deep Inelastic Scattering and QCD (DIS 99)*, Zeuthen, Germany, 1999, Nucl. Phys. B **79** (Proc. Suppl.) (1999) 529.

SMC: B. Adeva *et al.*, Measurement of the SMC muon beam polarization using the asymmetry in the elastic scattering off polarised electrons, Nucl. Instr. Meth. A **443** (2000) 1.

My personal contributions to the SMC experiment

november 1994 – – august 1995	writing of a new NMR software program in C for the polarized target *A. Tripet, N. de Groot and E. Sichtermann, SMC internal report, SMC/95/23 (1995): A User Guide for the NEW NMR Software for the SMC Polarized Target*
july 1995	helping in the production and irradiation of the NH_3 target beads in Bonn *A. Tripet, SMC internal report, SMC/95/31 (1995): Status of and Plans for the NH_3 Material for the SMC Polarized Target in 1996* *A. Deshpande, J. Kyynäräinen, A. Ogawa and A. Tripet, SMC internal report, SMC/96/07 (1996): Comparison of SMC (and Other) Target Materials and Expected Improvement in δg_1 from SMC–1996*
summer 1995	taking shifts for the polarized target
autumn 1995	calculation of the period P2A95 efficiencies *A. Tripet, SMC internal report, SMC/96/01 (1996): Efficiencies: New Function TYPE 20 Implemented for the Parametrization of W12 Efficiency*

winter 1995 – – spring 1996	some ST67 studies concerning the period P2B95
spring 1996 – – autumn 1996	taking care of the veto counters during data taking; taking shifts for the spectrometer
june 1996	alignment during the period P2A96
spring 1996 – – autumn 1996	some studies of the H2 calorimeter response *E. Rondio, J. Kiryluk and A. Tripet, SMC internal report, SMC/97/07 (1997): Inclusive asymmetry calculation using events with hadrons*
november 1996	systematic studies of the 1996 inclusive asymmetries
december 1996 – – march 1997	calculation of the 1996 hadrons efficiencies
17-21 march 1997	talk at the *DPG tagung in München* on behalf of SMC: *Combined Analysis of Spin-Dependent Structure Functions including SMC 1996 preliminary results*
spring 1997	preparation of the veto counters for the first COMPASS halo measurement
spring 1997 – – winter 1997	reprocessing of the 1993 data
january 1998	start of my Ph.D. subject: exclusive ρ^0 production
23-27 march 1998	talk at the *DPG tagung in Freiburg* on behalf of SMC: *The Hadron Method of Inclusive Asymmetry Calculation in SMC*

24-28 august 1998	poster presented at the *International Nuclear Physics Conference INPC/98* (Paris 1998) on behalf of SMC: *The SMC experiment at CERN: DIS of polarized muons off polarized p and d targets*
15-19 march 1999	talk at the *DPG tagung in Heidelberg* on behalf of SMC: *Exclusive ρ^0 production in polarized l-N scattering in SMC*
19-23 april 1999	talk at the *Workshop on Deep Inelastic Scattering and QCD, DIS '99* (Zeuthen 1999) on behalf of SMC: *Exclusive ρ^0 Production in Polarized DIS at SMC*

Abstract

The main subject of this thesis is the exclusive ρ^0 production in polarized lepton-nucleon scattering, $\vec{\mu} + \vec{N} \rightarrow \mu' + N' + \rho^0\,, (\rho^0 \rightarrow \pi^+\pi^-)$. Cross section spin-asymmetries for this process are reported. These asymmetries have been determined for the first time by the Spin Muon Collaboration experiment (SMC) at CERN at low Q^2 in the photo-production limit and at large Q^2 in the kinematical range of $0.01 < Q^2 < 60$ GeV^2 and $140 < W^2 < 310$ GeV^2 ($\langle W \rangle \simeq 15$ GeV). In this kinematical region, the unpolarized cross section for exclusive ρ^0 production rises slowly with W, which is in general interpreted in terms of Pomeron exchange. This study, therefore, can bring for the first time direct information on the spin dependence in diffraction. About 115,000 ρ^0's have been selected from the full SMC data set. Within the statistical precision no significant asymmetries have been observed at low Q^2.

This thesis also presents the complete and final results on the spin dependent structure functions for the proton and the deuteron from SMC in the kinematical range of $0.008 < x < 0.7$ and $0.2 < Q^2 < 80$ GeV^2. The QCD analysis of these data is described. The SMC results are compared to the theoretical predictions, which are the Bjorken and the Ellis-Jaffe sum rules. This comparison required a QCD evolution procedure of the data. The SMC results confirm the Bjorken sum rule, while they show that the Ellis-Jaffe sum rule is violated for both proton and deuteron, confirming the EMC findings that quarks carry only a small fraction of the nucleon's spin.

The SMC experiment used longitudinally polarized high energy muon scattering from longitudianlly polarized proton and deuteron targets, in order to measure the muon-proton and muon-deuteron inclusive and exclusive cross section spin-asymmetries.

Introduction

The atomic nucleus is built of protons and neutrons, spin-$\frac{1}{2}$ particles called nucleons. The intrinsic angular momentum or spin is a surprising property of the elementary particles, which arises naturally in relativistic quantum theories (Dirac equation), but does not have a counterpart in classical theories, which would aid our intuition: *[T]his property [spin] of elementary particles is peculiar to quantum theory... and therefore has in principle no classical interpretation... In particular, it would be wholly meaningless to imagine the 'intrinsic' angular momentum of an elementary particle as being the result of its rotation 'about its own axis'* [1].

Soon after the Stern-Gerlach experiment spin was recognized to be a fundamental property of particles as important as the elementary charge. Spin characterizes the fermions by Pauli's exclusion principle and Dirac's relativistic equation of motion. Under normal conditions of matter, however, the spatial projections of the spin of a fermion are equally populated, and thus observables related to the spin usually remain undetected. With the development of polarized beams and targets in the last decades, it has become possible to study the spin dependence of the interaction dynamics and of the nucleon structure in nuclear and particle physics.

Analogous to the Rutherford's scattering experiment with a beam of α particles striking a gold foil to probe the structure of the atom, in 1968 the scattering of a 20 GeV electron beam off a nucleon showed that the nucleon has a complex substructure [2]. In this experiment, performed at the Stanford Linear Accelerator Center (SLAC), it appeared that the electrons were behaving as if scattering off free pointlike spin-$\frac{1}{2}$ objects within the nucleon. These pointlike objects were called *partons* by Feynman [3] and had been identified with the quarks postulated in 1964 by Gell-Mann and Zweig [4]. That, indeed, gave real existence to

the quarks, which initially were considered only as mathematical entities.

The simplest picture of the nucleon structure is provided by the naive Quark Parton Model (QPM), in which the nucleon is composed of three spin-$\frac{1}{2}$ *valence* quarks, which carry the quantum numbers of the nucleon. The proton consists of two up (u) quarks with electric charge $\frac{2}{3}$ (in units of the proton's charge) and one down (d) quark with charge $-\frac{1}{3}$. The neutron is formed under isospin symmetry by exchanging the u quarks with d quarks and the d quark with a u quark; therefore it consists of two d quarks and one u quark. The *valence* quarks are surrounded by a *sea* of virtual quark-antiquark pairs and spin-1 gluons, which are the mediators of the strong force. In addition to the u and d quarks, the *sea* also consists of strange (s) quarks with charge $-\frac{1}{3}$, while the heavy quarks charm (c), bottom (b) and top (t) do not play a role at the energies of this experiment.

The naive QPM satisfactorily accounts for some of the static properties of the hadrons by simply adding up the quantum numbers of the valence quarks, like the anomalous magnetic moments of the baryons. The three valence quarks are assumed to carry all the spin of the nucleon, i.e. two quarks have opposite spins, and the spin of the nucleon is carried by the spin of the third quark. Once the proton wave function has been properly symmetrized, one finds $\Delta u = \frac{4}{3}$ and $\Delta d = -\frac{1}{3}$, where Δu (Δd) indicates the number of u (d) quarks with their spin parallel to the proton spin.

Quantum ChromoDynamics (QCD) is the best theory presently available of the nuclear interactions and it attempts to provide a complete dynamical description of the internal structure of the nucleon. According to QCD, the quarks are bound by spin-1 gluons, which are the mediators of the strong force. In addition to flavor, spin and electric charge, quarks as well as gluons carry *color*, i.e. the charge associated with the strong interaction that can assume three different values (red, green, blue).

Since the gluons themselves carry color, they can interact with other gluons. Thus the strong coupling constant α_s grows as the distance between the quarks increases, leading to confinement. Indeed, at large inter-quark distances free quarks have not been observed. The quarks are confined within hadrons, bound systems of quarks and antiquarks, which are color singlets. When a quark is knocked out of a nucleon by means of a deep inelastic scattering process, part of

that energy is converted into quark-antiquark pairs, and a stream or jet of hadrons is formed. At small inter-quark distances, the strong coupling constant is small and the quarks appear as almost free. This phenomenon is called asymptotic freedom and it allows the use of the perturbation theory within QCD at small distances.

The cross section for deep inelastic scattering (DIS) displays a phenomenon called *scaling*, i.e. it does not depend on the energy scale given by the 4-momentum transfer Q^2. This is attributed to the fact that the scattering centers are pointlike and free. The scaling behavior had been predicted by Bjorken in the limit of infinite momentum transfers [5], but was unexpected at momentum transfers as low as a few GeV^2. Scaling is easily understood in the QPM: the DIS cross section is the incoherent sum of the parton cross sections. Further, the nucleon structure is parametrized by the parton distribution functions, $f(x)$, which are related to the probability to find a parton of a certain type f carrying the fraction x of the nucleon's momentum. The cross section for the lepton–nucleon scattering is directly related to the so-called structure functions, which give the momentum and spin distribution of the quarks inside the nucleon.

As the resolution of the scattering probe increases, binding effects are revealed: what appears to be a pointlike parton (quark) at a certain distance (i.e. resolution) turns out to be a collection of quarks, antiquarks and gluons at a higher resolution (i.e. smaller distance). These effects lead to the so-called scaling violations of the structure functions, i.e. a small Q^2 dependence, which is well described by perturbative QCD (pQCD). Gluons are radiated by quarks and antiquarks, and can split into quark-antiquark pairs. The momentum distributions of quarks, antiquarks and gluons, however, cannot be calculated within pQCD. The zeroth-order approximation to pQCD is the naive QPM.

Since both quarks and gluons possess spin, and the forces between them are spin dependent, one can expect important information on these forces and on the nucleon structure to be obtained through the study of the spin dependent aspects of the nucleon interactions, as has been the case before in atomic and nuclear physics. Questions about the spin dependence of the nuclear reactions, therefore, tend to probe the underlying theory very deeply.

Polarized deep inelastic scattering experiments, aimed at the study of the

proton spin structure, started at SLAC in 1972 [6]. Much concern, however, from both the theoretical and the experimental point of view has been raised about 15 years later by the European Muon Collaboration (EMC), which probed the proton spin structure at the partonic level, and contrary to the expectations showed that the spin of the proton may not be completely accounted for by the spins of its valence quarks [7, 8].

The EMC spin-experiment was carried out at CERN in 1984-1985 with a 200 GeV muon beam produced by 450 GeV protons extracted from the SPS. Thanks to the higher beam energy, EMC significantly extended the kinematical range to lower values of x, mainly populated by sea quarks, down to $x \sim 0.01$. In 1988 EMC reported results about the proton spin [7], which disagreed with the simple model of the nucleon structure in which the proton intrinsic angular momentum is primarily carried by the valence quark spins. The EMC data in the larger x region were consistent with those of the first experiments carried out at SLAC. The combined EMC-SLAC result substantially differed from the predictions of the naive QPM description of the nucleon spin in terms of its valence quark spins. This result indicated that only (12 ± 16) % of the nucleon's spin was carried by the quark spins [8]. Within the experimental errors, the contribution from the quark spins to the nucleon spin was even consistent with zero. This discrepancy became to be known as the *proton spin crisis*.

The measurements of the polarized structure functions in polarized DIS have shown that the contributions from the quark spins are too small to account for the proton spin, that should therefore result from other sources. One possible interpretation of these measurements is that the polarization of the strange sea quarks is surprisingly large and negative. Soon it has been realized that this dramatic discrepancy from the simple quark models can be accounted for by pQCD, by also allowing the spin of gluons and the orbital angular momentum to contribute to the nucleon spin, which in units $\hbar = 1$ reads:

$$\text{proton spin} = \frac{1}{2} = \frac{1}{2}\Delta\Sigma + \Delta g + L_z \,. \tag{0.1}$$

$\Delta\Sigma$ represents the contribution to the proton spin from the valence and sea quark spins, Δg is the contribution from the gluon spins, and L_z is the orbital angular momentum of the proton constituents (quarks and gluons).

Since the 1988 findings an enormous theoretical effort was made to understand the implications of the EMC measurement. This surprising result stimulated the development of new experimental programs at CERN (SMC), SLAC and DESY (HERMES), which could validate the earlier results and further increase the measurement accuracy. There has also been a growing interest in the contribution of the quark spins to the neutron spin in order to test the isospin symmetry at the quark level (Bjorken sum rule), which constitutes a fundamental test of QCD. Measurements on polarized ^{3}He and deuteron targets have thus become necessary. These newer experiments, carried out in the 90's, in turn stimulated a new generation of experiments at CERN (COMPASS) and the RHIC Spin Program, which just started taking data.

The main topic of this thesis is the study of the exclusive ρ^0 lepto-production

$$\mu\, p \;\rightarrow\; \mu'\, \rho^0\, p' \tag{0.2}$$

in polarized muon–nucleon scattering. Such a measurement will add more insight into the exclusive ρ^0 production mechanism, as well as into its spin dependence. It will also allow to study the spin properties of the hadronic photon at very low Q^2. This thesis presents a search of possible spin dependences in the exclusive ρ^0 muo-production, which can be generalized to diffractive processes. It also presents a study on the internal spin structure of the nucleon. This work has been performed within the framework of the Spin Muon Collaboration (SMC) experiment at CERN [9].

SMC is a fixed target experiment using a longitudinally polarized 190 GeV μ^+ beam and longitudinally polarized nuclear targets. Data were taken with polarized deuteron targets (deuterated butanol) in 1992, 1994 and 1995, and with polarized proton targets in 1993 (butanol) and in 1996 (ammonia). The primary aim of the SMC experiment has been the study of the internal spin structure of the proton and of the neutron and the comparison of the associated first moments with the Ellis-Jaffe and Bjorken sum rules. The SMC results are expected to be useful to further test the nucleon models and to explore the contribution of the quark spins to the nucleon spin.

The exclusive vector meson production can be well described by the Vector Meson Dominance (VMD) model. The underlying idea of the VMD model is

that the photon, as allowed by the Heisenberg uncertainty principle, for part of its time, transforms into a hadron and behaves as a hadron. All lepton induced processes in the DIS regime, however, have shown until now that the virtual photon behaves at large Q^2 like a pointlike particle. At low Q^2 as well as in real photo-production, these processes, on the contrary, including the exclusive ρ^0 production, show the typical properties of a hadronic interaction. Therefore, it is commonly accepted that the photon has a hadronic component at low values of Q^2.

In the VMD model, the virtual photon, generated by the incident lepton beam, fluctuates into an intermediate virtual quark-antiquark hadronic state with the same quantum numbers of the photon, like an off-shell ρ^0 meson. This off-shell ρ^0 meson, by means of a hadronic strong interaction process, scatters off the target to an on-shell ρ^0 (real state), while the target nucleon emerges intact from the interaction. This process can be viewed as an elastic scattering of two hadrons, the ρ^0 and the target nucleon, and thus is also commonly referred to as elastic ρ^0 production. Phenomenologically, the interaction can be regarded either as the exchange of a Regge trajectory with the vacuum quantum numbers between the vector meson and the target or, at high energies within the pQCD, as the exchange of a gluon or quark pair between the virtual quark-antiquark pair and the constituents of the target nucleon.

Some aspects of the spin dependence in the exclusive vector meson production, in particular for the ρ^0 meson, have been already studied for some time. However, only the helicity transfer amplitudes from the virtual photon to the ρ^0, without taking into account the spin of the target nucleon, have been measured from the angular distributions of the vector meson production and decay. More recently, these data have shown a possible helicity non-conservation when transferring the photon helicity to the vector meson.

First studies of the exclusive ρ^0 production in polarized lepto-production have been recently presented by the SMC [10] and HERMES [11] experiments in 1999. The SMC data cover a very broad range in Q^2 from the photo-production limit to the DIS regime at medium W ($\langle W^2 \rangle \sim 240$ GeV^2), where the ρ^0 production is believed to be mediated by the Pomeron exchange. The HERMES data cover a considerably lower range in W ($\langle W^2 \rangle \sim 24$ GeV^2), where the ρ^0 production

is expected to be dominated by Reggeon exchanges. The naive expectations from models of vector meson production based on Regge theory suggest no spin dependence, since the exchanged objects are spin-0. In pQCD the exclusive process at medium-large W is described in terms of the exchange of a pair of gluons, thus a spin-asymmetry might result from the gluon polarization inside the polarized nucleon.

Exclusive processes represent an important class of phenomena known as diffractive scattering. In high energy scattering diffraction combines the aspects of the particle and the wave like nature of the strong interaction. For instance, the elastic hadron–hadron scattering differential cross section shows the pattern known from diffractive processes in optics with a dominant peak in the forward direction accompanied by minima and maxima. Diffraction, therefore, can be seen as another way to look at the nucleon and to study its interaction dynamics.

Diffraction covers a wide range of phenomena, from optics to quantum mechanics, and from nuclear to hadronic physics. The first interpretation of diffraction [12] was that different components of the projectile were differently absorbed by the target, leading to the creation of new particle states. That was the first indication of the composite nature of hadrons, even before the advent of DIS experiments. A general definition of diffraction is of a high energy reaction, in which no quantum numbers are exchanged between the colliding particles. In diffraction the energy transfer between the two interacting hadrons is generally small, but one (or both) hadron dissociates into multi-particle final states, preserving the quantum numbers of the associated initial hadrons.

Hadronic processes are generally classified as *soft* or *hard*. *Soft* processes are characterized by an energy scale of the order of the hadron size. Typical examples are the elastic hadron–hadron scattering and the diffractive processes. *Hard* processes are characterized by two energy scales: one is still the hadron size and the other, *hard*, the momentum transfer. A typical example is DIS, where the *soft* part is embodied in the non-calculable quark and gluon distribution functions, while the lepton–parton scattering at large Q^2 represents the *hard* part.

The main development of the last years in this field is the discovery and investigation of diffractive processes, which have *soft* and *hard* properties at the same time. A simple example is the exclusive ρ^0 lepto-production at large Q^2.

The interplay between *soft* and *hard* processes in diffraction is of particular importance due to its potential for elucidating the transition from preturbative to non-perturbative QCD. A full QCD based theoretical description of diffraction is still not available and the phenomenological models proposed to describe the data have only partially been successful.

This thesis is organized as follows. In chapter 1 the formalism and the theoretical background of deep inelastic scattering applied to polarized lepton–nucleon scattering is introduced. An overview of the exclusive ρ^0 lepto-production phenomenology including a general discussion of diffractive processes is presented in chapter 2, where the current understanding of these processes based on non-perturbative and perturbative theoretical models is also examined. The main components of the SMC experimental apparatus, including the polarized muon beam and the polarized target, are described in chapter 3. The reconstruction procedures of the events recorded with the SMC apparatus are summarized in chapter 4. In chapter 5 the inclusive spin asymmetry results are presented along with the asymmetry extraction procedure and the error evaluation. A comparison of the results with the theoretical predictions synthetized in the spin sum rules is also made. The main subject of this thesis is presented in detail in chapters 6 and 7: in chapter 6 the isolation of the exclusive ρ^0 sample from the bulk of inclusive events is described, while the spin-asymmetry results for the exclusive ρ^0 production are presented in chapter 7. A general discussion of the exclusive and inclusive results presented in this thesis and their physics implications and difficulties in their interpretation, as well as an outlook on future perspectives, conclude the thesis.

Chapter 1

The Spin Structure of the Nucleon

Polarized lepton nucleon deep inelastic scattering (DIS) is the unique tool available to physicists to study the spin structure of the nucleon. It can be depicted as similar to the dissection in biology, where the physicist's knife would be the polarized lepton probe and the physicist's mouse the polarized target nucleon. The higher the energy of the probe, the smaller the substructure probed of the nucleon will be, similar to the sharpness of the biologist's knife.

Here only an overview of the most important aspects of this subject is given. Unpolarized DIS is treated in detail in many textbooks, like for instance [13, 14], while the polarized case is covered mainly in several reviews and lecture notes, among which [15, 16, 17], in some textbooks, like [18, 19, 20], and in the recent monography [21]. This chapter is mainly based on the above quoted literature.

1.1 The Kinematics of Deep Inelastic Scattering

Figure 1.1 illustrates the scattering of a high energy polarized lepton[1] with 4-momentum $k^\mu = (E, \vec{k})$ and spin 4-vector s^μ off a polarized target nucleon of 4-momentum $p^\mu = (M, \vec{0})$ and spin S^μ. In this process a large amount of energy is transferred from the lepton to the target by a photon of high virtuality,

[1] muons in the case of the SMC experiment at CERN, electrons at SLAC and DESY

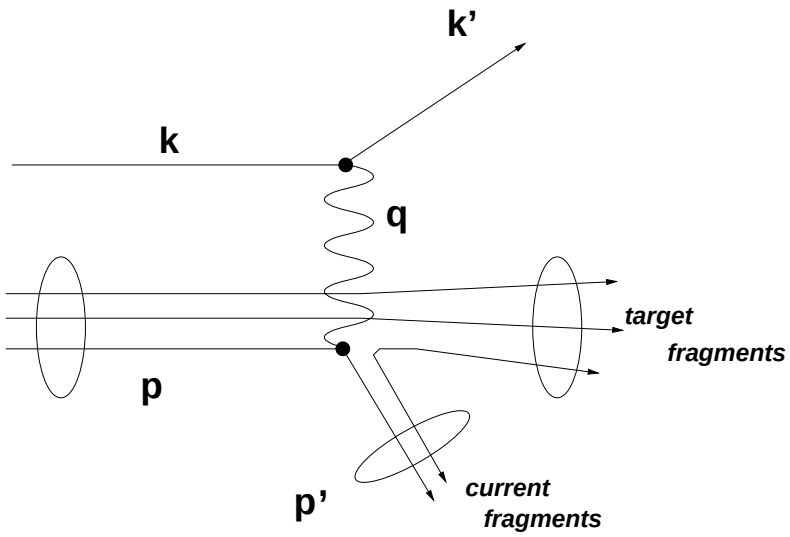

Figure 1.1: Deep Inelastic Scattering Feynman diagram.

which is accounted for by the 4-momentum transfer, q^μ. Usually, in an inclusive measurement the energy E' and the scattering angle ϑ of the outgoing lepton of 4-momentum $k^{\mu\prime} = (E', \vec{k}')$ are measured.

From the two measured quantities E' and ϑ, and the incident beam energy E, **three independent variables Q^2, x and y can be extracted**. The interaction is commonly described with the following variables (not all of them, however, are independent):

$$\begin{array}{rcccll} -q^2 = Q^2 & = & -(k-k')^2 & \approx & 4\,E\,E'\,\sin^2(\frac{\vartheta}{2}) & 0 \le Q^2 \le 2M\nu \\ x & = & \dfrac{Q^2}{2p\cdot q} & = & \dfrac{Q^2}{2M\nu} & 0 \le x \le 1 \\ y & = & \dfrac{p\cdot q}{p\cdot k} & = & \dfrac{\nu}{E} & 0 \le y \le 1 \\ \nu & = & \dfrac{p\cdot q}{M} & = & E - E' & 0 \le \nu \le E \\ W^2 & = & (q+p)^2 & = & M^2 + 2M\nu - Q^2 & \\ s & = & (k+p)^2 & = & \dfrac{Q^2}{xy} + M^2 & \end{array} \tag{1.1}$$

where

- q^2 is the squared 4-momentum transfer from the lepton to the nucleon, i.e. the squared 4-momentum of the exchanged virtual photon γ^*; since $q^2 < 0$, it is convenient to define $Q^2 = -q^2$ (thus $Q^2 > 0$). To the virtual photon an effective wavelength $\lambda = \dfrac{1}{\sqrt{Q^2}}$ can be assigned; therefore the higher the Q^2, the smaller the structure that can be probed, i.e. the higher the resolution;

- the dimensionless Lorentz - invariant kinematical variable x, known as the Bjorken scaling variable, is interpreted as the fraction of the nucleon momentum carried by the struck quark;
- y is the fraction of the incident lepton energy carried by the interacting virtual photon, i.e. the energy loss of the incident lepton;
- ν is the energy of the virtual photon;
- W^2 is the invariant mass squared of the final state hadronic system (as well as of the initial $\gamma^* - N$ system); in DIS, W^2 is much larger than the nucleon mass squared, $W^2 \gg M^2$, thus implying $x < 1$;
- and $\sqrt{s}$ is the total center of mass energy of the lepton – nucleon system.

The last part on the right-hand side of each equation holds only in the laboratory frame, where the target nucleon is at rest, while the last column gives the kinematical domain of each variable. The kinematics of an inclusive scattering, integrated in azimuth, can be completely described by only two of the six variables introduced above, usually x and Q^2. The deep inelastic or Bjorken limit is reached when Q^2 and ν both go to infinity with the ratio $x = \frac{Q^2}{2M\nu}$ finite and fixed.

In fixed target experiments, including this one, the dominant reaction mechanism is electromagnetism. The contribution from the parity violating Z^0 exchange can be neglected since $Q^2 \ll M_Z^2$ and the parity conserving one-photon exchange process (Born cross section) is an excellent approximation.

1.2 The Lepton–Nucleon Cross Section

The probability for a polarized lepton to scatter off a polarized nucleon is described by the spin-dependent cross section. The DIS cross section can be split into a spin-independent (i.e. unpolarized) term $\overline{\sigma}$ and two spin-dependent (i.e. polarized) terms, $\Delta\sigma_{\parallel}$ and $\Delta\sigma_{\perp}$:

$$\sigma = \overline{\sigma} + \frac{1}{2}\cos\psi\Delta\sigma_{\parallel} + \frac{1}{2}\cos\phi\sin\psi\Delta\sigma_{\perp}\,. \tag{1.2}$$

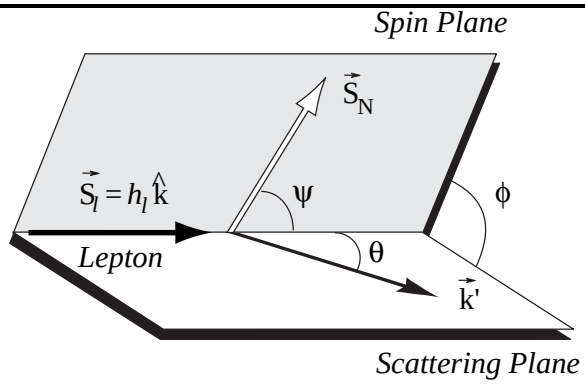

Figure 1.2: The scattering and the polarization (spin) planes including the three angles used to describe the scattering process.

The spin-dependent terms depend on the polar angle ψ between the spin polarization vector of the muon and that of the nucleon and the azimuthal angle ϕ between the lepton scattering plane and the spin vector of the nucleon (Figure 1.2). For the beam and the target longitudinally polarized ($\sin\psi = 0$), only $\Delta\sigma_{\parallel}$ contributes to the cross section, while for a transversely polarized target ($\cos\psi = 0$) only $\Delta\sigma_{\perp}$ contributes to the cross section.

The Born DIS differential cross section (i.e. the one-photon exchange process) for a lepton scattering off a nucleon, can be expressed as the product (contraction) of a leptonic tensor $L_{\mu\nu}$ and a hadronic tensor $W^{\mu\nu}$

$$\frac{d^3\sigma}{dx\, dQ^2\, d\phi} = \frac{y^2}{Q^2}\frac{\alpha^2}{Q^4} L_{\mu\nu} W^{\mu\nu} \,, \tag{1.3}$$

where $\alpha = \frac{e^2}{4\pi\hbar c}$ is the electromagnatic coupling constant and $\frac{\alpha^2}{Q^4}$ is the propagator of the exchanged virtual photon. This cross section can be rewritten as a function of any pair of variables given in Equation 1.1. To obtain the total DIS cross section, higher order QED corrections are typically applied (Section 5.3).

The **leptonic tensor** $L_{\mu\nu}$ can be calculated exactly in QED. After summing over the unmeasured final lepton spins (s'), it can be expressed as follows:

$$\begin{aligned} L_{\mu\nu}(k,k',s) &= \sum_{s'} \left[\overline{u}(k',s')\gamma_\mu u(k,s)\right] \left[\overline{u}(k',s')\gamma_\nu u(k,s)\right]^* \\ &= 2\, L^{(S)}_{\mu\nu}(k,k') + 2i\, L^{(A)}_{\mu\nu}(k,k',s) \,. \end{aligned} \tag{1.4}$$

The superscript (S) refers to the symmetric part of the tensor:

$$L^{(S)}_{\mu\nu}(k,k') = k_\mu k'_\nu + k'_\mu k_\nu - g_{\mu\nu}\,(k\cdot k' - m^2) \tag{1.5}$$

and the superscript (A) refers to its antisymmetric part:

$$L^{(A)}_{\mu\nu}(k,k',s) = m_l\,\epsilon_{\mu\nu\alpha\beta}\,s^\alpha(k-k')^\beta\ , \tag{1.6}$$

where $g_{\mu\nu}$ is the metric tensor, $\epsilon_{\mu\nu\alpha\beta}$ is the fully antisymmetric Levi-Civita tensor and s^α is the spinor (spin 4-vector) of the incoming lepton

$$s^\alpha = \frac{1}{2}\overline{u}(k,s)\gamma^\alpha\gamma_5 u(k,s) = \frac{2\lambda}{m_l}\left(|\vec{k}|, E\frac{\vec{k}}{|\vec{k}|}\right)\ , \quad s^\alpha s_\alpha = -1 \tag{1.7}$$

with λ the lepton helicity ($\lambda = \pm\frac{1}{2}$) and m_l its mass. From Equation 1.7 it might appear that all polarization effects are suppressed at high energy by a factor m_l ($s^\alpha \propto \frac{1}{m_l}$). However, in the case of longitudinal polarization (see Equation 1.6), $m_l s^\alpha \to k^\alpha$ and there is no suppression.

The **hadronic tensor** $W^{\mu\nu}$ describes the internal electromagnetic structure of the nucleon and it depends on the non-perturbative strong interaction dynamics. $W^{\mu\nu}$ cannot be expressed directly with the fundamental fields of the incoming and outgoing fermions and it is parametrized in terms of the Lorentz invariant structure functions, which have been determined experimentally.

The hadronic tensor can be expressed in terms of the hadronic current J^μ as

$$\begin{aligned} W^{\mu\nu}(q,p,S) &= \frac{1}{2\pi}\sum_X \langle p,S|J^\mu(0)|X\rangle\langle X|J^\nu(0)|p,S\rangle(2\pi)^4\delta^4(p+q-p_X) \\ &= \frac{1}{2\pi}\int d^4\xi e^{iq\xi}\langle p,S|[J^\mu(\xi),J^\nu(0)]|p,S\rangle\,, \end{aligned} \tag{1.8}$$

where S denotes the polarization vector of the spin-$\frac{1}{2}$ target nucleon, and p_X is the total momentum of the final hadronic state X. The sum over X runs over all possible final states. The step from the first to the second line in Equation 1.8 involves the completness relation of the final states X, $\sum_X = |X\rangle\langle X| = 1$ and the rewriting of the delta function as a Fourier integral. The space-time interval ξ between the points where the currents act, determines the scale (or the distance), which is probed in deep inelastic scattering [17]. In the Bjorken limit of DIS, $\xi \to 0$. This expression for $W^{\mu\nu}$ is the starting point of the *Operator Product Expansion* (OPE) approach [22], which expands the current commutators in terms of local operators and concentrates on their behavior on the light-cone.

Analogously to the leptonic tensor, the hadronic tensor can be split into a symmetric and an antisymmetric part:

$$W^{\mu\nu}(q,p,S) = W^{\mu\nu(S)}(q,p) + iW^{\mu\nu(A)}(q,p,S)\ . \tag{1.9}$$

Current conservation at the hadronic vertex, parity conservation and invariance under time reversal yield for the symmetric part of $W^{\mu\nu}$:

$$W^{\mu\nu(S)}(q,p) = \left(-g^{\mu\nu} + \frac{q^\mu q^\nu}{q^2}\right) W_1(p\cdot q, q^2) + \left[\left(p^\mu - \frac{p\cdot q}{q^2}q^\mu\right)\left(p^\nu - \frac{p\cdot q}{q^2}q^\nu\right)\right]\frac{W_2(p\cdot q, q^2)}{M^2}\ , \tag{1.10}$$

and for the antisymmetric part of $W^{\mu\nu}$

$$W^{\mu\nu(A)}(q,p,S) = \epsilon^{\mu\nu\alpha\beta}q_\alpha\left\{MS_\beta G_1(p\cdot q, q^2) + \left[(p\cdot q)S_\beta - (S\cdot q)p_\beta\right]\frac{G_2(p\cdot q, q^2)}{M}\right\}\ . \tag{1.11}$$

W_1 and W_2 are the spin-averaged structure functions and G_1 and G_2 the spin-dependent structure functions. Sometime they are also referred to as inelastic form factors [21].

In Equation 1.3 only products of definite symmetry give a non-zero contribution. When averaging over the incoming lepton helicity states (unpolarized beam), the antisymmetric part of the leptonic tensor vanish and, therefore, $W^{\mu\nu(A)}$ does not contribute to the cross section. In order to observe spin effects in the inclusive cross section, both the beam and the target have to be polarized.

First results from unpolarized DIS in the late sixties showed that the structure functions are approximately independent of Q^2 for Q^2 values above few GeV^2 [2]. This behavior has been already anticipated by Bjorken [5]. In the DIS limit of $Q^2 \to \infty$ and $\nu \to \infty$ at fixed x (Bjorken limit), the **structure functions** become approximately independent of Q^2, up to logarithms of Q^2 generated by the QCD radiative corrections, and depend only on the dimensionless **scaling variable** $x = \frac{Q^2}{2M\nu}$. This behavior is known as **scaling**. Within the **Quark Parton Model** this scaling property of the DIS cross section is interpreted as the elastic scattering of the incoming lepton *off a free parton (quark) in the target nucleon* via the exchange of a virtual photon and the scaling variable x represents the fraction of the total nucleon momentum carried by the struck quark.

In order to exhibit scaling explicitly, the structure functions should not depend on the nucleon mass, i.e. they should be dimensionless. The leptonic and hadronic tensors introduced above are indeed dimensionless, while the structure functions, as given in Equations 1.10 and 1.11, are not. They can be multiplied with factors

of M and ν in order to make them become dimensionless quantities and, in the Bjorken limit, they are commonly replaced with functions of x only:

$$\begin{aligned} M\,W_1(p\cdot q, q^2) &= F_1(x,Q^2) \;\to\; F_1(x) \\ \nu\,W_2(p\cdot q, q^2) &= F_2(x,Q^2) \;\to\; F_2(x) \\ M^2\nu\,G_1(p\cdot q, q^2) &= g_1(x,Q^2) \;\to\; g_1(x) \\ M\nu^2\,G_2(p\cdot q, q^2) &= g_2(x,Q^2) \;\to\; g_2(x)\,. \end{aligned} \tag{1.12}$$

1.3 The Virtual Photon–Nucleon Cross Section

The Feynman diagram in Figure 1.1 can also be interpreted as a virtual photo-absorption by a target nucleon, where the muon beam simply acts as a source of (interacting) virtual photons. The differential cross section can be written as a product of the flux of transversely and longitudinally polarized virtual photons, Γ_T and $\Gamma_L = \epsilon\Gamma_T$, and the photo-absorbtion cross section for transversely and longitudinally polarized virtual photons σ_T and σ_L:

$$\frac{d^2\sigma^{\mu p\to\mu' X}}{dx\,dQ^2} = \Gamma_T\left(\sigma_T^{\gamma^* p\to X}(x,Q^2) + \epsilon\sigma_L^{\gamma^* p\to X}(x,Q^2)\right) \tag{1.13}$$

with Γ_T the flux of transversely polarized virtual photons

$$\Gamma_T(x,Q^2) = \frac{\alpha}{2\pi}\frac{K}{Q^2E(1-\epsilon)}\,. \tag{1.14}$$

ϵ is the virtual photon polarization (i.e. the flux ratio of longitudinally to transversely polarized photons)

$$\epsilon = \frac{2(1-y) - \frac{\gamma^2y^2}{2}}{1 + (1-y)^2 + \frac{\gamma^2y^2}{2}} \tag{1.15}$$

and K a normalization factor (also referred to as the virtual photon flux), which is not a well defined quantity. According to the Hand's convention [23]

$$K = \nu - \frac{Q^2}{2M} = \nu(1-x) \tag{1.16}$$

and for real photons ($Q^2 \to 0$) it becomes $K = \nu$. γ is a kinematical factor

$$\gamma = \frac{2xM}{\sqrt{Q^2}} = \frac{\sqrt{Q^2}}{\nu}\,, \tag{1.17}$$

with $\gamma \to 0$ for $Q^2 \gg M^2$.

The virtual photo-absorbtion cross section is given by:

$$\sigma_\lambda^{\gamma^* p \to X} = \frac{4\pi^2\alpha}{K} \varepsilon_\lambda^{\mu *} \varepsilon_\lambda^\nu W_{\mu\nu}^{(S)} \,, \tag{1.18}$$

where $W_{\mu\nu}^{(S)}$ is the hadronic tensor introduced in the previous section and ε_λ is the polarization vector of the virtual photon of helicity λ ($\lambda = \pm 1\,, 0$) and mass $q^2 < 0$. Taking $\vec{q}$ along the z-axis, i.e. $q^\mu = (\nu, 0, 0, \sqrt{\nu^2 + Q^2})$, the polarization vectors of transversely (circularly) polarized and longitudinally polarized (or scalar) virtual photons are

$$\varepsilon_\pm^\mu = \mp \frac{1}{\sqrt{2}} \Big(0, 1, \pm i, 0\Big) \quad \text{and} \quad \varepsilon_0^\mu = \frac{1}{\sqrt{Q^2}} \Big(\sqrt{\nu^2 + Q^2}, 0, 0, \nu\Big) \,. \tag{1.19}$$

Note that the normalization factor K cancels in the physical cross section (Equation 1.13).

Equation 1.13 is known as the **Equivalent Photon Expression (EPE)**. This formalism can be easily generalized to the polarized case.

Via the **optical theorem** [1] the hadronic tensor $W_{\mu\nu}$ is related to the imaginary part (more precisely absorptive part) of the Feynman helicity amplitude for forward scattering of virtual photons off nucleons, i.e. to the forward virtual Compton helicity amplitude for

$$\gamma_h^* + N_H \to \gamma_{h'}^* + N_{H'} \,, \tag{1.20}$$

where $h(h')$ and $H(H')$ indicate the helicities of the virtual photon and of the nucleon in the initial (final) state. Thus (polarized) DIS can be described also in terms of helicity amplitudes. This approach is valid exclusively for purely inclusive scattering.

From parity and time reversal invariance, there are 4 independent helicity amplitudes $M_{hH;h'H'}$ for scattering off spin-$\frac{1}{2}$ nucleons, to which the 4 independent structure functions F_1, F_2 and g_1, g_2 are associated:

$$\begin{array}{lcll}
\sigma_T^{\frac{1}{2}} & \propto & \frac{1}{2\pi} Im(M_{+1-\frac{1}{2};+1-\frac{1}{2}}) & = \quad F_1 - g_1 + \gamma^2 g_2, \,, \\
\sigma_T^{\frac{3}{2}} & \propto & \frac{1}{2\pi} Im(M_{+1+\frac{1}{2};+1+\frac{1}{2}}) & = \quad F_1 + g_1 - \gamma^2 g_2, \,, \\
\sigma_L^{\frac{1}{2}} & \propto & \frac{1}{2\pi} Im(M_{0+\frac{1}{2};0+\frac{1}{2}}) & = \quad -F_1 + \frac{F_2}{2x}\,(1+\gamma^2)\,, \\
\sigma_{TL}^{\frac{1}{2}} & \propto & \frac{1}{2\pi} Im(M_{+1-\frac{1}{2};0+\frac{1}{2}}) & = \quad \gamma\,(g_1 + g_2)\,.
\end{array} \tag{1.21}$$

The superscripts $\frac{1}{2}$ and $\frac{3}{2}$ indicate the total angular momentum along the incident photon direction. The first two equations represent the absorption cross sections of transversely polarized photons (T), the third one the absorption cross section of longitudinally polarized photons (L), and the fourth one the single helicity flip cross section (TL), which is suppressed by a factor of $\frac{M}{Q}$ relative to the others and is due to the interference between the transverse and longitudinal photon scattering. It follows that also g_2 is suppressed by a factor of $\frac{M}{Q}$. This suppression of g_2 with increasing Q^2 is due to the fact that g_2 is a *higher twist* structure function [24], which represents quark - gluon correlations in the nucleon.

The total spin-independent and spin-dependent photo-absorption cross sections for transversely polarized virtual photons are given by the average and difference, respectively, of the two transversely polarized cross sections

$$\begin{aligned} \sigma_T &= \frac{1}{2}(\sigma_T^{\frac{1}{2}} + \sigma_T^{\frac{3}{2}}) \propto F_1 \,, \\ \Delta\sigma_T &= \frac{1}{2}(\sigma_T^{\frac{3}{2}} - \sigma_T^{\frac{1}{2}}) \propto g_1 - \gamma^2\, g_2 \,. \end{aligned} \tag{1.22}$$

At this point it is useful to introduce the longitudinal to transverse virtual photo-absorbtion cross section ratio R:

$$R = R(x,Q^2) \equiv \frac{\sigma_L^{\gamma^* p\to X}}{\sigma_T^{\gamma^* p\to X}} = (1+\gamma^2)\frac{F_2}{2xF_1} - 1 \,. \tag{1.23}$$

In the case of the spin-1 *deuteron target*, there are 8 independent helicity amplitudes to describe the DIS process and accordingly 4 more structure functions, denoted as $b_1 - b_4$ [25], are required. The virtual photo-absorption cross sections take the form

$$\sigma_T = \frac{1}{3}(\sigma_T^0 + \sigma_T^1 + \sigma_T^2)\,, \quad \sigma_L = \frac{1}{2}(\sigma_L^0 + \sigma_L^1)\,, \quad \sigma_{TL} = \frac{1}{2}(\sigma_{TL}^0 + \sigma_{TL}^1) \tag{1.24}$$

and an additional cross section $\sigma_{TT} = \sigma_{TT}^0$ appears. This cross section corresponds to the double helicity flip amplitude and is suppressed by a factor $\frac{M^2}{Q^2}$. The new structure functions b_3 and b_4 behave like the *higher twist* structure function g_2 and are suppressed by a factor of $\frac{M}{Q}$, while $b_2 \approx 2xb_1$. b_1 is expected to be very small [26] and in all analyses up to now it has been assumed that $b_1 \equiv 0$.

1.4 The Cross Section Asymmetries

To determine the nucleon spin structure function g_1, the cross section difference $\Delta\sigma_{\parallel}$ should be measured directly, but this is too difficult in practice. In a polarized DIS experiment it is far easier to measure the asymmetries of the lepton – nucleon cross sections.

The **longitudinal lepton - nucleon asymmetry** $A_{\parallel}$ is defined as

$$A_{\parallel} \equiv \frac{\Delta\sigma_{\parallel}}{\overline{\sigma}} = \frac{\sigma^{\vec{\Leftarrow}} - \sigma^{\vec{\Rightarrow}}}{\sigma^{\vec{\Leftarrow}} + \sigma^{\vec{\Rightarrow}}}\,, \tag{1.25}$$

where the incident lepton longitudinal polarization ($\rightarrow$) is parallel or anti-parallel to the longitudinal target polarization ($\Leftarrow$ or $\Rightarrow$). Analogously, the transverse lepton – nucleon asymmetry $A_{\perp}$ is defined as

$$A_{\perp} \equiv \frac{\Delta\sigma_{\perp}}{\overline{\sigma}} = \frac{\sigma^{\vec{\Downarrow}} - \sigma^{\vec{\Uparrow}}}{\sigma^{\vec{\Downarrow}} + \sigma^{\vec{\Uparrow}}}\,, \tag{1.26}$$

where the incident lepton longitudinal polarization ($\rightarrow$) is perpendicular to the transverse target polarization ($\Downarrow$ or $\Uparrow$). The spin orientations in Equations 1.25 and 1.26 refer to the laboratory frame, where the target nucleon is at rest.

The measured asymmetries $A_{\parallel}$ and $A_{\perp}$ do not have a straightforward physics interpretation and they also strongly depend on the incident beam energy, making the comparison between different experiments difficult. The scattering asymmetry results are therefore presented in terms of the more basic virtual one-photon exchange asymmetries A_1 and A_2, which have a simple physical interpretation:

$$A_1 \equiv \frac{\sigma_T^{1/2} - \sigma_T^{3/2}}{\sigma_T^{1/2} + \sigma_T^{3/2}}\,, \tag{1.27}$$

$$A_2 \equiv \frac{\sigma_{TL}}{\sigma_T^{1/2} + \sigma_T^{3/2}} \tag{1.28}$$

and are directly related to the g_1 and g_2 structure functions:

$$A_1 = \frac{g_1 - \gamma^2 g_2}{F_1}\,, \tag{1.29}$$

$$A_2 = \frac{\gamma(g_1 + g_2)}{F_1}\,. \tag{1.30}$$

The asymmetries A_1 and A_2 can be combined to obtain g_1 and g_2:

$$g_1 = \frac{F_1}{1+\gamma^2}\left(A_1 + \gamma A_2\right) = \frac{F_2}{2x(1+R)}\left(A_1 + \gamma A_2\right) , \tag{1.31}$$

$$g_2 = \frac{F_1}{1+\gamma^2}\left(\frac{A_2}{\gamma - A_1}\right) = \frac{F_2}{2x(1+R)}\left(\frac{A_2}{\gamma - A_1}\right) . \tag{1.32}$$

The virtual photon asymmetries are bound by the positivity relations [27, 28]

$$|A_1| \leq 1 \qquad \text{and} \qquad |A_2(x)| \leq \sqrt{R(x)(1+A_1(x))/2} , \tag{1.33}$$

which follow from the properties of the $M_{hH;h'H'}$ helicity amplitudes. The relation for A_2 corresponds to $|\sigma_{TL}| \leq \sqrt{\sigma_L \sigma_T}$.

The measured asymmetries $A_{\parallel}$ and $A_{\perp}$ can be related to the virtual photo-absorption cross section asymmetries A_1 and A_2 by

$$A_{\parallel} = D\left(A_1 + \eta A_2\right) , \tag{1.34}$$

$$A_{\perp} = d\left(A_2 - \xi A_1\right) , \tag{1.35}$$

where D and d are the depolarization factors, which account for the polarization transfer from the incident lepton to the virtual photon, and η and ξ are kinematical factors. The depolarization factor D, neglecting m_l, is given by

$$D = \frac{1-(1-y)\,\epsilon}{1+\epsilon\,R} \approx \frac{y\,(2-y)}{y^2 + 2\,(1-y)\,(1+R)} . \tag{1.36}$$

Assuming $R = 0$ (R and ϵ have been defined before, Equation 1.23 and 1.15), D becomes a simple function of y only; it vanishes for $y = 0$ and becomes unity for $y = 1$. Hence events with a high energy loss of the incoming lepton, i.e. large y, are the most sensitive to longitudinal polarization effects. The non-zero angle between the direction of the incoming lepton and that of the emitted virtual photon leads to a polarization component for the virtual photon orthogonal to the target polarization. This explains the presence of the small contribution of A_2 to $A_{\parallel}$ (Equation 1.34).

The other factors in Equations 1.34 and 1.35, in the high energy limit of large ν and neglecting the incident lepton mass, are given by

$$d = \sqrt{2\,\epsilon/(1+\epsilon)}\,D \approx \frac{2\sqrt{1-y}}{2-y}D \approx \frac{2y\sqrt{1-y}}{y^2 + 2\,(1-y)\,(1+R)} , \tag{1.37}$$

$$\eta = \gamma \frac{y\,\epsilon}{1-(1-y)\,\epsilon} \approx 2\,\gamma \frac{1-y}{2-y} \tag{1.38}$$

$$\xi = \eta \frac{1+\epsilon}{2\,\epsilon} \approx \frac{1}{2}\gamma\,(2-y) \tag{1.39}$$

Since the recently measured A_2 asymmetries were found to be very small or consistent with zero [29, 30, 31], and since also $\eta \ll 1$ in the kinematical range of this experiment, the term ηA_2 can be neglected and Equations 1.34 becomes

$$A_1 = \frac{A_\parallel}{D} - \eta A_2 \approx \frac{A_\parallel}{D}\,. \tag{1.40}$$

Finally the spin dependent structure function g_1 can be determined from the measured lepton – nucleon cross section asymmetry $A_\parallel$:

$$g_1 \approx \left(\frac{A_\parallel}{D}\right) F_1 \approx \left(\frac{A_\parallel}{D}\right) \frac{F_2}{2x(1+R)}\,. \tag{1.41}$$

1.4.1 The Deuteron Structure Function g_1^d

The asymmetries for the spin-1 deuteron target are given accordingly by

$$A_1 \equiv \frac{\sigma_T^0 - \sigma_T^2}{\sigma_T^0 + \sigma_T^2}\,, \tag{1.42}$$

$$A_2 \equiv \frac{\sigma_{TL}^0 + \sigma_{TL}^1}{\sigma_T^0 + \sigma_T^2}\,, \tag{1.43}$$

where it has been assumed that $b_1 \equiv 0$ (see the discussion following Equation 1.24).

In the deuteron the spins of the proton and the neutron are primarily parallel to the spin of the deuteron (S-state, L=0). There is, however, a small probability $\omega_D \approx 5$ % [32] to find the system in a state with the nucleons spins anti-parallel to the deuteron spin. In this case the two nucleons are in a state with 2 units of orbital angular momentum (D-state, L=2).

Since the deuteron is a weakly bounded state and since the nuclear effects are expected to be small, the deuteron structure function g_1^d can be considered as the average of the proton and neutron structure functions:

$$g_1^d = \frac{g_1^p + g_1^n}{2}(1 - \frac{3}{2}\omega_D)\,, \tag{1.44}$$

where the factor $\frac{3}{2}$ is a combination of several Clebsch-Gordan coefficients accounting for the deuteron D-state. From the measured proton and deuteron structure functions, g_1^p and g_1^d, the neutron spin-dependent structure function g_1^n can be therefore determined.

1.5 The Quark Parton Model

In the *naive* Quark Parton Model (QPM) [3] the nucleon is viewed as composed of free, massless, non-interacting constituents, which move colinearly within the nucleon. In the DIS process, the incident lepton scatters elastically off the point-like spin-$\frac{1}{2}$ constituents inside the nucleon. These constituents are called partons and are identified with the spin-$\frac{1}{2}$ quarks postulated by Gell-Mann and Zweig [4].

The QPM allows us thus to interpret the structure functions in terms of an incoherent sum of elastic scattering cross sections of two point-like spin-$\frac{1}{2}$ fermions, the incident lepton and the struck quark inside the nucleon. The probability to find inside a nucleon a parton of a certain type carrying a given momentum fraction is given by the parton distribution functions. The momentum fraction of the nucleon carried by the struck quark x in the Breit (or infinite momentum) frame is equivalent to the Bjorken scaling variable x. These distribution functions depend only on the variable x. Within the QPM the unpolarized structure functions F_1 and F_2 and the polarized structure function g_1 read

$$F_1(x) = \frac{1}{2}\sum_{i=1}^{n_f} e_i^2 q_i(x) \tag{1.45}$$

$$F_2(x) = \sum_{i=1}^{n_f} e_i^2 x\, q_i(x) = 2\,x\,F_1(x) \tag{1.46}$$

$$g_1(x) = \frac{1}{2}\sum_{i=1}^{n_f} e_i^2 \Delta q_i(x) \tag{1.47}$$

where

$$\begin{aligned} q_i(x) &= q_i^{\uparrow}(x) + q_i^{\downarrow}(x) + \overline{q}_i^{\uparrow}(x) + \overline{q}_i^{\downarrow}(x)\,, \\ \Delta q_i(x) &= q_i^{\uparrow}(x) - q_i^{\downarrow}(x) + \overline{q}_i^{\uparrow}(x) - \overline{q}_i^{\downarrow}(x)\,. \end{aligned} \tag{1.48}$$

$q_i^{\uparrow}(x)$, $\overline{q}_i^{\uparrow}(x)$ and $q_i^{\downarrow}(x)$, $\overline{q}_i^{\downarrow}(x)$ are the distribution functions of quarks and anti-quarks, respectively, with their spins parallel ($^{\uparrow}$) or anti-parallel ($^{\downarrow}$) to the nucleon

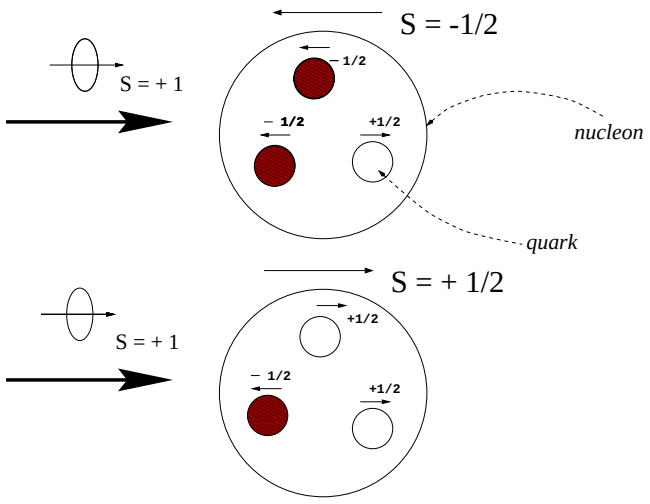

Figure 1.3: Schematic representation of a polarized photon interacting with quarks inside the polarized nucleon: a photon of helicity $+1$ (-1) can be absorbed only by a quark (filled circles) with a spin projection of $-\frac{1}{2}$ $(+\frac{1}{2})$.

spin; e_i is the electric charge of the quark of flavor i in units of the proton charge, and n_f is the number of *active* quark flavors. At the scale of this experiment, $\langle Q^2 \rangle \approx 10$ GeV^2, only the light quark flavors u, d and s contribute to the distribution functions and $n_f = 3$.

Thus, in the QPM the spin dependent structure function g_1 can be interpreted as the sum of the quark's polarizations inside a polarized nucleon, weighed with the square of their electric charges. In order to conserve the angular momentum, a virtual photon of helicity $+1$ (-1) can be absorbed only by a quark with a spin projection of $-\frac{1}{2}$ $(+\frac{1}{2})$ (Figure 1.3). Since $g_1 \approx \sigma_T^{\frac{1}{2}} - \sigma_T^{\frac{3}{2}}$, now it can be understood why the spin-dependent structure function g_1 contains information on the quark spin orientations with respect to the nucleon spin direction.

On the contrary the *higher twist* structure function g_2 does not have a simple interpretation and within the QPM $g_2 = 0$. In a sense, g_2 measures the correlation between the quarks and gluons inside the nucleon [24].

An important consequence of the Quark Parton Model is the so-called Callan-Gross relation [33]

$$F_2(x) = 2\,x\,F_1(x)\ , \tag{1.49}$$

which implies that the point-like constituents in the protons are spin-$\frac{1}{2}$ fermions. For spinless quarks F_1 would be identical to zero.

1.6 The QCD Treatment

Quarks interact via gluon exchange, which gives rise to a weak Q^2 dependence of the structure functions, known as scaling violations, which depend on logarithms of Q^2: $g_1(x) \to g_1(x, \ln Q^2)$. The presence of gluons is taken into account in the QCD improved QPM, in which each quark is surrounded by a cloud of quark-antiquark pairs (*sea* quarks) and gluons. As the virtuality Q^2 of the photon increases, smaller distances in the nucleon are probed, and more quarks and gluons are resolved over which the total nucleon momentum and spin are distributed. For instance, in addition to the polarized quark distributions, the polarized gluon distribution $\Delta g = g^{\uparrow} - g^{\downarrow}$ has to be included, since gluons split into quark-antiquark pairs, thus contributing indirectly to the quark distribution functions.

The treatment of g_1 in perturbative QCD (pQCD) follows closely that of the unpolarized parton distribution functions F_1 and F_2. At a given scale Q^2, g_1 is related to the polarized quark and gluon distributions through [34]

$$g_1(x,Q^2) = \tfrac{1}{2}\langle e^2\rangle \int_x^1 \frac{dy}{y} \Big[\begin{array}{l} C_q^S(\frac{x}{y}, \alpha_s(t))\, \Delta\Sigma(y,t) + \\ 2n_f C_g(\frac{x}{y}, \alpha_s(t))\, \Delta g(y,t) + \\ C_q^{NS}(\frac{x}{y}, \alpha_s(t))\, \Delta q^{NS}(y,t) \Big] . \end{array} \tag{1.50}$$

This expression is valid at all orders in pQCD. $\langle e^2\rangle = n_f^{-1}\sum_{k=1}^{n_f} e_k^2$ is the average of the quark charge squared, $t = \ln(\frac{Q^2}{\Lambda^2})$, α_s is the strong coupling constant, and Λ is the scale parameter of QCD.

$\Delta\Sigma$ and Δq^{NS} are the flavor singlet and non-singlet combinations of the polarized quark and antiquark distributions defined as:

$$\Delta\Sigma(x,t) = \sum_{i=1}^{n_f} \Delta q_i(x,t) \tag{1.51}$$

$$\Delta q^{NS}(x,t) = \sum_{i=1}^{n_f} \Big(\frac{e_i^2}{\langle e^2\rangle} - 1 \Big) \Delta q_i(x,t) \ . \tag{1.52}$$

C_q^S, C_q^{NS} and C_g are the quark flavor singlet, non-singlet and gluon coefficient functions. The coefficient functions are power series expansions in $\alpha_s(t)$ of the QCD higher order corrections, which are related to calculable short distance

(i.e. hard) photon-quark and photo-gluon cross sections. They are, however, renormalization scheme dependent.

QCD cannot predict the shape of the structure functions. Once the parton distributions are determined at a certain scale Q_0^2, these distributions can be *evolved* to a different scale Q^2 by a set of integro-differential equations, known as the DGLAP *evolution equations* [35]. As for the unpolarized distributions, the polarized singlet and gluon distributions are coupled by

$$\frac{d}{dt}\Delta\Sigma(x,t) = \frac{\alpha_s(t)}{2\pi}\int_x^1 \frac{dy}{y}\left[\begin{array}{l}\Delta P_{qq}^S(\frac{x}{y},\alpha_s(t))\Delta\Sigma(y,t) + \\ 2n_f\Delta P_{qg}(\frac{x}{y},\alpha_s(t))\Delta g(y,t)\end{array}\right], \tag{1.53}$$

$$\frac{d}{dt}\Delta g(x,t) = \frac{\alpha_s(t)}{2\pi}\int_x^1 \frac{dy}{y}\left[\begin{array}{l}\Delta P_{gq}(\frac{x}{y},\alpha_s(t))\Delta\Sigma(y,t)] + \\ 2n_f\Delta P_{gg}(\frac{x}{y},\alpha_s(t))\Delta g(y,t)\end{array}\right], \tag{1.54}$$

whereas the evolution of the non-singlet distribution is independent of the singlet and gluon distributions:

$$\frac{d}{dt}\Delta q^{NS}(x,t) = \frac{\alpha_s(t)}{2\pi}\int_x^1 \frac{dy}{y}\left[\,\Delta P_{qq}^{NS}(\frac{x}{y},\alpha_s(t))\Delta q^{NS}(y,t)\,\right]. \tag{1.55}$$

$\Delta P_{ij} = P_{i^\uparrow j^\uparrow} - P_{i^\downarrow j^\uparrow}$ are the QCD spin-dependent splitting functions for the polarized parton distributions. They describe the probabilities of finding a parton i carrying a momentum fraction $\frac{x}{y}$ of the parent parton j: P_{gq} and P_{gg} give the probability of a quark and of a gluon, respectively, to radiate a gluon with momentum fraction $\frac{x}{y}$, P_{qg} the probability of a gluon to split into a quark-antiquark pair and P_{qq} the probability to find a quark off a parent quark.

The full set of coefficient functions [36] and splitting functions [37] have been computed up to the next-to-leading order (NLO) order in α_s using the Operator Product Expansion technique [22]. This formalism allows a complete NLO QCD analysis of the scaling violations of the spin-dependent structure functions. At leading order $C_q^S = C_q^{NS} = \delta(1-x)$, $C_g = 0$ and the QPM expression for g_1 (Equation 1.47) is recovered, as well as g_1 decouples from Δg. In NLO the separation between $\Delta\Sigma$ and Δg becomes renormalization scheme dependent, and thus in principle ambiguous.

The ratio $\frac{g_1}{F_1} \approx A_1$ is expected to depend on Q^2, because the splitting functions, with the exception of P_{qq}, are different for the polarized and the unpolarized

case. For instance, the process $g \to q\overline{q}$ yields a quark-antiquark pair with opposite helicity regardless of the gluon polarization: the density of unpolarized quarks rises at small x, but not the density of polarized quarks, leading thus to a growth of the unpolarized structure function F_1, while no increase in the polarized structure function g_1 can be expected at small x from this sub-process.

1.7 The Sum Rules

A physical interpretation of the structure functions can be obtained by studying their moments and by comparing them with theoretical predictions. In general, such predictions are called **sum rules**. The first moment of g_1, denoted by Γ_1, is related to the nucleon spin *puzzle*, and is defined as the integral of g_1 over the entire x range of $0 \leq x \leq 1$ at fixed Q^2:

$$\Gamma_1(Q^2) \equiv \int_0^1 g_1(x, Q^2)dx \ . \tag{1.56}$$

In the QPM, Γ_1 gives the contribution of the quarks to the nucleon spin weighed by the square of their electric charges. With only the light quark flavors u, d and s contributing to the first moment of g_1^p for the proton is given by:

$$\Gamma_1^p \equiv \int_0^1 g_1^p(x)dx = \frac{1}{2}\left(\frac{4}{9}\Delta u + \frac{1}{9}\Delta d + \frac{1}{9}\Delta s\right) , \tag{1.57}$$

while the first moment of g_1^n for the neutron is obtained from the isospin symmetry by interchanging the u quarks with the d quarks ($u \leftrightarrow d$):

$$\Gamma_1^n \equiv \int_0^1 g_1^n(x)dx = \frac{1}{2}\left(\frac{1}{9}\Delta u + \frac{4}{9}\Delta d + \frac{1}{9}\Delta s\right) . \tag{1.58}$$

The contributions of the quarks of a certain flavor to Γ_1 is denoted with the somehow imprecise but widely used notation

$$\Delta q = \int_0^1 \Delta q(x)dx. \tag{1.59}$$

Γ_1^p and Γ_1^n can be expressed in terms of the matrix elements of the flavor singlet $J_{5\mu}^0$ and flavor octet $J_{5\mu}^k$ axial-vector currents, defined as:

$$\begin{array}{rcl} \langle P,S|J_{5\mu}^0|P,S\rangle & \equiv & \langle P,S|\overline{\psi}\ \frac{1}{2}\gamma_\mu\gamma_5\ \psi|P,S\rangle \ \equiv \ MS_\mu a_0 \\ \langle P,S|J_{5\mu}^k|P,S\rangle & \equiv & \langle P,S|\overline{\psi}\ \gamma_\mu\gamma_5\frac{\lambda_k}{2}\ \psi|P,S\rangle \ \equiv \ MS_\mu a_i \end{array} \tag{1.60}$$

where ψ represents the quark field triplet (ψ_u, ψ_d, ψ_s) and the λ_k's are the Gell-Mann SU(3) matrices. The non-zero axial-vector charges can be expressed in terms of the quark distributions by

$$\begin{array}{rclcrcrcl} a_3 & = & \Delta u - \Delta d & = & F + D & = & 1.267 \pm 0.0035 & = & \left| \frac{g_A^{n\to p}}{g_V^{n\to p}} \right| \\ a_8 & = & \Delta u + \Delta d - 2\Delta s & = & 3F - D & = & 0.585 \pm 0.025 & & \\ a_0 & = & \Delta u + \Delta d + \Delta s & = & \Delta\Sigma & & . & & \end{array} \tag{1.61}$$

$|g_A/g_V|$ is the axial-vector coupling in the neutron β decay, and F and D are the coupling constants in the semi-leptonic hyperon decays [20, 38]. The a_0 term is often referred to as $\Delta\Sigma$, since it is recognized as the total contribution of the quark spins to the nucleon spin.

Thus, with the use of the axial-vector charges, the first moment of the polarized structure function g_1 can be rewritten as

$$\Gamma_1^{p(n)} = +(-)\frac{1}{12}\left|\frac{g_A^{n\to p}}{g_V^{n\to p}}\right| + \frac{1}{36}(3F - D) + \frac{1}{9}\Delta\Sigma \ . \tag{1.62}$$

After the introduction of the QCD radiative corrections $\Gamma_1^{p(n)}$ becomes:

$$\Gamma_1^{p(n)}(Q^2) = C_1^{NS}(Q^2)\left(+(-)\frac{1}{12}\left|\frac{g_A^{n\to p}}{g_V^{n\to p}}\right| + \frac{1}{36}(3F - D)\right) + C_1^S(Q^2)\,\frac{1}{9}\Delta\Sigma \ . \tag{1.63}$$

The first term on the right-hand side represents the quark non-singlet contribution to $\Gamma_1^{p(n)}$, while the last term the quark singlet contribution. $C_1^{NS}(Q^2)$ and $C_1^S(Q^2)$ are the non-singlet and singlet functions for Γ_1.

At leading twist, the only gauge invariant contributions to Γ_1^p and Γ_1^n are due to the quark singlet and non-singlet axial-vector currents [39]. The scale dependence, which appears beyond leading order, remains only in $\Delta\Sigma$, i.e. $\Delta\Sigma = \Delta\Sigma(Q^2)$. This dependence follows from the non-conservation of the singlet axial current $J_{5\mu}^0$ and is caused by the anomalous gluon contribution, the so-called axial anomaly [40], which generates a *screening effect* of the quark polarizations as measured in polarized DIS. The non-singlet currents, instead, are conserved and thus the matrix elements a_3 and a_8 are Q^2 independent.

In a polarized DIS experiment Γ_1^p and Γ_1^n are determined from the measured cross section spin-asymmetries. Thus, taking g_A, F and D from the semi-leptonic baryon weak decay rates, the total contributions of the quark spins $\Delta\Sigma$ to the proton and neutron spins can be evaluated from Equation 1.62.

Two sum rule predictions for Γ_1^p and Γ_1^n have been derived by Bjorken in 1966 [41] and by Ellis and Jaffe in 1974 [42]. Both sum rule predictions have been tested using the SMC and the world data.

1.7.1 The Bjorken Sum Rule

The Bjorken sum rule [41] relates the difference of the first moments of the proton Γ_1^p and of the neutron Γ_1^n to the neutron β decay constant $|g_A^{n\to p}/g_V^{n\to p}|$. Γ_1^p and Γ_1^n differ only in the sign of the $|g_A/g_V|$ term in Equation 1.62. Using current algebra and isospin symmetry only, Bjorken derived that

$$\Gamma_1^p - \Gamma_1^n = \frac{1}{6}\left|\frac{g_A^{n\to p}}{g_V^{n\to p}}\right| = 0.182 \pm 0.005\ . \tag{1.64}$$

This sum rule is recognized as a rigorous prediction and cornerstone of QCD, as well as a fundamental test of this theory. In order to be tested, both g_1^p and g_1^n have to be measured.

After the introduction of the QCD radiative corrections (Equation 1.63) this sum rule becomes

$$\Gamma_1^p - \Gamma_1^n\,(Q^2) = C_1^{NS}(Q^2)\,\frac{1}{6}\left|\frac{g_A^{n\to p}}{g_V^{n\to p}}\right|\ . \tag{1.65}$$

The QCD corrections (i.e. the coefficient function $C_1^{NS}(Q^2)$) have been computed up to $\mathcal{O}(\alpha_s^3)$ (also known as Larin formula) [43] and have been estimated to $\mathcal{O}(\alpha_s^4)$ [44].

1.7.2 The Ellis-Jaffe Sum Rules

Later, Ellis and Jaffe derived a sum rule for the proton and neutron separately, assuming exact SU(3) symmetry [42]. Ellis and Jaffe also assumed that the strange quark sea is not polarized, i.e. $\Delta s = 0$ (in their own words: *there are no strange quarks in the nucleon, and if there were, surely they would not be polarized*) leading to $a_0 = a_8$, i.e. $\Delta\Sigma = 3F - D$ (Equation 1.61). Thus Equation 1.62 can be rewritten entirely in terms of the already determined baryon weak decay coupling constants g_A, F and D:

$$\Gamma_1^{p(n)} = +(-)\frac{1}{12}\left|\frac{g_A^{n\to p}}{g_V^{n\to p}}\right| + \frac{1}{36}(3F - D) + \frac{1}{9}(3F - D)\ . \tag{1.66}$$

The last two terms on the right-hand side have not been added in order to keep the quark non-singlet and singlet contributions separate.

Also this sum rule receives QCD corrections and it becomes

$$\Gamma_1^{p(n)}(Q^2) = C_1^{NS}(Q^2)\left[+(-)\frac{1}{12}\left|\frac{g_A^{n\to p}}{g_V^{n\to p}}\right| + \frac{1}{36}(3F-D)\right] + C_1^S(Q^2)\,\frac{1}{9}\Delta\Sigma\ . \quad (1.67)$$

The QCD corrections for the quark non-singlet part $C_1^{NS}(Q^2)$ are the same as for the Bjorken sum rule. The corrections for the singlet term $C_1^S(Q^2)$ have been computed up to $\mathcal{O}(\alpha_s^2)$ [45] and have been estimated to $\mathcal{O}(\alpha_s^3)$ [46].

1.7.3 The *small-x* Behavior of g_1

The evaluation of the first moment Γ_1 requires the knowledge of $g_1(x)$ over the entire x region of $0 \le x \le 1$. Experimentally only a limited range of x is accessible and therefore extrapolations to $x \to 1$ and $x \to 0$ are required.

Altough it is expected that a quark with a large fraction of the nucleon momentum has it spin more likely parallel then anti-parallel to the nucleon spin [47], which would imply that $A_1^{p(n)} \to 1$ for $x \to 1$, the extrapolation of $g_1(x)$ to $x \to 1$ is not critical since for $x \to 1$ there are not so many quarks and therefore $g_1(x)$ is expected to be small, bringing thus only a small contribution to the integral.

The *small-x* behavior of $g_1(x)$ is, however, not well established and much more delicate. From Regge Theory it is expected that for fixed and not too large Q^2 and $\nu \to \infty$, i.e. $x \to 0$, $g_1^p + g_1^n$ and $g_1^p - g_1^n$ behave like $x^{-\alpha}$ [48], where α is the intercept of the lowest contributing Regge trajectories [52]. These trajectories are those of the pseudo-vector mesons f_1 for the iso-singlet combination $g_1^p + g_1^n$ and of the meson a_1 for the iso-triplet combination $g_1^p - g_1^n$. Their intercepts are negative and assumed to be equal and in the range $-0.5 < \alpha < 0$. This would imply that $g_1(x)$ is not divergent and that $A_1(x \to 0) \to 0$. Such behavior has been assumed in most extrapolations of $g_1(x)$ to $x \to 0$.

In pQCD it is expected that $|g_1(x, Q^2)|$ at high Q^2 and small x rises faster than any power of $\ln(1/x)$ [49]. It is, however, not yet known at which value of Q^2 that rise will set in, and any simple Regge behavior at lower Q^2 will soon be masked at higher Q^2 by the perturbative rise. Alternatively, the *small-x* behavior can be derived directly from a NLO QCD analysis of the experimental data [50].

Chapter 2

The Exclusive ρ^0 Production

In this chapter the phenomenology of the exclusive lepto-production of the ρ^0 vector meson at the energy of this experiment is discussed. First the kinematics of the $\mu+p \rightarrow \mu'+p'+\rho^0$ process is introduced. Then the relationship between muo- and photo-production is examined. This leads to the exploring of the hadronic character of the photon. The exclusive ρ^0 production is well described within the VMD model, in which the photon fluctuates into an intermediate hadronic state. The virtual hadron or the virtual $q\bar{q}$ pair then scatters elastically off the target nucleon by means of a strong interaction process, which can be either described by the exchange of Regge trajectories in non-perturbative models or by the exchange of gluon and/or quark pairs in models based on perturbative QCD. Subsequently the ρ^0 meson is formed.

The non-perturbative aspects of the exclusive ρ^0 production, including the theory before the advent of QCD are discussed in [51, 52], while the QCD approach is examined in [53]. The most recent developments are reviewed in [54, 55] and an overview of the experimental results can be found in [56, 57].

2.1 Kinematics

The exclusive muo-production process of the ρ^0 vector meson

$$\mu\, p \;\; \rightarrow \;\; \mu'\, \rho^0\, p' \tag{2.1}$$

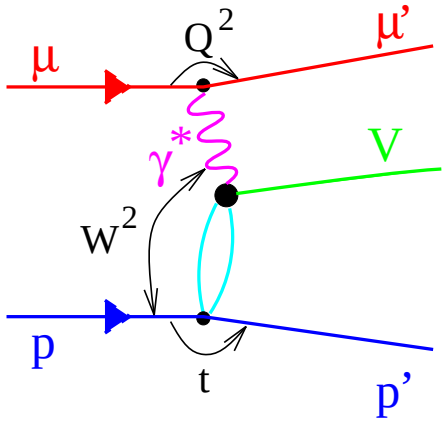

Figure 2.1: Kinematics of the exclusive ρ^0 production: the μp scattering can be interpreted as a $\gamma^* p$ scattering with the muon beam acting as the source of virtual photons. This process is characterized by the momentum transfer t at the proton vertex.

is illustrated in Figure 2.1. The only particle produced in this reaction is the ρ^0, while the target nucleon emerges intact from the interaction. This process, in which the interacting photon produced by the incoming muon is excited to a ρ^0, is commonly named *elastic* since it can be viewed as the elastic scattering of the virtual hadronic state (γ^* fluctuating into a ρ^0) off the target nucleon, in analogy with elastic hadron–hadron scattering, where the two incoming hadrons emerge intact from the interaction.

The most relevant characteristic of the exclusive ρ^0 production is that no quantum numbers are exchanged between the incoming virtual photon and the target nucleon. The quantum numbers of the ρ^0 meson, $J^{PC} = 1^{--}$, are indeed the same as those of the photon. The exclusive ρ^0 production process can be therefore described by the $t-$channel exchange [58] of an hypothetical, colorless particle carrying the quantum numbers of the vacuum, $J^{PC} = 0^{++}$. This object is commonly referred to as the Pomeron [59]. More recently, it has been argued that the Pomeron might behave as a vector rather than as a scalar [60].

In additon to the kinematical variables introduced in the previous chapter to describe the inclusive DIS process (Section 1.1), the study of the exclusive ρ^0 production requires the introduction of a few more variables:

- the Mandelstam variable t, i.e. the 4-momentum transfer squared at the

proton vertex, defined as

$$t = (p - p')^2 = (q - v)^2 \simeq -p_T^2 \ , \tag{2.2}$$

which also describes the 4-momentum transfer squared between the incoming virtual photon and the outgoing ρ^0. By construction $t < 0$. p_T is the ρ^0 transverse momentum with respect to the γ^* direction.
The minimum value of $|t|$ kinematically required for this process to occur is

$$|t|_{min} = M_p^2 \frac{(M_\rho^2 + Q^2)^2}{W^4} \ . \tag{2.3}$$

In this case the ρ^0 is produced along the γ^* direction in the $\gamma^* - N$ center of mass and $p_T = 0$;

- the invariant mass of the two pions originating from the decay of the ρ^0 meson $M_{\pi\pi}$;

- the angles describing the production and the decay of the ρ^0 [61].

All the kinematical variables required to describe the exclusive ρ^0 production are summarized in Table 2.1. Some of them will be introduced in Chapter 6.

In the case of the exclusive ρ^0 production off nuclei two different production regimes coexist: the coherent and non-coherent production. If the target is a nucleus, which emerges intact from the process, the reaction is **coherent**. The coherent production dominates at low p_T, typically for $p_T < 300$ MeV/c [62]. Indeed, the 4-momentum transfer $|t|$ can be associated with the scale (i.e. distance) probed in the scattering process. If this distance is bigger than the radius of the nucleus (i.e. at low $|t|$) the ρ^0 scatters elastically off the field generated by the nucleus as a whole, since the individual nucleons cannot be resolved.

For larger values of p_T the scattering is **non-coherent**, i.e. the ρ^0 scatters elastically off one of the various nucleons inside the nucleus. As a consequence of this interaction the nucleus can be excited to a higher mass states, which subsequently decays, or can break up immediately. Typically, in non-coherent interactions the interacting nucleon is ejected from the nucleus; the ejected nucleon then emerges unaltered from the interaction. The transition between the

k	4-momentum of the incident muon
k'	4-momentum of the scattered muon
$q = k - k'$	4-momentum of the virtual photon
$-Q^2 = q^2$	invariant mass squared of the virtual photon
p	4-momentum of the incident (target) nucleon
p'	4-momentum of the scattered (target) nucleon
m_v $(M_{\pi\pi})$	invariant mass of the 2 pions emerging from the ρ^0 decay
$v^2 = (m_v)^2$	4-momentum squared of the ρ^0
M_ρ	ρ^0 mass
M_p	proton mass
$\nu = p \cdot q \,/\, M_p$	energy of the virtual photon in the lab. frame
$x = Q^2 \,/\, 2p \cdot q$	Bjorken scaling variable
$y = p \cdot q \,/\, p \cdot k$	fraction of the lepton energy lost in the lab. frame
$W^2 = (q + p)^2$	total energy squared in the $\gamma^* - N$ system
$s = (k + p)^2$	total energy squared of the $\mu - N$ system
$t = (p - p')^2$	4-momentum transfer squared at the proton vertex, i.e.
$= (q - v)^2$	4-momentum transfer squared between the γ^* and the ρ^0
p_T	transverse momentum of the ρ^0 w.r.t. the γ^* direction
$M_X^2 = (p + q - v)^2$	missing mass squared of the undetected recoiling system
$I = (M_X^2 - M_p^2)/W^2$	inelasticity
$\Delta E = (M_X^2 - M_p^2)/2M_p$	energy balance between the γ^* and the target nucleon

Table 2.1: Kinematical variables used for the study of the exclusive ρ^0 production.

two regimes occurs around 300 MeV/c of p_T and depends on the size of the nucleus [62]. When scattering off free nucleons this distinction, obviously, does not apply.

A process competing with the exclusive ρ^0 production (Figure 2.1) is the proton diffractive dissociation illustrated in Figure 2.2. In this process the proton breaks up (dissociates) into a hadronic final state with the same quantum numbers of the initial proton but mass $M_X > M_p$. This process is also referred to as the double diffractive dissociation, since strictly speaking also the photon dissociates into the ρ^0. Since the momenta of the hadrons produced in the proton dissociation

are low (the proton is at rest), most of them do not enter into the acceptance of this experiment. These events, therefore, represent, a primary background to the exclusive process of Figure 2.1, as will be discussed in Chapter 6.

2.1.1 Classification

In hadron–hadron and lepton–nucleon scattering the interactions are classified by the characteristics of the hadronic final states. In diffractive scattering the energy transfer between the two interacting particles is usually small, but one or both particles dissociates into multi-particle final states with the same quantum numbers of the associated initial particles. The emerging particles or groups of particles are well separated in space with essentially no hadrons in between. This large gap in the phase space between the emerging particles, which contains no final state particles, is referred to as the *rapidity gap* and is used to distinguish diffractive events from non-diffractive ones.

The elastic hadron–hadron scattering differential cross section shows the pattern known from diffractive processes in optics with a dominant peak in the forward direction, which is accompanied by minima and maxima. In analogy with optics, such a scattering can be approximated by the absorption of a quantum mechanical wave by a black disk, where the cross section depends only on the impact parameter, hence the name **diffraction** [59]. Predictions based on classical optics and a comparison with data is given in [51]. Extending further the analogy with optics it can be shown that the slope of the p_T^2 (or t) distribution is

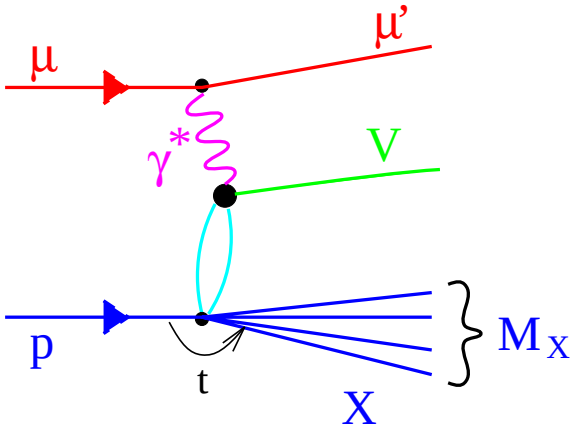

Figure 2.2: Proton dissociative diffraction.

proportional to the radius squared of the nucleus, from which the ρ^0 scatters off elastically. Therefore, the steeper the slope, the larger the radius of the nucleus.

The elastic (or exclusive) scattering of particles in *diffractive* interactions is peripheral (i.e. with a big impact parameter) with **no quantum numbers exchanged** except the angular momentum. Diffractive events occur via the exchange of color singlet objects with the same quantum numbers as the vacuum, $J^{PC} = 0^{++}$. At high energy this hypothetical object is known as the Pomeron [59]. The Pomeron was originally introduced to explain the slow rise of the hadronic cross sections with energy as well as to describe some aspects of the elastic proton–proton scattering.

The deep inelastic scattering events, which have been presented in the previous chapter (Figure 1.1), result from the break up of the nucleon into several hadrons, leading to hadronic final states of higher masses with $W^2 \gg M_p^2$. They belong to the so-called *non-diffractive* events. In an inclusive measurement, however, only the scattered muon is detected. Therefore, the events selected on the basis of the muon kinematics only are not necessarily pure DIS events. They can also originate from elastic or quasi-elastic processes, which do not carry any information on the internal structure of the nucleon and represent a background to the DIS events (section 5.3).

The exclusive ρ^0 **production process**, $\mu p \to \mu' \rho^0 p'$ belongs to the so-called **diffractive processes**. The exclusive ρ^0 production, as well as any other exclusive vector meson production in photon–hadron interactions, can be legitimally considered as an *elastic* scattering process in the framework of the Vector Meson Dominance (VMD) model (Section 2.5), in which its contribution to $\sigma_{tot}^{\gamma^* p \to X}$ is of the same magnitude as the elastic hadronic cross section $\sigma_{elastic}^{hh \to hh}$ to the total hadronic one $\sigma_{tot}^{hh \to X}$, i.e. $\frac{\sigma_{excl.\rho^0}^{\gamma^* p \to \rho^0 p'}}{\sigma_{tot}^{\gamma^* p \to X}}$ is of the same magnitude as $\frac{\sigma_{elastic}^{hh \to hh}}{\sigma_{tot}^{hh \to X}}$.

According to the hadronic final states of the $\gamma^* p$ interaction sub-processes, the diffractive processes are separated into elastic and dissociative ones. In general, the *diffractive dissociative* scattering occurs when

- either the proton, i.e. proton dissociation $\gamma^* p \to V\mathbf{X}$ (Figure 2.2),
- or the photon, i.e. photon dissociation $\gamma^* p \to \mathbf{Y}p$ (Figure 2.1),

- or both, i.e. double dissociation : $\gamma^* p \rightarrow \mathbf{YX}$

break up into final states of higher masses, with the same quantum numbers as the incoming particles.

2.2 The Exclusive ρ^0 Cross Section

The exclusive ρ^0 muo-production can be factorized according to the diagram shown in Figure 2.1, where the muon beam acts as a source of virtual photons. It can be described in terms of the virtual photo-production process

$$\gamma^* \; p \quad \rightarrow \quad \rho^0 \; p' \tag{2.4}$$

multiplied with the virtual photon flux. Experimentally it has been known, that also the $\rho^0 p$ vertex factorizes, i.e. that it is almost energy independent. This remarkable fact has been also proven theoretically for the exclusive lepto-production of vector mesons at not too low Q^2 [63].

Following the discussion of section 1.3 to derive the Equivalent Photon Expression (Equation 1.13), and using the same arguments to described the lepton–nucleon cross section $\frac{d^2\sigma^{\mu p \rightarrow \mu' X}}{dx\, dQ^2}$ as the product of the virtual photon flux and the photo-absorbtion cross section $\sigma^{\gamma^* p \rightarrow X}$, the exclusive ρ^0 lepto-production cross section $\frac{d^2\sigma^{\mu p \rightarrow \mu' \rho^0 p'}}{dx\, dQ^2}$ can be also expressed in terms of the $\gamma^* p \rightarrow \rho^0 p'$ sub-process as:

$$\frac{d^2\sigma^{\mu p \rightarrow \mu' \rho^0 p'}}{dx\, dQ^2} = \Gamma_T \left(\sigma_T^{\gamma^* p \rightarrow \rho^0 p'}(x, Q^2) + \epsilon\, \sigma_L^{\gamma^* p \rightarrow \rho^0 p'}(x, Q^2) \right) , \tag{2.5}$$

or equivalently as

$$\frac{d^2\sigma^{\mu p \rightarrow \mu' \rho^0 p'}}{dx\, dQ^2} = \Gamma_T \; \sigma_T^{\gamma^* p \rightarrow \rho^0 p'}(x, Q^2) \; \left(1 + \epsilon\, R(x, Q^2) \right) , \tag{2.6}$$

where $\sigma_T^{\gamma^* p \rightarrow \rho^0 p'}$ and $\sigma_L^{\gamma^* p \rightarrow \rho^0 p'}$ are the exclusive ρ^0 photo-production cross sections for transversely and longitudinally polarized virtual photons, respectively. R is the ratio of these cross sections: $R = \frac{\sigma_L^{\gamma^* p \rightarrow \rho^0 p}(x, Q^2)}{\sigma_T^{\gamma^* p \rightarrow \rho^0 p}(x, Q^2)}$ (cf. Equation 1.23), Γ_T is the flux of the transversely polarized virtual photons (Equation 1.14) and ϵ their polarization (Equation 1.15). Inserting Γ_T and ϵ explicitly into Equation 2.5, the

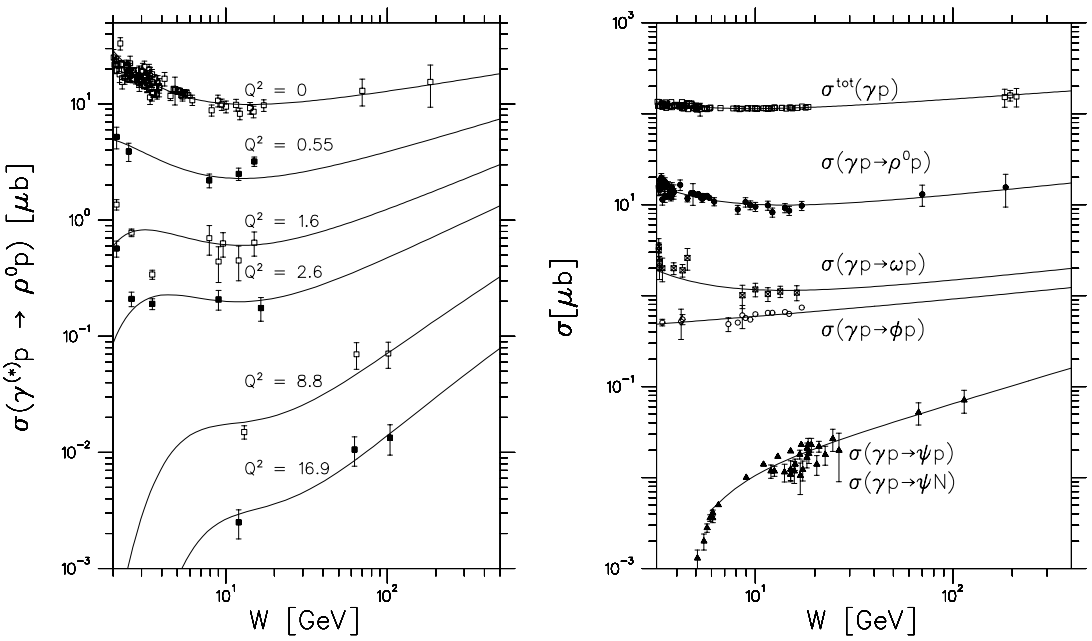

Figure 2.3: (left) Exclusive ρ^0 photo-production cross sections as a function of W for different values of the photon virtuality Q^2 from fixed target experiments and the HERA collider; (right) Total photo-production and exclusive vector meson photo-production cross sections by real photons. The data are from [64]. The solid line is one [65] of the several phenomenological fits to the data.

exclusive cross section becomes:

$$\frac{d^2\sigma^{\mu p \to \mu' \rho^0 p'}}{dx\, dQ^2} = \frac{\alpha}{2\pi} \frac{1+(1-y)^2}{Q^2 x} \left(\sigma_T^{\gamma^* p \to \rho^0 p}(x,Q^2) + \frac{2\,(1-y)}{1+(1-y)^2}\, \sigma_L^{\gamma^* p \to \rho^0 p}(x,Q^2) \right) . \tag{2.7}$$

Figure 2.3 shows a compilation of exclusive ρ^0 photo-production cross sections as a function of W ($W^2 \approx Q^2/x$) for different values of Q^2. The photo-production cross sections can be derived from the measured lepto-production cross sections using the above relations.

The scaling variable x is a property of the $\mu - \gamma^*$ (lepton) vertex. Only within the QPM the variable x describes the momentum of the struck quark. The QPM, however, does not apply to exclusive processes, like the ρ^0 production. The variable W, which describes the energy of the final hadronic system is more directly linked to the interacting nucleon and therefore W appears more appropriate to describe these data.

2.3 The Model Approaches

In real photo-production as well as in lepto-production of the light vector mesons at not too large Q^2 ($Q^2 <$ few GeV^2) and sufficiently high energies $W \geq 10$ GeV, some characteristic features of the soft hadronic diffraction are observed:

- weak energy dependence of the cross section;
- steep exponential $|t|$ dependence with the steepness of the $|t|$ slope increasing with energy (*shrinkage*);
- $s-$channel helicity conservation: the ρ^0 is produced predominantly in the ± 1 helicity states;
- a total cross section which can be related to the absorptive part of the forward elastic scattering amplitude.

This similarity with the hadronic processes has been accounted for in the framework of the Vector Meson Dominance (VMD) model (section 2.5), in which the photon fluctuates into a vector meson with the same quantum numbers of the photon. This intermediate state then scatters off the target nucleon by a strong hadronic interaction similar to the one in elastic hadron–hadron scattering, which is mediated by the exchange of the Pomeron (Figure 2.4 left). The Pomeron exchange, or more general the exchange of any meson trajectory is modelled within the Regge theory (section 2.6). At present the nature of the Pomeron is far from clear (see for instance [53]). This picture is the basis of the phenomenological approach in the so-called **soft models**.

At larger values of Q^2, the exclusive ρ^0 production cross section shows a quite different behavior and it departs substantially from the predictions of the VMD model and Regge theory:

- stronger rise of the cross section with energy;
- fast decrease of the cross section with Q^2, up to $1/Q^6$;
- shallower $|t|$ dependence, which is also energy independent (no *shrinkage*);
- the ρ^0 is produced predominantly in the 0 helicity state.

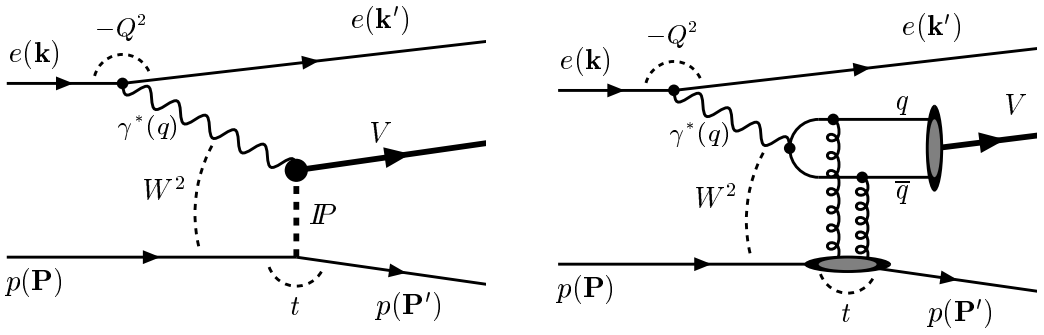

Figure 2.4: Different representations of diffraction: (left) Pomeron exchange, (right) two gluon exchange.

The picture in which the photon fluctuates into an unbound $q\bar{q}$ state of high virtuality (Figure 2.4 right) rather than into hadrons seems to better describe the features of the exclusive ρ^0 production at large Q^2. The $q\bar{q}$ pair then scatters off the target nucleon and transforms into the ρ^0. In the QCD inspired models of diffractive processes, the Pomeron can be described as an object whose partonic composition is dominated by gluons, and the exchange of a Pomeron is usually depicted as a two gluon exchange in a color singlet state [66, 67]. In this picture the cross section is proportional to the square of the gluon distribution in the proton. Individual models however differ in the way these gluons are described, ranging from non-perturbative approaches to perturbative ones. Models also differ in the description of the intermediate $q\overline{q}$ state and on the vector meson wave function. The various pQCD models, nevertheless, give qualitatively similar predictions for the cross section.

Figure 2.4 illustrates these two approaches to the diffractive process. Both the hadronic and the pQCD descriptions may be appropriate in the kinematic range of this experiment. Though pQCD models make use of a picture very similar to the soft models, the predictions for the cross section behavior are very different.

2.4 The Hadronic Character of the Photon

The photo-production results are usually interpreted in terms of the **hadronic character of the photon**. These data can be phenomenologically interpreted as if the photon, for part of its time, transforms into a kind of hadron. In this

picture the features of the photon–hadron interaction should be similar to the features of the hadron–hadron interactions, except that the cross sections are much smaller compared to the hadronic ones by approximately the magnitude of the fine structure constant (more precisely by α/π). Indeed, $\sigma_{tot}^{pp} \simeq 40$ mbarn and $\sigma_{tot}^{\gamma p} \simeq 100$ μbarn at $W \simeq 10$ GeV [38].

The phenomenological explanation, in which the scattering $\gamma^* p \to \rho^0 p'$ can be viewed as the photon–hadron counterpart of the elastic hadron–hadron scattering holds, since $\frac{\sigma_{excl.\rho^0}^{\gamma^* p \to \rho^0 p'}}{\sigma_{tot}^{\gamma^* h \to X}}$ is of the same magnitude as $\frac{\sigma_{elastic}^{hh \to hh}}{\sigma_{tot}^{hh \to X}}$.

The **Heisenberg's uncertainty principle** allows a photon propagating in free space to transform into a virtual hadronic state with the same quantum numbers of the photon, similar to the $\gamma \to e^+e^- \to \gamma$ fluctutations in QED, provided that the $\Delta E \Delta t \sim \hbar$ relation is respected; or in other words: **the photon** propagating in free space **can fluctuate**, within a time Δt, **into a virtual hadronic state** of mass ΔE ($\hbar = 1$), which has the **same quantum numbers as the photon**, i.e. $J^{PC} = 1^{--}$. The photon is thus continuously making transitions, back and forth, between its bare photon state $|\gamma_B\rangle$ and its hadronic state $|h\rangle$. The photon–hadron interaction can accordingly be interpreted as the interaction between the photon hadronic state and the hadron.

The photon $|\gamma\rangle$ can be described as a superposition of two states: a bare photon $|\gamma_B\rangle$ and a small hadronic component $\sqrt{\alpha}\,|h\rangle$:

$$|\gamma\rangle = \sqrt{Z_3}|\gamma_B\rangle + \sqrt{\alpha}\,|h\rangle\ , \tag{2.8}$$

where Z_3 is a normalization factor. The probability of finding the photon in the hadronic state is small, of the order α. This picture also applies to mildly virtual photons. The hadronic component of the photon is significantly reduced with increasing Q^2. In fact, at large Q^2 the photon behaves mainly as a pointlike particle. Fluctuations to a hadronic state still occur, but are described within pQCD in terms of $\gamma \to q\bar{q} \to \gamma$ fluctuations and photon structure functions [68].

As the vector mesons ρ^0, ω and ϕ, which are copiously produced in photo-production, have the same quantum numbers as the photon and are not too massive ($m_\phi \sim 1$ GeV/c^2), they are the best candidates for supplying important contributions to the photo-production cross section.

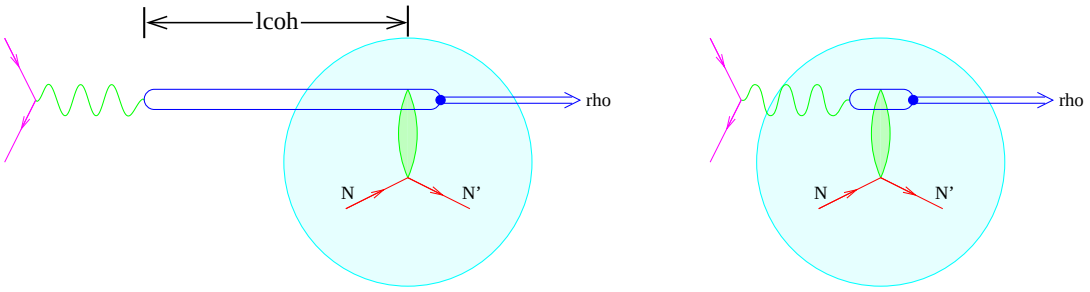

Figure 2.5: Large coherence length (left) and small coherence length (right).

If the virtual hadronic state into which the photon fluctuates is a vector meson of mass M_V, the time t_f allowed for this fluctuation in the proton rest frame is

$$t_f \approx \frac{2\nu}{Q^2 + M_V^2} \,. \tag{2.9}$$

The variable $l_c = 2\nu/(Q^2 + M_V^2)$, referred to as the **coherence length**, can be viewed as the distance travelled in the laboratory system by the virtual ρ^0 fluctuation. If l_c is much larger than the nucleon size, i.e. $l_c \gg 1$ fm, the interaction between the photon and the nucleon may look like a hadron–hadron interaction (Figure 2.5 left). In order to apply such a description, M_V and Q^2 have to be small enough.

2.5 The Vector Meson Dominance Model

The Vector Meson Dominance (VMD) model [69] is based on the hypothesis that in photo–hadron interactions the bare component of the photon does not contribute to the scattering process and that the hadronic component of the photon is a superposition of the three lightest vector mesons ρ^0, ω and ϕ. The hadronic component of the photon thus can be written as

$$\sqrt{\alpha}|h\rangle = \sum_{V=\rho^0,\omega,\phi} \frac{1}{f_V} \frac{M_V^2}{M_V^2 + Q^2} |V\rangle \,, \tag{2.10}$$

where the coupling constants f_V measure the coupling of each vector meson V to the photon. f_V can be determined from e^+e^- annihilations into vector mesons or from the vector meson decay partial width $\Gamma_{V\to e^+e^-}$.

According to the VMD model the hadronic matrix element $\langle X|J_\mu|p\rangle$ in the reaction $\gamma^* p \to X$ (Equation 1.8) can be related to the corresponding matrix element $\langle X|J^V_\mu|p\rangle$ of the reaction $Vp \to X$ via Equation 2.10 :

$$\langle X|J_\mu|p\rangle \;=\; \sum_V \frac{1}{f_V}\,\frac{M_V^2}{M_V^2+Q^2}\,\langle X|J^V_\mu|p\rangle\,, \tag{2.11}$$

where J^V_μ represents the current density of the vector meson field. In the VMD model the matrix elements $\langle X|J^V_\mu|p\rangle$ are supposed to be almost Q^2 independent with the Q^2 dependence being factored out.

The transverse $\sigma_T^{\gamma^* p\to X}$ and longitudinal $\sigma_L^{\gamma^* p\to X}$ photo-absorption cross sections can be represented as [20]

$$\sigma_T^{\gamma^* p\to X} \;=\; \frac{4\pi^2\alpha}{K}\sum_X |\langle X|J_\perp|p\rangle|^2\,\frac{1}{4\pi m_p}(2\pi)^4\delta^4(p+q-p')\,, \tag{2.12}$$

$$\sigma_L^{\gamma^* p\to X} \;=\; \frac{4\pi^2\alpha}{K}\frac{Q^2}{\nu^2}\sum_X |\langle X|J_\parallel|p\rangle|^2\,\frac{1}{4\pi m_p}(2\pi)^4\delta^4(p+q-p')\,, \tag{2.13}$$

after the current J_μ has been decomposed into its transverse ($\perp$) and longitudinal ($\parallel$) components. The factor K gives the virtual photon flux (Equation 1.16).

The transverse and longitudinal $\gamma^* p$ cross sections can be expressed with the use of the $\langle X|J^V_\mu|p\rangle$ matrix elements as ($\sigma_T^{Vp\to X}$ and $\sigma_L^{Vp\to X}$ are the corresponding cross sections for transversely and longitudinally polarized vector meson fields):

$$\sigma_T^{\gamma^* p\to X}(W_{\gamma^* p},Q^2) \;=\; \sum_V \frac{4\pi\alpha}{f_V^2}\left(1+\frac{Q^2}{M_V^2}\right)^{-2}\sigma_T^{Vp\to X}(W_{\gamma^* p})\,, \tag{2.14}$$

$$\begin{aligned}\sigma_L^{\gamma^* p\to X}(W_{\gamma^* p},Q^2) \;&=\; \sum_V \frac{4\pi\alpha}{f_V^2}\left(1+\frac{Q^2}{M_V^2}\right)^{-2}\frac{Q^2}{M_V^2}\,\sigma_L^{Vp\to X}(W_{\gamma^* p}) \\ &=\; \sum_V \frac{4\pi\alpha}{f_V^2}\left(1+\frac{Q^2}{M_V^2}\right)^{-2}\frac{Q^2}{M_V^2}\,\xi_V\,\sigma_T^{Vp\to X}(W_{\gamma^* p})\end{aligned} \tag{2.15}$$

where, at first order, the ratio

$$\xi_V = \frac{\sigma_L^{Vp\to X}(W_{\gamma^* p})}{\sigma_T^{Vp\to X}(W_{\gamma^* p})} \tag{2.16}$$

does not depend on $W_{\gamma^* p}$. The photo-absorption cross section, written in a form similar to the Equivalent Photon Expression (Equations 1.13 and 2.6), becomes

$$\sigma^{\gamma^* p\to X}(W_{\gamma^* p},Q^2) \;=\; \sum_V \frac{4\pi\alpha}{f_V^2}\frac{1}{\left(1+Q^2/M_V^2\right)^2}\,\sigma_T^{Vp\to X}(W_{\gamma^* p})\left(1+\frac{Q^2}{M_V^2}\xi_V\right)\,. \tag{2.17}$$

2.5.1 The Exclusive ρ^0 Production Case

In the case of the exclusive ρ^0 production the final hadronic state X is the $\rho^0 p'$ system and the vector meson V is the ρ^0. The Q^2 dependence of the transverse and longitudinal $\gamma^* p \to \rho^0 p$ cross sections, assuming no off-diagonal terms (i.e. that the initial V does not transform to a final, different V', see [75]), reduces to

$$\sigma_T^{\gamma^* p \to \rho^0 p'}(W_{\gamma^* p}, Q^2) = \frac{4\pi\alpha}{f_\rho^2}\left(1+\frac{Q^2}{M_\rho^2}\right)^{-2} \sigma_T^{\rho^0 p \to \rho^0 p'}(W_{\gamma^* p}) \,, \tag{2.18}$$

$$\sigma_L^{\gamma^* p \to \rho^0 p'}(W_{\gamma^* p}, Q^2) = \frac{4\pi\alpha}{f_\rho^2}\left(1+\frac{Q^2}{M_\rho^2}\right)^{-2} \frac{Q^2}{M_\rho^2}\,\xi_{\rho^0}\,\sigma_T^{\rho^0 p \to \rho^0 p'}(W_{\gamma^* p}) \tag{2.19}$$

and $R_{excl.\rho^0}$ (Equation 1.23) is given by

$$R_{excl.\rho^0} = \frac{\sigma_L^{\gamma^* p \to \rho^0 p'}}{\sigma_T^{\gamma^* p \to \rho^0 p'}} \overset{VMD}{=} \frac{Q^2}{M_{\rho^0}^2}\,\xi_{\rho^0} = \frac{Q^2}{M_{\rho^0}^2}\,\frac{\sigma_L^{\rho^0 p \to \rho^0 p}}{\sigma_T^{\rho^0 p \to \rho^0 p}} \,. \tag{2.20}$$

$R_{excl.\rho^0}$ depends only on Q^2 and it can be determined experimentally by studying the Q^2 dependence of the exclusive ρ^0 cross section $\sigma^{\gamma^* p \to \rho^0 p'}$ at different energies or by measuring the ρ^0 alignment (polarization) [61].

In summary, for the exclusvie ρ^0 production the VMD model predicts:

- $\sigma_T^{\gamma^* p \to \rho^0 p'}$ falls with increasing Q^2 as $(1+Q^2/M_\rho^2)^{-2}$,
- $\sigma_L^{\gamma^* p \to \rho^0 p'}$ falls with increasing Q^2 as $Q^2(1+Q^2/M_\rho^2)^{-2}$,
- $R_{excl.\rho^0}$ grows linearly with increasing Q^2.

All these features of the exclusive ρ^0 cross section are observed in the data [70, 71, 72, 73] at not too high Q^2.

2.6 Regge Theory (Reggeons and Pomerons)

The energy dependence of the cross section for the exclusive photo-production of the light vector mesons is related to the interaction dynamics of the intermediate hadronic state with the target nucleon and is described reasonably well by the **Regge Theory**. Regge theory [76] has been developed in the early 60's, before

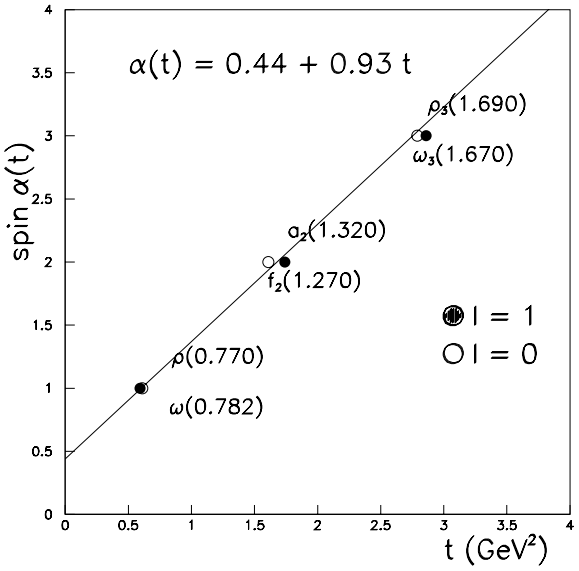

Figure 2.6: Regge trajectory (spin versus mass squared) for two meson families: mesons with isospin 1 (ρ, a_2, ρ_3), and mesons with isospin 0 (ω, f_2, ω_3).

the advent of QCD, with the aim of describing the asymptotic behavior of the strong interactions. Its predictions are valid in the so-called Regge limit of large s and small t. This regime is also achieved in DIS at large s and not too high Q^2, i.e. at low x [77]. Although Regge theory was originally developed in the context of hadron–hadron interactions, it also applies to the description of the photon–hadron collisions, when the photon behaves as a hadron within the VMD model. Regge theory, although remarkable in describing many features of the strong interactions, fails to predict the *spin effects* observed in hadronic interactions.

Regge theory is based on the idea of singularities in the S-matrix that appear in a partial wave analysis of the two body hadronic interactions [76]. These singularities are known as **Regge poles**. Depending on the interaction under study and the considered potential, the position of the Regge poles in the complex angular momentum plane depends on the energy. A remarkable phenomenological fact is that the Regge poles lie on a straight line, called the **Regge trajectory**. The interaction takes place by the exchange in the $t-$channel of these Regge trajectories.

Mesons (and baryons) with the same quantum numbers are said to belong to the same family. When the spins of the mesons from the same family are

plotted versus their masses squared, these mesons also lie on a straight line. This plot is known as the **Chew-Frautschi plot** [78] and the straight line as **Regge trajectory**. Figure 2.6 shows a Chew-Frautschi plot for two different families of mesons: the ρ trajectory of isospin 1 and the ω trajectory of isospin 0. The Regge trajectories can be parametrized as

$$\alpha(t) = \alpha(0) + \alpha' \cdot t\,, \tag{2.21}$$

where $\alpha(0)$ is the intercept and α' is the slope of the trajectory. The slope and the intercept are characteristic of a meson family and cannot be calculated from first principles. As in Figure 2.6, different Regge trajectories can have the same slope and intercept.

The interaction thus proceeds by the exchange in the $t-$channel of an object of fixed quantum numbers, referred to as the **Reggeon**. The Reggeon consists of a superposition of different mesons belonging to the same family (i.e. with the same quantum numbers).

According to Regge theory [52] and from the $s-$dependence of the hadron scattering amplitudes the differential cross section for elastic scattering asymptotically behaves as

$$\frac{d\sigma_{el}(s,t)}{d|t|} \propto e^{-b_0|t|} \left(\frac{s}{s_0}\right)^{2\,[\alpha(t)\,-\,1]}\,, \tag{2.22}$$

where s_0 and b_0 are process dependent constants. The $|t|-$dependence of the cross section is not predictable from the theory and the exponential fall-off is introduced based on experimental observations. The scale factor s_0 is of the order of 1 GeV^2, while the slope b_0 is of the order of 10 GeV^{-2}. Using Equation 2.21 the above expression can be rewritten as

$$\frac{d\sigma_{el}(s,t)}{d|t|} \propto e^{-b|t|} \left(\frac{s}{s_0}\right)^{2\,[\alpha(0)\,-\,1]}\,, \tag{2.23}$$

with

$$b(s) = b_0 + 2\alpha' \ln\frac{s}{s_0}\,. \tag{2.24}$$

The exponential slope b is coupled to the energy s and increases logarithmically with s. Since $t < 0$, this coupling leads to a steeper exponential fall-off of the cross

section with increasing s. This behavior is called the **shrinkage** of the diffractive forward peak and it has been observed experimentally in several processes.

After integrating over $|t|$, Equation 2.23 becomes:

$$\sigma_{el}(s) \propto \frac{1}{b(s)} \left(\frac{s}{s_0}\right)^{2\,[\alpha(0)-1]} . \tag{2.25}$$

From the intercept of the Regge trajectory that dominates a particular scattering process and the optical theorem, it follows that the asymptotic behavior of the total cross section σ_{tot} is given by

$$\sigma_{tot} \sim s^{[\alpha(0)-1]} . \tag{2.26}$$

All the known Regge trajectories have intercept values smaller than unity; the family of the ρ meson (Figure 2.6) has the largest intercept value with $\alpha(0) \approx 0.5$. It follows that the total cross sections should decrease with increasing s. On the contrary, at higher values of s, typically for $s > 100$ GeV^2, the cross sections slowly increase with s [38] (Figure 2.7).

In order to reproduce the slow rise of the cross sections with s within the Regge model, an additional trajectory with an intercept slightly larger than unity ($\alpha(0) \approx 1.08$) has been hypothetized. The single Regge pole associated with this trajectory is called the **Pomeron** and carries the quantum numbers of the vacuum [59]. Hence, at high energies the scattering of two hadrons proceeds by the exchange in the $t-$channel of the Pomeron. The Pomeron exchange can also explain and reproduce some features of the elastic proton–proton scattering cross section. Particles with the quantum numbers of the vacuum are difficult to detect, but they can exist in QCD as bound states of gluons (i.e. glueballs).

In the attempt to describe the energy dependence of different hadronic cross sections within the Regge theory using a reduced set of parameters, **Donnachie and Landshoff** [79] have fitted these cross sections with the following expression:

$$\begin{array}{rcccc} \sigma_{tot} & = & X\left(\frac{s}{s_0}\right)^{\varepsilon} & + & Y\left(\frac{s}{s_0}\right)^{-\eta} \\ & & \mathit{Pomeron} & & \mathit{Reggeon} \end{array} , \tag{2.27}$$

where $\varepsilon = |\alpha_P(0) - 1|$ and $\eta = |\alpha_R(0) - 1|$. $\alpha_P(0)$ and $\alpha_R(0)$ are the intercepts of the exchanged Pomeron and Reggeon trajectories, respectively. This fit turned

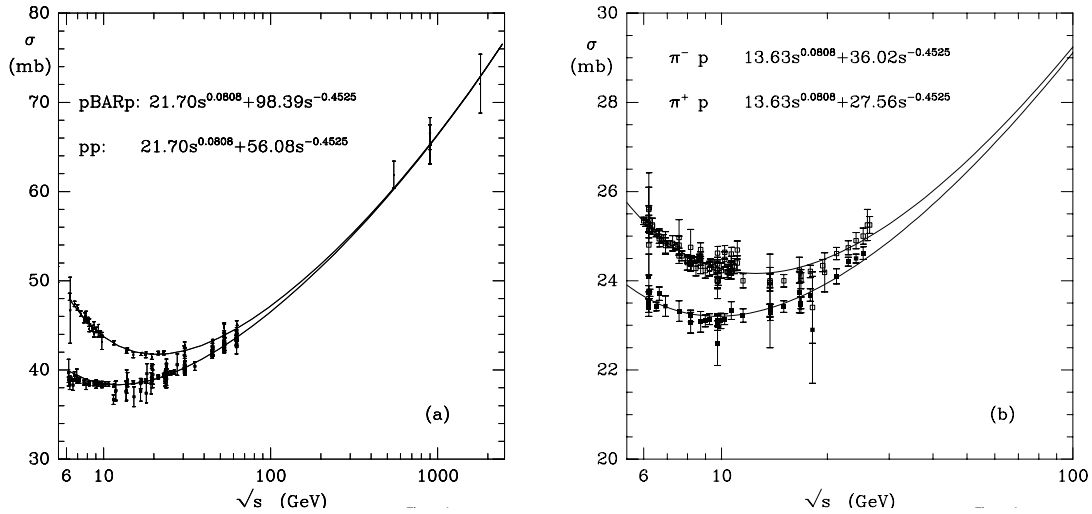

Figure 2.7: Hadron–hadron total cross sections from [38], fitted with Equation 2.27

.

out to be very successful in parametrizing all the data (Figure 2.7) with the same values for $\eta = 1.0808$ and $\varepsilon = 0.4525$, including the total photon–hadron cross section. The slope of the Pomeron trajectory α'_P, instead, has been extracted from elastic proton–proton scattering data and found to be about 0.25 GeV^{-2}.

Thus the total cross sections are described as being dominated at low s by the Reggeon exchange, while at high s the Pomeron exchange dominates, as expressed in Equation 2.27.

Within Regge theory the exclusive ρ^0 photo-production is modelled by the exchange in the $t-$channel of a Regge trajectory with the quantum numbers of the vacuum between the vector meson (into which the photon has fluctuated) and the target nucleon. The variable $\sqrt{s}$, which in this case describes the energy of the lepton–nucleon, is replaced with the variable W, which describes the energy of the photon–nucleon system. For $W > 10$ GeV the ρ^0 production is mediated by Pomeron exchange. The effective power of the W dependence of the cross section (Equation 2.25), W^δ, is $\delta \simeq 4(\alpha_P(0) - 1 + \alpha'/b)$, yielding $\delta \simeq 0.22$, in good agreement with measurements (see Figure 2.8 left).

Figure 2.8 shows a compilation of vector meson photo-production cross sections over a very broad energy range from fixed target experiments to the HERA collider compared to the predictions of the Regge theory for $W > 10$ GeV. This

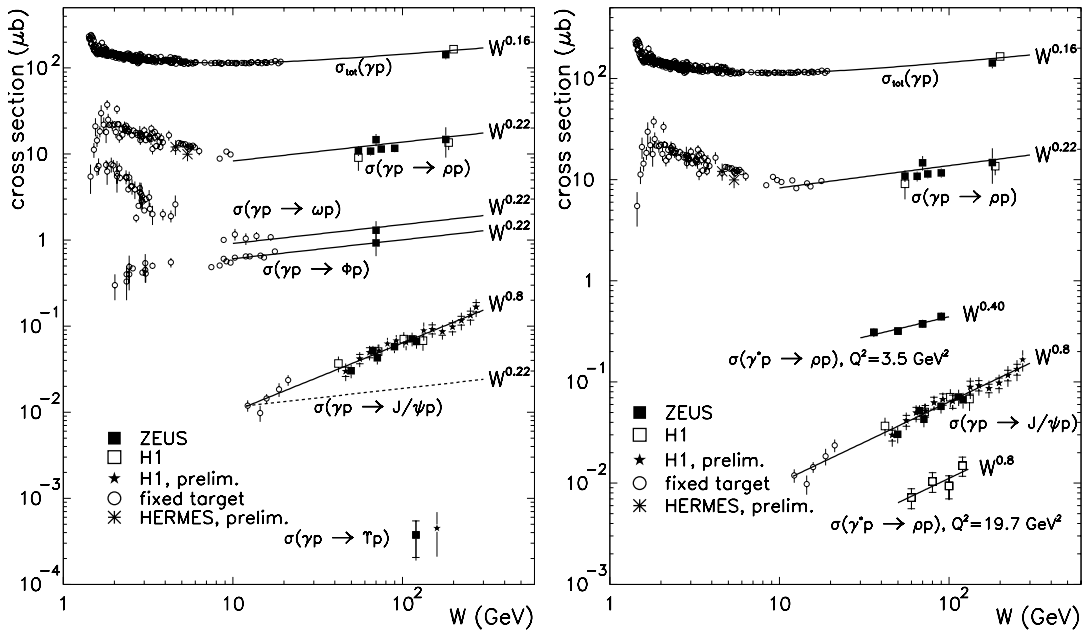

Figure 2.8: Exclusive photo-production cross sections of different vector mesons as a function of W from fixed target experiments and the HERA collider [64]. The lines represent a fit to the data of the form W^{δ}.

approach, however, fails to describe the energy dependence of the exclusive J/Ψ photo-production as shown in the same figure. The slope of the measured t dependence leads to a prediction of $\delta \simeq 0.22$ in contrast to the measured value of $\delta \simeq 0.8$ [80]. Also the W dependence of the exclusive ρ^0 photo-production cross section at large Q^2 resembles the W dependence of the J/Ψ cross section in photo-production (Figure 2.8 right).

2.7 Models Based on Perturbative QCD

The models based on perturbative QCD (pQCD) are not suited to describe the diffractive interactions at low or medium transverse momenta since the coupling constant for the strong interaction $\alpha_s(Q^2)$ as well as the interactions of the struck parton with the partons in its vicinity are too large. Although some non-perturbative QCD inspired models try to predict the properties of vector

meson production at high Q^2, the main role at high energies is played by the models based on pQCD. This implies the existence in the diffractive process of a scale μ^2 large enough, so that $\alpha_s(\mu^2) \ll 1$ for the pQCD approach to be valid.

In the language of QCD, the candidate for vacuum exchange with the properties of the Pomeron is the two gluon exchange [66, 67] (Figure 2.9 left). As a result of interactions between the two gluons, a ladder structure develops (Figure 2.9 right). In pQCD the properties of this ladder depend on the energy and scales involved in the interaction, implying a non-universal character of the interaction.

The diffractive cross section can be expressed in terms of a transition amplitude $M_{\lambda\lambda'}$ as

$$\frac{d\sigma_{\lambda\lambda'}}{dt} = \frac{1}{16\pi s^2}|M_{\lambda\lambda'}|^2\,, \tag{2.28}$$

where λ and λ' are the helicities of the virtual photon and of the vector meson, respectively.

The expression for the transition amplitude $M_{\lambda\lambda'}$ can be factorized into the three following sub-processes [63]:

1. first the virtual photon fluctuates into an unbound $q\overline{q}$ pair;

2. next the $q\overline{q}$ pair interacts with the target nucleon: the colorless exchange that takes place between the $q\overline{q}$ pair and the nucleon is treated as a perturbative two gluon exchange (Figure 2.9 left), or in even more sophisticated description as a gluon ladder exchange (Figure 2.9 right);

3. the $q\overline{q}$ pair finally recombines forming the vector meson.

This factorization applies only to longitudinally polarized vector mesons. The terms for the coupling of the virtual photon to the $q\overline{q}$ pair as well as those for the coupling of the $q\overline{q}$ pair to the vector meson do not converge in the case of transversely polarized vector mesons, so that the fluctuation of a transversely polarized virtual photon into a $q\overline{q}$ pair is still non-perturbative even at large Q^2.

At large Q^2 the cross section is predicted to be dominated by longitudinally polarized virtual photons scattering into vector mesons of 0 helicity sate. This cross section is given by [81]:

$$\frac{d\sigma_L^{\gamma^* p\to Vp'}}{d|t|}|_{t=0} = \frac{A}{Q^6}\,\alpha_s^2(Q^2)\,\left|\left(1+\frac{i\pi}{2}\frac{d}{d\ln x}\right)x\,g(x,Q^2)\right|^2 \propto g^2(x,Q^2)\,, \tag{2.29}$$

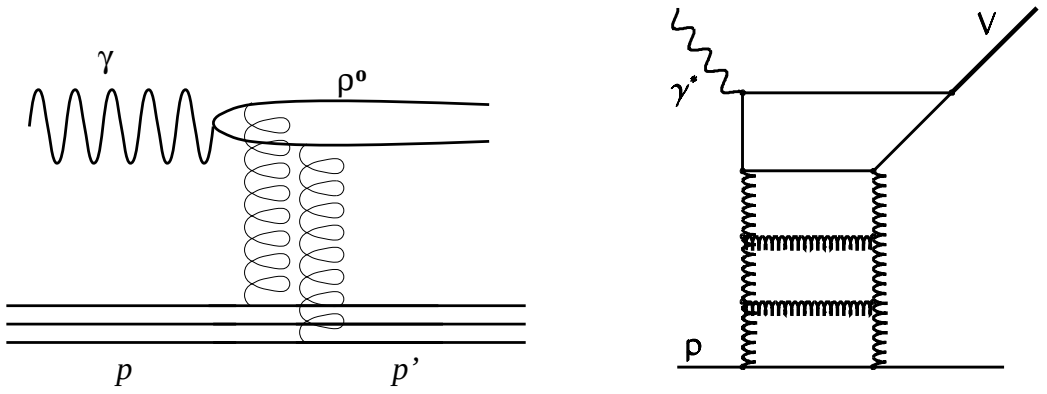

Figure 2.9: (left) A typical two-gluon exchange and (right) gluon-ladder exchange contributions to the amplitude $M_{\lambda\lambda'}$ for $\gamma^* p \to Vp$.

where A is a constant that depends on the vector meson wave function and $g(x, Q^2)$ is the gluon distribution function. This perturbative model introduced by **Brodsky et al.** [81] is valid for the production of light vector mesons, provided that $W^2/M_V^2 \gg 1$, $W^2/Q^2 \gg 1$ and $t \ll Q^2$. The cross section is proportional to the square of the gluon density $g^2(x, Q^2)$ and contains a factor $1/Q^6$. When the gluon density is taken into account, the Q^2 dependence for $\sigma_L^{\gamma^* p \to \rho^0 p'}$ becomes of the type $1/Q^5$.

Ryskin et al. [82] suggested that, in the case of the exclusive J/Ψ lepto-production, the hard scale required for the perturbative calculations could be provided by the heavy vector meson itself, regardless of the Q^2 of the interaction. This model predicts a rise of the cross section with $g(x, Q^2)^2$ evaluated at the effective values of Q^2 and x given by $\frac{M_V^2 + Q^2}{4}$ and $\frac{M_V^2 + Q^2}{W^2}$, respectively. The diffractive photo-production of J/Ψ's at HERA [80], which shows an energy dependence of the cross section much steeper than expected for a soft process, is well described by this model. This model can be generalized to the light vector mesons at large Q^2 and large W^2. The predictions of this model are equivalent to the predictions of [81], when a non-relativistic pair of quarks is assumed for the vector meson.

Similar calculations to [81] have been made by **Frankfurt et al.** [83], who additionally included contributions from the sea quarks inside the nucleons, and considered the important role of the Fermi motion of quarks within the vector meson.

Martin et al. [84] studied the production of vector mesons also by trans-

versely polarized photons. The cross section for transversely polarized vector mesons is predicted to decrease with Q^2 at least as $1/Q^8$. They addressed the behavior of the cross section as a function of Q^2 based on the open production of light $q\overline{q}$ pairs and the parton–hadron duality. Their predictions are made in terms of gluon densities; they also account for the observed deviations of $R(Q^2) = \frac{\sigma_L^{\gamma^* p \to \rho^0 p'}}{\sigma_T^{\gamma^* p \to \rho^0 p'}}$ from linearity at high Q^2.

These models based on pQCD, however, are affected by large uncertainties. These uncertainties are related to the assumptions made for the ρ^0 wave function and the factorization scales, as well as for the choice of the parametrization of the gluon distribution in the proton.

In summary, in the kinematical region of $Q^2 \gg M_V^2$ and $W^2 \gg Q^2 \gg -t$, in spite of these differences, all models give qualitatively similar predictions, which are in agreement with the observations [70, 71, 72, 74]:

- a Q^2 dependence for $\sigma_L^{\gamma^* p \to \rho^0 p'}$ of the type $\frac{1}{Q^5}$;
- when applicable, $\sigma_T^{\gamma^* p \to \rho^0 p'}$ decreases at least as $\frac{1}{Q^8}$;
- the t and W dependences are not coupled and no shrinkage of the forward peak with increasing energy is expected;
- strong, almost linear increase of the cross section with the energy of the type $W^{0.8-0.9}$;
- linear growth of R with Q^2;
- flavor independence of the interaction with the cross sections in the proportion $9 : 1 : 2 : 8$ for the $\rho^0 : \omega : \phi : J/\Psi$.

Chapter 3

The SMC Experiment

The SMC experiment was carried out at CERN, in Geneva by the Spin Muon Collaboration (SMC). It used a high energy muon beam produced by the Super Proton Synchrotron (SPS). Its geographical location is shown in Figure 3.1.

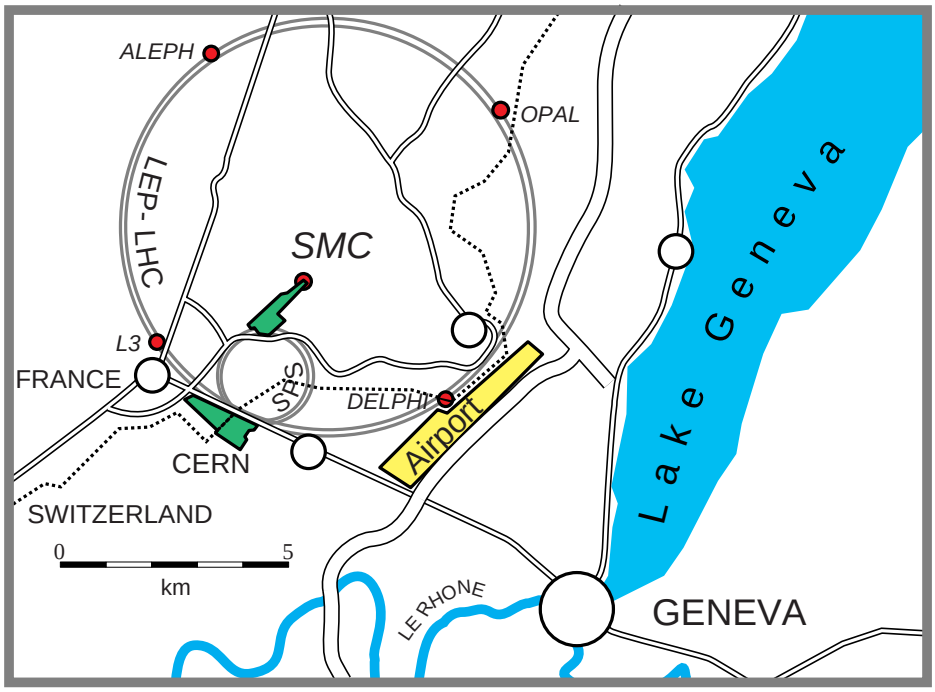

Figure 3.1: General layout of the SPS and LEP accelerators at CERN. The SMC experiment was located in the North Area of the CERN laboratory.

Overview of the SMC apparatus

The main components of the SMC experiment are schematized in Figure 3.2.

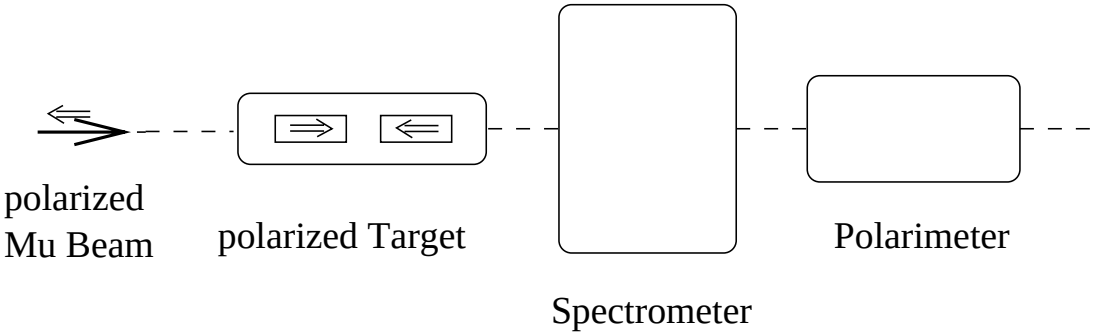

Figure 3.2: The main components of the SMC experiment.

A high energy longitudinally polarized μ^+ beam (section 3.1) enters at the left of Figure 3.2. It interacts with a solid polarized target (section 3.2) consisting of two target cells polarized in opposite directions and exposed simultaneously to the same μ^+ beam, so that the systematic effects connected with flux variations get reduced.

The momenta of the scattered muon and of the charged particles produced in the interaction are measured by an open forward magnetic spectrometer (FSM) (section 3.3) equipped with wire chambers of various construction.

Downstream of the main apparatus a polarimeter measures the polarization of the muon beam (section 3.1.1).

3.1 The Polarized Muon Beam

The SMC experiment was located at the end of the CERN SPS muon M2 beam line [85]. The schematic layout of the M2 beam line is shown in Figure 3.3. The CERN SPS accelerates protons up to 450 GeV, which are then extracted in long pulses (spills) of 2.4 s. The accelerator repetition rate is 14.4 s, with an intensity of about 4×10^{13} protons per pulse.

The protons extracted from the SPS are incident on a primary beryllium target (T6 in Figure 3.3) and scatter inelastically producing a high intensity secondary beam consisting among other particles of an admixture of π's and K's.

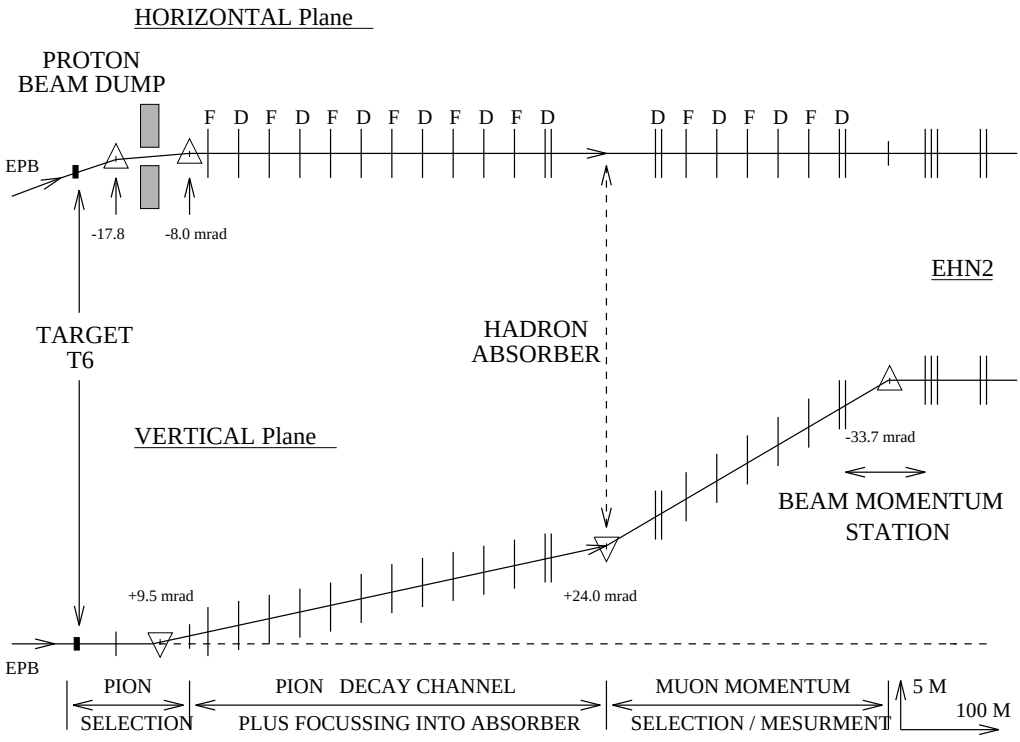

Figure 3.3: Schematic layout of the M2 muon beam line.

The intensity of the primary proton beam impinging on T6 was approximately 5×10^{12} protons/spill.

As shown in Figure 3.3, the beam line can be divided into three main sections. In the first section, the π/K beam is then deflected horizontally in order to dump the unusued primary protons and to select, in a well defined momentum interval, the positive (negative) mesons necessary to obtain the μ^+ (μ^-) beam. The resulting π^+/K^+ mixture is about 3 % K^+. Next, in the 500 m long pion decay channel, consisting of a series of focussing and defocussing quadrupole magnets, about 10 % of the π^+'s decay into μ^+ via the weak interaction ($\pi^+ \rightarrow \mu^+ \nu_\mu$). At the end of the decay channel a 7.7 m beryllium absorber stops the hadrons, while the μ^+'s pass through it. After the absorber the ratio of π^+'s to μ^+ is of the order of 10^{-6} only. Downstream of the hadron absorber, a dipole magnet selects the muon momentum, which is about 9 % lower than the parent meson momentum. For instance, to obtain a 190 GeV muon beam, one starts typically with 205 GeV mesons. The last muon section of the beam line is 300

m long and contains a series of quadrupole magnets, which focuss and transport the muon beam, and a set of scrapers, which clean up the beam. A final bend brings the muon beam back to the horizontal direction.

The muon beam is accompanied by a halo, composed essentially of energetic muons. The reduction of the halo is achieved by magnetized iron collimators (scrapers). It is a non-trivial task, because of the penetrating nature of muons, and the suppression of the halo in the measurement required the use of veto counters in anticoincidence with the main triggers.

At the polarized target the muon beam has an intensity of 4.5×10^7 per SPS pulse and a spot size of about 1 cm r.m.s. (diameter less than 5 cm), a divergence of about 1 mrad r.m.s., and a momentum spread of about 3 %. The small spot size allowed the use of a target with a relatively small diameter of 5 cm.

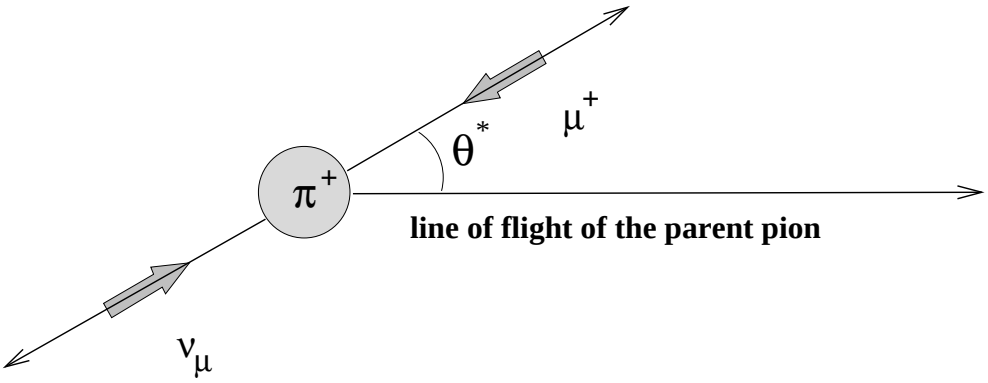

Figure 3.4: Pion decay: since the neutrino is in a negative helicity state, angular momentum conservation requires the muon to also be in a negative helicity state.

The muons originate in the weak decay of pions or kaons (Figure 3.4):

$$\pi^+ \to \mu^+ + \nu_\mu \; (K^+ \to \mu^+ + \nu_\mu) \, . \tag{3.1}$$

Since the ν_μ has a negative helicity, angular momentum conservation in the decay of the spinless π^+ requires that also the μ^+ has a negative helicity in the π^+ rest frame. Hence the muons are naturally longitudinally polarized. The muon polarization P_μ in the laboratory frame is given by [86]:

$$P_\mu = -\frac{m_\pi^2 + (1 - 2E_\pi/E_\mu)m_\mu^2}{m_\pi^2 - m_\mu^2} \, , \tag{3.2}$$

where m_π and m_μ are the pion and muon masses, respectively; E_π and E_μ are the pion and muon energies in the laboratory, respectively.

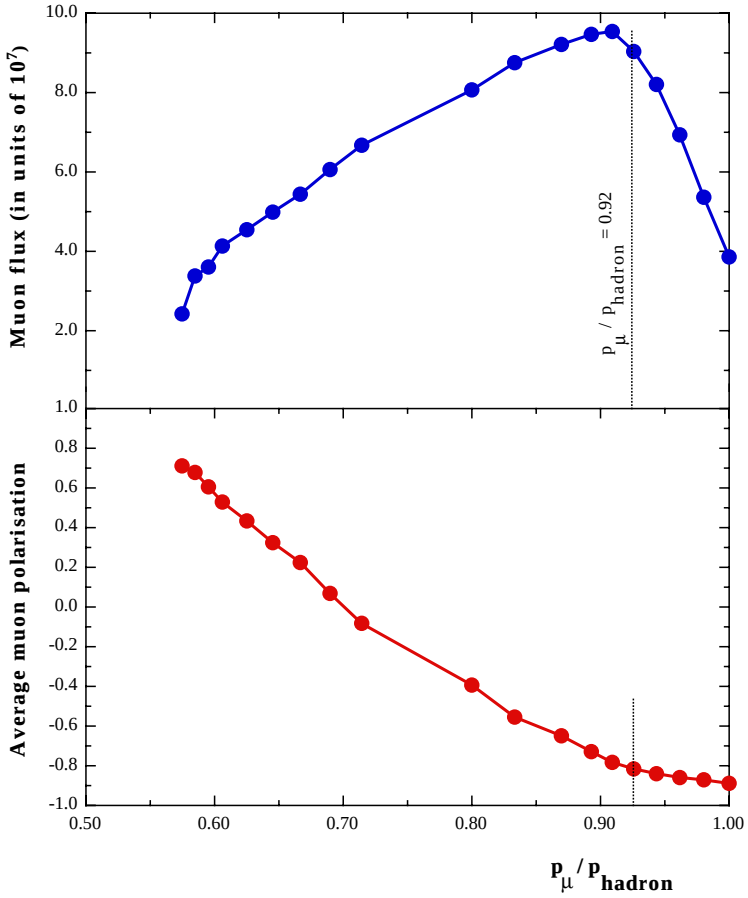

Figure 3.5: Muon flux and polarization as a function of the p_μ/p_π ratio from a Monte Carlo simulation of the M2 beam line [87].

The muon polarization depends on the ratio E_μ/E_π, which is related to the muon decay angle, θ^* (see Figure 3.4), in the pion rest frame by

$$E_\mu/E_\pi \simeq (E^*_\mu + p^*_\mu \cos\theta^*)/m_\pi \tag{3.3}$$

where E^*_μ and p^*_μ are the muon energy and momentum in the pion rest frame. Muons which are emitted forward (backwards) in the pion rest frame will have a high (small) energy in the laboratory system and a negative (positive) helicity.

Figure 3.5 shows the muon flux and polarization as a function of the ratio p_μ/p_π ($\simeq E_\mu/E_\pi$). To optimize between the muon flux Φ and polarization P_μ

(i.e. maximize the figure of merit $\Phi^2 \cdot P_\mu$) the muon to hadron momentum ratio $E_\mu/E_\pi = 0.92$ was selected. It corresponds to an average muon polarization of about $P_\mu = -0.8$ for μ^+'s.

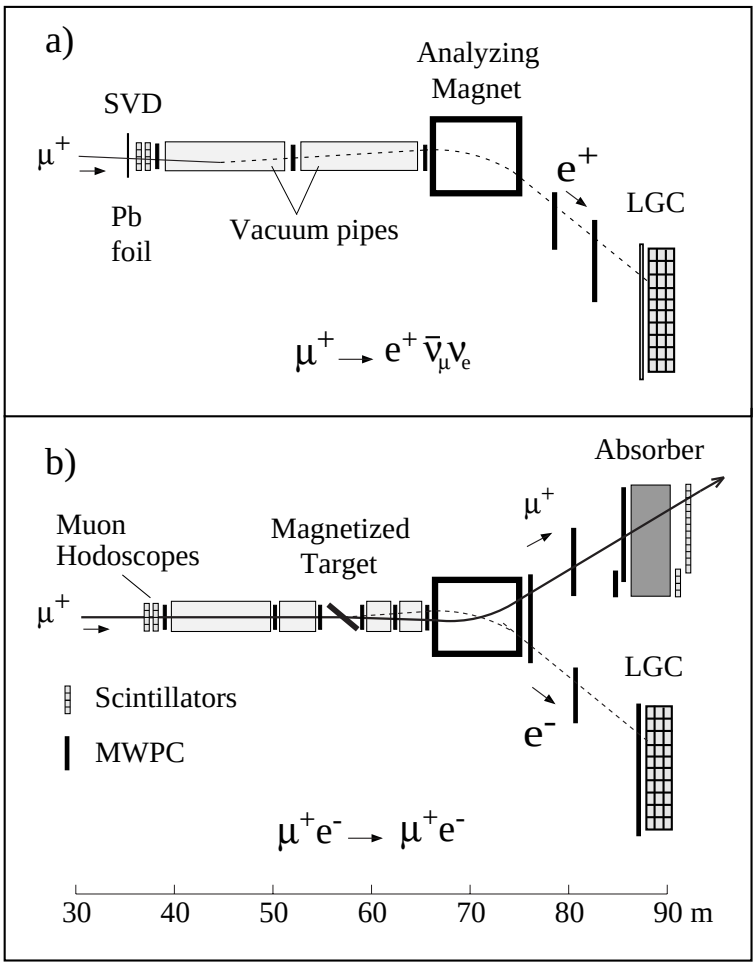

Figure 3.6: Schematic layout of the polarimeter used a) in the decay method and b) in the elastic muon-electron scattering method.

3.1.1 Beam Polarization Measurements

The polarization of the muon beam was measured with a dedicated apparatus, located downstream of the main SMC spectrometer (Figure 3.6). The polarimeter ran independently of the main experiment and could be seen as an experiment

of its own. Two independent methods have been used:

- the *Decay Method* [88] measured the energy spectrum (Michel spectrum) of positrons from muon decays $\mu^+ \to e^+ \overline{\nu}_\mu \nu_e$; the shape of the Michel spectrum depends on P_μ;
- the *Scattering Method* [89] measured the spin-dependent cross section asymmetry of the polarized muon - electron elastic scattering.

Decay Method

The energy spectrum of electrons produced in muon decays, known as Michel spectrum [90], depends on the parent muon polarization P_μ, and is calculable in QED. At L.O. in QED, for μ^+ decays, it is given by

$$\frac{dN}{dy} = N\left[\frac{5}{3} - 3y^2 + \frac{4}{3}y^3 - P_\mu\left(\frac{1}{3} - 3y^2 + \frac{8}{3}y^3\right)\right] , \tag{3.4}$$

where $y = E_e/E_\mu$ is the ratio of positron to muon energy and N (normalization factor) is the number of decays. Figure 3.7 shows the Michel spectrum for three extrem cases of $P_\mu = -1,\ 0,\ +1$.

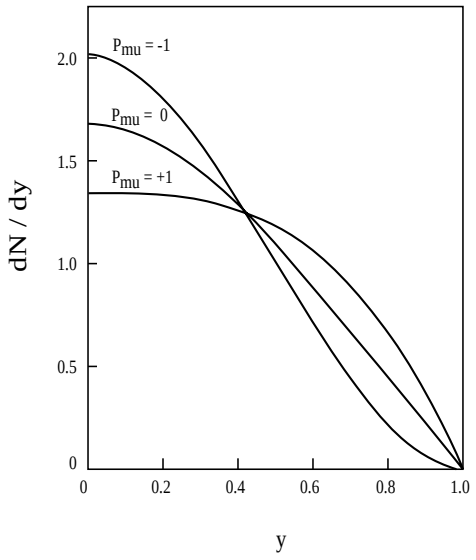

Figure 3.7: Energy spectrum of positrons from muon decays, as a function of $y = E_e/E_\mu$, for the three different muon longitudinal polarizations $P_\mu = -1,\ 0,\ +1$.

The muon polarization P_μ can be determined from the slope of the $\frac{dN}{dy}$ spectrum by fitting the observed y distribution with the Michel spectrum (Equation 3.4). In the case of μ^-'s the sign in front of P_μ is reversed.

The layout of the *decay* polarimeter is shown in Figure 3.6a:

- a shower veto counter (SVD) to reject incident background positrons and to define the beginning of the muon decay volume;
- a 33 m long evacuated decay volume where the μ^+'s decayed into e^+'s;
- a 6 m long dipole magnet with a field integral $\int \vec{B} \cdot d\vec{\ell}$ of about 11.70 Tm;
- a set of multiwire proportional chambers (MWPC), placed upstream and downstream of the magnet, to measure the decay e^+ tracks;
- a lead glass calorimeter (LGC) to identify and to measure the energy of the e^+'s.

In the offline reconstruction, the upstream and downstream tracks measured in the MWPC's are required to intersect in the magnet. The angle between the two segments determines the momenta of the decay e^+'s. In order to reject events where the μ^+'s decayed in the magnet, the e^+ momentum measured in the MWPC's has to match the momentum determined from the energy deposited in the LGC. A Monte Carlo simulation was used to correct the measured positron energy spectrum. It took into account the radiative effects at the vertex, external bremsstrahlung, the geometry of the setup and the MWPC efficiencies as well. The muon polarization was determined by fitting Equation 3.4 to the measured positron energy spectrum.

Scattering Method

The elastic $\mu\, e \to \mu\, e$ process (Möller scattering) is a spin dependent reaction. By measuring the cross section spin asymmetry for elastic scattering of longitudinally polarized muons from longitudinally polarized electrons in a magnetized foil, P_μ can be determined. The spin-dependent cross section at first order in QED is given by [91]:

$$\frac{d\sigma}{dy} = \frac{2\pi r_e^2 m_e}{E_\mu} \left(\frac{1}{y^2} - \frac{1}{yY} + \frac{1}{2} \right) (1 + P_e P_\mu A_{\mu e}) \tag{3.5}$$

where $r_e = e^2/(4\pi\epsilon_0 m_e c^2)$ is the classical electron radius (m_e is the electron mass), E_μ is the muon energy, $y = 1 - \frac{E'_\mu}{E_\mu}$, and $Y = (1 + m_\mu^2/2m_e E_\mu)^{-1}$ is the kinematical upper limit of y. The longitudinal target electron and longitudinal beam muon polarizations are indicated by P_e and P_μ, respectively. The cross section asymmetry $A_{\mu e}$ for antiparallel ($\rightleftarrows$) and parallel ($\rightrightarrows$) spin orientations of the incoming muon ($\rightarrow$) and target electron ($\Rightarrow$) in the laboratory is given by:

$$A_{\mu e} = \frac{d\sigma^{\rightleftarrows} - d\sigma^{\rightrightarrows}}{d\sigma^{\rightleftarrows} + d\sigma^{\rightrightarrows}} = y\,\frac{1 - y/Y + y/2}{1 - y/Y + y^2/2}\ . \tag{3.6}$$

The measured asymmetry $A_{\mu e}^{exp}$ is related to $A_{\mu e}$ as follows:

$$A_{\mu e}^{exp} = \frac{N^{\rightleftarrows} - N^{\rightrightarrows}}{N^{\rightleftarrows} + N^{\rightrightarrows}} = P_e P_\mu A_{\mu e}\ , \tag{3.7}$$

where the N terms are the event counts for the labelled orientation of muon and electron polarizations.

The schematic layout of the *Scattering* polarimeter is shown in Figure 3.6b; several elements are common to the *Decay* setup. The *Scattering* polarimeter makes use of a two arm spectrometer:

- the first arm allows the detection of the muons, which scatter from the polarized electron target
- the second arm (same as in the *Decay* setup) detects the scattered electrons.

The polarized electron target consisted of a 2.7 mm thick ferromagnetic alloy placed in a strong magnetic field of 2.3 T. The target was positioned at an angle of about 25° with respect to the beam axis in order to have an electron polarization component parallel to the beam. To suppress systematic effects the polarity of the target magnetic field was reversed each SPS spill, and the target was rotated from $+25°$ to $-25°$ and vice versa every two hours. The electron polarization was determined from the magnetization measured by the pick up coils wound around the target [92], using the magnetomechanical ratio g′ of a similar alloy. It was found to be $|P_e| = 0.0834 \pm 0.0010$ along the beam axis.

Elastic scattering events were reconstructed by demanding that the tracks determined by the MWPCs intersected in the target and satisfied the 2-body kinematics of an elastic process. Most of the background was eliminated by requiring

energy conservation between the initial and final states: $E_\mu - (E'_\mu + E'_e) < 40$ GeV. The contribution from the main background process, $\mu^+ \to \mu^+\gamma \to \mu^+e^+e^-$, was measured by taking special runs with a μ^- beam. The contribution from a possible false asymmetry was studied by using a Monte Carlo simulation of the apparatus (acceptance check) and by taking data with an unpolarized polystyrene target: it was found to be consistent with zero.

3.1.2 Results for the Beam Polarization

The values of the beam polarization obtained with the two methods are summarized in Table 3.1. Both results are compatible within their uncertainties. The combined result (1993 to 1996 data) for the mean muon beam energy of 187.4 GeV is:

$$P_b\left(\langle E_b\rangle = 187.4 \text{ GeV}\right) = -0.799 \pm 0.015 \ , \tag{3.8}$$

and, for the mean muon beam energy of 99.4 GeV (1992 data), P_b is:

$$P_b\left(\langle E_b\rangle = 99.4 \text{ GeV}\right) = -0.80 \pm 0.04 \ . \tag{3.9}$$

As discussed before (Figure 3.5), the beam polarization P_b depends on the beam energy. Since the beam has a momentum spread of about 3 %, in a precise asymmetry measurement the muon energies have to be taken into account for the determination of the corresponding polarizations. This effect is seen in the data and is accounted for on an event by event basis in the calculation of the cross section asymmetries.

Method	Beam Polarization
Scattering	-0.797 ± 0.016
Decay	-0.806 ± 0.029
Combined	-0.799 ± 0.015

Table 3.1: Muon beam polarization at 190 GeV.

3.2 The Polarized Target

Figure 3.8 shows the SMC target. The target consists of two target cells polarized in opposite directions along the beam. In order to cancel the time dependent fluctuations in the spectrometer acceptances and beam flux variations, the polarization of the target cells was often reversed. Different solid materials were used as SMC target materials (section 3.2.3). In order to polarize the materials and to maintain their polarization, very low temperatures ($\ll 1$ K) and strong magnetic fields (2.5 to 5 T) are needed. This requires the use of a dilution refrigerator (section 3.2.4) and of a superconducting magnet (section 3.2.5). With the Dynamic Nuclear Polarization (DNP) method (section 3.2.2), which requires a microwave system (section 3.2.6), much higher target polarizations than in thermal equilibrium (section 3.2.1) can be reached. Ten NMR coils were used to measure the target polarization (section 3.2.7).

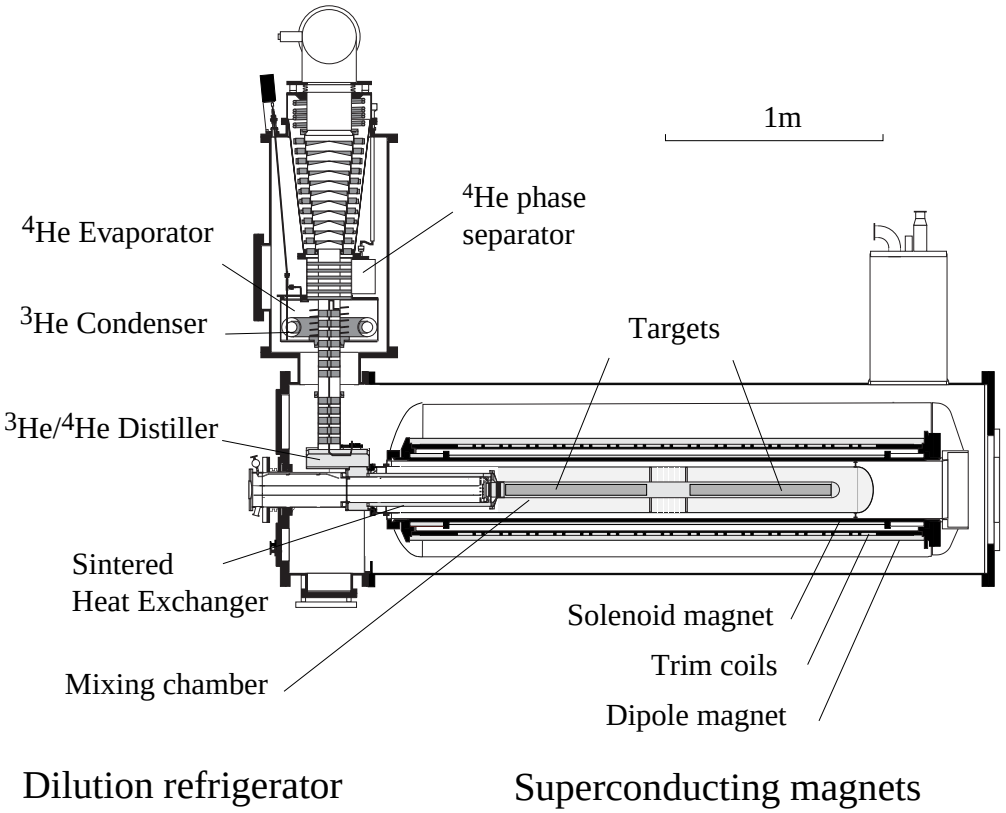

Figure 3.8: The SMC polarized target cryostat. The muon beam traverses the cryostat from left to right.

3.2.1 Polarization in Thermal Equilibrium

Inside an external magnetic field, a particle of spin $\vec{S}$ (e.g. an electron, a proton, or an atomic nucleus) interacts with the field with an energy E proportional to its magnetic moment $\vec{\mu} = g\mu\vec{S}$ and to the magnitude of the magnetic field $\vec{B}$:

$$E = -\vec{\mu} \cdot \vec{B} = -g_i \mu_i \vec{S} \cdot \vec{B} \ . \tag{3.10}$$

μ_i is the particle magneton and g_i is the corresponding g-factor (related to the anomalous magnetic moment). This energy can assume only (2S+1) discrete values, because the spin $\vec{S}$ and its z-component S_z are quantized:

$$E_m = -m g_i \mu_i B \ , \tag{3.11}$$

where m is the value of the z-component of the spin in $\hbar$ units, the quantization z-axis being parallel to the magnetic field.

In the case of an ensemble consisting of a large number of particles with equal spins (e.g. a crystal), a thermodynamical equilibrium between the various energy levels is reached after a characteristic relaxation time through the interactions with the environmental lattice. The relaxation time depends strongly on environmental parameters like the temperature and the magnetic field. The occupancies N_m of the (2S+1) energy levels then follow a Boltzmann distribution:

$$N_m \propto e^{-\frac{E_m}{k_B T}} \ , \tag{3.12}$$

where k_B is the Boltzmann constant and T the lattice temperature.

The (vector-)polarization for such an ensemble of particles, which gives a measure of the relative occupancies, is defined as the expectation value of the spin z-component:

$$P_V = \frac{< S_z >}{S} = \frac{\sum_{m=-S}^{S} m N_m}{S \sum_{m=-S}^{S} N_m} \tag{3.13}$$

and is described by the Brillouin function:

$$P_V = \frac{2S+1}{2S} \coth\left(\frac{2S+1}{2S} x\right) - \frac{1}{2S} \coth\left(\frac{1}{2S} x\right) \tag{3.14}$$

where $x = \frac{\hbar\omega_0}{k_B T}$ and $\omega_0 = \frac{g_i \mu_i B}{\hbar}$ is the Larmor frequency.

For spin $\frac{1}{2}$ particles (electrons, protons, ^{13}C nuclei, etc.) the polarization is given by:

$$P_{\frac{1}{2}} = \frac{N_{+\frac{1}{2}} - N_{-\frac{1}{2}}}{N_{+\frac{1}{2}} + N_{-\frac{1}{2}}} = \tanh\left(\frac{\hbar\omega_0}{2k_BT}\right) \tag{3.15}$$

and for spin 1 particles (deuterons, ^{14}N nuclei, etc.) is given by:

$$P_1 = \frac{N_{+1} - N_{-1}}{N_{+1} + N_0 + N_{-1}} = \frac{4\tanh\left(\frac{\hbar\omega_0}{2k_BT}\right)}{3 + \tanh^2\left(\frac{\hbar\omega_0}{2k_BT}\right)} \tag{3.16}$$

The polarizations of electrons and protons in thermal equilibrium are given in Table 3.2 for different temperatures and values of the magnetic field.

T	B = 0.5 T		B = 2.5 T		B = 5 T	
in K	P_e	P_p	P_e	P_p	P_e	P_p
300	0.11	0.0001	0.56	0.001	1.12	0.002
77	0. 44	0.0006	2.18	0.003	4.36	0.007
4.2	7.97	0.012	38.0	0.061	66.4	0.12
1	32.4	0.05	93.8	0.26	99.8	0.51
0.05	99.99	1.02	100	5.1	100	10.1
0.01	100	5.1	100	25.0	100	47.0

Table 3.2: Electron and proton thermal polarizations in % for different temperatures and magnetic fields.

The highest polarizations can be reached at the highest magnetic fields B and the lowest temperatures T, as it can be deduced from Equation 3.14. For a field of 2.5 T and a temperature well below 1 K the electrons are fully polarized. Under the same conditions, instead, the protons are only slightly polarized, because of the smallness of the proton magnetic moment (about 660 times lower) compared to the electron one.

3.2.2 The DNP Method

The proton polarization can be significantly enhanced by irradiating the material with microwaves via the so-called Dynamic Nuclear Polarization (DNP). In solids

the DNP method allows to transfer the high polarization of the electrons to the nuclei. Two models, the Solid State Effect (SSE) and the Equal Spin Temperature (EST), briefly introduced below, are usually used to describe the DNP process.

The Solid State Effect

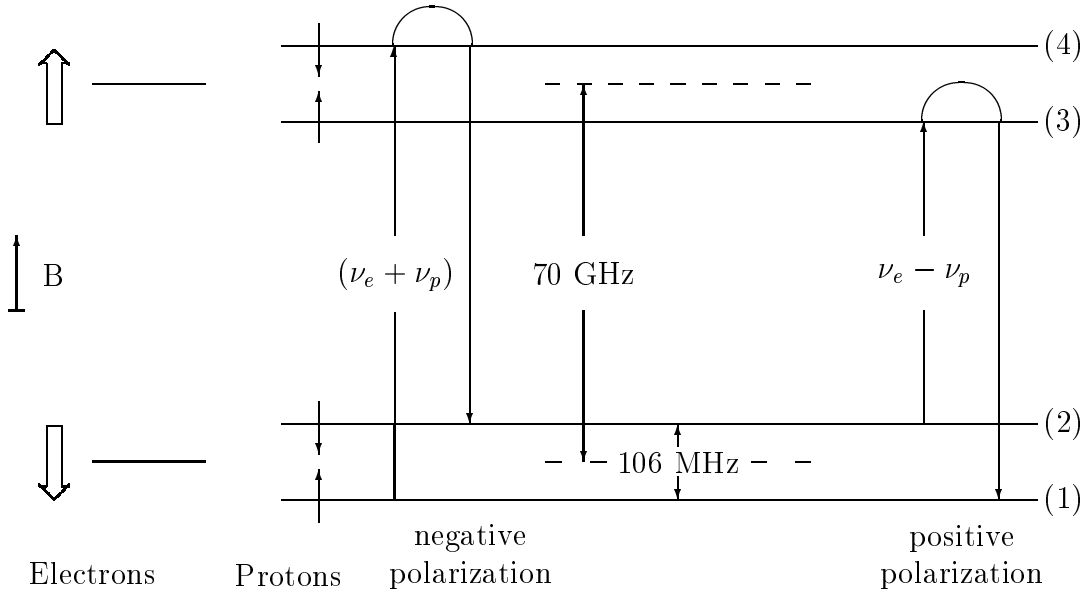

Figure 3.9: The energy level diagram of an electron-proton spin pair in an external magnetic field B. The frequencies shown correspond to B = 2.5 T.

The simplest description of the DNP technique is the Solid State effect. It can be illustrated in the simple model of electron-proton pairs in a magnetic field B. The energy levels of such a pair are shown in Figure 3.9. At temperatures well below 1 K, the magnetic moment of the electron is anti-aligned with respect to the magnetic field B. When irradiating the system with microwaves of frequency $\omega_e + \omega_p$ ($\omega_e - \omega_p$), as illustrated in Figure 3.9, the transition $1 \rightarrow 4$ ($2 \rightarrow 3$) is induced. This results in a simultaneous flip of the electron and of the proton spins. ω_e and ω_p are the Larmor frequencies of the electron and of the proton, respectively. For a 2.5 T magnetic field (like in SMC), $\omega_e/2\pi$ = 70 GHz and $\omega_p/2\pi$ = 106 MHz.

In such transitions only *free* electrons or *free* radicals can participate. Such paramagnetic centers are introduced by chemical doping of the material with a Cr V complex or by irradiation in the case of ammonia (*free* radicals).

Because of the interactions with the phonons of the lattice, the electrons return to their thermal equilibrium states after a relaxation time of a few msec. On the contrary, the relaxation time for the protons at mK temperatures is of the order of days. Thus the system ends up in the state 2 (1).

The electrons can make again the transition $1 \rightarrow 4$ ($2 \rightarrow 3$) with another proton in their vicinity, while the proton which just participated to the transition remains in the more (less) energetic state. This leads to a build-up of a negative (positive) proton polarization (with respect to the magnetic field direction) in the vicinity of the paramagnetic centers.

Proton spins not in the vicinity of electron spins become also polarized due to the spin diffusion process involving a simultaneous spin-flip of two opposite proton spins. This cross-relaxations rate contributes to the polarization build-up time, as well.

A large concentration of paramagnetic centers ($\geq 10^{-4}$) is required to polarize the sample. In the SMC target materials the relative concentration of paramagnetic centers compared to the protons or the deuterons is of the order of 10^{-3}. This concentration of paramagnetic centers is higher than in other laboratories. This simple model, however, is not always describing correctly the observed polarization behaviour of the materials used in the SMC target. The DNP process, instead, is well described by the Equal Spin Temperature (EST) model.

The Equal Spin Temperature Model

In this approach the whole system is seen as an ensemble of electrons and protons in thermodynamical equilibrium. The electron-electron spin interactions induce a splitting of the Zeeman levels into quasi-continuous bands. The occupation probability inside these bands is described by the Boltzmann distribution with a characteristic spin-spin temperature T_{SS}. In thermal equilibrium $T_{SS} = T_{Ze} = T_L$ (Figure 3.10.a), where T_{Ze} is the Zeeman temperature related to the occupations of these bands, and T_L is the lattice temperature.

By irradiating the sample with microwaves around the electron Larmor fre-

quency ω_e (the system is immersed in a magnetic field), it is possible to change the electron occupancies in these energy bands by flipping the electron spins, and thus to modify T_{SS} and T_{Ze}. Indeed, a slightly lower (higher) frequency ω leads to a missing (additionnal) energy which has to be balanced from the cooling (heating) of the spin-spin reservoir, so that T_{SS} is smaller (higher) than the lattice temperature T_L. This is illustrated in Figure 3.10.b (Figure 3.10.c).

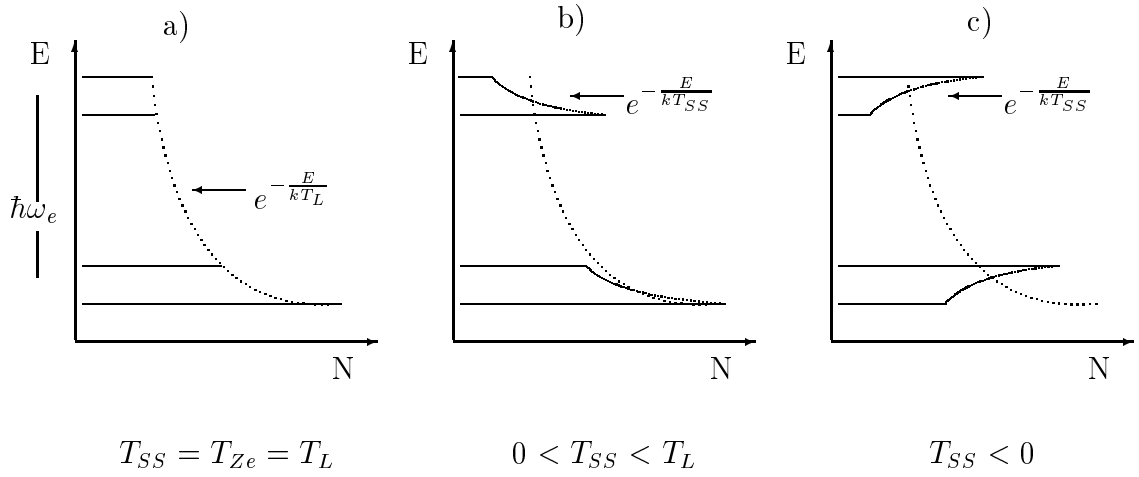

Figure 3.10: a) Thermal equlibrium with the lattice, the separation between the bands is $\hbar\omega_e$, b) cooling with the microwave frequency $\omega < \omega_e$, c) heating with the microwave frequency $\omega > \omega_e$.

Because of the hyperfine interaction, there is a thermal contact between the spin-spin reservoir of the electrons (T_{SS}) and the Zeeman-reservoir of the nucleons (T_{ZN}), which induces transitions involving proton spin-flips. In this way T_{Ze} and T_{ZN} get balanced. The polarization of the nucleon can then be calculated with the Brillouin function (Equation 3.14) using T_{ZN} instead of T_L for the temperature.

In this model the Zeeman temperatures of different spin nuclei of the same target material become equal. In SMC the validity of the EST theory could be verified (section 3.2.7) by measuring the proton polarization as well as the ^{14}N polarization of the ammonia target (NH_3).

3.2.3 The Target Materials

The various target materials used in SMC are listed in Table 3.3. They are known to reach high polarizations with the DNP technique. The paramagnetic centers were introduced by chemical doping of the material with paramagnetic compounds in the case of butanol (EHBA-Cr V), and by irradiating the material with electron beams in order to create the free radicals in the case of ammonia.

Year	Beam Energy [GeV]	Target Material	$\langle$ Polarization $\rangle$	$\Delta P/P$ in %
1992	100	Deut. Butanol: C_4D_9OD	0.40	± 5.0
1993	190	Butanol: C_4H_9OH	0.86	± 3.0
1994	190	Deut. Butanol: C_4D_9OD	0.49	± 5.4
1995	190	Deut. Butanol: C_4D_9OD	0.50	± 2.1
1996	190	Ammonia: NH_3	0.89	± 2.7

Table 3.3: The SMC targets including the target mean polarizations.

Initially (year 1992), SMC used a polarized target system originally designed and constructed by EMC [7, 93, 94]. Because of the relatively low intensity of the muon beam and the smallness of the μN cross section, it was necessary to use a long (thick) target, in order to obtain a sufficiently large luminosity (event yield). A new polarized target system, therefore, has been developed and has been used from 1993 on: it had larger target cells, a more homogeneous magnetic field and a stronger dipole magnet.

The target material was contained in two 65 cm long cylindrical cells (60 cm during the 1993 run) with a diameter of 5 cm. The two cells, referred to as the *upstream* and the *downstream* target cell, were separated by 20 cm (30 cm in 1993) along the beam direction, so that it was easy to separate the interactions occuring in a particular target cell.

The target material was in the form of small spheres (in the case of butanol) or in the form of chips (in the case of ammonia) to facilitate its cooling well below

1 K; only about 60 % of the target volume was occupied by this material, the rest being a mixture of liquid ^{3}He/^{4}He in which the chips were immersed. The volume fraction occupied by the material is known as the packing fraction κ_m.

Ammonia as a Target Material for the Year 1996

To compare the effectiveness of various materials, the figure of merit $\mathcal{M}$

$$\mathcal{M} = \kappa_m \, \rho \, f^2 \, P^2 \tag{3.17}$$

is used. κ_m is the packing fraction, ρ the density of the target material, f the dilution factor (described below), and P the average target nuclear polarization. The precision of the spin asymmetry measurement, δA, depends, among other factors, on $\mathcal{M}$ as:

$$\delta A \propto 1/\sqrt{\mathcal{M}} \; . \tag{3.18}$$

Therefore, the larger $\mathcal{M}$ the better will be the statistical precision of the measurement for the same beam time (luminosity).

The packing fraction of the butanol was determined by weighing the material after unloading the target at the end of the 1993 proton run: $\kappa_{C_4H_9OH} = 0.62 \pm 0.04$. For the following discussion, the packing fraction of ammonia is assumed to be the same as the butanol one. Indeed, after unloading of the ammonia target at the end of the 1996 run, it was found to be: $\kappa_{NH_3} = 0.58 \pm 0.01$. This lower packing fraction is due to the irregular shape of the ammonia chips.

The dilution factor f measures the ratio of polarizable protons in the material to the total number of nucleons in the molecule of the target material:

$$f = \left(1 + \Sigma_A \frac{n_A \sigma_A}{n_{p(d)} \sigma_{p(d)}} \right)^{-1} \; , \tag{3.19}$$

where the sum over A runs over the various elements comprised in the target. Naively: $f_{C_4H_9OH} = \frac{9+1}{4 \cdot 12 + 9 + 16 + 1} = 0.135$ and $f_{NH_3} = \frac{3}{14+3} = 0.176$, so that $\left(\frac{f_{NH_3}}{f_{C_4H_9OH}} \right)^2 = 1.71$. By taking into account the water and the paramagnetic complex, as well as a reduction due to density (coils, helium, etc.), this was estimated to become: $\left(\frac{f_{NH_3}}{f_{C_4H_9OH}} \right)^2 = 1.79$.

Assuming the same muon beam flux and the same target volume as in 1993, it follows that:

$$\begin{aligned}\frac{\mathcal{M}_{\mathrm{NH_3}}}{\mathcal{M}_{\mathrm{C_4H_9OH}}}(P_{\mathrm{NH_3}}) &= \left(\frac{\rho_{\mathrm{NH_3}}}{\rho_{\mathrm{C_4H_9OH}}}\frac{f^2_{\mathrm{NH_3}}}{f^2_{\mathrm{C_4H_9OH}}}\frac{1}{P^2_{\mathrm{C_4H_9OH}}}\right)\cdot P^2_{\mathrm{NH_3}} \\ &= \left(\frac{0.853}{0.985}\cdot 1.79\cdot\frac{1}{0.86^2}\right)\cdot P^2_{\mathrm{NH_3}} \approx 2.1\cdot P^2_{\mathrm{NH_3}} \quad (3.20)\end{aligned}$$

as plotted in Figure 3.11. Assuming further that it would be possible to reach with the ammonia target polarizations as high as those obtained with the butanol target ($\langle P_{\mathrm{NH_3}}\rangle \geq 0.86$), then $\frac{\mathcal{M}_{\mathrm{NH_3}}}{\mathcal{M}_{\mathrm{C_4H_9OH}}} \geq 1.55$. A run with the ammonia target, therefore, would be statistically equivalent to an at least 1.5 times longer run with a butanol target, for the same beam flux. Therefore ammonia was chosen as a target for the 1996 proton run.

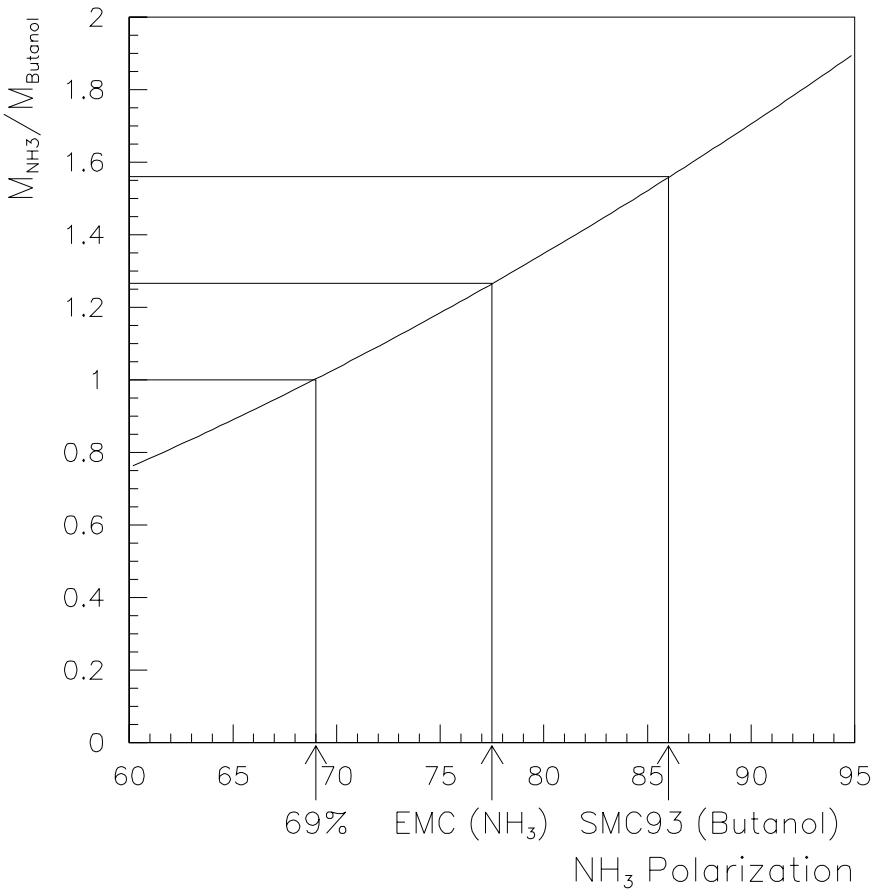

Figure 3.11: The figure of merit of NH3 versus butanol.

Ammonia Preparation

About 2 kg of ammonia have been processed in order to prepare the polarizable target material. The ammonia was delivered in the liquid state with a vapor pressure of 8.6 bar at a temperature of 293 K. The purity of the raw ammonia was 99.98 %, with the ^{14}N isotope content higher than 99.6 %. At a pressure of 1 bar, its boiling point is 240 K and its melting point is 195 K.

The liquid ammonia was solidified in a slow process. A solidification apparatus with a continuous cooling system was used to liquify and to freeze the gaseous ammonia. A fast solidification would produce brittle chips that tend to disintegrate during irradiation. It would also generate some bubbles, which would make it difficult to well define the target density.

The solidification apparatus is schematized in Figure 3.12. Nitrogen gas (1) was cooled by guiding it through a liquid nitrogen vessel (2). It then passed through a heat exchanger immersed in an ethanol bath (3), which surrounded a cylindrical glass tube (4). A Pt100 sensor (thermometer) monitored and regulated (5) the temperature of the ethanol bath, which controlled the nitrogen flow rate (6) to within ± 1 K. The flow of the ammonia gas to the tube (4) was regulated with an inlet (7). As soon as the temperature of the cooling ethanol (3) decreased below 240 K, the ammonia gas was condensed in the cylindrical glass tube (4). The condensing pressure was stabilized at 500 mbar.

Typically, after 1 hour the ethanol bath (3) reached the desired temperature of 190 K. Once an amount of about 150 cm^3 of ammonia was liquified, the ammonia gas flow was stopped. The liquid ammonia immediately started to freeze at the wall towards the center of the glass tube (4). At the same time the vapor pressure was decreasing towards the triple point of about 60 mbar. At this stage the glass tube (4) was filled with 500 mbar of argon (8), which allowed the liquid ammonia to freeze very homogeneously in order to form a transparent block of ammonia ice.

After removing the lid, the cylinder was filled with liquid nitrogen which caused the material to crack. The material was then crushed into pieces and sifted at 77 K to chips of 2-3 mm size.

Each solidification process took about 6 hours. The resulting batch of about

125 cm^3 of ammonia chips were stored in liquid nitrogen. As soon as it was ready, each batch was irradiated in order to introduce the paramagnetic centers.

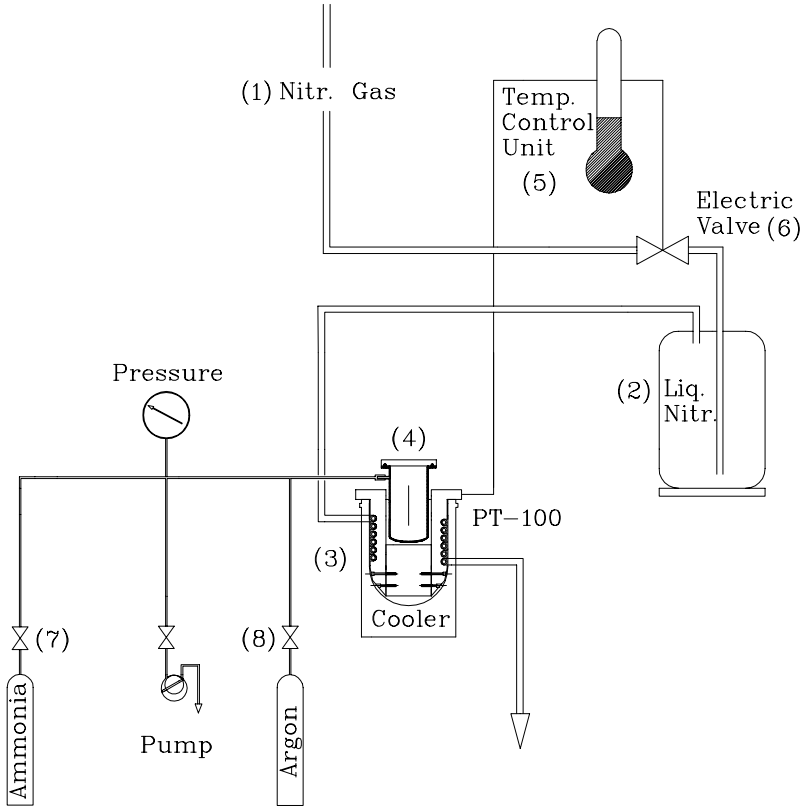

Figure 3.12: The solidification apparatus for the ammonia material. The operation is described in the text.

Production of the Paramagnetic Centers

A paramagnetic center density of the order of 10^{19} e^-/cm^3 (free radicals in form of $\dot{N}H_2$) in the solid ammonia chips is required to make the DNP technique efficient. The $\dot{N}H_2$ radicals were created by irradiating the material with 20 MeV electrons at an average beam current of 30 μA delivered by the injection linac of the Elsa accelerator in Bonn. In this way each batch could be tested individually.

Figure 3.13 shows a schematic diagram of the irradiation set up with a detailed view of the sample container. The cryostat was designed in such a way to

guarantee to all ammonia chips an equal dose of irradiation and an homogeneous repartition of the paramagnetic centers. The cryostat consisted of a thermally isolated inner part (1) containing the argon, which was liquified by a nitrogen heat exchanger (2). The argon level (3) is indicated by the shaded area. Since at 1 bar, the boiling and freezing points (87.3 K, 83.8 K) of argon are close, the temperature of the argon coolant in the sample container (4) was kept constant at 87 K by controlling the liquid nitrogen level in the heat exchanger with the argon vapor pressure. The material was put in the sample container (4) which could contain at most 150 cm^3 of solid ammonia chips, i.e. 1 batch. A current integrator (8) was connected by a rotating feed-through (5) to the sample container. It measured the flow of electrons emitted by the material and captured by the container walls.

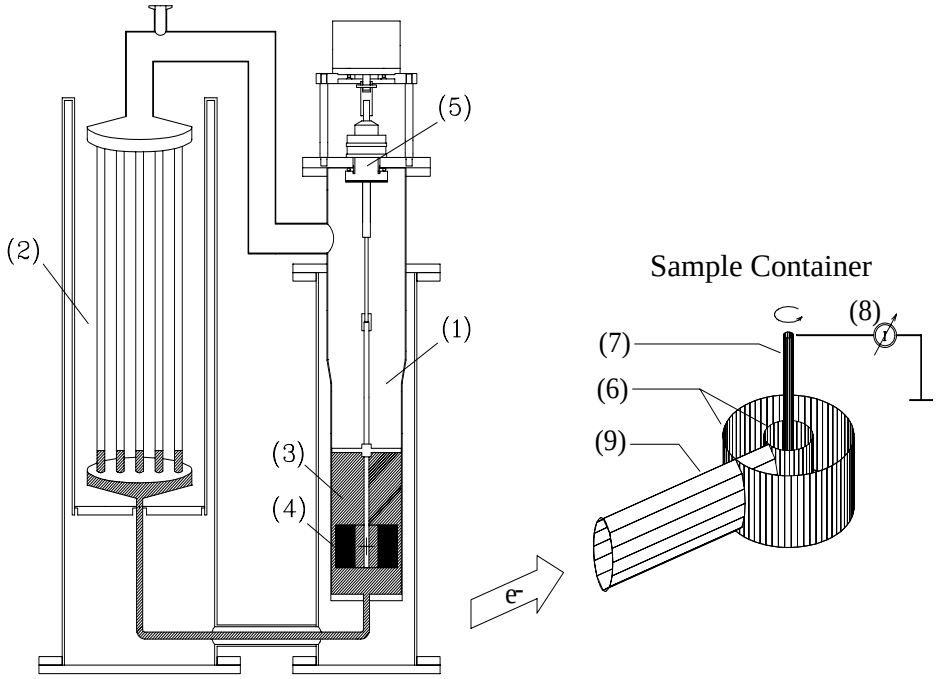

Figure 3.13: Schematics of the irradiation cryostat (left) and the sample container detail (right).

An homogeneous irradiation could be reached thanks to the geometry of the sample container in combination with the vertical spread of the beam (9) and the rotation of the sample container at 1 rps. By irradiation, the color of the

ammonia chips turned into violet.

After the irradiation process, each batch of solid ammonia was polarized at Bonn, in order to verify that the material was highly polarizable. The various batches had similar properties and polarization behaviors (build-up time, maximum polarization, etc.). It was expected that after gathering all the batches (about 3 liters) in the two SMC target cells, which could be cooled to lower temperatures and thus allowing the use of a more powerful microwave frequency generator (section 3.2.6), equal or even higher polarizations would be achieved.

The exact irradiation current could not be measured due to the unknown amount of secondary electron emission. Thus, the amount of the integrated current (10^{17} e^-/cm^3) that the batches were requested to receive was inferrred from the polarization behaviour of several test batches which received different amounts of irradiation. It was indeed used as a relative measure for the density of the paramagnetic centers, which was estimated to be 6×10^{19} cm^{-3} from previous measurements.

3.2.4 The Dilution Refrigerator

The cooling of the target materials well below 100 mK was needed, in order not to loose the target polarizations because of spin-lattice relaxation. This was particularly important during the polarization reversal when the magnetic field (section 3.2.5) was lowered from 2.5 T to only 0.5 T. In order to reach such low temperatures, a ^{3}He-^{4}He dilution refrigerator was used.

One of the design features of the SMC dilution refrigerator is that the target could be loaded at a temperature below 100 K. This was extremely important since the SMC target materials have critical temperatures in the range of 100 K to 120 K related to the devitrification or to the decay of radicals in ammonia.

The principle of a ^{3}He-^{4}He dilution refrigerator is based on the fact that, for temperatures below 0.87 K and ^{3}He concentrations higher than 6.5 %, the ^{3}He-^{4}He mixture separates into 2 phases:

- a ^{3}He-rich concentrated phase floating on top of
- a ^{4}He-rich dilute phase,

as shown at the bottom of Figure 3.14.

At low temperatures all the ^{4}He atoms can occupy the lowest energy state (^{4}He is a boson) and below 2.17 K ^{4}He becomes superfluid. The ^{3}He atoms immersed in the superfluid ^{4}He can move freely and behave like a gas. This is why the lower ^{4}He-rich dilute phase is referred to as quasigas and the upper ^{3}He-rich concentrated phase as quasifluid.

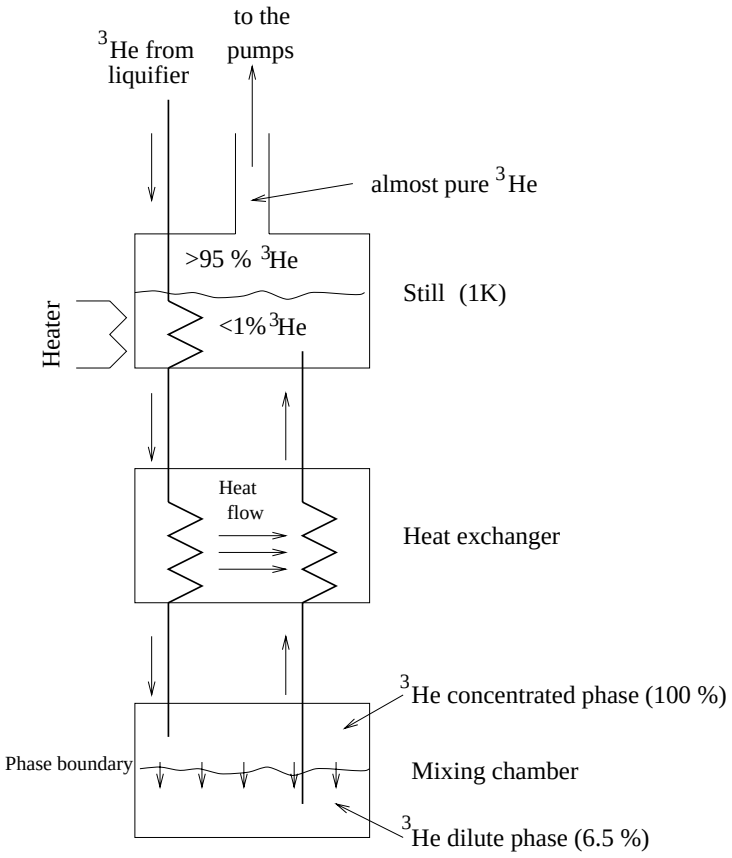

Figure 3.14: Schematic diagram of a ^{3}He–^{4}He dilution refrigerator.

Pumping on the dilute phase reduces the ^{3}He concentration in it: the more energetic ^{3}He atoms from the concentrated phase cross the phase boundary, in order to maintain the equilibrium concentration, resulting in the cooling of the ^{3}He-rich phase. This is analogous to evaporation from the concentrated phase which cools, as the "latent heat of vaporisation" is removed.

In SMC the cooling takes place in the mixing chamber, which contains the

target cells. The flow of ^{3}He across the phase boundary is maintained by pumping on the dilute phase. This is achieved in the still, which is heated to about 1 K and is connected to the mixing chamber via a heat exchanger, as shown in Figure 3.14. Below 1 K the vapor in equilibrium with the dilute ^{3}He-^{4}He mixture is composed mainly of more volatile ^{3}He (97 % at 0.7 K). So by slightly heating (1 K) the mixture in the still, ^{3}He can be preferentially pumped away. A higher temperature in the still would allow to pump away ^{3}He more quickly, increasing the rate at which ^{3}He crosses the phase boundary in the mixing chamber and therefore the cooling power. But excessive quantities of ^{4}He would also evaporate from the mixture in the still, putting an unnecesssarily high load on the pumping system, for a little increase in the cooling power.

To maintain continuous cooling, the ^{3}He vapor removed from the refrigerator is compressed and liquified using an external ^{4}He supply, and then recirculated in the ^{3}He-rich concentrated phase in the mixing chamber via the heat exchangers.

In the heat exchanger before the mixing chamber, the recirculated ^{3}He liquid is cooled by the ^{3}He dilute phase flowing between the mixing chamber and the still. This guarantees that the ^{3}He is returned to the mixing chamber close to the same temperature as the ^{3}He liquid already there, thus minimizing unwanted heat input and the base temperature that can be reached. As the ^{3}He concentration in the dilute phase is of 6.5 % at zero temperature (i.e. it does not vanish), a dilution refrigerator can reach mK temperatures, while a ^{4}He evaporation refrigerator is limited to about 1 K due to the decreasing vapor pressure with lower temperature.

The rate at which the phase transition of the ^{3}He occurs in the mixing chamber determines the cooling power. In SMC, with a pumping rate of 13500 m^3/h, a cooling power of about 1 W was obtained for a typical temperature of 400 mK (30-50 mK) in the polarizing (frozen spin) mode with (without) microwave irradiation.

3.2.5 The Superconducting Magnet

A high magnetic field with a field homogeneity ΔB / B better than 10^{-4} throughout the target volume is required by the DNP technique in order to reach a maximum and a uniform nuclear polarization.

The superconducting magnet consisted of:

- an inner solenoid with a compensation coil at each end and with 16 correction coils distributed along it;
- an outer dipole with a saddle coil type.

The 2.5 T solenoid field was aligned parallel to the incident muon beam. With the help of the 16 correction coils, an homogeneity better than $\Delta B / B = 10^{-5}$ could be reached over the target volume of 150 cm length and 5 cm diameter.

The 0.5 T maximum vertical dipole field was perpendicular to the main solenoid. It was used to maintain the polarization during the rotation of the spins, as described below. It also allowed a transverse target polarization. Since it was not used for neither DNP nor NMR (Nuclear Magnetic Resonance, section 3.2.7), a 2 % field homogeneity was sufficient.

Polarization Reversal

The spin directions in the target cells were reversed about every 5 hours by rotating the magnetic field. 30 minutes to 1 hour before starting a polarization reversal, the microwaves were switched off (frozen spin mode) in order to cool rapidly the target to temperatures of about 50 mK, thus ensuring long spin-lattice relaxation times in a lowered (0.5 T) magnetic field. Each field rotation required about 35 minutes.

As schematized in Figure 3.15, the solenoid field was reversed from $+(-)$ 2.5 T to $-(+)$ 2.5 T. It was first lowered to 0.5 T, and then slowly reduced to zero while increasing the dipole field to its maximum value of 0.5 T, by keeping the resulting field constant to 0.5 T. The dipole field was then lowered again to zero while the solenoid field was increased, but with the reversed polarity. In this way the total magnetic field was always constant to 0.5 T during rotation. The polarities of the correction coils were reversed when the solenoid field was zero.

A considerable loss of the negative polarization due to superradiance was observed during the first field rotations of the 1993 proton data taking. This effect was later suppressed by applying suitable currents to the correction coils, so that the magnetic field became inhomogeneous during the rotation procedure.

The spin directions in the target were also reversed by microwaves every 2 to 3 weeks, to cancel possible systematic effects connected to the direction of the solenoid field: within the statistical precision, such effects were never observed.

During the microwave reversal, the 2 microwave frequencies are exchanged and the polarization was destroyed. Each time it was necessary to build up the polarization again, which took several hours.

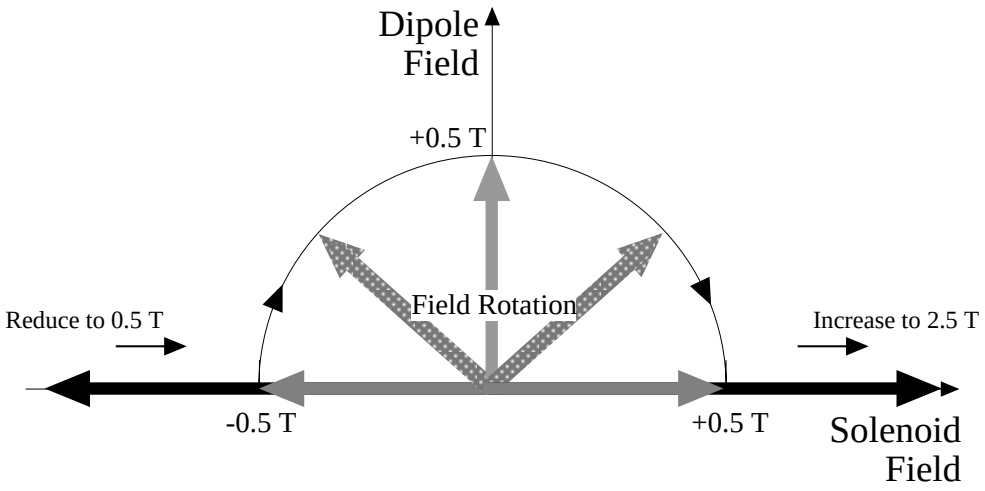

Figure 3.15: The resulting magnetic field vector during a field rotation. Using the 0.5 T dipole magnet the direction of the magnet field can be rotated in both directions -0.5 T $\leftrightarrow$ $+0.5$ T with minimum depolarizations.

3.2.6 The Microwave System

Two independent microwave sources were required in order to polarize oppositely the two target cells. One of them was connected to the upstream part and the other to the downstream part of the cylindrical multimode copper cavity (21 cm in diameter and 170 cm in length). The two parts of the microwave cavity were separated by graphite coated copper baffles and a copper reflector: these microwave stoppers provided an attenuation of 20-30 dB without hindering a free flow of the helium coolant.

The microwaves operated close to the Larmor frequency of the paramagnetic centers which was around 70 GHz in the 2.5 T field of SMC and with a spacing of

about 0.4 GHz. The microwave power was generated by 2 Extended Interaction Oscillator (EIO) tubes, delivering up to 20 W of continuous power around 70 GHz in a band of about 2 GHz.

The frequency could be set coarsely by changing the cavity size of the EIO: this was used for changing (typically every 2 to 3 weeks) the polarization sign of the target cells. It could also be fine-tuned by adjusting the cathode voltage of the HV power supply, allowing a fine control of the frequency by 0.25 MHz/V within a band of about 200 MHz. This fine-tuning of the microwaves had to be done during DNP, in order to obtain a faster polarization growth: the typical polarization build-up times are of few hours, but it takes several days to reach the maximum value.

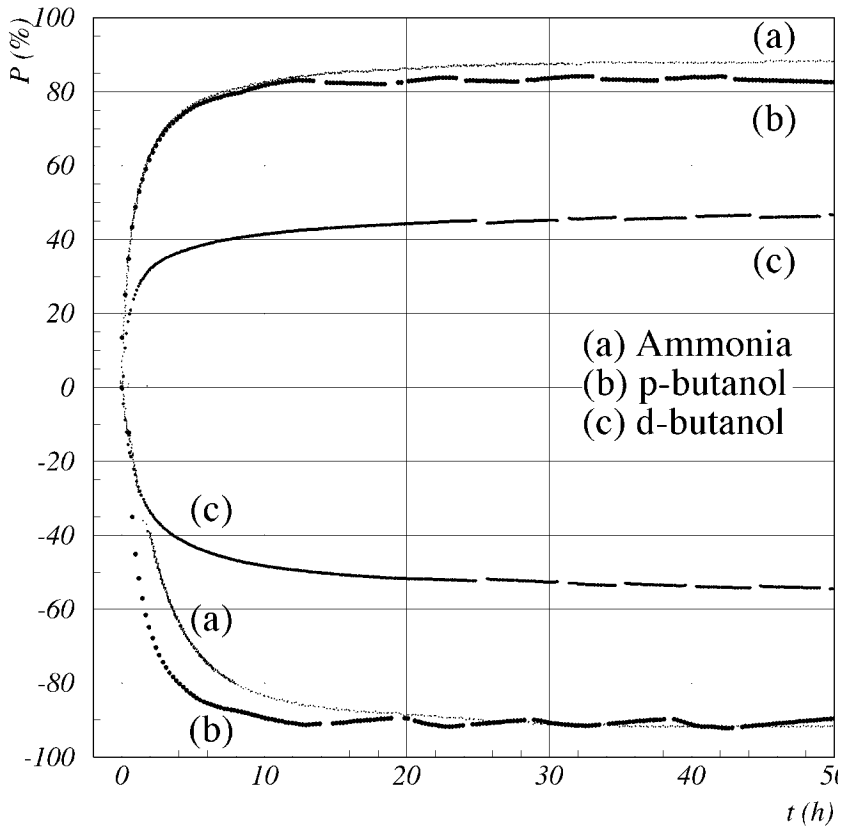

Figure 3.16: Typical polarization build-up time for the target materials, (a) ammonia, (b) butanol, and (c) deuterated butanol followed during 50 hours. The breaks in the data sets are due to interruptions of the measurements during the field rotations.

During the 1992 deuteron run, SMC accidentally found that a modulation of the microwave frequency improved the polarization build-up (speed and final value). The Frequency Modulated DNP (FM DNP) by a modulated microwave frequency in a band of 30 MHz at a rate of about 1 kHz was done by applying an additional triangular waveform to the cathode voltage. It allowed to increase the final plarizations values of 0.2 to above 0.4 for the deuteron targets, as shown in Table 3.3, while a small increase of 0.05 was observed in the already high plarization of the proton material.

Typical polarization build-up curves obtained by FM DNP for the ammonia (a), butanol (b) and deuterated butanol (c) are shown in Figure 3.16. In the case of the proton, (a) and (b), (resp. deuteron (c)) targets, only 10 (resp. 40) hours of FM DNP were needed to obtain about 95% of the maximum polarization, which was reached in 24 (resp. 180) hours.

3.2.7 The Polarization Measurement

The target polarization was determined via Nuclear Magnetic Resonance (NMR), which measures the magnetic susceptibility of the target materials.

Ten NMR coils (5 per target cell) connected to Q-meters were embedded [1] in the target materials and distributed along the target length.

Figure 3.17 shows the schematic layout of the NMR circuit: each coil is the inductive part of an LCR circuit, coupled to an RF power source generated by a synthesizer. As the frequency is swept in 400 frequency steps around the proton's (deuteron's) Larmor frequency, $\omega_p/2\pi = 106$ MHz ($\omega_d/2\pi = 16$ MHz), the material absorbs or emits energy, causing a change in the inductance of the coil, which in turns changes the impedance in the circuit.

The inductance L and the total impedance Z of the Q-meter circuit depends on the susceptibility of the target material located in the NMR coil. The inductance of a coil is given by:

$$L(\omega) = L_0 \left(1 + 4\pi\kappa_m(\chi'(\omega) + i\chi''(\omega))\right) , \tag{3.21}$$

[1] during the 1994 deuteron run, the coils, instead, were mounted on the outer surface of the target cells.

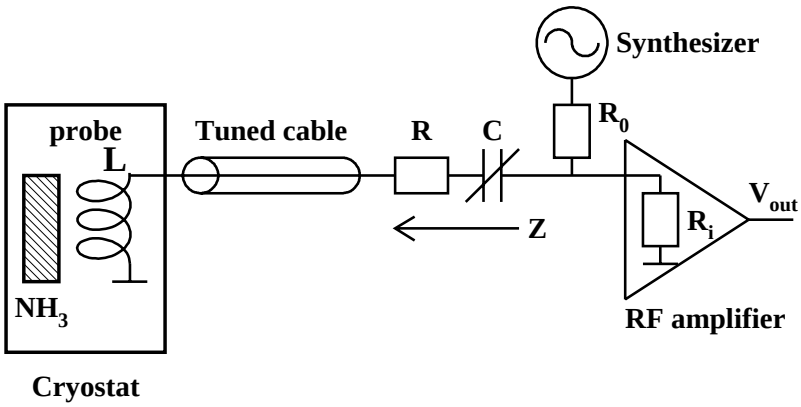

Figure 3.17: Schematic layout of a series Q-meter NMR circuit. Z is the total impedance of the Q-meter circuit, L is the coil inductance, C is the tuning capacitor, R is the damping resistor, R_0 is the current limiting resistor, and R_i is the input impedance of the RF amplifier.

where L_0 is the inductance of the coil in vacuum, κ_m is the packing fraction, χ' is the dispersive and χ'' the absorptive part of the complex susceptibility of the target material around the coil.

The relation between the polarization and χ'' is given by

$$P \propto \int \chi''(\omega) d\omega \propto \int_{\omega_0 - \Delta w/2}^{\omega_0 + \Delta\omega/2} S(w) d\omega \,, \tag{3.22}$$

where $S(\omega)$ is the measured signal size, ω_0 is the Larmor frequency and $\Delta\omega$ is the frequency range over which the signal is measured (typically 400-600 kHz).

Each NMR signal measured with the NMR circuit is a superposition of the wanted NMR signal and of the parabola-shaped Q-curve of the circuit itself.

The Q-curve was measured in dedicated runs, where the Larmor frequency was shifted out of the resonance of the circuit by shifting the solenoid field by few %; in the case of ammonia it was shifted by ± 1.5 %. This was usually done when ramping up the solenoid at the end of a field rotation. After subtraction of the Q-curve, the area under the signal is proportional to the wanted polarization.

Figure 3.18 shows proton and deuteron NMR signals for the different target materials. Depending on the population difference of the magnetic sublevels which defines postive (negative) polarization, the NMR spectrum shows absorption (emission) and therefore a positive (negative) signal.

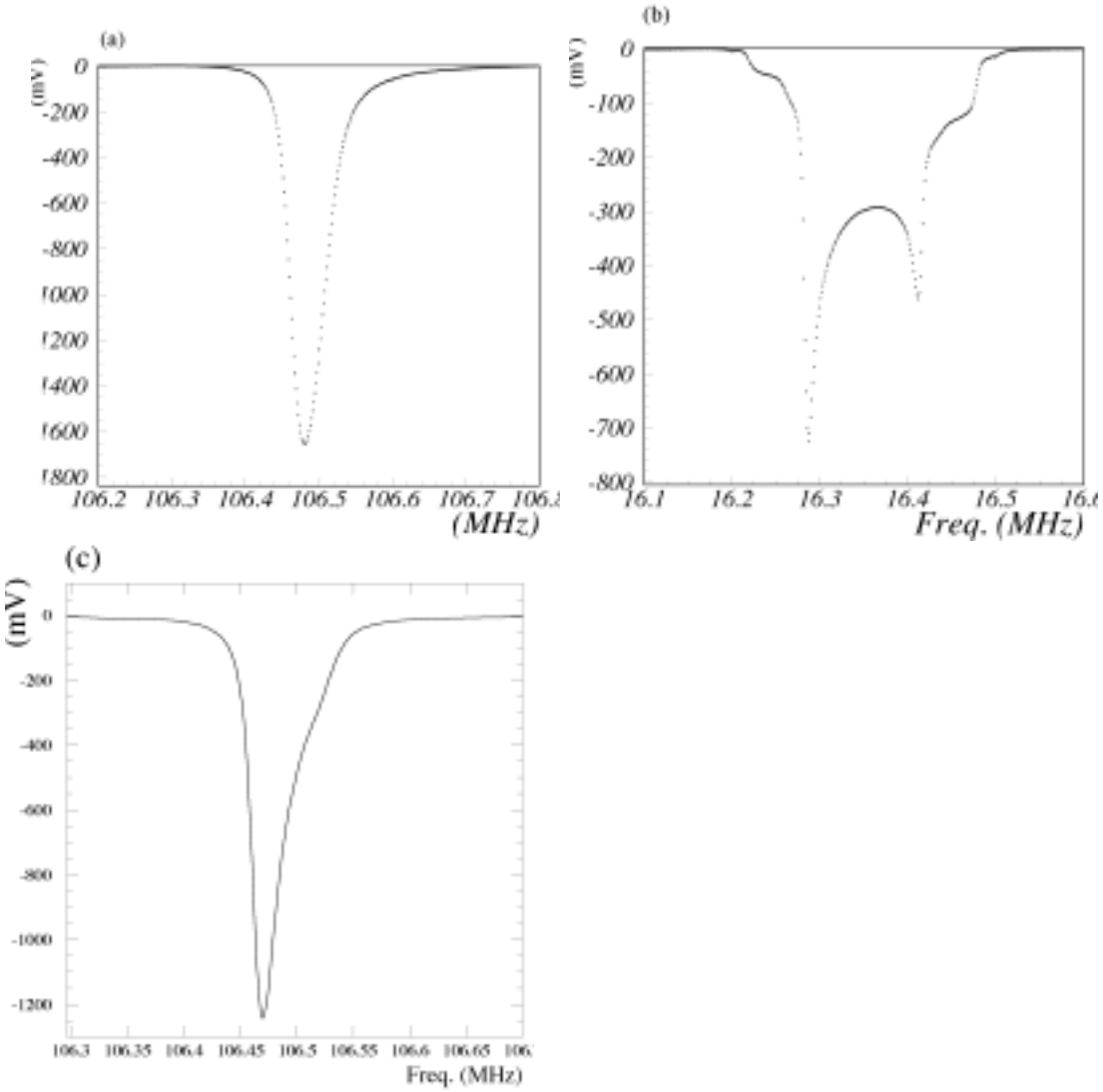

Figure 3.18: NMR signals measured by the SMC polarized target system: proton (upper left) and deuteron (upper right) in butanol, proton (bottom) in ammonia. Note the larger asymmetric lineshape in ammonia compared to butanol.

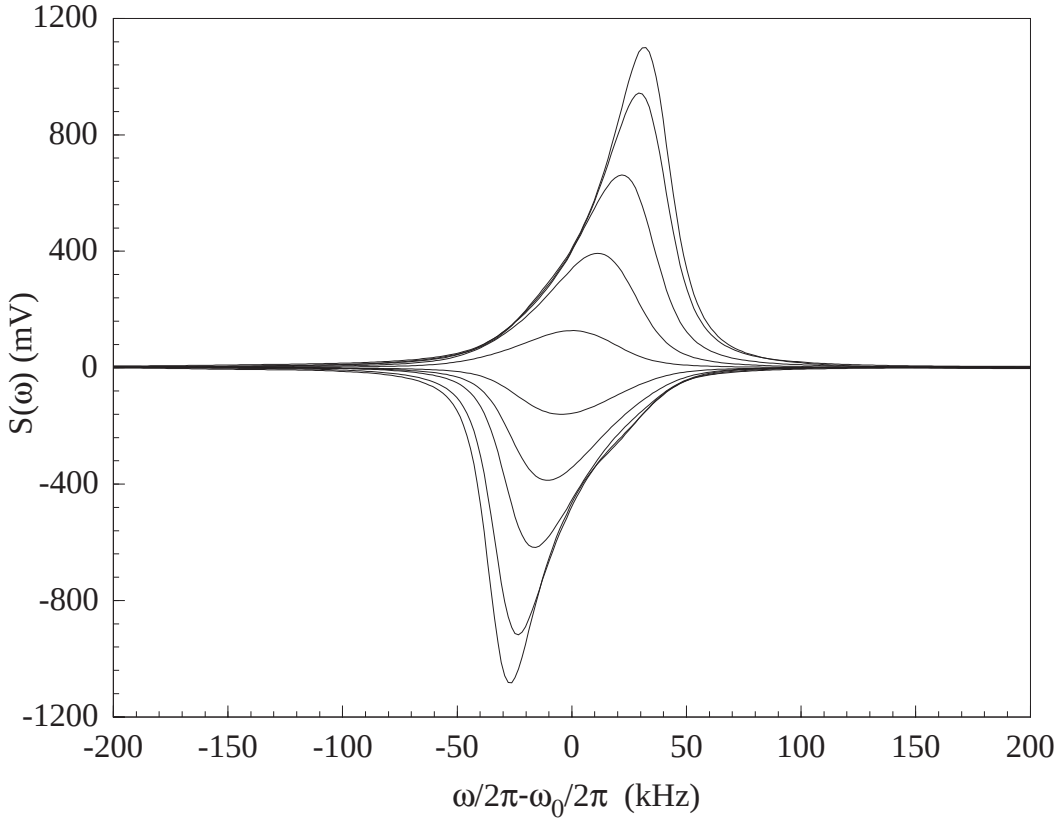

Figure 3.19: The measured proton NMR signals in ammonia for both signs and various polarization values. As the polarization grows, the asymmetry of the line-shape becomes larger.

The net electric field from the dipole moments of the nuclei distorts the signal, leading to an asymmetric line-shape. The ammonia signal has a larger asymmetric lineshape than the butanol one, because the ^{14}N atoms of ammonia have spin 1, while the O and C atoms of butanol are spinless. As the polarization of the material grows, the NMR line-shape becomes more asymmetric (Figure 3.19), since the higher polarization corresponds to a bigger net resulting field. This is the reason why the microwaves had to be fine-tuned during the DNP process as the polarization was growing.

The area under the NMR signal, which is proportional to the wanted polarization, was *calibrated* about 3 times per year by dedicated measurements of the polarization in thermal equilibrium (TE). In order to enhance the TE signal to noise ratio, 2000 (10000) frequency sweeps were averaged for proton (deuteron),

instead of the few hundreds sweeps taken during data taking. The calibration was done at 1 K with pure ^{4}He circulating in the refrigerator, rather than in the dilution mode, in order to guarantee a stable temperature. The TE polarization at a given magentic field (2.5 T) and at a well known temperature (1 K) can be deduced from Equation 3.14. The calibration constant corresponds to the magnitude of the NMR signal when the target polarization is 1 %.

By multiplying the area under the integrated NMR signal with the calibration constant obtained from the TE calibration at 1 K, the polarization is known.

The spin-1 ^{14}N nuclei inside ammonia get also polarized, and thus introduce a polarized background that has to be accounted for in the extraction of the spin asymmetries. Therefore the ^{14}N polarization has also to be known. Since measurements performed in $^{15}NH_3$ and in $^{15}ND_3$ led to conflicting results, and the EST hypothesis had not been verified beyond $|P| = 80$ % in ammonia, the ^{14}N polarization was also measured.

The ^{14}N in ammonia has a Larmor frequency of 7.7 GHz at 2.5 T. The 2 peaks occur around 6.5 MHz and 8.9 MHz; the huge broadening of the peaks is due to the large quadrupole moment of ^{14}N. The Q-meters which were used in SMC don't allow to cover the NMR signal in a single frequency sweep, i.e. preventing from oberserving the 2 peaks at the same time. Two small regions around each peak were measured, instead. Each peak was measured at a different magnetic field. With an NMR frequency of 6.47 GHz, the peaks were found at fields of 1.68 T and 2.45 T. For this purpose, one coil was specially designed for measuring the ^{14}N signals. This coil could also measure the proton signals (without optimization). The whole signal was then reconstructed by fitting a theoretical line-shape to the 2 NMR signals.

Figure 3.20 shows the 2 fragments as well as the reconstructed line-shape of a ^{14}N NMR signal, with the fitted function.

The normal NMR line-shape of a spin-1 particle is similar to that of deuterated butanol, because of the interaction between the quadrupole moment and the electric field gradients (e.g. C-D and O-D bonds in deuterated butanol) of the material, depending on the orientation of the electric field gradients with respect to the external magnetic field. In absence of an effective electric field, e.g. ^{6}LiD which has a face-centered cubic crystal structure so that the electric field gradients

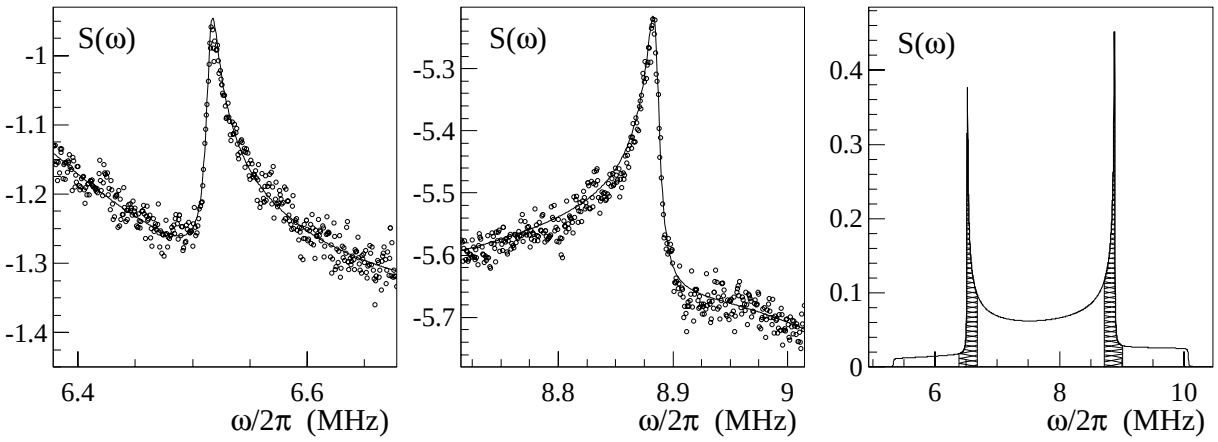

Figure 3.20: The two measured parts of a nitrogen subtracted NMR signal and the entire signal reconstructed from the line-shape model. Left and Middle: The measured left and right signal peaks. The solid lines are fits to the data points. Right: The reconstructed signal at 2.5 T with the residual background removed. The hashed areas represent the measured regions.

cancel, the NMR line-shape is again a gaussian.

Two methods were used in order to determine the polarization. The first *Asymmetry* method made use of the fit to the reconstructed line-shape, which gave the values of the ^{14}N polarization from the signal asymmetry. The *Asymmetry* method was not used for the deuterad butanol because it was too imprecise.

The second *Area* method was relying on a non-standard TE calibration. The small amplitude of the ^{14}N signal at 1 K prevented a direct TE calibration. For this reason the calibration of the N/p coil was done (at 1 K) with proton signals by moving the magnetic field to a value where the proton Larmor frequency corresponds to the Larmor frequency at which the ^{14}N signals were measured. This ensured that the Q-meter gain did not change. Once the so-called cross-calibration constants were determined (with a 2.5 % relative error), the *Area* polarization of the ^{14}N was obtained by multiplying the cross-calibration constants with the area under the integrated NMR signal.

The ^{14}N polarization corresponding to the signal of Figure 3.20 is determined to be $P_{\mathrm{N}} = 9$ % from both the *Area* and *Asymmetry* methods. The ^{14}N polarization measurements with the two methods gave consistent results, as shown in Figure 3.21. They support an overall agreement with the EST prediction over a

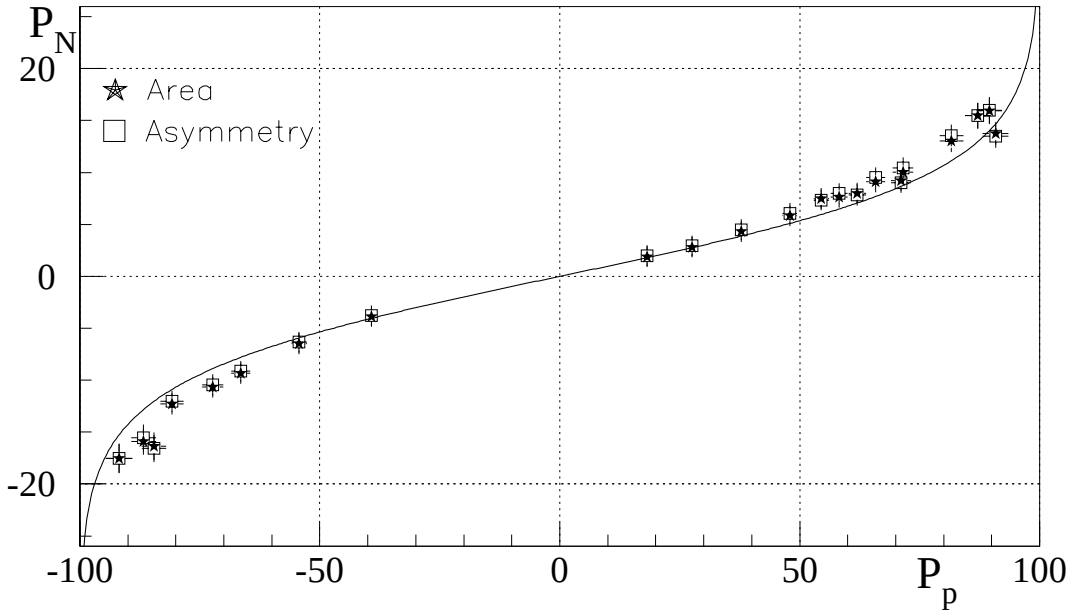

Figure 3.21: The ^{14}N polarization determined by the cross calibration area and asymmetry methods is plotted as a function of the proton polarization. The solid line is the expected relation if the EST hypothesis is valid.

large range of polarization. As the ^{14}N signals were too small at low polarizations, there are no data points there.

The radial homogeneity of the deuteron polarization was investigated by using small coils placed in the inner and outer target regions, at the same longitudinal position: no significant radial dependence was found; the uncertainty is included in the polarization error.

The averaged polarizations and accuracies of the SMC target materials are listed in Table 3.3.

3.3 The Spectrometer

The general layout of the SMC spectrometer is shown in Figures 3.22 and 3.23. It consisted of about 150 planes of proportional chambers, drift chambers, streamer tubes, and scintillating hodoscopes. This large number of planes ensured a redundancy in the tracking and hence a minimization of the systematic uncertainties. The spectrometer had no hadron identification, only the sign of the hadron charge could be determined. The spectrometer can be divided in three parts:

- The "Beam Definition" section, which consists of a set of veto counters, P0's MWPC and beam hodoscopes to measure the track of the incoming muon.

- The "Magnetic Spectrometer" with a large acceptance dipole analyzing forward magnet (FSM) located between the polarized target and a massive iron absorber. It provides the momentum measurement of the scattered muon and of the charged particles produced in the interaction. It also included a calorimeter, H2, used to separate hadrons from electrons; H2 was located at the end of this section.

- The "Muon identification" performed by detecting and tracking the scattered muons downstream of a 2 m thick iron absorber, which stopped electrons and hadrons, but not the muons.

The SMC spectrometer is an upgrade of the apparatus originally built by the European Muon Collaboration (EMC) [95] in 1978 and later also used by the New Muon Collaboration (NMC) [107]. The SMC apparatus had more trackers and provided a bigger kinematical coverage at low x and low Q^2 (trigger).

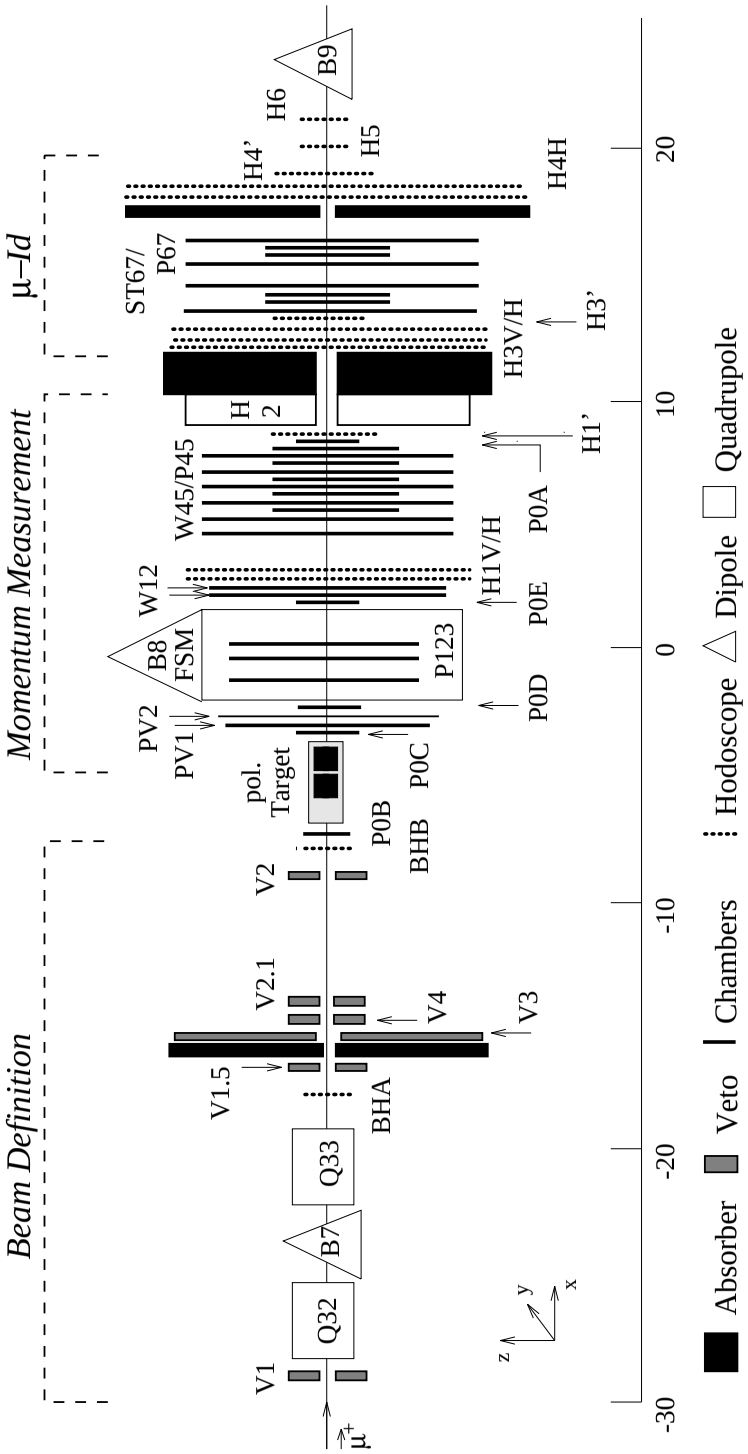

Figure 3.22: Top view of the SMC spectrometer.

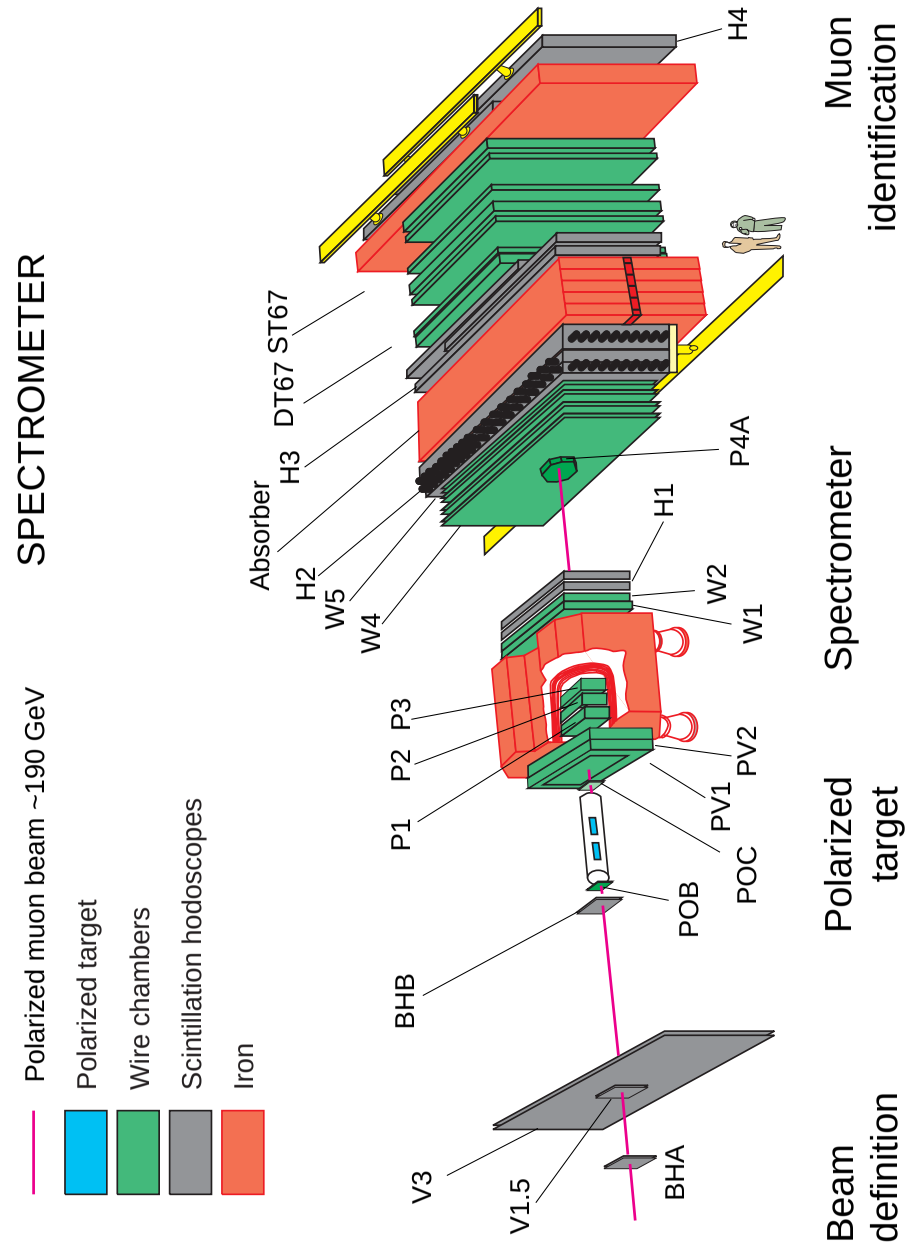

Figure 3.23: Artistic view of the SMC spectrometer.

The SMC Reference Frame

The center of the Forward Spectrometer Magnet (FSM) defined the origin of the experiment coordinate system. The SMC reference frame had the positive x–axis directed along the muon beam direction. The z–axis pointed vertically upwards and the y–axis pointed horizontally to the beam left side (Jura mountain) in order to generate an orthogonal right handed reference system. In this frame, the center of the polarized target was located at $x = -4.855$ m, $y = -0.061$ m, and $z = -0.005$ m.

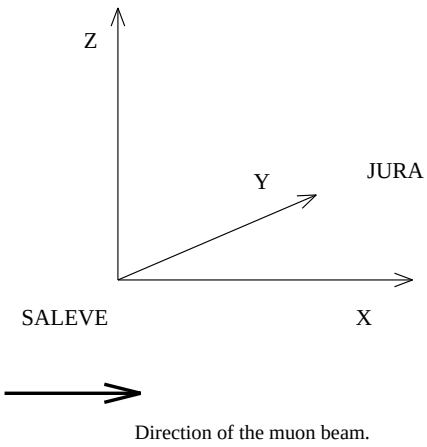

Figure 3.24: Reference system used by SMC.

3.3.1 Beam Muon Detection

The momentum of each incoming muon is measured in the Beam Momentum Station (BMS) with a typical precision $\delta P/P$ of 0.3 %. The BMS consisted of 4 stations of segmented scintillating hodoscopes, 2 upstream and 2 downstream of a set of bending dipole magnets, which measured the deflection of the beam in the vertical plane.

After passing through the BMS, the incoming muons enter the experimental hall from the left of Figure 3.22. Before entering the spectrometer, the beam particles have to pass through the holes of five veto scintillation counters, referred to as V1, V1.5, V3, V2.1 and V2. Halo muons, extending up to a few meters from the beam center, are detected by the veto counters and then rejected. It can happen that some halo muons have peculiar trajectories and pass through

all the holes of the vetos. In this case they are not rejected. However, these halo tracks represent a very small fraction. Particles other than muons, which are in the far halo of the beam, are absorbed by the 40 cm thick iron wall in front of the large V3 veto counter. Halo muons passing the large V3 hole are vetoed by V2.1 and V2, which define the maximum acceptable diameter of the beam by their adjustable hole size of about 6 cm in diameter. A description of the veto counters is given in Table 3.4.

The trajectories of the incoming muons, upstream of the polarized target, were measured with two beam scintillator hodoscopes BHA, BHB, in conjunction with the MWPC P0B (Figure 3.22). A precise measurement of the trajectory is needed in order to reconstruct the interaction vertex and to determine the muon scattering angle.

Veto Counter	x Position m	Width $\times$ Height cm^2	Size of the central hole cm
V1	-28.00	48×48	14.0×8.0
V1.5	-16.5	60×60	$\oslash$ 13.0
V3	-15.0	650×400	50.0×50.0
V2.1	-14.5	40×40	$\oslash$ 3.0
V2	-11.5	50×50	$\oslash$ 3.0

Table 3.4: Characteristics and positions of the SMC veto counters.

3.3.2 The Magnetic Spectrometer

The magnetic spectrometer stretched about 15 m from the polarized target to the H2 calorimeter. More than 100 planes of tracking devices upstream and downstream of the dipole spectrometer magnet (FSM) determined the trajectory and momentum of the scattered muons and of the charged particles produced in the interaction. The characteristics of the tracking devices are summarized in Table 3.5.

The FSM analyzes the momentum of the scattered particles. It is a large

dipole magnet 4 m long with an opening of 2 m$\times$1 m in the $y-$ resp. $z-$direction. For a beam energy of 190 (100) GeV, it was operated at 4000 (2000) A corresponding to a $\int \vec{B} \cdot d\vec{\ell}$ of 4.4 (2.3) Tm. During the experimental data taking, the field stability was monitored with an NMR probe and several Hall probes.

Upstream of the FSM, the MWPC's, P0C, P0D and PV12, measured the scattered muon and hadron tracks, with an angular resolution of about 0.4 mrad. For the pattern recognition the detection of the particle trajectories inside the FSM was necessary, because of the high particle multiplicities and magnet length. For this purpose, 4 MWPC's, P1A, P1B, P2 and P3, were used inside the FSM. Downstream of the FSM the drift chambers W12 and W45, and the MWPC's P0E, P45 and P0A, measured the particles which passed through the magnet. The overall resolution of the momentum measurement of the tracked particles is about $\delta P'/P' \sim 1$ %.

The 2 m thick H2 calorimeter (section 3.3.4) consisting of an electromagnetic and an hadronic section is used to separate electrons and positrons from hadrons.

3.3.3 Scattered Muon Detection

Downstream of H2 a 2 m thick iron absorber stopped the electrons and the hadrons, while the muons penetrated through it. The particle tracks found after this absorber were identified as muons. Four stations of plastic streamer tubes (ST67) [96] of 1 cm cell size, equipped with plane strip readout, tracked the muons. Close to the beam, where the flux was higher, MWPC's (P67) complemented the tracking system. Because of the high particle flux the streamer tubes could not be operated in the HV plateau. This caused a strong dependence of the chamber efficiencies on the pressure and temperature of the chamber gas. Therefore a feedback loop was developed to stabilize the streamer charge and thus the chamber efficiency by adjusting the HV.

Following these detectors, there is a third thinner iron absorber to protect the trigger hodoscope planes H4 located just downstream of it from electromagnetic showering.

Chamber Name	Planes Orientations	Wire spacing $mm.$	Resolution $\mu m.$	Size $cm.$	Dead area $cm.$	x Position $m.$
P0B	UUYYZZVV	1	290	$\oslash$ 14.4	–	-7.1
P0C	UUYYZZVV	1	290	$\oslash$ 14.4	–	-3.2
P0D	ZZUYYVZZ	1	290	$\oslash$ 14.4	–	-1.9
P0E	UUYYZZVV	1	290	$\oslash$ 14.4	–	$+2.3$
P0A	UUYYZZVV U, V = $\pm 60°$	1	290	$\oslash$ 14.4	–	$+8.3$
MSAB	YZUV	0.2	90	10×10	–	$-11.30, -9.16$
MSCD	YZUV U, V = $\pm 45°$	0.2	90	10×10	–	$-3.76, -3.11$
PV1	UYVY U, V = $\pm 80°$	2	580	150×94	–	-2.6
PV2	$YU_1U_2V_2V_1Y$ $U_1, V_1, U_2, V_2 = \pm 45°, \pm 72°$	2	580	154×100	$\oslash$ 13	-2.2
P1A	ZYU	2	–	182×80	$\oslash$ 13	-1.6
P1B	ZYU	2	–	182×80	$\oslash$ 13	-1.0
P2	VYZ	2	–	182×80	$\oslash$ 13	-0.3
P3	VYZ U, V = $\pm 70°$	2	–	182×80	$\oslash$ 13	0.3
W1	VYUZVYUZ	20	$280 - 415$	224×124	$\oslash$ 12	2.6
W2	ZVYUVYUZ U, V = $\pm 60°$	20	$280 - 415$	224×124	$\oslash$ 12	3.1
W45	YYZZUUYY	40	$310 - 600$	524×260	$\oslash$ 12-25	6.4-7.8
	ZZUUYYZZ	40	$310 - 600$	524×260	$\oslash$ 12-25	6.4-7.8
	UUYYZZUU U = $60°$	40	$310 - 600$	524×260	$\oslash$ 12-25	6.4-7.8
P45	YVYUYVYUYU	2	580	$\oslash$ 90	$\oslash$ 12	6.8-8.1
P67	YUYVYUYV U, V = $\pm 30°$	2	580	$\oslash$ 90	$\oslash$ 12	14.0-17.0
ST67	UYUYZVZV	10	350	410×410	$\oslash$ 16	13.8-17.1
	VZVZYUYU	10	350	410×410	$\oslash$ 16	13.8-17.1
	UYUYZVZV	10	350	410×410	$\oslash$ 16	13.8-17.1
	VZVZYUYU U, V = $+22.5°, -67.5°$	10	350	410×410	$\oslash$ 16	13.8-17.1
DT67	3 (2Y 2Z)	52	$530 - 800$	500×420	100×100	13.5-17.3

Table 3.5: Characteristics and positions of the SMC spectrometer chambers.

3.3.4 The H2 Calorimeter

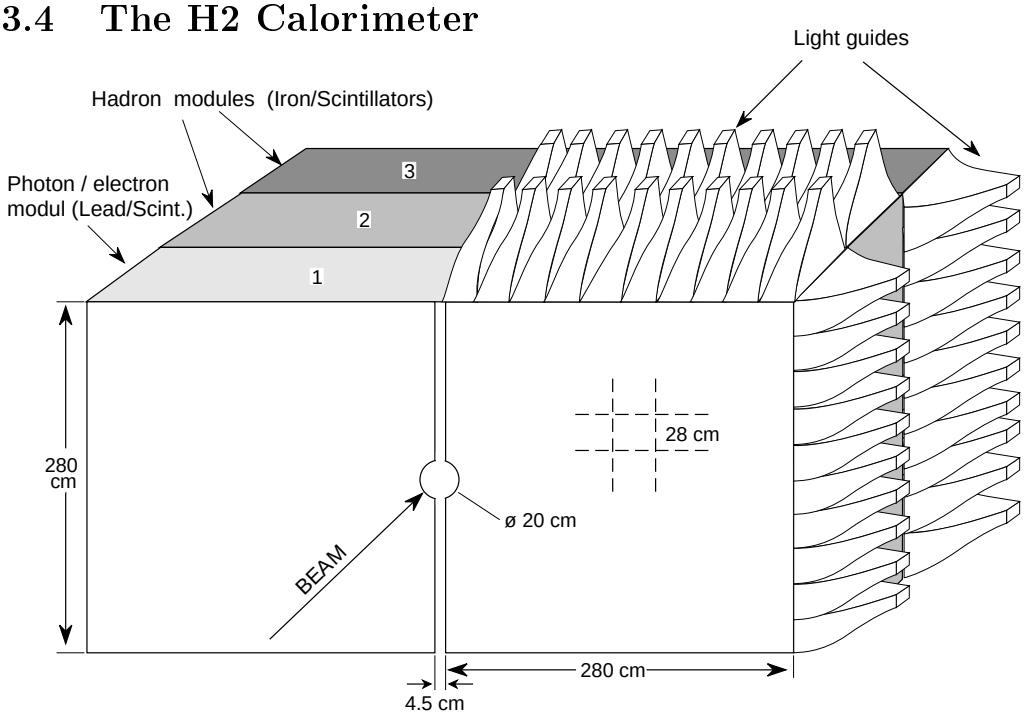

Figure 3.25: The H2 calorimeter. It consists of an electromagnetic section (module 1) and of an hadronic section (modules 2 and 3).

The H2 calorimeter [95] was used to separate hadrons from electrons. As shown in Figure 3.25, it had a $\oslash$ 20 cm hole to allow for the passage of the beam, and consisted of:

- an electromagnetic section made of alternating scintillator and lead planes. The twelve scintillator planes consist of 1 cm thick, 28 cm wide and 280 cm long scintillator plates alternatively vertical and horizontal. Between the scintillator planes lead planes of 0.6 and 1 cm thickness were inserted. The 6 horizontal and the 6 vertical scintillator planes are grouped by coupling them to lightguides (Figure 3.25) and read out separately by 125 mm photomultipliers. The electromagnetic section of the H2 calorimeter corresponds to about 20 radiation lengths and about 1 interaction length.

- an hadronic section (2 successive modules) made of alternating scintillator and 4 cm thick iron planes (used as passive material). The first module had the scintillators vertically oriented, the second module had only horizontally

oriented scintillator planes. The total thickness of the 2 hadron modules corresponds to about 4.5 nuclear interaction lengths.

The entire calorimeter gives a total of about 5.5 interaction lengths. The energy resolution is $\sigma/E = 0.4/\sqrt{E(\mathrm{GeV})}$ for the electrons and $\sigma/E = 1.5/\sqrt{E(\mathrm{GeV})}$ for the hadrons [95]. For each shower the ratio of the energy deposited in the electromagnetic part to the total deposited energy, $emagf = E_{em}/E_{tot}$, was calculated. Electrons are removed by requiring $emagf < 0.8$, i.e. the particle has to deposit at least 20% of its energy in the hadronic section to be considered an hadron.

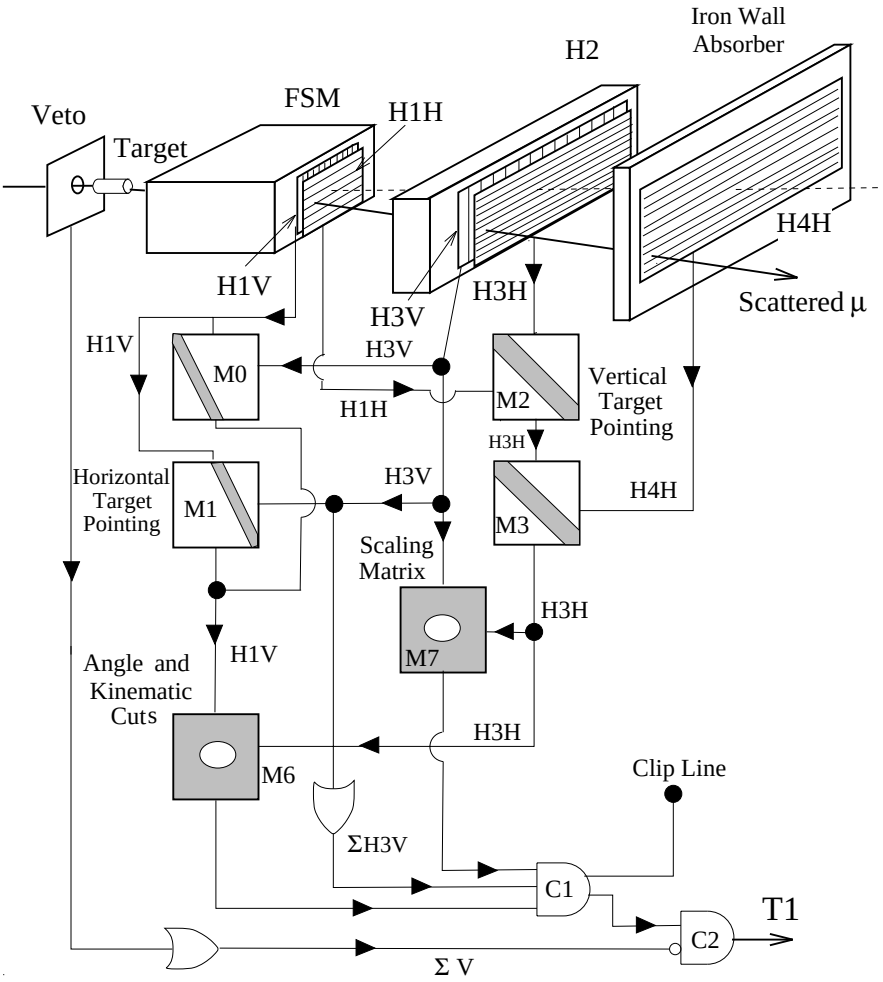

Figure 3.26: The main physics T1 trigger logic for the SMC experiment.

3.3.5 The Triggers

The triggers are formed with three arrays of scintillator counters. They require a predefined coincidence pattern between the elements of these hodoscopes in anticoincidence with the veto counters. The anticoincidence with the veto counters prevented signals from halo muons already detected upstream of the target.

Depending on the kinematical intervals covered and recording purposes different logics were implemented and various selection criteria were used. All the physics triggers (except T15) consisted of scintillation counter elements arranged in three planes. The first hodoscope (H1) was located just downstream of the FSM, the second plane (H3) was installed behind the hadron absorber and the last plane (H4) behind a second iron absorber further downstream.

the large angle physics trigger: T1

The physics trigger T1 selects events with muons scattered at large angles, which correspond to large x and Q^2. The general layout of T1 is given in Figure 3.26. The scintillator hodoscopes planes are segmented horizontally (labelled with an H, e.g. H1H, H3H or H4H) and vertically (labelled with a V, e.g. H1V, H3V or H4V). T1 enforces a rough vertical and horizontal target pointing (cf. Figure 3.27) by requiring patterns of hits in the horizontal and vertical planes. These patterns are programmed into fast coincident matrix modules labelled with M in Figure 3.26. The coincidence of the signals of either two hodoscopes planes is checked by these coincident matrix modules, which in fact are 2-dim arrays of logical AND's. Moreover a minimal angle cut of the scattered muon is performed. A trigger can occur only if the coincident patterns are anticoincident with the veto counters.

the small angle triggers: T2 and T14

These two small angle triggers used three highly segmented hodoscopes (H1$'$, H3$'$ and H4$'$), which covered part of the large hodoscopes holes. They thus allowed to access a lower x and Q^2 acceptance than T1. A detailed description of T2 and T14 can be found in [97]. The T2 and T14 counters were placed on the horizontal bending side of the spectrometer magnet, close to the beam axis, so that they could trigger on muons which scattered at smaller angles compared to the trigger

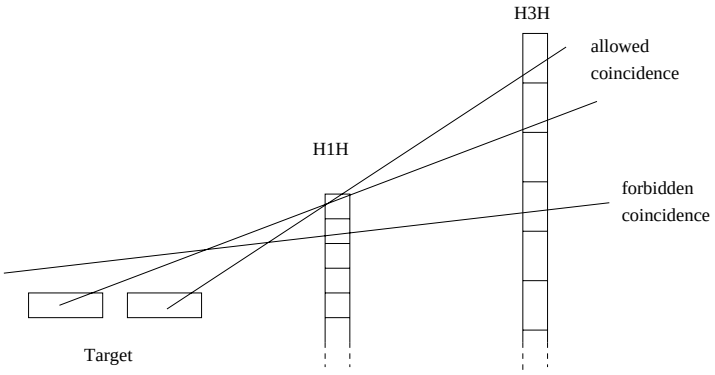

Figure 3.27: Vertical *target pointing* in the trigger: the track is ensured to originate from the target by requiring a defined combination of the hodoscopes planes via the coincident matrix modules.

T1.

the calorimetric trigger: T15

This trigger was introduced to access the very low x and Q^2 region. It was used in 1995 and 1996. Figure 3.28 shows the detectors used for the definition of T15. This trigger used only two scintillator hodoscopes, H1H and H3V (H3C), in conjunction with an hadron signature from the H2 calorimeter. The coincidence H1H$\times$H2 selected the charged hadrons. The scattered muons were selected by requiring a hit in either H3V or H3C hodoscopes. Because of the high trigger rate, T15 was prescaled by a factor of 8 for the 1995 deuteron run and by a factor of 4 for the 1996 proton run.

the random trigger: T10

A random trigger (T10) was used for the beam flux normalization. It is started by a radioactive source 500 m away from the experiment in order to exclude any interference with the beam. The stop signal is generated by a beam track.

In addition, special alignment triggers which trigger on the beam (T5), on the near (T7) and far (T8) halo, (not described here) were used for calibration runs.

In the SMC software a trigger hierarchy has been established: if an event

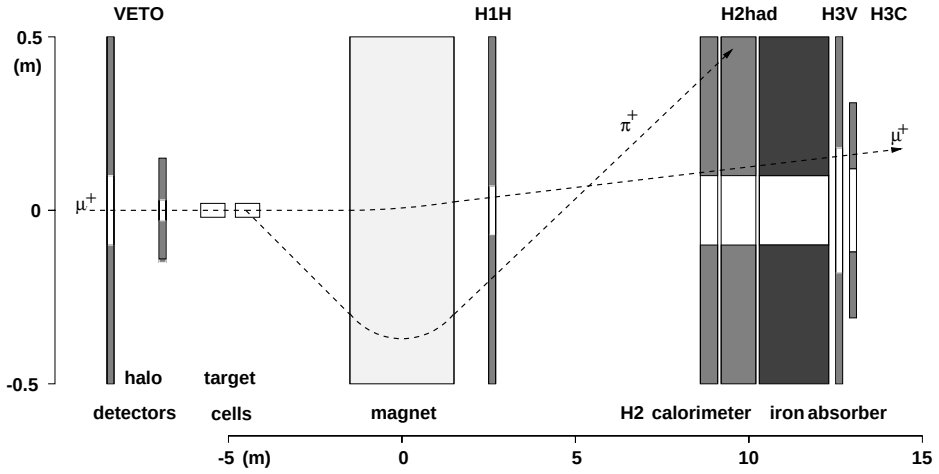

Figure 3.28: Trigger T15 elements viewed in the horizontal bending plane of the magnet.

satisfies multiple triggers, the lowest trigger number is assigned to it. For instance, if an event satisfies T2 and T14, it is assigned to be T2. The kinematical domain for the SMC physics triggers, for a beam energy of 190 GeV, is represented in Figure 3.29.

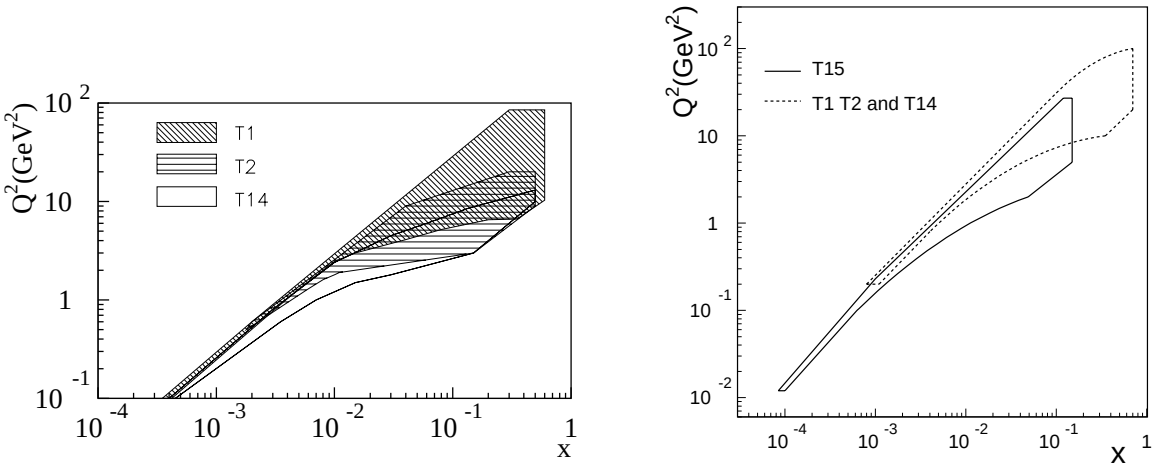

Figure 3.29: The kinematical domain for the SMC physics triggers (for a beam energy of 190 GeV).

3.3.6 Data taking of a run

For each event accepted by the trigger, the corresponding *raw* data are written between the SPS spills onto a magnetic exabyte tape. The *raw* data are arbitrary divided into so-called runs. Each exabyte tape contains about 20 runs which represent something like 30Gb. Typically 20 minutes are needed to take about 30,000 events gathered as a single run.

Chapter 4

Event Reconstruction

With the experimental apparatus described in the previous chapter, about 100 millions raw data events have been collected between 1992 and 1996. As schematized in Figure 4.1, several off-line reconstruction packages bring the acquired raw data, which contain all the relevant information about the event, into a form suitable for the physics analysis. The reconstructed events are written in a highly condensed form to the so-called Micro Data Summary Tapes (in short micro DST's), used for the physics analysis. This first stage of analysis is also known as *production*.

The *production* proceeds in three steps (Figure 4.1): Phoenix, Geometry and Snomux. Phoenix finds track segments in groups of detector planes. Geometry links these segments together, fits the resulting tracks, determines their momenta and slopes, and finds the interaction vertex. Snomux processes the remaining parts of the raw data event and selects events for the physics analysis (data reduction). The production chain includes additional specialized programs for the alignment and calibration of the apparatus studies.

For the physics analysis, the trajectories and momenta of the incoming muon, of the scattered muon and of the other outgoing detected particles are of primary interest. This is realized with the MICRO package, which reads the micro DST's and produces the physics information about the event.

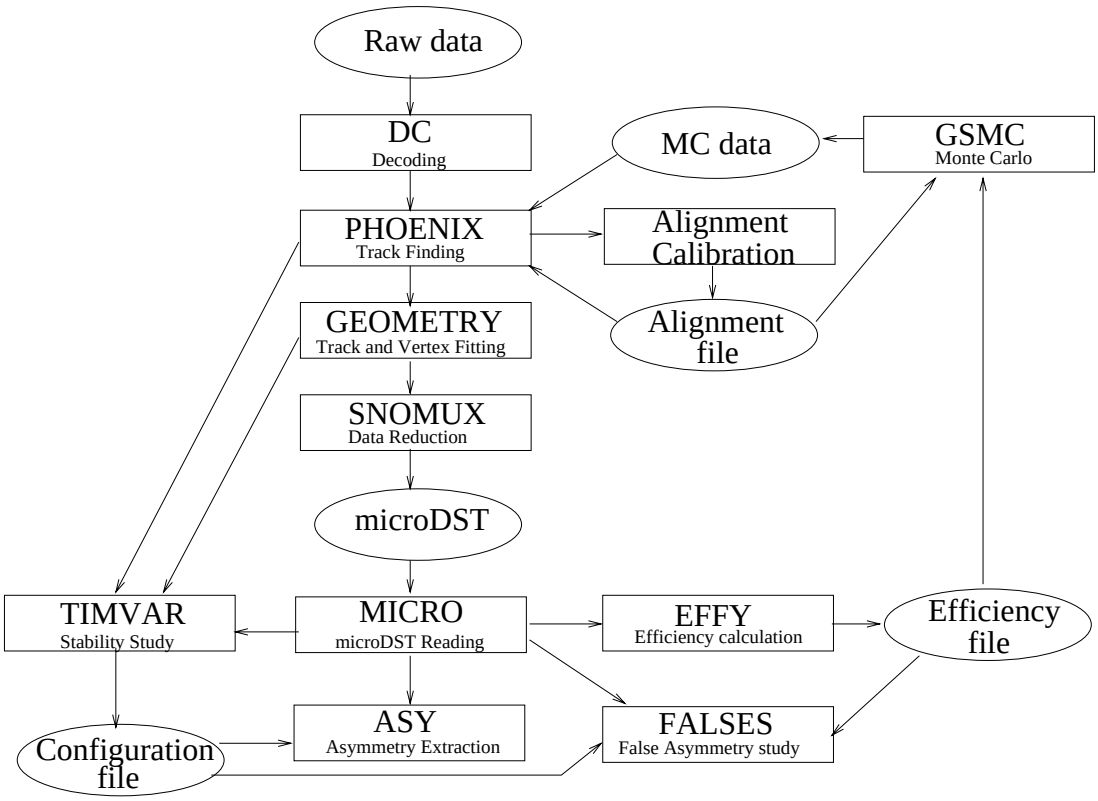

Figure 4.1: The SMC data analysis chain.

4.1 The Event Reconstruction Chain

In the offline analysis, the raw data pass through several software packages following the so-called production chain (Figure 4.1):

decoding of raw data

In this first stage, the binary data words of each detector are translated into a form suitable for further processing: hit wires into positions, ADC values into pulse heights and TDC values into timings. For some detectors (like ST67) the effective hit position is calculated for each cluster of hits by properly weighing each element with its ADC value. For each event, space and time information of the hodoscopes and of the detectors planes have to match, in order to separate background hits from the hits belonging to the tracks associated with the trigger. At this stage, some events are lost due to hardware and readout errors.

PHOENIX: track finding

For each event record, PHOENIX reconstructs the tracks of the incoming muon, of the scattered muon and of any other detected outgoing particle. Before the *pattern recognition* (track finding) can start, the various detectors must be aligned and calibrated in the reconstruction software.

Each full track consists of several segments which are reconstructed from the hits recorded in the trackers along the experiment. For each of the planes composing the tracker (projections Z, Y, U, V) only those hits laying within a fixed distance from a line (straight in the case the tracker is not inside a magnetic field) given by an external prediction are considered. This line is known as *tagging road*; the maximum allowed distance from this line is known as *tagging road width*.

For instance, the tagging road in the muon section of the apparatus is defined by a series of hits in the hodoscopes H3 and H4.

Depending on the trigger type, different directions for the road are chosen: for a physics trigger it should point towards the target, while for a halo trigger it should be parallel to the beam axis. The road width is about 10 cm, corresponding to the width of the hodoscope elements. When extrapolating a track segment to another set of trackers, the direction of the *tagging road* is determined by the track segment already reconstructed, and its width by the uncertainty in the extrapolation. The road widths and slopes have all been determined during the tuning of the reconstruction algorithms.

Next, all hits in each pair of two planes per projection are tried: if the line connecting the hits is sufficiently parallel to the tagging road, it is used to define a *track road*. Then hits close to the *track road* are searched in each of the remaining planes in the same projection. The width of the *track road* is given by the resolution of the detector under study: for a 2 mm pitch MWPC it is typically 2 mm. If a sufficient number of hits can be unambiguously assigned to the *track road*, they are assumed to be part of a track segment. In this case, the track is said to satisy the *minimum plane requirement*. Since the detector planes are not 100 % efficient, it is not required that each plane contributes a hit.

To define the track precisely, a line is fitted through all the planes that have

contributed a hit by minimizing the χ^2:

$$\chi^2 = \sum_{planes} \left(\frac{T_{hit} - T_{pred}}{\sigma} \right)^2 , \tag{4.1}$$

where T_{hit} is the coordinate of the actual hit, T_{pred} is the predicted coordinate from the fit and σ is the resolution of the given plane.

When the tracker efficiency is low and the background is high, fake hits, which do not belong to the track, might still lay within the track road width. Such hits tend to distort the reconstructed track from its real trajectory, resulting in the drop of that track in a later stage.

Finally, the track projections found in the previous step are combined together, with the help of the inclined projections (U and V), in order to form three dimensional space tracks. The tracks are then fitted in space by using all the available projections by minimizing their χ^2's.

The track segment reconstructed so far is then extrapolated to a neighboring detector system, and the track reconstruction procedure is repeated.

The **incoming muon** is reconstructed in the beam hodoscopes and beam chambers by forming straight beam tracks upstream of the target. Its momentum is measured in the beam momentum station (BMS). The beam track is determined with a precision of about 0.1 mrad, and is correlated to the momentum measurement (BMS) by timing. When several track candidates are found in the same event, the correct beam track is determined by comparing the times of the beam hodoscope hits with the trigger time. About 5 % of the data are lost at this stage.

Muons are identified by their ability to traverse thick absorbers. The finding of the **scattered muon** track starts in the muon section of the apparatus, downstream of the thick iron absorber wall (Figure 3.22) with the chambers ST67/P67, where the track multiplicity is the lowest and the tracks are maximally separated. Among the particles emerging from the target, only muons can pass the absorber wall, so that the hit multiplicities in this section are much lower than upstream. However, there is a sizeable background from electromagnetic showers originating mainly in the beam hole in the calorimeter and in the absorber wall. If a track candidate, satisfying the minimum plane requirement, is identified in the

ST67/P67 detector system, the event is further processed, and the track candidate is labelled as muon. About 15 % of the data are lost at this stage.

The next step is to search for tracks in the **field free region** between the FSM magnet and the H2 calorimeter. The muon tracks are extrapolated upstream through the absorber and through the H2 calorimeter to the W45/P45 chambers, which consist of 24 large area drift planes (W45) and of 10 MWPC planes (P45). Taking into account the multiple scattering in the H2 calorimeter and in the absorber wall, *tagging roads* are defined in the W45/P45 chamber system, where hits are looked for and partial tracks are reconstructed. The information from the chambers downstream of the absorber is discarded, because of its limited precision once an upstream continuation of the track is found. The tracks found in W45/P45 are then extrapolated further upstream to the W12/P0E chambers (16 large area drift planes and 8 MWPC planes in the beam region) located just at the exit of the FSM.

The muon reconstruction continues by propagating the tracks **inside the magnet** using the P1A, P1B, P2, P3 and P0E chambers and **taking into account the bending due to the FSM field**. In the magnet, the track reconstruction is more involved because of the magnetic field, and proceeds in **several steps**. In the vertical, non bending projection, the muon trajectory is nearly a straight line. In the horizontal plane it forms an arc of a circle. The tracks found so far in the W12/P0E chambers are tangent to that circle.

In order to define this circle an additional (third) point is required and determined in the following way. First the W12/P0E track is extrapolated straight to the plane in the center of the FSM and normal to the beam axis. Then this point is joined by a straight line to the center of the target. The intersection of this track with the entrance plane of the FSM defines the third point needed to determine that circle. Since the magnetic field is not homogeneous, an effective entrance plane is defined, assuming a perfect box field between this plane and the FSM exit plane with the same field integral as the real FSM field. The straight line in the non bending plane together with the arc of the circle thus determined define the *tagging road* where to look for hits in the P1A, P1B, P2, P3 chambers. Each chamber consists of 3 MWPC planes. The width of this *road* is larger compared to the widths of the *roads* downstream of the FSM, because of

the approximate way this road was defined and because the track (e.g. Λ) might not originate from the center of the target.

The width of this *tagging road* is particularly relevant for the hadron reconstruction. Since the momenta of the outgoing hadrons are generally smaller compared to the momenta of the scattered muons, the hadron trajectories will deviate more from an ideal circle than the scattered muon ones. In order to assure a good reconstruction efficiency also for the hadrons with relatively low momenta, the width of this *road* had to be accurately tuned.

In the **next step**, **using the FSM field map**, the width of the *tagging road* is reduced and the hits, which do not belong to the track, are removed. When several possible continuations are found, the one with the best χ^2 is kept. The track found inside the FSM is fitted with a quintic spline and joined to the straight W12/P0E track found downstream of the FSM.

The tracks thus reconstructed in the FSM are then extrapolated to the target using the PV1/PV2/P0C chambers located between the polarized target and the FSM. The PV1 and PV2 MWPC trackers, with a total of 10 planes, cover the magnet aperture, while the P0C MWPC tracker covers the beam region with 8 planes.

Incoming and scattered muon tracks are matched in the target on the basis of their relative timing. At any stage of the reconstruction, a failure to reconstruct a segment of the muon track in any detector system results in the drop of the event.

At each extension step, if the continuation for the track segment is not found, the event is rejected.

Typically 60 % of the events survive the reconstruction phase (PHOENIX).

Tracks found downstream of the FSM but not with a matching muon candidate in the muon section of the apparatus are **identified as hadrons or electrons** and kept for the hadron reconstruction. The reconstruction of the **other tracks** starts in the W45/P45 chamber system. There are no starting *tagging roads* defined in these chambers as in the case of the scattered muon track. All possible combinations of hits in pairs of planes, not belonging to the muon tracks, are tried in defining narrow *tagging roads* pointing roughly to the target. If a sufficient number of hits is found along these *roads*, the track segments are

then extrapolated further upstream. The reconstruction proceeds further as for the muon track. The hadron track, however, does not need to be also found upstream of the FSM in the PV1/PV2/P0C chambers, because the track might have originated from the decay of a hadron, which itself originated in the target.

GEOMETRY: track and vertex fitting

The track segments found by PHOENIX are linked together and fitted, throughout the whole spectrometer up to the absorber, using a fifth order or quintic spline, in order to determine the tracks momenta and the track parameters precisely. An iterative procedure is used to reject points that contribute to the overall χ^2 of the fit above a given tuneable value. At this point, the scattered muon candidate track is required to satisfy the trigger conditions: the hodoscope elements hit by this track have to reproduce the correct patterns of the predefined logic combinations of the trigger correlation matrices. Otherwise the trigger has been faked by background or uncorrelated tracks, and the event is rejected. The compatibility of the W45 and ST67 tracks is also verified by the quality of the link.

The momentum of the scattered muon and of the other outgoing charged particles is determined from the curvature of their tracks in the FSM magnetic field. The momentum of the incoming muon is found from its bending angle in the BMS. For the beam energy of 190 GeV the precision of the momentum measurement is $\Delta p/p = 0.5$ %. In this fit the momentum of the scattered muon is determined with an average precision of $\Delta p'/p' = 1$ % and the scattering angle ϑ with a precision of 0.4 mrad.

The position of the muon interaction vertex in the target is then derived by extrapolating and by intersecting the incoming muon and the scattered muon tracks into the target volume.

Allowing for uncertainties from multiple scattering and energy loss, the space-time point of closest approach determines the vertex position. The average uncertainties in the reconstruction of the interaction vertex are 0.3 mm transverse to the beam and 30 mm in the beam direction, the latter depending strongly on the scattering angle. Figure 4.2 shows a typical vertex distribution along the beam. As it can be seen, the target cells are well resolved. The interaction point

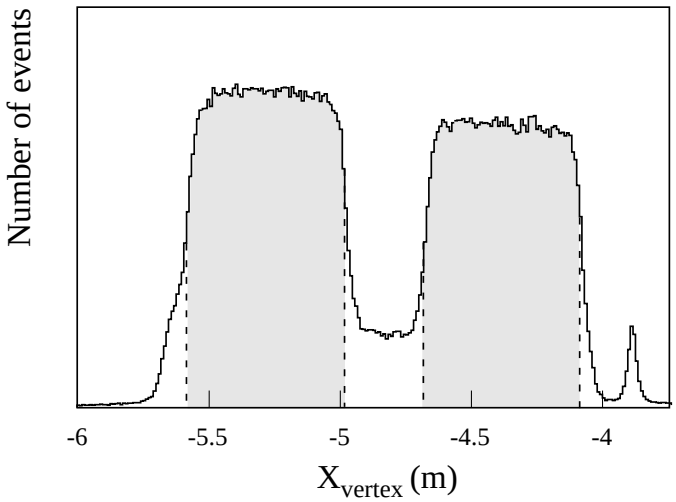

Figure 4.2: Typical vertex distribution along the beam direction. The two target cells are bounded by the dashed lines. The peak on the right side reflects the microwave cavity exit wall.

defines the target cell and thus the polarization direction of the target nucleon. Events outside the cells originate mostly from the ^{3}He/^{4}He coolant and from the metals used for the microwave cavity and the microwave isolation material. Figure 4.3 shows the reconstructed interaction vertices in the plane normal to the beam direction: the cross section of one NMR coil is clearly visible because of its larger density compared to the target material one.

A fit is then also applied to the remaining muon and hadron tracks, as well as to the secondary (decay) hadron vertices. All tracks, which seem to originate from the muon interaction vertex, are used to locate with higher precision the interaction vertex, although it might be biased by secondary interaction effects. This procedure is very useful when the muon scattering angle is small (low Q^2).

The vertex defined with the incoming and scattered muon only is referred to as vertex of type 1, while the vertex defined with the use of additional tracks is referred to as vertex of type 3.

In the analysis, tracks which were fitted to the main vertex are referred to as *fitted tracks*, while those tracks which could not be fitted to the main vertex are referred to as *close tracks*.

An example of a fully reconstructed event in the SMC apparatus is shown in Figure 4.4.

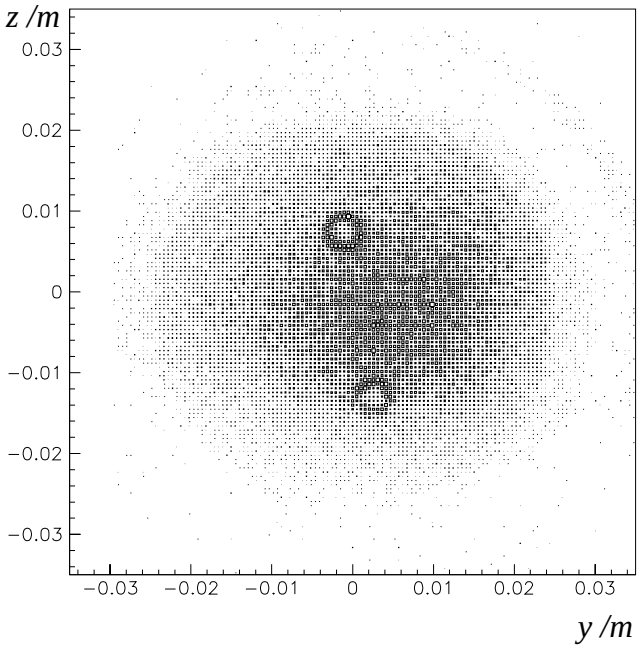

Figure 4.3: Typical vertex distribution transverse to the beam direction. The two small circles reflect the cross section of one NMR coil used in 1993.

SNOMUX: data reduction

Depending on the trigger type, the reconstruction efficiency of this stage was about 60 %. The overall reconstruction efficiency, including the previous stage (PHOENIX), was about 40 %.

The accurate track information is now available. In SNOMUX, the calorimeter data are associated to tracks, so that the remaining particles of the event are, to some extent, identified as hadrons or electrons. There is also some additional elementary event selection, like requiring that a straight extrapolation of the beam track fully passes through both the upstream and downstream target cells, in order to ensure that the same flux is seen by both target cells.

In this final stage of the production, only the minimum amount of information needed for the physics analysis is written in a highly condensed form on the so-called micro DST's (micro Data Summary tapes). Here, for instance, the raw data record is not available anymore.

Through the MICRO package, each micro DST gives access, for each event, to

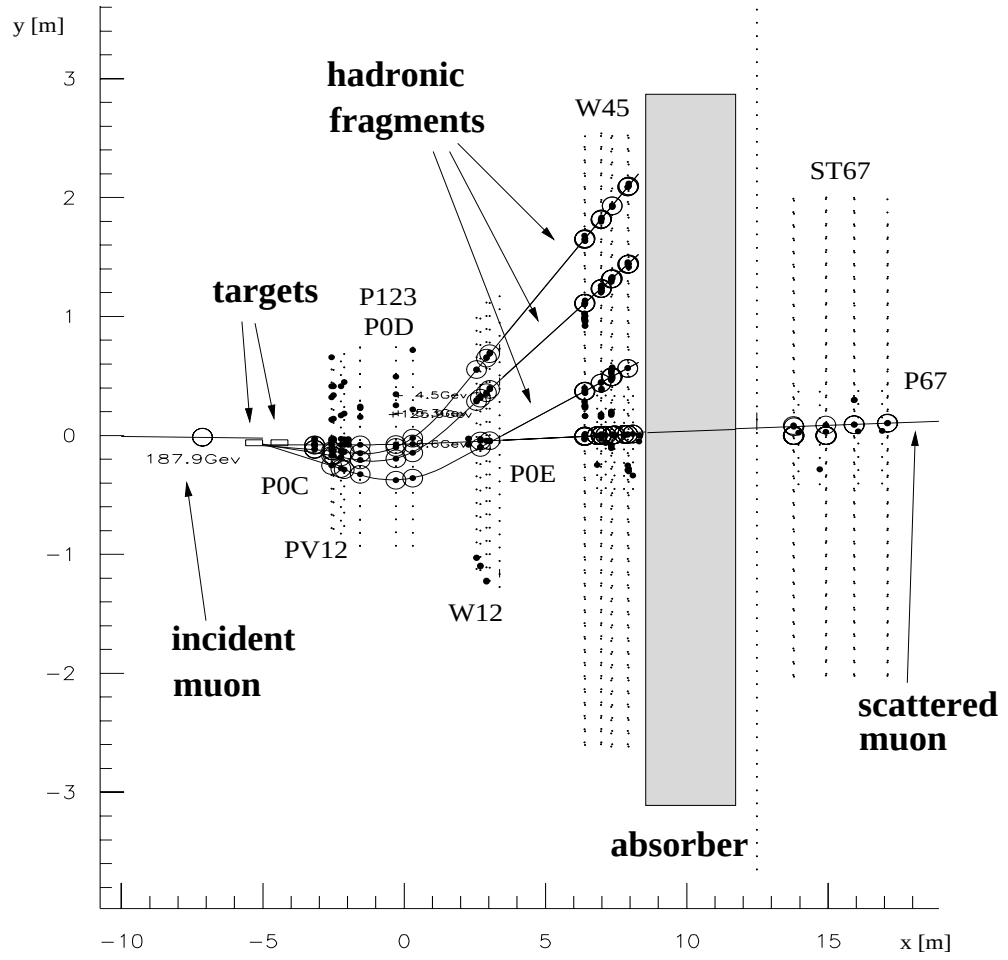

Figure 4.4: An example of a fully reconstructed event: the absorber stops the hadrons allowing the identification and the measurement of the scattered muon.

the physics variables describing the event kinematics, the track information, the vertex position together with the associated errors and some quality estimators of the event reconstruction. This information is needed in order to accomplish the various SMC analyses.

4.2 Alignment and Calibration of the Detectors

The position of each chamber has to be known as accurately as possible in order to correct the space and time information of the raw data events before the *production* can start. This is realized

- first by the surveyors, who determine optically the positions of each detector along the beam axis as well as the transverse y and z coordinates with an accuracy of about 1 mm;

- second, in the offline mode, the y and z positions are getting more accurate.

All chambers are aligned with respect to each other, in an iterative method based on tracks finding in a detector or in a set of detectors (tracking station). For this purpose special calibration and alignment data were taken in dedicated runs with lower beam intensity using the alignment triggers (Chapter 3), and with the FSM magnet switched off in order to have straight tracks. Using the initial positions of the chambers from the optical survey, straight tracks are reconstructed. The alignment and calibration procedure is described in detail in [98]. Most of the alignment work is done with PHOENIX.

After each iteration, the residual distribution, i.e. the difference between the position of the hit wire and the reconstructed track, which is determined plane by plane, is usually fitted with a gaussian. The planes are shifted (software) in y or z-position until the distributions are centered around zero. Due to the finite resolution of the detectors and to the multiple scattering, even for a perfectly aligned system, the residuals will not be zero. Typical distributions of residuals for some drift chambers are shown in Figure 4.5. The widths of the distributions of the residuals reflect the chambers resolutions. The procedure is repeated as long as further improvements are possible, but usually only two or three iterations are needed.

At the end of this procedure, the chambers are aligned in y and z with a precision of few 100 μm. Calibration and alignment runs are taken at least once for each data taking period (typically of one week). Each time a chamber has been moved because of an intervention on the chamber, a chamber replacement or a change in the electronics, the alignment procedure is repeated.

All the relevant geometry information of each detector plane (position of the first wire, pitch between wires, number of wires in the plane, etc.) is written to the so-called alignment files. For each period of data taking, a separate alignment file is created. The alignment files are then used as an input to the event data reconstruction.

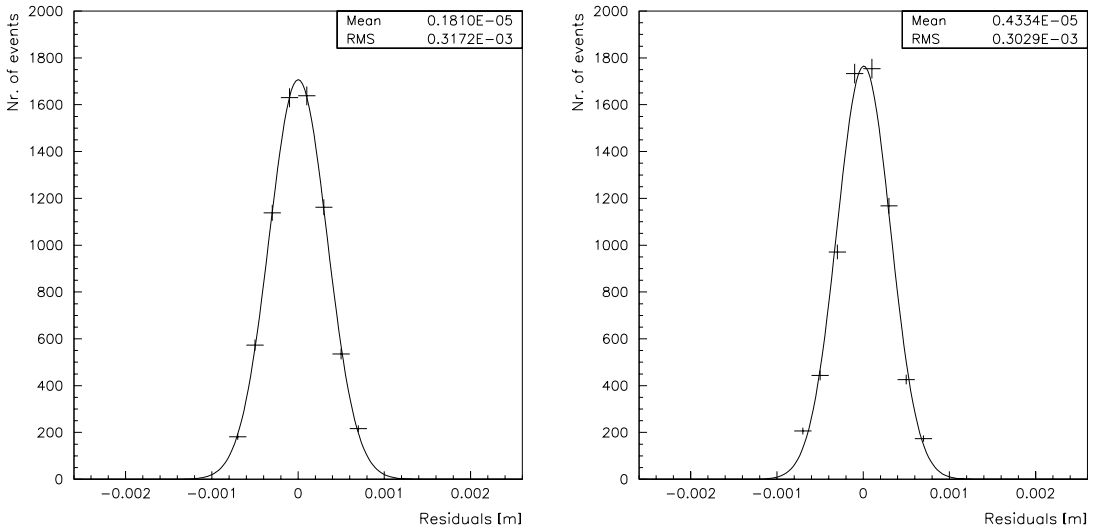

Figure 4.5: Example of a distribution of residuals for the planes T2 and Z4 of the drift chambers W12 and W45, respectively, during the data period P2A96.

4.2.1 The Detector Efficiencies

In order to estimate the acceptance stability of the spectrometer and to simulate accurately the behavior of the apparatus, a detailed study of the detectors efficiencies is needed.

For each detector plane, the efficiency ε_{plane} measures the probability that the chamber will register a hit when traversed by a charged particle, and is defined as the ratio of the number of tracks which register a hit to the total number of tracks traversing the sensitive zone of the detector:

$$\varepsilon_{plane} = \frac{N_{Hits}}{N_{Hits} + N_{NoHits}} \quad . \tag{4.2}$$

Before using a track in the efficiency calculation, it is verified that the track can be reconstructed without that particular plane, i.e. that the minimum plane requirement for the track reconstruction is met without taking into account the plane under investigation. Clearly, a track which satisfies exactly the minimum plane requirement cannot be used for this purpose. In this way it is possible to avoid a bias arising from the particular plane for which the efficiency is calculated.

The efficiency introduced in Equation 4.2 is an average over the full active area and over a certain period of time; that is why **dead regions** and **dead**

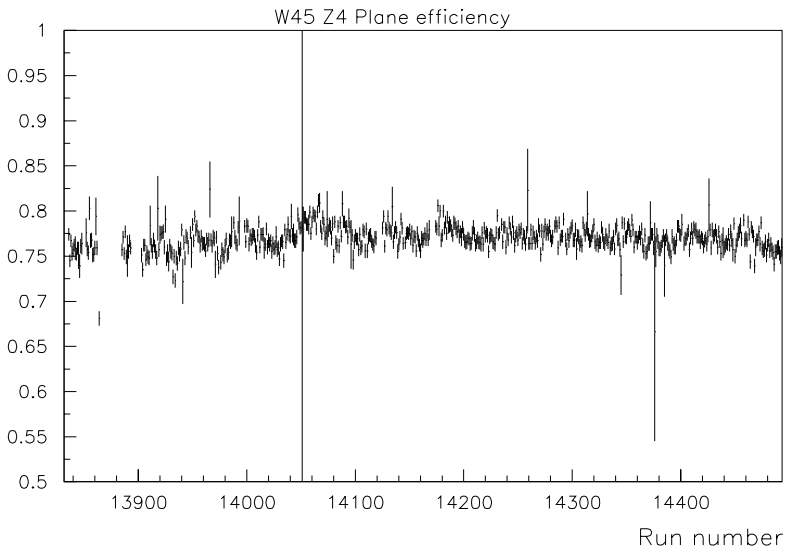

Figure 4.6: Example of plane efficiency: run by run efficiency ε for the plane Z4 of W45 during the data period P2A95.

wires have to be determined and excluded from the efficiency calculations. The central region of the large proportional and drift chambers has been made inactive (dead) in order to stand the high flux rates. This central region is covered by the P45, the P67 and the small P0 chambers, which were designed to stand the higher flux. These inactive regions are created by introducing plastic support wires (supporting the anode wires) glued perpendicularly to the signal wires.

In Figure 4.6 the efficiencies are plotted as a function of the run number (**global plane efficiencies**) for the plane Z4 of W45. The global plane efficiencies are studied in order to identify, for each plane, the time intervals of stable plane efficiencies; a gas mixture or voltage modification or aging can indeed affect the chamber efficiencies. For each plane, the average efficiencies for the single sense wires, (**wire efficiencies**), shown in Figure 4.7 (left), help in finding the dead wires: for an entire period, signals belonging to a dead wire are excluded from further efficiencies studies.

In addition to the global efficiencies, for each interval of stable plane efficiency, the efficiencies are also studied as a function of the distance from the center of the chamber, the so-called **radial efficiencies**, shown in Figure 4.7 (right).

Different "smooth" functions [99] are fitted to these radial efficiency distribu-

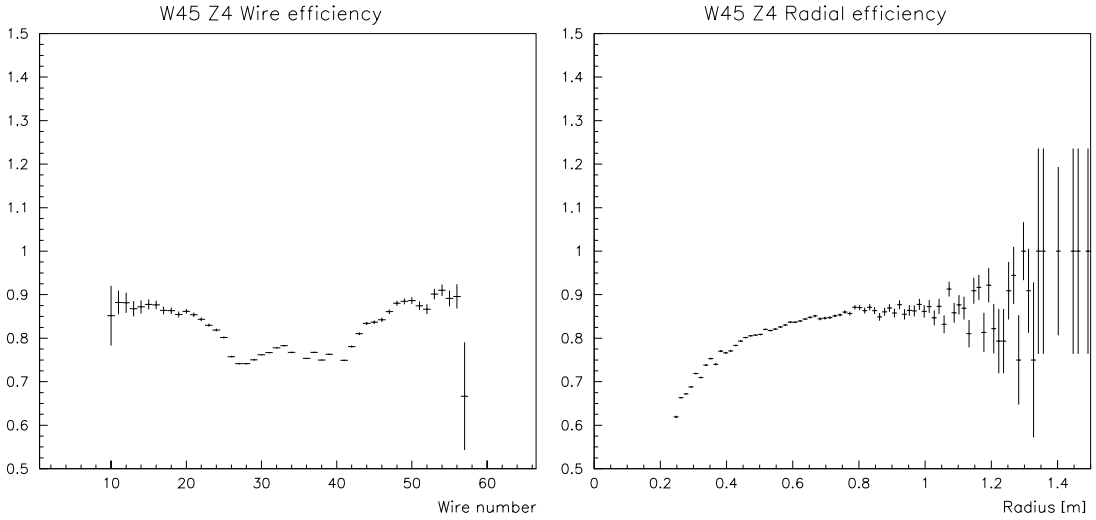

Figure 4.7: The efficiency ε for the plane Z4 of W45 (during the data period P2A95) as a function of the wire number (left) and of the distance from the plane center (right).

tions. In this way a time and position dependent parametrization of the efficiencies is obtained. A detailed description of the procedure is given in [100, 101]. To describe the efficiencies with such universal functions, the elements must behave similarly (i.e. not huge variations) following a smooth trend. Bad elements, dead wires, etc. are excluded from the fitting procedure.

For many trackers the efficiency can be parametrized using a one dimensional function. For example, the radial efficiency of the P0 chambers can be described with functions like

$$\varepsilon(R) = a_1 - a_2 \exp(-R/a_3) \; , \tag{4.3}$$

where R is the distance from the beam axis (center of the chamber) and the a_i are fit constants. For the drift chambers (W12, W45), the efficiency also depends on the position in the drift cell, in particular an efficiency drop around the sense and potential wires is observed. To take this effect into account, the structure of the drift cell is folded with the radial efficiency and the parametrization takes the form

$$\varepsilon(R,d) = 1 - (1 - \varepsilon(R))(1 - \varepsilon(d))/a_0 \tag{4.4}$$

$$\varepsilon(d) = a_1 - a_2 d - a_3 \exp(-d/a_4) - a_5 \exp(-d/a_6) \; . \tag{4.5}$$

Here, $\varepsilon(d)$ gives the efficiency in the drift cell as a function of the distance d from the sense wire.

For each data taking period, **efficiency files** containing the relevant information (dead regions and wires, plane efficiencies, fitted function parameters of the radial dependent efficiencies) are created. The efficiencies are also needed for the calculation of possible false asymmetries (section 5.1.3) arising from changes in the chamber efficiencies. Thanks to a redundancy in the chamber planes, a high level of stability could be achieved, so that the false asymmetries are small.

The Hadron Efficiencies

In general the hit profiles for the hadrons in the chambers, in particular downstream of the magnet, are different from the scattered muons ones, because of wider scattering angles, different momenta and charges. Therefore a difference in the efficiencies might show up.

The efficiencies for the hadron tracks were required in order to compute the false asymmetries for the semi-inclusive analyses and for the hadron method analysis (section 5.3.1). It had to be checked that the hadron efficiencies were close enough to the muon ones, so that the muon efficiencies could be used in these analyses.

The efficiencies were computed for five sets of tracks: muons, "all hadrons" (H2 calorimeter information not used to remove the electrons), "selected hadrons" (electrons rejected by the H2 calorimeter), positive, and negative hadrons separately.

First the average efficiency for a period was studied. For most of the chambers the plots of the efficiency versus the wire number and versus the radius have the same shape for the different sets of events. However the efficiencies for the "selected hadrons", as well as those for the "all hadrons", are lower than for the muon ones by typically 2% and 4% respectively (Figure 4.8).

This might be due to the fact that the road widths used in the track reconstruction are tuned only for muons; while hadrons require larger road widths and a few percents of them can be systematically lost. Another difference is that hadrons appear up to larger angles than muons (Figure 4.9), so that the radial efficiency is required in regions where no muon efficiency is available. Also in these

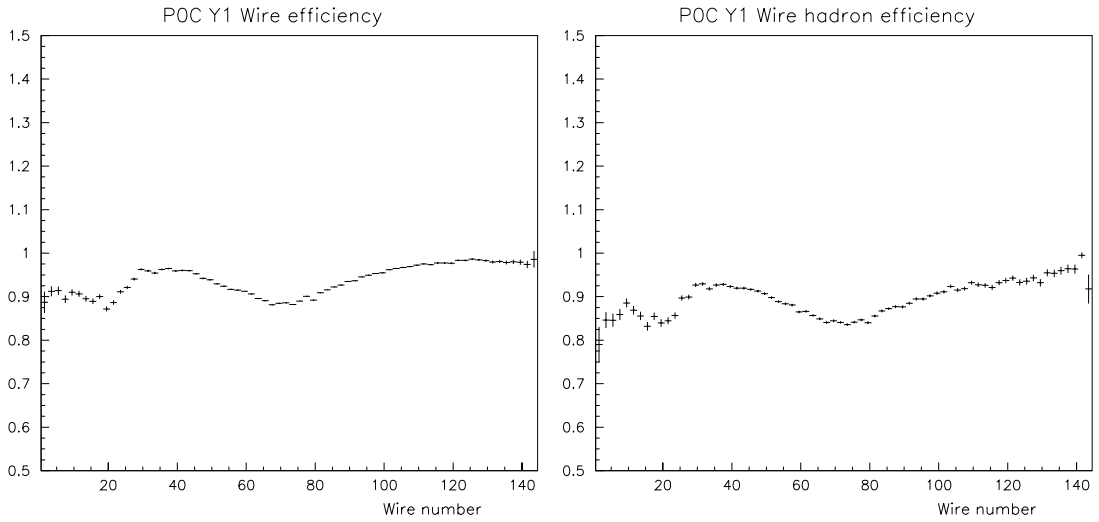

Figure 4.8: The efficiency ε for the plane Y1 of P0C (period P1A96) as a function of the wire number for the scattered muons (left) and for the hadrons (right).

regions there were no muons to tune the road widths which can then be quite bad: this can explain why the hadron radial efficiency is sometimes dropping in the outer region where the fluxes are low (Figure 4.10).

Comparison of Muon and Hadron Efficiencies

The study of the hadron efficiencies showed that they are as stable as the muon ones. The ratio of the muon to the hadron efficiencies as a function of the run number was fitted with a line. The slopes of the muon to the "selected hadrons" efficiencies ratios, as shown in Figure 4.11, are compatible with zero, i.e. there is no time dependence. The conclusion is that the hadron efficiencies are close to the muon ones.

The false asymmetries were computed using the muon efficiencies and then using the hadron efficiencies. The results showed no difference in terms of false asymmetries and therefore the muon efficiencies could be used instead of the hadron ones.

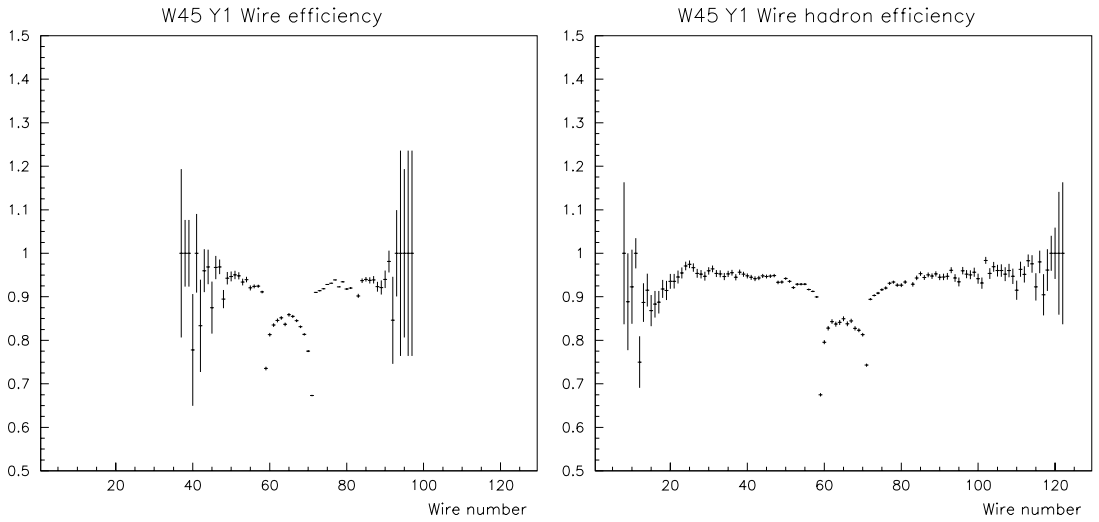

Figure 4.9: The efficiency ε for the plane Y1 of W45 (period P2B96) as a function of the wire number for the scattered muons (left) and for the hadrons (right). In the muon case (left) the efficiency is not calculated in the outer region of the plane because there are no muons in this region.

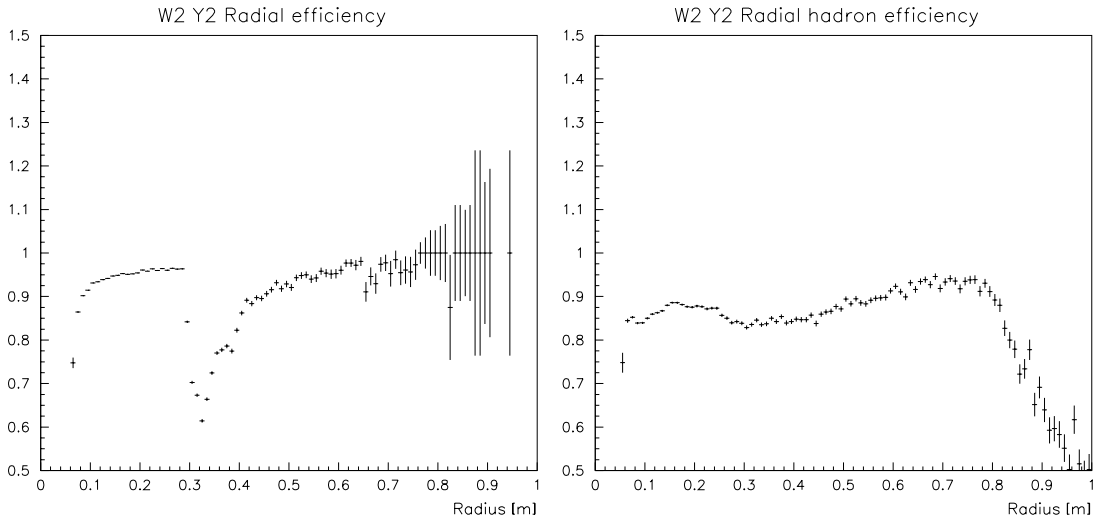

Figure 4.10: The efficiency ε for the plane Y2 of W2 (period P2B96) as a function of the distance from the center of the plane for the scattered muons (left) and for the hadrons (right).

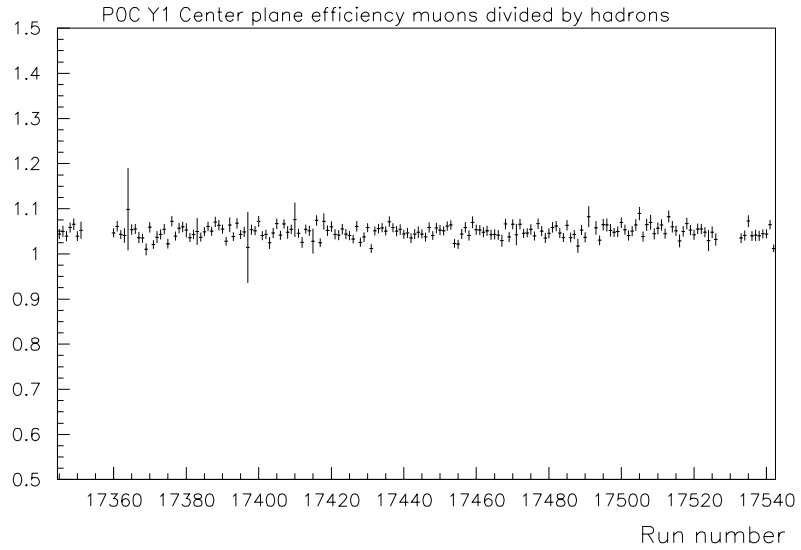

Figure 4.11: Ratio of the muon to the *selected hadrons* efficiencies for the central part of the plane Y1 of P0C (period P1A96) as a function of the run number.

4.2.2 Re-production of the 1993 data

A series of improvements in the data analysis chain lead in 1997 to the reprocessing of the 1993 data:

- the magnet chamber P1B installed between 1992 and 1993 was not yet included in the software for the original production;
- with the current software it was possible to handle in a better way the T2 and T14 overlapping triggers as well as the hadron information of T14;
- T14 reconstruction efficiency could be improved.

At the production level, a gain of about 10% in the number of reconstructed events was achieved mainly at low x_{Bj} and low Q^2. Due to the additional magnet chamber, the tracking inside the magnet was more stable and less runs needed to be removed from the analysis. The reproduced efficiencies were consistent with the original ones.

Chapter 5

Inclusive Spin Results

The extraction of the inclusive one-photon exchange spin asymmetries for the proton, A_1^p, and the deuteron, A_1^d, from the counting rates in the two oppositely polarized twin target cells will be discussed in this chapter. The spin dependent structure functions for the proton, g_1^p, and the deuteron, g_1^d, will be determined from these asymmetries. Finally, the evaluation of the relevant sum rules will be presented and a comparison to the theoretical predicitons will be drawn.

5.1 Asymmetry Extraction

The lepton-nucleon cross section spin asymmetry for a longitudinally polarized beam and target (see Equation 1.25 and the following discussion)

$$A_{\parallel} = \frac{\Delta\sigma_{\parallel}}{\overline{\sigma}} = \frac{\sigma^{\overrightarrow{\Leftarrow}} - \sigma^{\overrightarrow{\Rightarrow}}}{\sigma^{\overrightarrow{\Leftarrow}} + \sigma^{\overrightarrow{\Rightarrow}}} \tag{5.1}$$

is determined from the counting rates in the two target cells.

The total number of DIS events N coming from one target cell, which contains polarized and unpolarized nucleons, is given by:

$$N = a\Phi\left(n\overline{\sigma} - nP_b P_t \Delta\sigma_{\parallel} + \Sigma_A(n_A\sigma_A)\right) \tag{5.2}$$

where

- a is the acceptance (efficiency) of the detection system

- Φ is the incoming muon beam flux crossing both target cells,
- n is the number of polarizable nucleons per unit area,
- $\overline{\sigma} = \frac{1}{2}\left(\sigma^{\overrightarrow{\Leftarrow}} + \sigma^{\overrightarrow{\Rightarrow}}\right)$ is the spin summed lepton-nucleon cross section,
- $\Delta\sigma_{\parallel} = \frac{1}{2}\left(\sigma^{\overrightarrow{\Leftarrow}} - \sigma^{\overrightarrow{\Rightarrow}}\right)$ is the corresponding spin difference cross section,
- P_b is the beam polarization,
- P_t is the absolute value of the target polarization,
- n_A and σ_A are the numbers and cross sections, respectively, of other unpolarizable nuclei in the target.

The event yield N can be rewritten in terms of the spin asymmetry $A_{\parallel}$ as

$$N = a\Phi n\overline{\sigma}(1 - fP_bP_tA_{\parallel})\,, \tag{5.3}$$

where the dilution factor f measures the ratio of polarizable nucleons to the total number of nucleons in the target material:

$$f = \frac{n_{p,d}\sigma_{p,d}}{n_{p,d}\sigma_{p,d} + \sum_A (n_A\sigma_A)}\ . \tag{5.4}$$

In section 5.3 f will be redefined in order to also include the so-called *radiative corrections*.

By using two oppositely polarized target cells and reversing their spin orientations, four different event yields can be construced: for the upstream (u) and downstream (d) target halves, before (no $\prime$) and after ($\prime$) a polarization reversal:

$$\begin{aligned} N_u &= a_u\Phi n_u\overline{\sigma}(1 + fP_bP_{t,u}A_{\parallel}) \\ N_d &= a_d\Phi n_d\overline{\sigma}(1 - fP_bP_{t,d}A_{\parallel}) \\ N'_u &= a'_u\Phi' n_u\overline{\sigma}(1 - fP_bP'_{t,u}A_{\parallel}) \\ N'_d &= a'_d\Phi' n_d\overline{\sigma}(1 + fP_bP'_{t,d}A_{\parallel})\,. \end{aligned} \tag{5.5}$$

The direction of the muon beam polarization was opposite to its motion (μ^+ beam) and did not change (section 3.1), whereas the polarization direction of the twin target cells was reversed about every 5 hours (section 3.2.5). The relative

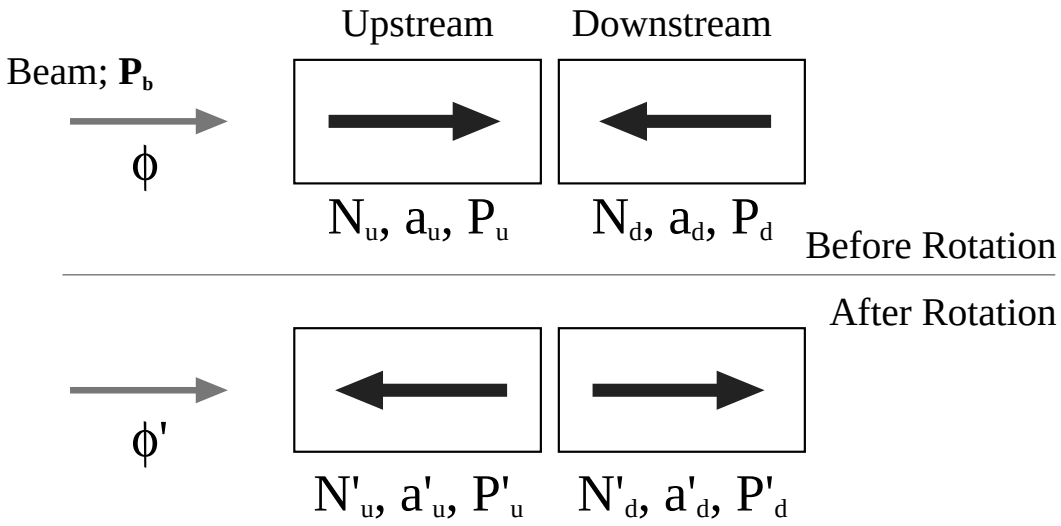

Figure 5.1: Target and beam spin configurations before and after the rotation of the target magnetic field.

spin orientations for the beam and target polarizations, before and after the rotation of the target magnetic field, are shown in Figure 5.1.

The asymmetry in the counting rates, also known as *raw* asymmetry, is extracted from the event yields given in Equation 5.5, before the target polarization reversal:

$$A_{raw} = \frac{N_u - N_d}{N_u + N_d} = \frac{a_u n_u - a_d n_d - f P_b (a_u n_u P_{t,u} - a_d n_d P_{t,d}) A_{\parallel}}{a_u n_u + a_d n_d - f P_b (a_u n_u P_{t,u} + a_d n_d P_{t,d}) A_{\parallel}} \ , \tag{5.6}$$

and after the polarization reversal:

$$A'_{raw} = -\frac{N'_u - N'_d}{N'_u + N'_d} = -\frac{a'_u n_u - a'_d n_d - f P_b (a'_u n_u P'_{t,u} - a'_d n_d P'_{t,d}) A_{\parallel}}{a'_u n_u + a'_d n_d - f P_b (a'_u n_u P'_{t,u} + a'_d n_d P'_{t,d}) A_{\parallel}} \ . \tag{5.7}$$

The last term in the denominators is of the order 10^{-3} and is in general much smaller than the first terms, thus it can be neglected.

With the introduction of the ratios of the spectrometer acceptance for the upstream and downstream target cells multiplied by the number of nucleons in each cell, also referred as *acceptance ratios*,

$$r = \frac{a_u n_u}{a_d n_d} \quad \text{and} \quad r' = \frac{a'_u n_u}{a'_d n_d} \tag{5.8}$$

Equations 5.6 and 5.7 can be rewritten as

$$A_{raw} = \frac{r-1}{r+1} - f P_b \frac{r P_{t,u} + P_{t,d}}{r+1} A_{\parallel} \ , \tag{5.9}$$

and

$$A'_{raw} = -\frac{r'-1}{r'+1} + fP_b\frac{r'P'_{t,u} + P'_{t,d}}{r'+1}A_{\parallel} \ . \tag{5.10}$$

These expressions can be further simplified by introducing a mean target polarization $\langle P_t \rangle$. This makes sense, because the target polarization was uniform throughout the target volume and it was constant for at least one run. $\langle P_t \rangle$ is obtained by weighing the target polarization with the number of events coming from each target cell, and by taking the average of this quantity before and after a field reversal:

$$\langle P_t \rangle = \frac{1}{2}\left[\frac{|P_{t,u}|N_u + |P_{t,d}|N_d}{N_u + N_d} + \frac{|P'_{t,u}|N'_u + |P'_{t,d}|N'_d}{N'_u + N'_d}\right] \ . \tag{5.11}$$

The *raw* asymmetries A_{raw} and A'_{raw}, obtained before and after the polarization reversal, respectively, are then averaged:

$$\frac{1}{2}\left(A_{raw} + A'_{raw}\right) = -fP_b\langle P_t \rangle A_{\parallel} + \frac{1}{2}\left(\frac{r-1}{r+1} - \frac{r'-1}{r'+1}\right) \ . \tag{5.12}$$

It follows that the extraction of the spin asymmetries does not require the knowledge of the unpolarized cross sections (they are however implicitly contained in the dilution factor f, see Equation 5.4), the beam flux, the number of nucleons in the target, the apparatus acceptance and the *acceptance ratio* r, assuming that $r = r'$. The cancellation of these quantities in the asymmetry calculation substantially reduces the systematic error.

The lepton-nucleon cross section asymmetry, $A_{\parallel}$, is then given by:

$$A_{\parallel} = \frac{-1}{fP_b\langle P_t \rangle}\frac{1}{2}\left(A_{raw} + A'_{raw}\right) - A_{\parallel}^{false} \ , \tag{5.13}$$

where

$$A_{\parallel}^{false} = \frac{-1}{fP_b\langle P_t \rangle}\frac{1}{2}\left(\frac{r-1}{r+1} - \frac{r'-1}{r'+1}\right) \tag{5.14}$$

is the so-called *false* asymmetry, which may arise from the time variation of the acceptance ratio r and which has to be carefully looked at. In this way, the *false* asymmetry, caused by the acceptance difference between the upstream and downstream target halves ($r \neq r'$), is also reduced.

By neglecting the $A_{\parallel}^{false}$ term as well as A_2, A_1 can finally be obtained in terms of the measured event yields:

$$A_1 \simeq \frac{1}{D}A_{\parallel} = \frac{-1}{fDP_b\langle P_t \rangle}\frac{1}{2}\left[\frac{N_u - N_d}{N_u + N_d} - \frac{N'_u - N'_d}{N'_u + N'_d}\right] \ . \tag{5.15}$$

The factor $\frac{1}{2}$ recalls that the asymmetries, obtained before and after the reversal of the target magnetic field, are averaged.

5.1.1 fDP_b Method

The dilution factor f, the depolarization factor D and the beam polarization P_b depend on the event kinematics and on the beam energy. They vary from event to event. In order to take these variations into account, each event is weighed with its corresponding fDP_b factor, which is calculated on the basis of the event kinematics. This weighing procedure is known as the fDP_b *method*, and Equation 5.15 can be rewritten as:

$$A_1 = \frac{-1}{\langle P_t \rangle} \frac{1}{2} \left[\frac{\sum_u (fDP_b)_u - \sum_d (fDP_b)_d}{\sum_u (fDP_b)_u + \sum_d (fDP_b)_d} - \frac{\sum_u (fDP_b)'_u - \sum_d (fDP_b)'_d}{\sum_u (fDP_b)'_u + \sum_d (fDP_b)'_d} \right] \quad (5.16)$$

and by introducing the weight $w = fDP_b$, it becomes:

$$A_1 = \frac{-1}{\langle P_t \rangle} \frac{1}{2} \left[\frac{\sum_u w_u - \sum_d w_d}{\sum_u w_u + \sum_d w_d} - \frac{\sum_u w'_u - \sum_d w'_d}{\sum_u w'_u + \sum_d w'_d} \right] . \quad (5.17)$$

The sums run over all the events for each target cell, before and after the field reversal.

The statistical error on A_1 extracted from Equation 5.17 is given by:

$$\sigma_{fDP_b} = \frac{1}{\langle P_t \rangle} \frac{1}{2} \sqrt{\frac{1}{\sum_u w_u^2 + \sum_d w_d^2} + \frac{1}{\sum_u w_u'^2 + \sum_d w_d'^2}} \quad (5.18)$$

The fDP_b weight can be considered as the *analyzing power* of that event. This makes sense, because an event with a high value for the fDP_b product contributes more to the asymmetry than an event with a low value of the fDP_b product. For this reason the fDP_b weights are used also in the calculation of the average values of the kinematical variables, such as x, Q^2, and W. For instance, the average value of x is calculated as

$$\langle x \rangle = \frac{\sum_1^N x(fDP_b)^2}{\sum_1^N (fDP_b)^2} = \frac{\sum_1^N xw^2}{\sum_1^N w^2} , \quad (5.19)$$

where the sum runs over the number of events in a given kinematical bin.

Also the false asymmetry can be rewritten as:

$$A_1^{false} = \frac{-1}{\langle P_t \rangle_{N_u, N_d}} \frac{1}{2} \left(\left\langle \frac{1}{fDP_b} \right\rangle_{N_u, N_d} \frac{r-1}{r+1} - \left\langle \frac{1}{fDP_b} \right\rangle_{N'_u, N'_d} \frac{r'-1}{r'+1} \right) . \quad (5.20)$$

5.1.2 Data Grouping

The data obtained with opposite field orientations of the target magnet have to be combined, i.e. spin sorted, for the calculation of A_1. This procedure is known as *data grouping*.

The *data grouping* consists in identifying the time periods of stable spectrometer acceptances in order to prevent the onset of the *false* asymmetries. For this reason, unreliable data, bad runs, etc., had to be identified and removed from the analysis.

This was a very time consuming procedure. It consisted of looking at the histograms of various detectors efficiencies and rates, and also of tracking the hardware failures, which were detected, repaired and documented in the logbook. Some checks were also performed on the behaviour of the average values of the kinematical variables x, Q^2, and ν as a function of the run number. Runs with big deviations, for these variables, from the mean values (jumps) were disregarded in the further analysis. Also the target polarization was not allowed to vary by more than 6 % per run with respect to its mean value.

All that is achieved through the construction of the so-called *configuration files*, which are created for each SPS data taking period separately. Each run in this file is specified by an orientation number (even or odd number), which also reflects the orientation of the target magnetic field.

During the data taking a detector element could have a shift in efficiency or rate. Even if small shifts do not necessarily have an effect on the event reconstruction efficiency, the *configuration* file also took these effects into account and was created in a way that prevented from combining data before and after an observed change in the efficiency or rate. This was done by introducing the so-called *hard cuts*; their final effect in the *configuration* file was to attribute a different orientation number to the run following that particular change. A *hard cut* was also introduced in order to forbid the combination of data before and after a data taking interruption of more than several hours.

As illustrated in Figure 5.2, there are many ways to combine the data:

- the **full** configurations:
  all the *good* runs of one target polarization orientation (let's call them $\oplus$)

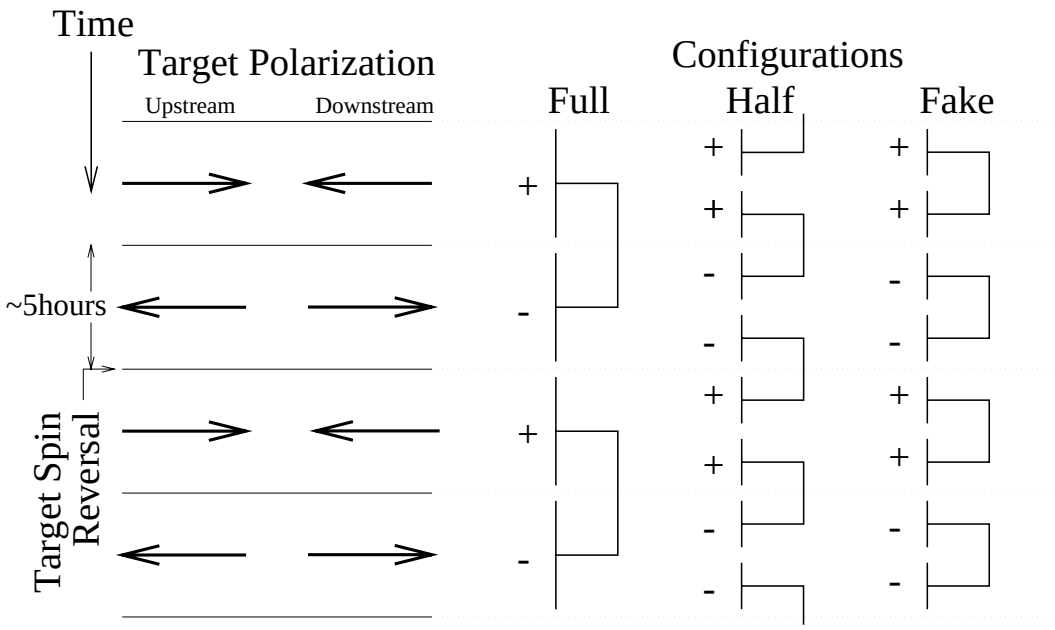

Figure 5.2: The different ways of grouping the data from consecutive magnetic field orientations of the target solenoid.

are combined with all the good runs of the next opposite target polarization orientation (let's call them $\ominus$), i.e. **consecutive pairs of $\oplus$ and $\ominus$ orientations are combined**, creating a so-called configuration pair.

- the **sum** configurations:
  all the $\oplus$ orientations are combined with all the $\ominus$ orientations between two *hard cuts*. This configuration can include several field rotations.

- the **persum** configurations:
  all the $\oplus$ orientations are combined with all the $\ominus$ orientations within one data taking period.

- the **half** configurations:
  the first half of the data of a full configuration (for instance $\oplus$) is combined with the last half of the previous full configuration ($\ominus$). This serves as a check on gradual changes in the spectrometer acceptance. For instance, one can imagine that a detector has a gradual decline in its efficiency over a long period of time. In the case of full orientations, the $\oplus$ orientations

will always be combined with the slightly less efficient $\ominus$ orientations, so that the efficiency problem will not be observed. However, for the half configurations, the order of combination with respect to the gradual fall in efficiency is opposite, so that the decline of the efficiency will be noticed. The advantage in using the half configurations is that small acceptance variations are cancelled, while big efficiency drops are notified.

- the **fake** configurations:
  They are made by shifting a half configuration by one, so that the data with the same spin orientations are combined amongst themselves ($\oplus$ with $\oplus$, $\ominus$ with $\ominus$). The asymmetry obtained from fake configurations should be zero, because, by construction, there is no physical asymmetry. A non zero value for this asymmetry would indicate an instrumental asymmetry. The fake configurations were used to monitor the stability of the data.

As a systematic check, the SMC inclusive A_1 asymmetries have been extracted with the full and with the half configurations: in both cases the results were extremely close. This showed that nothing unusual was going on with the data grouping. For the final analysis of A_1 the full configuration files were actually used.

5.1.3 Estimation of False Asymmetries

Although the magnetic field orientation of the target solenoid was often reversed, the acceptance ratios r and r' (Equation 5.8) might have changed with time. This change might have led to the appearance of a *false* asymmetry (Equation 5.14). If $r = r'$, $A^{false} = 0$, i.e. there is no *false* asymmetry.

Since the runs, which showed a large acceptance change, were removed from the analysis, the main source of the variations of the acceptance ratio r is due to slow changes in the chamber efficiencies. The chambers efficiencies can, for instance, slowly decrease because of aging, or fluctuate because of temperature and pressure variations in the experimental hall, typically from day to night. An uniform drop in the efficiency, however, does not necessarily lead to a *false* asymmetry, since only a change in the acceptance ratio r and not in the acceptance itself generates a *false* asymmetry.

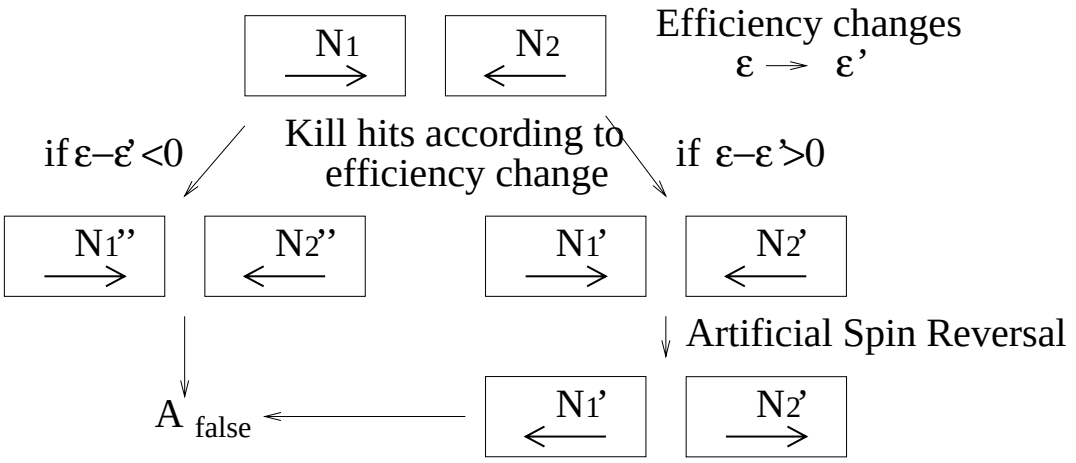

Figure 5.3: Diagram of the false asymmetry determination. $\epsilon - \epsilon'$ is the change of the efficiency with time.

The false asymmetry is estimated from the same data set used for the asymmetry calulation. The procedure is schematized in Figure 5.3 and described below. Rather than correcting the data for the *false* asymmetry, the contribution of the *false* asymmetry, based on this study, is included in the systematic error.

First, one set of data with one target spin orientation (N_u, N_d) is duplicated as (N'_u, N'_d) and (N''_u, N''_d), still with the same spin orientation. In order to simulate the efficiency changes between the two identical data sets, (N'_u, N'_d) and (N''_u, N''_d), some events were randomly removed from one set or the other, on the basis of the previously determined detector efficiencies. For each event, the efficiency ϵ of each tracker plane was compared to an evenly distributed random number z between 0 and 1. If $\epsilon < z$, the hit in that plane was dropped from the reconstructed muon track

- from the event in the data set (N'_u, N'_d), if $(\epsilon - \epsilon') > 0$,
- from the event in the data set (N''_u, N''_d), if $(\epsilon - \epsilon') < 0$,

where $(\epsilon - \epsilon')$ represents the change of the efficiency with time. The event with the rejected hits had to fulfill the reconstruction requirements (see section 4.1), otherwise it was rejected from the data set (N'_u, N'_d) or (N''_u, N''_d). In order to mimic as closely as possible the real efficiency fluctuations of the spectrometer,

the efficiencies were evaluated for each detector plane (section 4.2.1) run by run and recorded in the so-called efficiency files.

Next, the target polarization of the data set (N'_u, N'_d) was artificially reversed. At this stage, the data sets (N''_u, N''_d) and (N'_u, N'_d) formed a configuration ($\oplus$, *fake* $\ominus$) with different spin orientations and different acceptances, and A_1^{false} could finally be evaluated by using Equation 5.14. In the case no events would have been dropped at all, the data set (N''_u, N''_d), would be identical to the data set (N'_u, N'_d), thus the false asymmetry would be zero.

For example, the false asymmetry of the reprocessed 1993 data sample was found to be consistent with zero for all x bins within an error of 0.005, and the largest value found for A_1^{false} was 0.003, which is much smaller than the statistical error. Similar results for A_1^{false} were found for all data samples.

5.1.4 Polarized Background Correction

The measured asymmetries also include a contribution from the polarized background in the target material, where unwanted nuclei can become polarized as well: nitrogen nuclei in the case of the ammonia target and protons in the case of the deuterated butanol target, in addition to the various materials present in this target cell. In order to extract A_1, this contribution had to be estimated and subtracted from the asymmetry. The uncertainty of this correction was included in the systematic error.

The Polarized Proton Background

In addition to the polarized protons **in the (d-)butanol**, there are some other polarizable nuclei as background in the target:

- 1.1% of carbon in nature is the isotope ^{13}C which contains a polarizable neutron; according to the EST theory (section 3.2.2), the ^{13}C polarization is about 1/3 of the proton polarization. The estimated ^{13}C contribution to the asymmetry is at most 0.1 %,
- the liquid ^{3}He is not affected by the DNP (section 3.2.2) but is polarized up to 0.5% due to brute force. The ^{3}He contribution is about 0.1 %,

- there are some other polarizable nuclei in the target material as a dope to create free radicals. Their concentration was very low and their effect is negligeable,

- **the only significant correction is the hydrogen in the deuterated butanol target** because only (99.4 ± 0.3) % [102] of the hydrogen atoms could be replaced with deuteron ones in the butanol molecule. The remaining protons also become polarized during the polarization process. After including the scattering from the polarized protons, Equation 5.3 becomes:

$$N \propto \left[1 - P_t^d P_b f D \left(A_1^d + \frac{P_t^p}{P_t^d}\frac{\sigma_p}{\sigma_d}\frac{n_p}{n_d}A_1^p\right)\right] , \tag{5.21}$$

where P_t^p and P_t^d are the proton and deuteron polarizations, respectively. From the EST theory, $P_t^p = 2 \times P_t^d$, and a relative error of 20 % was assigned to it. $\frac{n_p}{n_d} = 0.006 \pm 0.003$ is obtained from the deuterization of the material. A correction for this effect, which varies between 0.5% and 2%, reaching at most 5% in a bin, was applied to the A_1^d data.

The Nitrogen Correction

Since ^{14}N has spin 1, it also becomes polarized during the DNP (section 3.2.2). The contribution to the asymmetry $A_\parallel$, however, is expected to be small.

By considering scattering from polarized ^{14}N's, the number of events N generated in a target cell, as well as the measured asymmetry $A_\parallel$ become

$$N = \Phi a \Big[n_p\sigma_p(1 - P_b P_p A_p) + n_N\sigma_N(1 - P_b P_N A_N) + \Sigma_A n_A \sigma_A\Big] , \tag{5.22}$$

$$A_\parallel = \frac{\sigma^{\rightleftarrows} - \sigma^{\rightrightarrows}}{\sigma^{\rightleftarrows} + \sigma^{\rightrightarrows}} = f P_b P_p \left(A_p + \frac{n_N P_N}{n_p P_p}\frac{\sigma_N A_N}{\sigma_p}\right) , \tag{5.23}$$

where the notation of Equation 5.3 is used and A_p and A_N are the scattering asymmetries from protons and nitrogen, respectively.

In the nuclear shell model, ^{14}N can be treated as a ^{12}C core with spin 0 and an extra *free* proton and neutron in a $^1P_{\frac{1}{2}}$ state. The probability to find the proton and neutron with their spins anti-parallel to the spin of the ^{14}N nucleus is twice as likely as to find them with their spins parralel to it, and

$$\sigma_N A_N = -\frac{1}{3}(\sigma_p A_p + \sigma_n A_n) \simeq -\frac{2}{3}\sigma_d A_d \tag{5.24}$$

where A_N, A_n and A_d are the scattering asymmetries from ^{14}N, neutrons and deuterons, respectively, and σ_N, σ_n and σ_d the corresponding cross sections.

From more sophisticated analyses of the nitrogen nucleus, which include higher orbital (excited) states and higher order corrections to the nuclear shell model, an error estimate of ± 0.16 is determined for the $-\frac{2}{3}$ factor on the right hand side of Equation 5.24. This error covers the spread of values obtained from various calculations.

The correction to the asymmetry δA_1^p is equal to the negative of the second term in parenthesis of Equation 5.23 :

$$\delta A_1^p = -\frac{n_N P_N}{n_p P_p} \frac{\sigma_N A_N}{\sigma_p} \,. \tag{5.25}$$

By using the average values $P_N = (13.5 \pm 1.1)$ % and $P_p = (89.5 \pm 2.5)$ %, and $\frac{n_N}{n_p} = \frac{1}{3}$ for NH_3 and Equation 5.24 for $\sigma_N A_N$, the following correction for the 1996 A_1^p values was obtained

$$\delta A_1^p = (0.034 \pm 0.009) \frac{A_1^d \sigma_d}{\sigma_p} \,, \tag{5.26}$$

where for A_1^d a parametrization of the measured asymmetry from SMC [30] and from E143 [106] is used, and for $\frac{\sigma_d}{\sigma_p}$ a parametrization from NMC [107] is used. The correction δA_1^p is added bin by bin to the calculated A_1^p. This correction is found to be less than 3 % of the A_1^p values for every x bin, and the error on the correction is included as a systematic error.

5.2 Selection of the Inclusive Events

The events used to extract the inclusive spin-asymmetries were selected according to the following criteria:

a) $Q^2 > 0.2$ GeV^2 for the beam energy of 190 GeV ($Q^2 > 1$ GeV^2 for the beam energy of 100 GeV, i.e. 1992 data),

b) $\vartheta > 2$ mrad [1] ($\vartheta > 13$ mrad for the beam energy of 100 GeV, i.e. 1992 data) in the case of the asymmetries extractions, allowing to know from which target half the scattered muon originated from, as the acceptance of the trigger rapidly changes for small scattering angles,

c) energy lost by the incident muon $\nu = E - E' > 15$ GeV ($\nu = E - E' > 10$ GeV for the beam energy of 100 GeV, i.e. 1992 data) in order to ensure a good kinematical resolution for the scattered muon,

d) ratio of the energy transfer ν to the incident muon energy E, $y < \mathbf{0.9}$, since the uncertainty on the contribution of radiative events increases at large y,

e) scattered muon momentum $E' > 19$ GeV ($E' > 15$ GeV for the beam energy of 100 GeV) to ensure that the muons from hadronic decays are not mistakenly identified as muons scattered from the target,

f) beam definition: The reconstructed incoming muon trajectory must pass through both target halves to ensure that both target halves see the same beam flux, so that this quantity can safely be canceled out when extracting the spin asymmetries.

Due to the non-applicability of QCD at too low values of Q^2, a minimum Q^2 of 1 GeV^2 has been required for the QCD analysis of the polarized structure functions (section 5.5.4), and the selections **a)** and **b)** have been replaced by

a′) $Q^2 > 1$ GeV^2,

b′) $\vartheta > 9$ mrad.

5.3 Radiative Corrections

The experimentally measured unpolarized and polarized cross sections σ^{tot} and $\Delta\sigma^{tot}$, and the corresponding spin asymmetry $A_1^{tot} = \frac{1}{D}\frac{\Delta\sigma^{tot}}{\sigma^{tot}}$ also receive con-

[1] These selections depend on the trigger type:
for T1 $Q^2 > 1.0$ GeV^2 and $\vartheta > 9$ mrad,
for T2 and T14 $Q^2 > 0.2$ GeV^2 and $\vartheta > 2$ mrad,
for T15 $Q^2 > 0.01$ GeV^2 and $\vartheta > 2$ mrad.

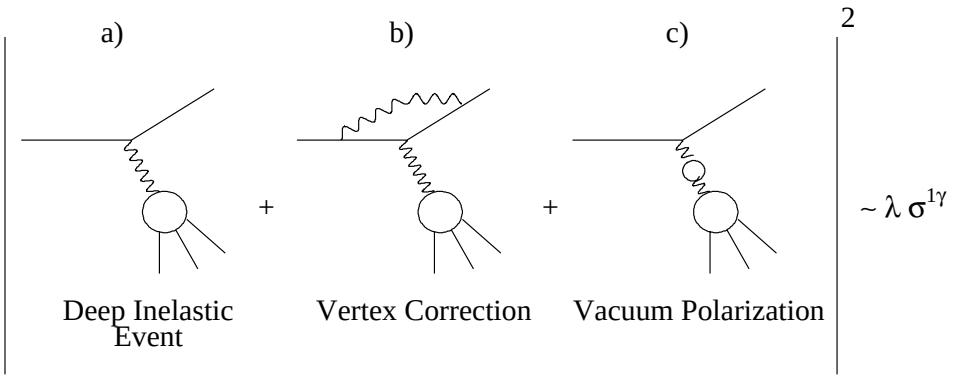

Figure 5.4: One-photon lepton-nucleon cross sections and contributions from virtual photon radiation from second order in α_{em}.

tributions from higher order electromagnetic processes. For the study of the nucleon structure and the extraction of the (polarized) structure functions, the one-photon exchange cross sections $\sigma^{1\gamma}$ and $\Delta\sigma^{1\gamma}$, also referred to as Born cross sections, and the corresponding spin asymmetry $A_1^{1\gamma} = \frac{1}{D}\frac{\Delta\sigma^{1\gamma}}{\sigma^{1\gamma}}$ are of interest [2].

In order to extract $A_1^{1\gamma}$ from A_1^{tot}, the measured spin asymmetry has to be corrected for higher order electromagnetic processes (radiative events). The second order radiative events in α_{em} are shown in Figures 5.4 and 5.5. These corrections, called the *radiative corrections*, can be calculated exactly in QED from the measured event kinematics.

The main contributions to the radiative corrections are given by:

- the vertex correction (Figure 5.4b),
- the vacuum polarization (Figure 5.4c),
- the *radiative tails* due to the emission of a real photon in the initial or in the final state that can be further separated in:
  – DIS on target nuclei $l + N \rightarrow l + \gamma + hadrons$ (Figure 5.5a), where the γ is emitted by the lepton,
  – elastic scattering on target nuclei (Figure 5.5b) and free target nucleons,
  – quasi-elastic scattering on target nuclei (Figure 5.5c).

[2] In this section the notation $A_1^{1\gamma}$ is used to distinguish the one-photon exchange asymmetry from A_1^{tot}, whereas throughout this thesis $A_1^{1\gamma}$ is indicated by A_1.

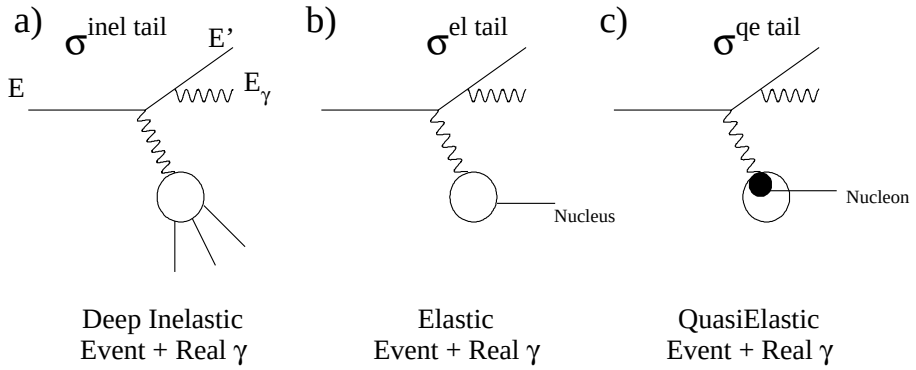

Figure 5.5: Radiative events which contribute to the total lepton-nucleon cross section. These processes are spin dependent.

The first class of radiative events (i.e. vertex corrections and vacuum polarization) are spin independent to all orders in α_{em}. The radiative tails, however, depend on the polarization. These corrections are treated differently: the first as a multiplicative correction, the second as an additive correction.

The radiative tails simulate an event with a defined x lower than the x at the vertex of the virtual photon, resulting in a migration of events to lower x bins. This can be understood by expressing x in terms of the energy loss ν and of the scattering angle ϑ of the muon:

$$x \simeq \frac{E(E-\nu)\vartheta^2}{2M\nu} \,. \tag{5.27}$$

The muon scattering angle θ changes only smoothly with the radiation of a photon, while the measured ν accounts for the exchanged virtual photon as well as for the radiated photon energy, so that the measured x is smaller than the actual DIS one.

The lepton-nucleon cross section can be decomposed as

$$\sigma^{tot} = \lambda\sigma^{1\gamma} + \sigma_{tail} = \lambda\sigma^{1\gamma} + \sigma^{inel}_{tail} + \sigma^{el}_{tail} + \sigma^{qe}_{tail} \,, \tag{5.28}$$

and, for the polarized case, as

$$\Delta\sigma^{tot} = \lambda\Delta\sigma^{1\gamma} + \Delta\sigma_{tail} = \lambda\Delta\sigma^{1\gamma} + \Delta\sigma^{inel}_{tail} + \Delta\sigma^{el}_{tail} + \Delta\sigma^{qe}_{tail} \,, \tag{5.29}$$

where σ_{tail} is the contribution to σ^{tot} from the *radiative tails* and has been decomposed according to Figure 5.5, and $\Delta\sigma_{tail}$ is the corresponding polarized quantity.

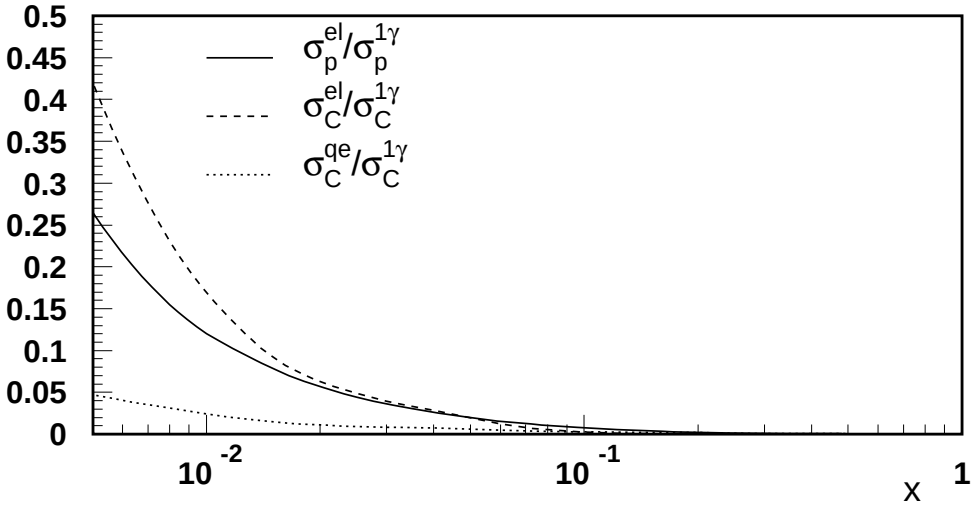

Figure 5.6: The relative contributions $\sigma_p^{el}/\sigma_p^{1\gamma}$, $\sigma_C^{el}/\sigma_C^{1\gamma}$ as well as $\sigma_C^{qe}/\sigma_C^{1\gamma}$ to the the cross section of the one-photon exchange.

λ is a polarization independent multiplicative correction and accounts for all the higher order virtual photon processes (see Figure 5.4). These processes do not change the event kinematics. λ also includes contributions from the inelastic tail events close in x, which are due to the emission of soft photons of very low energy. These events only smoothly modify the kinematics, so that the kinematical bins from DIS and from the inelastic tail are not changed. The inclusion of the soft photon radiation in the definition of λ is to some extent arbitrary and ambiguous.

In order to compute λ, the structure functions as well as the electric and magnetic form factors of the various nuclei present in the target are required. The unpolarized radiative corrections were computed with the program TERAD [103], which also includes additional corrections for the hadronic vertex. In the kinematical range of the SMC data, TERAD gives $0.98 < \lambda < 1.03$. In the SMC analysis, λ is set to unity and all the radiative corrections are included in σ_{tail} and $\Delta\sigma_{tail}$.

Figure 5.6 shows the relative contributions $\sigma_p^{el}/\sigma_p^{1\gamma}$, $\sigma_C^{el}/\sigma_C^{1\gamma}$, as well as $\sigma_C^{qe}/\sigma_C^{1\gamma}$ to the one-photon exchange cross section. The radiative corrections contribute mainly at small x. Elastic scatterings off high Z nuclei are dominant, since the cross section is proportional to Z^2.

The lepton-nucleon cross section asymmetry (neglecting A_2)

$$A_1^{tot} = \frac{1}{D} \cdot \frac{\Delta\sigma^{tot}}{\sigma^{tot}} \tag{5.30}$$

can be rewritten, with the use of Equations 5.28 and 5.29, as

$$A_1^{tot} = \frac{1}{D} \cdot \frac{\lambda\Delta\sigma^{1\gamma} + \Delta\sigma_{tail}}{\sigma^{tot}} = \frac{\lambda\sigma^{1\gamma}}{\sigma^{tot}} \left(A_1^{1\gamma} + \frac{1}{D} \frac{\Delta\sigma_{tail}}{\lambda\sigma^{1\gamma}} \right) , \tag{5.31}$$

where

$$A_1^{1\gamma} = \frac{1}{D} \cdot \frac{\Delta\sigma^{1\gamma}}{\sigma^{1\gamma}} \tag{5.32}$$

is the wanted one-photon exchange spin asymmetry. It follows that

$$A_1^{1\gamma} = \frac{\sigma^{tot}}{\lambda\sigma^{1\gamma}} \cdot A_1^{tot} - \frac{1}{D} \frac{\Delta\sigma_{tail}}{\lambda\sigma^{1\gamma}} = \rho \cdot A_1^{tot} - A_1^{RC} . \tag{5.33}$$

The multiplicative term $\rho = \frac{\sigma^{tot}}{\lambda\sigma^{1\gamma}}$ and the additive term $A_1^{RC} = \frac{1}{D} \frac{\Delta\sigma_{tail}}{\lambda\sigma^{1\gamma}}$ were calculated with the program POLRAD [104] neglecting the contribution from A_2. In order to calculate $\Delta\sigma_{tail}$ at a given x, the knowledge of A_1 at higher x's is needed. The corrections can be calculated by using the measured A_1 starting from the highest measured x bin. This is an iterative procedure repeated until convergence is reached. More accurate calculations were performed by using a parametrization of A_1 (for the proton and deuteron) based on the available world data:

$$A_1^p = x^{p_1}(1 - e^{-p_2 x}) + p_3 \tag{5.34}$$

$$A_1^d = (e^{p_1 x} - 1)(p_2^{p_3} - x^{p_3}) + p_4 \tag{5.35}$$

with the parameters listed in Table 5.1. The uncertainty on A_1^{RC} is estimated by varying the input parameters of A_1 within the experimental errors.

Since the radiative correction A_1^{RC} varies a lot within an x bin and is strongly correlated in y within the same x bin, it was calculated event by event and then averaged over a configuration pair in a similar way as done for x in Equation 5.19. This contribution is then subtracted from the asymmetry extracted from the corresponding configuration pair.

The multiplicative term ρ and the additive radiative correction A_1^{RC}, calculated for the proton and the deuteron, are shown in Figure 5.7 for the inclusive

parameter	proton	deuteron
p_1	-0.015 ± 0.08	10.608 ± 4.79
p_2	1.915 ± 0.236	0.036 ± 0.017
p_3	0.013 ± 0.12	0.146 ± 0.013
p_4		-0.0002 ± 0.013

Table 5.1: Fitted parameters used to describe A_1^p and A_1^d in Equations 5.34 and 5.35.

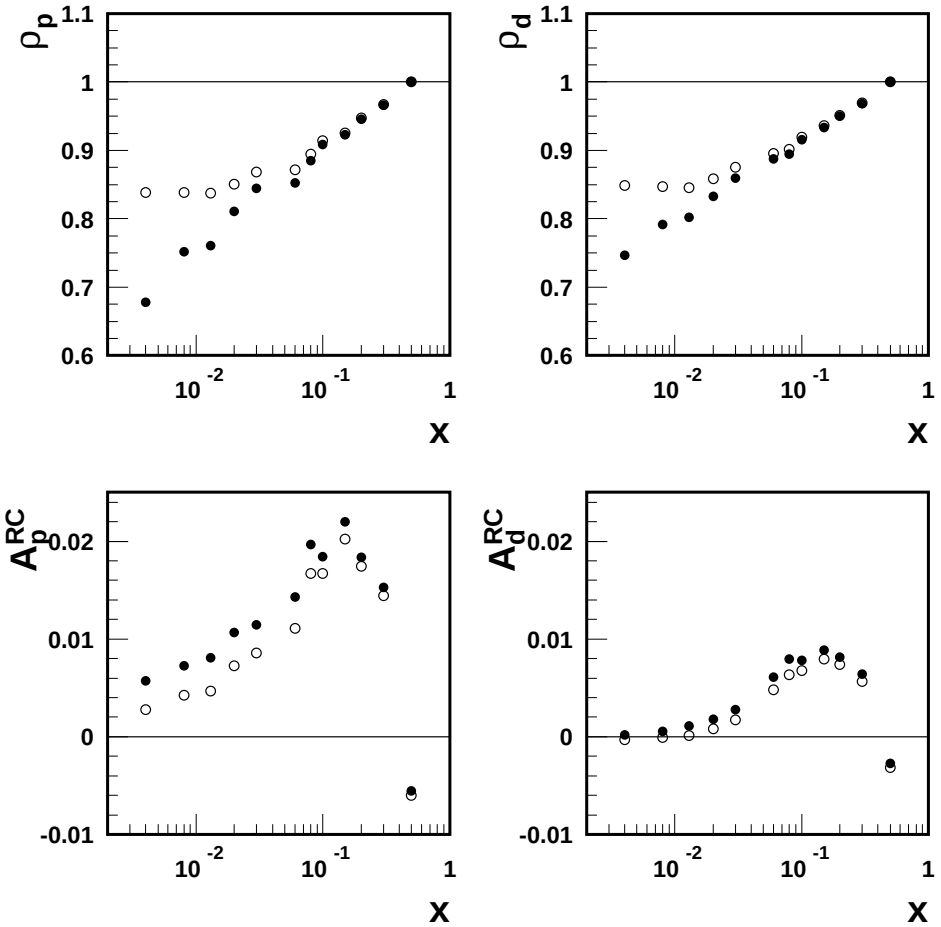

Figure 5.7: Multiplicative ($\rho_{p,d}$) and additive ($A_{p,d}^{RC}$) radiative corrections for the photon-nucleon asymmetry A_1. for the inclusive ($\bullet$) and the semi-inclusive ($\circ$) events. The corrections are calculated at the average y of each bin.

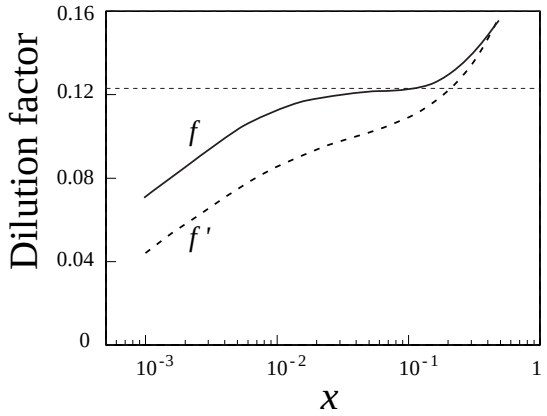

Figure 5.8: Comparison of the dilution factor f (solid line) and the effective dilution factor $f^{RC} = \rho \cdot f$ (dashed line), as a function of x, for the butanol target of 1993.

and for the corresponding semi-inclusive events. Elastic and quasi-elastic processes do not contribute to the radiative tails for the semi-inclusive events and therefore the radiative corrections are smaller. The maximal values found for A_1^{RC} are 0.02 for the proton and 0.01 for the deuteron; they are small compared to the statistical errors of the asymmetries. However, ρ strongly varies with x, and the difference between A_1^{tot} and $A_1^{1\gamma}$ at low x reaches 30%.

Scattering from non polarizable material in the target, as well as scattering from polarized nucleons via a non deep inelastic process dilute the spin asymmetries. From this point of view, the multiplicative term $\rho = \frac{\sigma^{tot}}{\lambda\sigma^{1\gamma}}$ can be viewed as an additional dilution factor. It has been included in the definition of an *effective* dilution factor (Equation 5.4):

$$f^{RC} = \rho \cdot f = \left(\frac{\sigma_{p,d}^{1\gamma}}{\sigma_{p,d}^{tot}}\right) \cdot \left(\frac{n_{p,d}\sigma_{p,d}^{tot}}{\Sigma_A n_A \sigma_A^{tot}}\right) . \tag{5.36}$$

Figure 5.8 shows the dilution factor f and the effective dilution factor f^{RC} as a function of x. The unceratinty Δf^{RC} on the effective dilution factor f^{RC} represents one of the major contributions to the systematic error on A_1, which, initially, has been forgotten in the SMC analysis.

The radiative events degrade the statistical accuracy of the measurement as

$$\delta A_1^{1\gamma} \propto \frac{1}{f^{RC}} \cdot \frac{1}{\sqrt{N}} . \tag{5.37}$$

Using the weight

$$w = f^{RC} D P_b \tag{5.38}$$

in Equation 5.17 for the extraction of the spin asymmetry instead of the weight $w = f D P_b$ one obtains directly $A_1^{tot}\rho$ and thus $A_1^{1\gamma}$ after the subtraction of A_1^{RC}.

5.3.1 Hadron Method

Since in a DIS process the struck quark and the nucleon remnant fragment into several hadrons, the contributions of the radiative tails to the total cross sections can be reduced by requiring at least one relatively fast hadron in the final state, in addition to the scattered muon [3]. The nucleus hit in an elastic scattering process or the nucleon expelled from the nucleus in a quasi-elastic process are too slow to escape from the target and therefore are not detected in the SMC spectrometer.

The presence of these hadrons (one or more) guarantees that the observed event is due to a DIS process and not to a radiative process with a DIS-like Q^2. In this case the radiative corrections are significantly smaller, particularily at low x. This determines the basis and usefulness of the hadron method.

These hadron-tagged events thus do not include any contribution from $\sigma_{tail}^{el} + \sigma_{tail}^{qe}$. Hence, the total cross section for the hadron-tagged events reduces to (compare with Equation 5.28):

$$\sigma_{tot}^{hadron-tagged} = \lambda\sigma_{1\gamma} + \sigma_{tail}^{inel} \,. \tag{5.39}$$

Moreover, in the presence of a hadron with $z = E_{had}/\nu$, the maximum energy of a radiated (real) photon E_γ^{max} is reduced to $E_\gamma^{max} = (E - E') \cdot (1 - z)$, and the contribution of σ_{tail}^{inel} to σ^{tot} decreases as well.

In the calculation of the *effective* dilution factor f^{RC} (Equation 5.36) for the hadron-tagged events, the reduction of the contribution of σ_{tail} to σ^{tot} must be taken into account. It results in an increase of f^{RC}, in particular at low x. This effect is illustrated in Figure 5.9 for the ammonia target.

[3] Since only charged particle tracks can be reconstructed in the SMC spectrometer, neutral hadrons can be indirectly observed via their charged decay products.

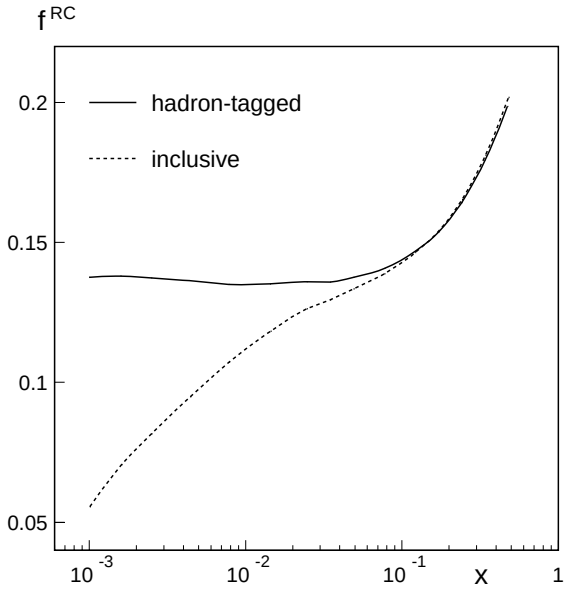

Figure 5.9: Comparison of the dilution factor f^{RC}, as a function of x, for the hadron-tagged events and for the inclusive events from the ammonia target.

The additional hadron requirement results in a loss of the number N of events. This loss of events, however, is more than compensated for by the reduction of the statistical error on the asymmetry $A_1^{1\gamma}$ due to the dilution factor (Equation 5.37). The net result of this hadron method is that the statistical error on $A_1^{1\gamma}$ at low x is smaller than for the inclusive case. This is illustrated in Figure 5.10, where the ratio of the statistical errors for $A_1^{1\gamma}$ from hadron-tagged events and from inclusive events is plotted as a function of x, for the proton and the deuteron targets.

The use of the hadron-tagged events in the asymmetry calculation $A_1^{1\gamma}$ might introduce a bias on $A_1^{1\gamma}$. Possible side effects have been carefully looked for and been checked with Monte Carlo simulations, using the program POLDIS [108], to make sure that no biases were introduced in the asymmetries obtained with the hadron-tagged events (hadron method), compared to the standard inclusive method.

In addition to the kinematical cuts similar to these for the inclusive events, the hadron tagged events also have to satisfy the following requirements:

i) either one or more hadron tracks points to the muon interaction vertex,

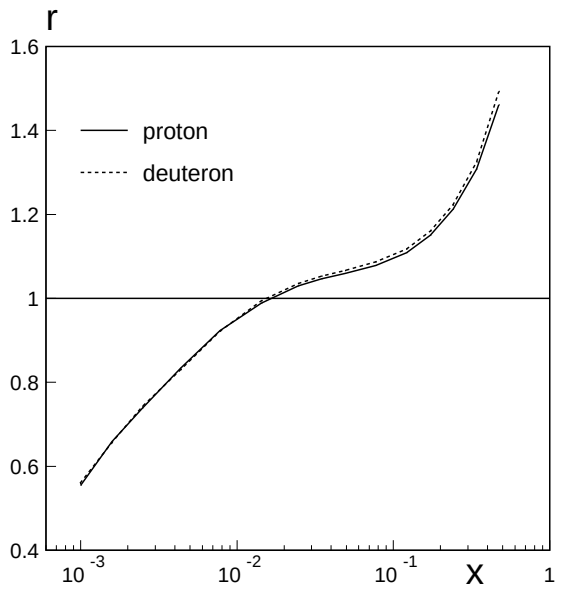

Figure 5.10: The ratio r of statistical errors for $A_1^{1\gamma}$ from hadron-tagged events and from inclusive events as a function of x, for the proton and the deuteron targets.

ii) or a pair of oppositely charged hadron tracks originates from a secondary vertex (V^0).

Moreover, the electrons due to radiative γ conversion have to be rejected, while the ones coming from γ's from π^0 decays can be kept. This is realised by rejecting events for which:

a) $emagf = E_{em}/E_{tot} > 0.8$, where $emagf$ is the ratio of the energy deposited in the electromagnetic part to the total deposited energy in the SMC H2 calorimeter (section 3.3.4),

b) $y > 0.6$,

c) $\alpha < 4\ mrad$, where α is the angle between the reconstructed electron track and the direction of the (real or virtual) γ reconstructed from the muon kinematics.

The cuts a) to c) are also applied to tracks that could not be identified by the calorimeter due to the limited acceptance close to the muon beam or due to multiple tracks pointing to the same module.

5.4 A_1 Results

The one-photon exchange spin asymmetries A_1 obtained by SMC are shown in Figure 5.11 as a function of x for the proton (1993 and 1996 data combined) and the deuteron (1992, 1994 and 1995 data combined) [4]. The results obtained with the inclusive method (section 5.2) and the hadron method (section 5.3.1) event selections are displayed. As can be noticed, the differences between the two event selections are small except for the two lowest x bins of the proton data.

As discussed in section 5.3.1 and illustrated in Figure 5.10, the hadron method gives results with smaller statistical errors at low x, while for the inclusive one the results are more precise at high x. The optimal set of the SMC A_1 results is obtained by using for $x < 0.02$ the results obtained with the hadron method and for $x > 0.02$ the results obtained with the inclusive method.

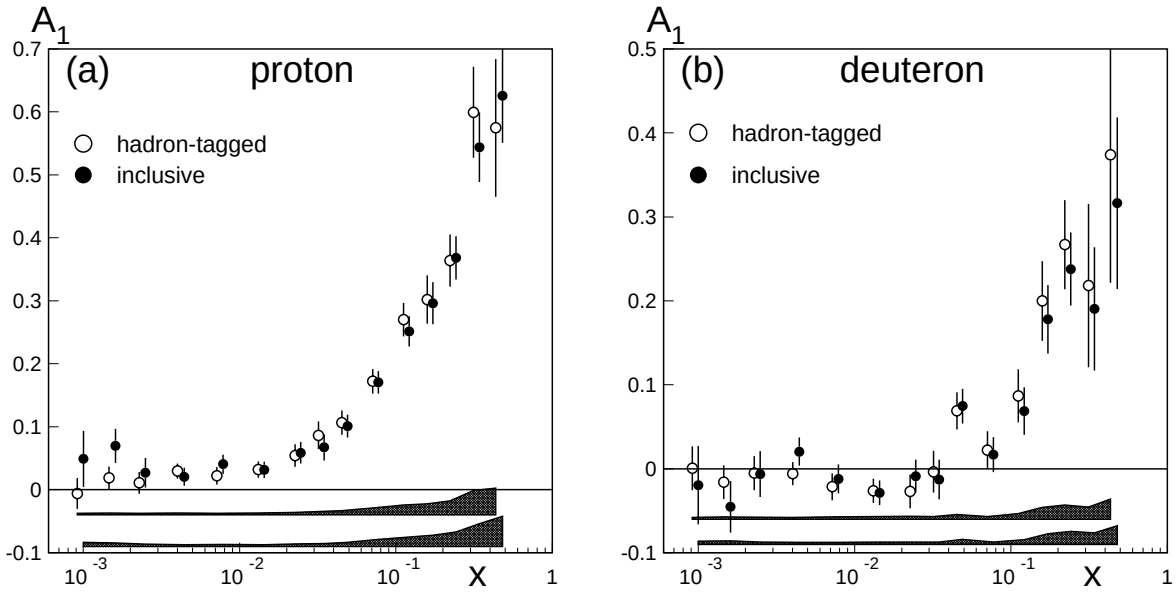

Figure 5.11: A_1 values for the inclusive and the hadron-tagged event selections. The upper shaded bands indicate the systematic uncertainty of A_1 for the hadron-tagged selection, while the lower shaded bands indicate the systematic uncertainty of A_1 for the inclusive selection.

[4] The dates refer to the year when the data were taken.

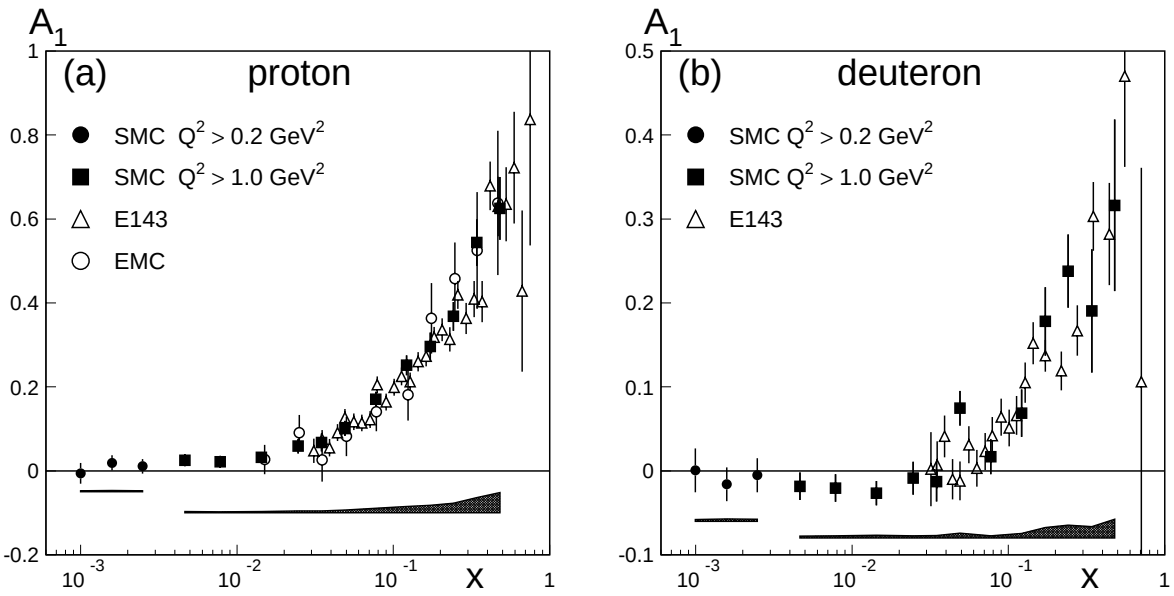

Figure 5.12: The optimal set of SMC results for A_1 together with the results from EMC [7] and E143 [106]. Statistical errors are shown as error bars, while the shaded bands below the data points indicate the systematic uncertainty for the SMC measurements.

The final A_1 values (optimal set) from SMC [105] are displayed in Figure 5.12 and detailed in Tables 5.2 and 5.3 in bins of x. The various contributions to the systematic errors are discussed in section 5.4.2 and detailed in [105]; their quadratic sum is shown as a band in the A_1 plots (Figures 5.11 and 5.12).

x Range	$\langle x \rangle$	$\langle Q^2 \rangle$ (GeV^2)	A_1^{p}
0.0008–0.0012	0.001	0.3	$-0.004 \pm 0.025 \pm 0.002$
0.0012–0.002	0.002	0.5	$0.021 \pm 0.018 \pm 0.003$
0.002–0.003	0.002	0.7	$0.014 \pm 0.017 \pm 0.003$
0.003–0.006	0.005	1.3	$0.029 \pm 0.014 \pm 0.003$
0.006–0.010	0.008	2.1	$0.026 \pm 0.014 \pm 0.003$
0.010–0.020	0.014	3.6	$0.036 \pm 0.013 \pm 0.003$
0.020–0.030	0.025	5.7	$0.059 \pm 0.017 \pm 0.004$
0.030–0.040	0.035	7.8	$0.068 \pm 0.021 \pm 0.004$
0.040–0.060	0.049	10.4	$0.101 \pm 0.018 \pm 0.006$
0.060–0.100	0.077	14.9	$0.170 \pm 0.018 \pm 0.011$
0.100–0.150	0.122	21.3	$0.252 \pm 0.024 \pm 0.015$
0.150–0.200	0.173	27.8	$0.296 \pm 0.033 \pm 0.018$
0.200–0.300	0.242	35.6	$0.368 \pm 0.034 \pm 0.023$
0.300–0.400	0.342	45.9	$0.544 \pm 0.055 \pm 0.036$
0.400–0.700	0.480	58.0	$0.625 \pm 0.075 \pm 0.048$

Table 5.2: Optimal set of asymmetries for the proton, $A_1^{\mathrm{p}}(x)$, from the SMC data. The first error is statistical and the second is systematic. The first three bins have $Q^2 > 0.2$ GeV^2, while the remaining ones have $Q^2 > 1$ GeV^2.

x Range	$\langle x \rangle$	$\langle Q^2 \rangle$ (GeV^2)	$A_1^{\rm d}$
0.0008 – 0.0012	0.001	0.3	$0.001 \pm 0.026 \pm 0.002$
0.0012 – 0.002	0.002	0.5	$-0.016 \pm 0.020 \pm 0.003$
0.002 – 0.003	0.002	0.7	$-0.005 \pm 0.020 \pm 0.002$
0.003 – 0.006	0.005	1.3	$-0.018 \pm 0.016 \pm 0.002$
0.006 – 0.010	0.008	2.1	$-0.020 \pm 0.016 \pm 0.003$
0.010 –0.020	0.014	3.5	$-0.027 \pm 0.015 \pm 0.003$
0.020 – 0.030	0.025	5.5	$-0.009 \pm 0.020 \pm 0.003$
0.030 – 0.040	0.035	7.5	$-0.013 \pm 0.024 \pm 0.003$
0.040 – 0.060	0.049	10.0	$0.075 \pm 0.021 \pm 0.006$
0.060 – 0.100	0.077	14.4	$0.017 \pm 0.021 \pm 0.003$
0.100 – 0.150	0.121	20.6	$0.069 \pm 0.028 \pm 0.006$
0.150 – 0.200	0.172	26.8	$0.178 \pm 0.041 \pm 0.013$
0.200 – 0.300	0.241	34.3	$0.238 \pm 0.044 \pm 0.015$
0.300 – 0.400	0.342	43.9	$0.190 \pm 0.073 \pm 0.014$
0.400–0.700	0.479	54.8	$0.316 \pm 0.102 \pm 0.022$

Table 5.3: Optimal set of asymmetries for the deuteron, $A_1^{\rm d}(x)$, from SMC data, otherwise same explanations as for Table 5.2.

5.4.1 The Q^2 dependence of A_1

The SMC combined proton and deuteron asymmetries are presented in Tables 5.4 and Tables 5.5, respectively, and are also displayed in Figure 5.13 and Figure 5.14 as a function of Q^2 for several x bins. For comparison, the EMC [7] and E143 [106] results are also shown in the same figures. The error bars display the statistical uncertainties only. The SLAC E143 data complement the low Q^2 region of the asymmetries at high x, which was not covered by SMC. The EMC data at high Q^2 show consistency with the SMC data. At high x the asymmetries span a wider Q^2 range, than at lower x.

From perturbative QCD a different behavior in Q^2 is expected for the structure functions F_1 and g_1, which would imply that $A_1 \simeq g_1/F_1$ should be also Q^2-dependent. This dependence follows from the DGLAP evolution equations [35]. The Q^2 dependence was studied in SMC with a QCD analysis (section 1.7) performed at Next-to-Leading Order (NLO) of the asymmetries. The QCD fits are shown as solid lines in Figures 5.13 and 5.14; they follow the data well. The dashed lines represent, instead, the mean values of A_1, i.e a fit to the asymmetries with no Q^2-dependence; they also follow the data well.

Within the precision of the data, the Q^2-dependence of A_1^p and A_1^d is not visible, even at low x where the Q^2-dependence should be more apparent due to a higher gluon density compared to the high x region. In other words, these asymmetries are compatible with the hypothesis of no Q^2-dependence.

$\langle x \rangle$	$\langle Q^2 \rangle$ (GeV^2)	$A_1^{\rm p}$	$\langle x \rangle$	$\langle Q^2 \rangle$ (GeV^2)	$A_1^{\rm p}$
0.0009	0.25	-0.023 ± 0.037	0.0342	5.80	0.130 ± 0.048
0.0010	0.30	-0.023 ± 0.043	0.0344	7.77	0.034 ± 0.033
0.0011	0.34	0.062 ± 0.051	0.0359	10.14	0.094 ± 0.039
0.0014	0.38	0.056 ± 0.028	0.0472	4.29	0.076 ± 0.101
0.0016	0.46	0.051 ± 0.033	0.0474	5.85	0.083 ± 0.064
0.0018	0.55	-0.057 ± 0.034	0.0479	7.83	0.103 ± 0.038
0.0022	0.59	0.006 ± 0.029	0.0485	10.95	0.091 ± 0.027
0.0025	0.70	0.032 ± 0.030	0.0527	14.72	0.123 ± 0.040
0.0028	0.82	0.002 ± 0.031	0.0737	5.47	0.168 ± 0.094
0.0035	0.89	0.055 ± 0.023	0.0744	7.88	0.138 ± 0.056
0.0042	1.14	0.003 ± 0.019	0.0750	11.08	0.181 ± 0.036
0.0050	1.44	0.059 ± 0.024	0.0762	16.30	0.170 ± 0.028
0.0056	1.71	0.025 ± 0.038	0.0856	23.10	0.172 ± 0.043
0.0069	1.44	-0.047 ± 0.040	0.1189	7.40	0.335 ± 0.098
0.0071	1.76	-0.007 ± 0.029	0.1196	11.14	0.309 ± 0.065
0.0075	2.04	0.073 ± 0.027	0.1200	16.48	0.225 ± 0.045
0.0083	2.34	0.060 ± 0.032	0.1205	24.82	0.239 ± 0.041
0.0090	2.64	0.069 ± 0.041	0.1293	34.31	0.254 ± 0.057
0.0095	2.94	-0.098 ± 0.059	0.1711	10.18	0.179 ± 0.096
0.0114	1.75	-0.021 ± 0.109	0.1715	16.51	0.253 ± 0.076
0.0119	2.07	0.032 ± 0.070	0.1717	24.89	0.194 ± 0.065
0.0123	2.36	0.003 ± 0.052	0.1718	34.94	0.427 ± 0.069
0.0125	2.66	0.034 ± 0.043	0.1770	45.47	0.371 ± 0.077
0.0126	2.96	0.015 ± 0.037	0.2368	10.53	0.317 ± 0.125
0.0131	3.30	0.009 ± 0.030	0.2392	21.49	0.288 ± 0.059
0.0145	3.74	0.046 ± 0.030	0.2398	34.94	0.391 ± 0.080
0.0163	4.43	0.084 ± 0.027	0.2462	52.75	0.438 ± 0.054
0.0183	5.44	0.022 ± 0.043	0.3388	15.25	0.413 ± 0.150
0.0231	2.78	0.132 ± 0.104	0.3404	25.00	0.491 ± 0.142
0.0236	3.31	0.227 ± 0.099	0.3407	34.97	0.691 ± 0.145
0.0235	3.77	-0.008 ± 0.072	0.3436	61.83	0.553 ± 0.074
0.0237	4.54	0.093 ± 0.039	0.4688	21.85	0.845 ± 0.170
0.0241	5.75	0.058 ± 0.028	0.4751	34.98	0.366 ± 0.218
0.0263	7.41	0.028 ± 0.032	0.4843	72.10	0.614 ± 0.090
0.0339	4.23	0.032 ± 0.068			

Table 5.4: Optimal set of asymmetries $A_1^{\rm p}(x, Q^2)$ from SMC data. The errors are statistical only.

$\langle x \rangle$	$\langle Q^2 \rangle$ (GeV^2)	$A_1^{\rm d}$	$\langle x \rangle$	$\langle Q^2 \rangle$ (GeV^2)	$A_1^{\rm d}$
0.0009	0.25	-0.067 ± 0.040	0.0342	3.57	-0.042 ± 0.108
0.0010	0.30	0.052 ± 0.046	0.0342	4.54	-0.129 ± 0.089
0.0011	0.34	0.046 ± 0.052	0.0342	5.80	-0.036 ± 0.056
0.0014	0.38	-0.028 ± 0.032	0.0344	7.78	0.033 ± 0.038
0.0016	0.46	-0.069 ± 0.037	0.0359	10.13	-0.023 ± 0.045
0.0018	0.55	0.052 ± 0.037	0.0476	2.63	0.257 ± 0.187
0.0022	0.59	0.076 ± 0.035	0.0476	3.59	0.322 ± 0.140
0.0025	0.70	-0.043 ± 0.035	0.0479	4.52	0.034 ± 0.108
0.0027	0.82	-0.049 ± 0.035	0.0477	5.83	0.047 ± 0.069
0.0038	0.65	0.020 ± 0.073	0.0480	7.82	0.101 ± 0.044
0.0035	0.90	0.034 ± 0.029	0.0484	10.95	0.093 ± 0.032
0.0042	1.14	-0.015 ± 0.023	0.0527	14.72	-0.006 ± 0.047
0.0050	1.44	-0.024 ± 0.028	0.0744	3.95	-0.019 ± 0.120
0.0056	1.71	-0.025 ± 0.045	0.0743	5.82	0.034 ± 0.108
0.0074	1.09	-0.074 ± 0.066	0.0746	7.85	0.026 ± 0.062
0.0071	1.47	0.026 ± 0.052	0.0753	11.05	0.090 ± 0.041
0.0071	1.77	-0.043 ± 0.034	0.0760	16.30	-0.025 ± 0.033
0.0075	2.04	-0.053 ± 0.031	0.0855	23.07	-0.004 ± 0.051
0.0083	2.34	0.035 ± 0.037	0.1187	5.00	-0.062 ± 0.162
0.0090	2.64	-0.005 ± 0.047	0.1194	10.23	0.056 ± 0.063
0.0095	2.94	-0.010 ± 0.069	0.1201	16.43	0.069 ± 0.054
0.0128	1.59	-0.018 ± 0.064	0.1203	24.82	0.076 ± 0.050
0.0131	2.06	0.016 ± 0.074	0.1289	34.25	0.093 ± 0.069
0.0128	2.36	-0.019 ± 0.061	0.1709	9.72	0.231 ± 0.106
0.0125	2.66	-0.024 ± 0.050	0.1714	16.47	0.062 ± 0.091
0.0125	2.96	-0.033 ± 0.043	0.1716	24.84	0.249 ± 0.081
0.0130	3.30	-0.082 ± 0.035	0.1739	39.62	0.171 ± 0.065
0.0144	3.74	-0.008 ± 0.035	0.2368	10.06	0.264 ± 0.140
0.0163	4.44	-0.003 ± 0.031	0.2386	16.52	0.205 ± 0.111
0.0184	5.44	-0.023 ± 0.050	0.2393	24.86	0.093 ± 0.096
0.0237	2.13	-0.067 ± 0.110	0.2391	34.93	0.265 ± 0.105
0.0239	2.82	0.071 ± 0.091	0.2454	52.73	0.294 ± 0.072
0.0242	3.30	-0.063 ± 0.102	0.3388	14.77	0.194 ± 0.178
0.0239	3.76	-0.004 ± 0.084	0.3404	29.55	0.084 ± 0.132
0.0237	4.54	-0.079 ± 0.045	0.3431	61.80	0.244 ± 0.102
0.0241	5.75	0.008 ± 0.032	0.4706	21.18	0.185 ± 0.208
0.0263	7.41	0.013 ± 0.037	0.4763	34.87	0.558 ± 0.289
0.0341	2.59	-0.042 ± 0.138	0.4827	71.76	0.317 ± 0.129

Table 5.5: Optimal set of asymmetries $A_1^{\rm d}(x, Q^2)$ from SMC data. The errors are statistical only.

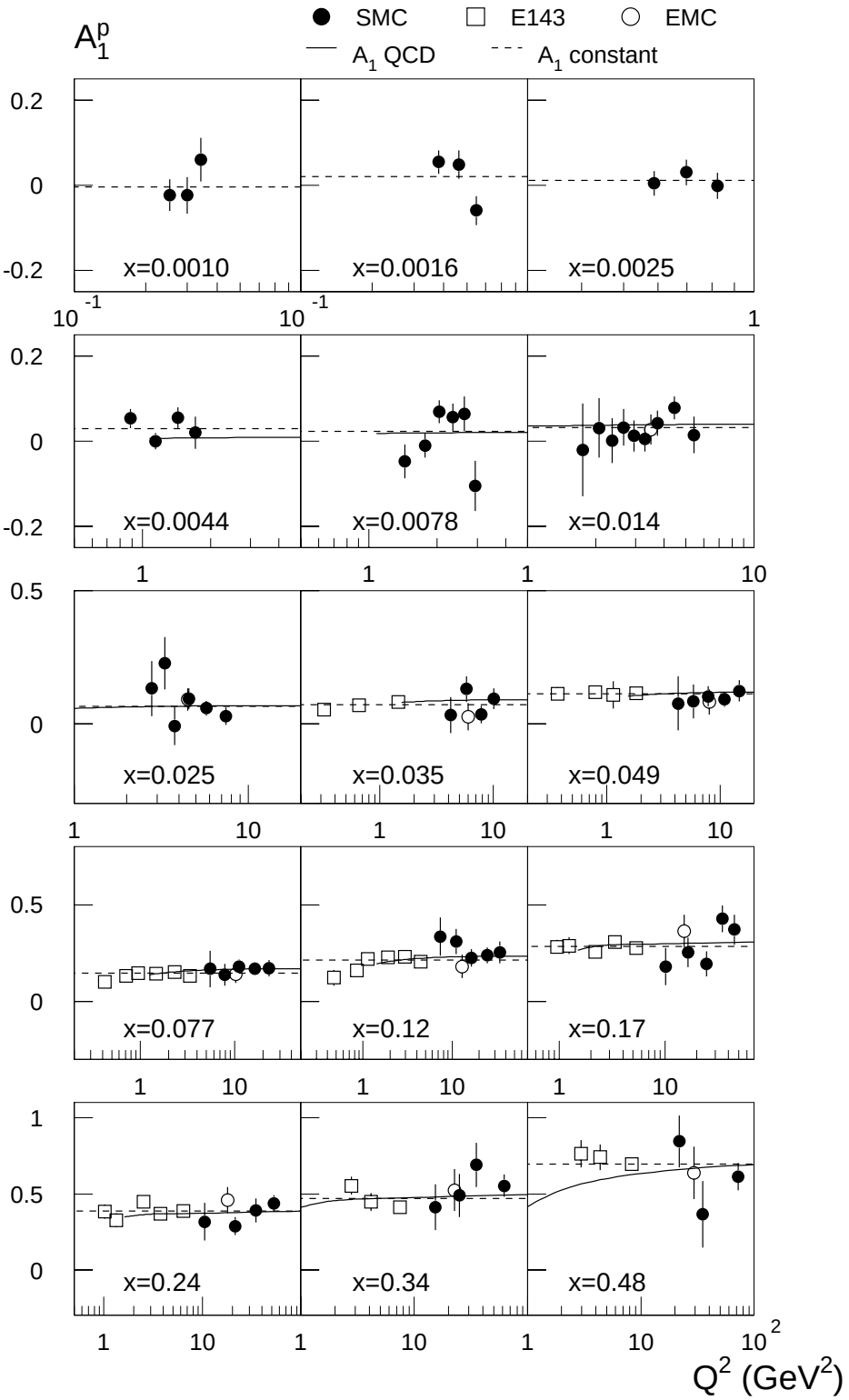

Figure 5.13: A_1^p as a function of Q^2 for different bins of x for the SMC data, where the value of x is the average value in each bin. The EMC [7] and E143 [106] results are also shown for comparison. Error bars show statistical uncertainties only. The solid line is a result of the QCD analysis described in section 5.5.4, while the dashed line is the fit assuming no Q^2 dependence.

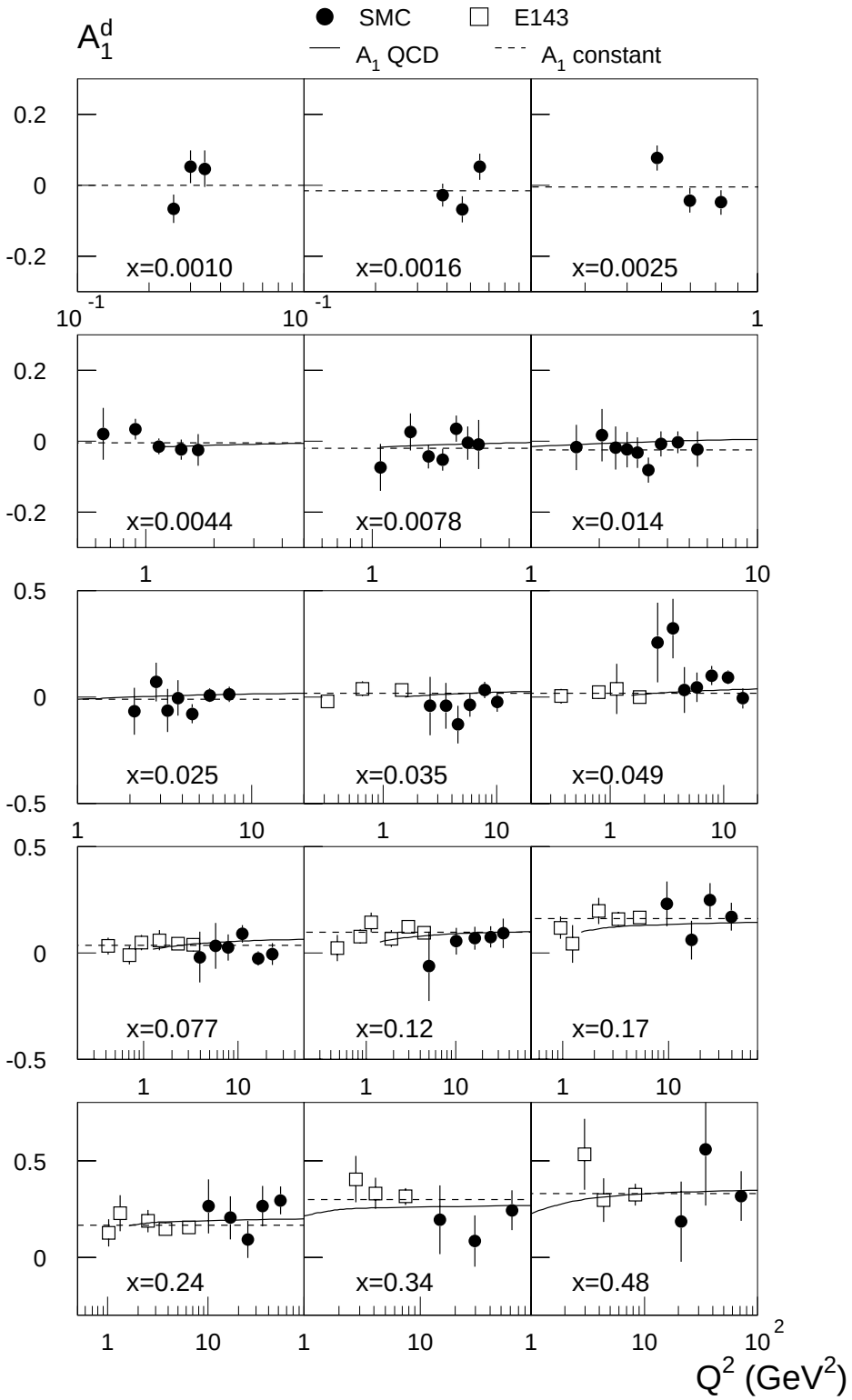

Figure 5.14: $A_1^{\rm d}$ as a function of Q^2 for different bins of x for the SMC data, where the value of x is the average value in each bin. The E143 results [106] are also shown for comparison. Otherwise same explanations as for Figure 5.13.

5.4.2 Systematic Uncertainties on A_1

Several different sources contribute to the total systematic error on A_1. The main ones are described in detail below. In the analysis all the individual systematic errors are treated as independent ones and are added in quadrature (i.e. assuming no correaltion among them) in order to obtain the total systematic error on A_1^p and A_1^d.

Uncertainty due to the acceptance variation

Given their smallness, the false asymmetries defined in section 5.1.3 are considered as a systematic effect on A_1 rather than a correction factor. The effect of the false asymmetry on A_1 is given by

$$\delta A_1^{false} = \frac{1}{4fDP_bP_t}(\kappa - 1) \tag{5.40}$$

and is estimated for each x bin. The value of $\kappa = \frac{r'}{r}$ (Equation 5.8) per x bin is used for quoting a systematic error on A_1.

Uncertainty due to the target polarization

The contributions to the systematic error from the target polarization $\frac{\delta P_t}{P_t}$ are described in depth in [109]. The estimation of $\frac{\delta P_t}{P_t}$ is summarized in Table 3.3 and

$$\delta A_1^{P_t} = \left(\frac{\delta P_t}{P_t}\right) A_1 \,. \tag{5.41}$$

Uncertaintiy due to the beam polarization

The error on the beam polarization $\frac{\delta P_b}{P_b}$ is reported in Table 3.1 and

$$\delta A_1^{P_b} = \left(\frac{\delta P_b}{P_b}\right) A_1 \,. \tag{5.42}$$

Uncertainty due to the dilution factor

It arises from the errors in the unpolarized cross section ratios, and from the uncertainties in the determination of the various concentrations of nuclei in the target material with respect to the polarizable target material and

$$\delta A_1^f = \left(\frac{\delta f}{f}\right) A_1 \,. \tag{5.43}$$

Uncertainty due to the radiative corrections

The radiative corrections are calculated using the program POLRAD (section 5.3)

with the A_1 asymmetries as an input parameter to the calculation. The systematic error on the radiative corrections δA_1^{RC} is estimated by varying the input asymmetries by one standard deviation up and down of their statistical errors. From that, an upper and lower limit of the radiative corrections is determined. The larger of the two is taken as the systematic error. This is an additive corrections, while the preceeding ones are multiplicative corrections.

Uncertainty due to the neglect of A_2

In evaluating A_1 from

$$A_1 = \frac{A_{||}}{D} - \eta A_2 \,, \tag{5.44}$$

the second term proportional to A_2 was neglected. The effect of neglecting A_2 is included in the systematic error. The uncertainty of A_1 due to A_2 is estimated by taking the maximal value of A_2 at a 95 % confidence level (i.e. 2 σ's).

Uncertainty due to R

A_1 depends on the structure function R through the depolarization factor D. The uncertainty of A_1 due to the uncertainty of R is given by

$$\delta A_1^R = \frac{2(1-y)}{y(2-y)} A_{||} \delta R \,. \tag{5.45}$$

The uncertainty δR is obtained from the errors on the parameters used in the parametrization of R.

Uncertainty due to the proton background

The error on the deuteron asymmetry A_1^d due to the polarized proton background arises mainly from the uncertainties in the hydrogen polarization and in the proton asymmetry A_1^p.

Uncertainty due to the nitrogen background

The uncertainty due to the nitrogen background arises from the uncertainty of the last term of Equation 5.24 and from the uncertainty of the deuteron asymmetry A_1^d.

Uncertainty due to the momentum measurements

The kinematics of the incoming and scattered muon are affected by the resolution of their momenta. This results in a smearing of the kinematical variables $x \pm \delta x$ and $Q^2 \pm \delta Q^2$. The effects on A_1 due to this phenomenon is estimated and included as a systematic error. The uncertainties of the incoming energy, δE, and of the scattered energy, $\delta E'$, of the muons depends on the calibrations of

the BMS and FSM, respectively. The uncertainty in the scattered muon energy ($\delta E'$) is estimated from the comparison of the J/Ψ and K_s^0 mass distributions with their particle data book values. From these comparisons, $\frac{\delta E}{E}$ is estimated to be 0.2 %, while $\frac{\delta E'}{E'}$ is estimated to be 0.3 %. These values are propagated throughout to the uncertainty in A_1. In the asymmetry extraction method, the only parameters that depend on the kinematics are f and D. The uncertainty in A_1 due to smearing of f and D is of the order of 10^{-4} for all x bins.

$\langle x \rangle$	$\Delta A_{\rm false}$	$\Delta P_{\rm t}$	ΔP_μ	$\Delta f'$	Δrc	ΔA_2	ΔR	ΔMR	$\Delta P_{\rm bg}$
0.0010	0.0019	0.0001	0.0001	0.0002	0.0008	0.0010	0.0002	0.0000	0.0006
0.0016	0.0019	0.0006	0.0005	0.0012	0.0008	0.0012	0.0007	0.0001	0.0006
0.0025	0.0019	0.0004	0.0003	0.0008	0.0008	0.0013	0.0004	0.0000	0.0006
0.005	0.0018	0.0009	0.0007	0.0015	0.0009	0.0005	0.0009	0.0000	0.0005
0.008	0.0019	0.0008	0.0006	0.0013	0.0009	0.0007	0.0007	0.0001	0.0005
0.014	0.0020	0.0011	0.0009	0.0017	0.0008	0.0008	0.0013	0.0001	0.0004
0.025	0.0018	0.0018	0.0014	0.0011	0.0007	0.0003	0.0028	0.0002	0.0004
0.035	0.0018	0.0020	0.0016	0.0013	0.0008	0.0003	0.0027	0.0003	0.0004
0.049	0.0019	0.0030	0.0024	0.0019	0.0009	0.0003	0.0041	0.0005	0.0003
0.077	0.0019	0.0051	0.0040	0.0032	0.0009	0.0004	0.0079	0.0008	0.0004
0.122	0.0020	0.0076	0.0059	0.0049	0.0010	0.0005	0.0099	0.0012	0.0008
0.173	0.0021	0.0089	0.0069	0.0059	0.0010	0.0005	0.0118	0.0017	0.0010
0.242	0.0021	0.0110	0.0086	0.0078	0.0010	0.0022	0.0157	0.0023	0.0013
0.342	0.0021	0.0163	0.0127	0.0138	0.0009	0.0025	0.0258	0.0029	0.0017
0.480	0.0021	0.0188	0.0147	0.0223	0.0009	0.0029	0.0348	0.0034	0.0021

Table 5.6: Contributions to the systematic error for $A_1^{\rm p}(x)$ are the uncertainties of: the false asymmetry contribution, $\Delta A_{\rm false}$; the target and the beam polarizations, $\Delta P_{\rm t}$ and ΔP_μ; the effective dilution factor, $\Delta f'$; the radiative corrections, Δrc; the neglect of A_2, ΔA_2; the ratio R, ΔR; the momentum resolution, ΔMR; and the polarized background from ^{14}N in the ammonia target, $\Delta P_{\rm bg}$. The first three bins have $Q^2 > 0.2$ GeV^2, while the rest have $Q^2 > 1$ GeV^2.

5.5 The g_1 Structure Function

The spin dependent structure function g_1 is evaluated from the measured A_1 asymmetries reported in Tables 5.2 and 5.3 from Equation 1.31:

$$g_1^{p,d} = \frac{F_2^{p,d}}{2x(1+R)}(A_1^{p,d} + \gamma A_2^{p,d}) \ , \tag{5.46}$$

where the A_2 contribution has been neglected. The unpolarized structure function F_2 and the ratio R are evaluated at the x and Q^2 of the A_1 measurement by using the parametrizations described below.

5.5.1 F_2 Parametrization

The unpolarized structure functions $F_2^p(x,Q^2)$ and $F_2^d(x,Q^2)$ are determined with a phenomenological fit to the available unpolarized DIS data. The proton fit used data from measurements on protons made by BCDMS [110], E665 [111], NMC [116], SLAC [112], H1 [113] and ZEUS [114], while the data used for the deuteron fit came from measurements on deuterons made by BCDMS [110], E665 [111], NMC [116] and SLAC [112] and from the precise measurements of the ratio F_2^d/F_2^p made by NMC [116].

The parametrization used was the one originally proposed by BCDMS [110], and later used by NMC :

$$F_2^{fit}(x,Q^2) = A(x) \cdot \left[\frac{\ln(Q^2/\Lambda^2)}{\ln(Q^2/\Lambda^2)}\right]^{B(x)} \left[1 + \frac{C(x)}{Q^2}\right] \ , \tag{5.47}$$

where

$$\begin{aligned} A(x) &= x^{a_1}(1-x)^{a_2}[a_3 + a_4(1-x) + a_5(1-x)^2 + a_6(1-x)^3 + a_7(1-x)^4] \\ B(x) &= b_1 + b_2 x + b_3/(x+b_4) \\ C(x) &= c_1 x + c_2 x^2 + c_3 x^3 + c_4 x^4. \end{aligned}$$

This 15 parameter functional form has been fitted to the F_2^p and F_2^d data separately at $Q_0^2 = 20$ GeV^2 with $\Lambda = 0.25$ GeV. All the parameters and the complete covariance matrices were determined and were then used to determine the one standard deviation of the upper and lower limits of F_2^p and F_2^d. The upper and lower limit values were propagated as a systematic error on g_1.

Parameter	F_2^p	F_2^p limits	
		Upper limit	Lower limit
a_1	−0.24997	−0.24810	−0.25196
a_2	2.3963	2.3632	2.4297
a_3	0.22896	0.23643	0.21913
a_4	0.08498	−0.03241	0.21630
a_5	3.8608	4.2268	3.4645
a_6	−7.4143	−7.8120	−6.9887
a_7	3.4342	3.5822	3.2771
b_1	0.11411	0.09734	0.13074
b_2	−2.2356	−2.2254	−2.2465
b_3	0.03115	0.03239	0.02995
b_4	0.02135	0.02233	0.02039
c_1	−1.4517	−1.4361	−1.4715
c_2	8.4745	8.1084	8.9108
c_3	−34.379	−33.306	−35.714
c_4	45.888	44.717	47.338

Table 5.7: The values of the parameters of Equation 5.47 for F_2^p and for the upper and lower limits of F_2^p.

The values for the fitted parameters are given in Tables 5.7 and 5.8. The upper and lower limit parameter values correspond to the total uncertainty of F_2^p and F_2^d.

The fitted parametrizations are valid and can be used only in the kinematical range of the data sets, which covers $3.5 \cdot 10^{-5} < x < 0.85$ and $0.2 < Q^2 < 5000\,\mathrm{GeV}^2$ for F_2^p and $9 \cdot 10^{-4} < x < 0.85$ and $0.2 < Q^2 < 220\,\mathrm{GeV}^2$ for F_2^d. The above parametrization of F_2 must be used with the proper values of R to reproduce the measured cross sections. A detailed description of the fitting procedure can be found in [115].

5.5.2 R Evaluation

The determination of the unpolarized structure function R (Equation 1.23), the ratio of the absorption cross section for longitudinally and transversely polarized virtual photons, requires cross section measurements at different energies, and

Parameter	F_2^d	F_2^d limits	
		Upper limit	Lower limit
a_1	−0.28151	−0.28047	−0.28178
a_2	1.0115	0.82170	1.1694
a_3	0.08415	0.06904	0.09973
a_4	−0.72973	−0.60191	−0.85884
a_5	2.8647	2.2618	3.4541
a_6	−2.5328	−1.6507	−3.3995
a_7	0.47477	0.08909	0.86034
b_1	0.20040	0.18711	0.20865
b_2	−2.5154	−2.4711	−2.5475
b_3	0.02599	0.02802	0.02429
b_4	0.01858	0.01973	0.01760
c_1	−1.3569	−1.3762	−1.3513
c_2	7.8938	7.6113	8.3602
c_3	−29.117	−27.267	−31.710
c_4	37.657	35.100	41.106

Table 5.8: The values of the parameters of Equation 5.47 for F_2^d and for the upper and lower limits of F_2^d.

has been determined by several experiments.

The parametrization of R measured by NMC [116] has been used for $x < 0.12$, while for $x > 0.12$ the parametrization of SLAC [117] has been used. The SLAC parametrization covers the kinematical range of $0.1 < x < 0.9$ and $0.6 < Q^2 < 30$ GeV^2 and has been extrapolated to higher values of Q^2 in order to cover the whole Q^2 range of the SMC data. The NMC parametrization has been determined in the range of $0.002 < x < 0.12$ and $1.0 < Q^2 < 25$ GeV^2 and covers essentially the whole *low-x* range of the SMC data. Moreover, NMC has measured also the difference $R_p - R_d$ and found it to be consistent with zero [118]. Therefore, the same parametrizations of R are used for both the proton and deuteron data.

5.5.3 Results of g_1 at the Measured Q^2

The results of the spin dependent structure function g_1 at the measured Q^2 are presented in Figure 5.15 and Tables 5.9 and 5.10, down to $x = 0.0008$. The lowest

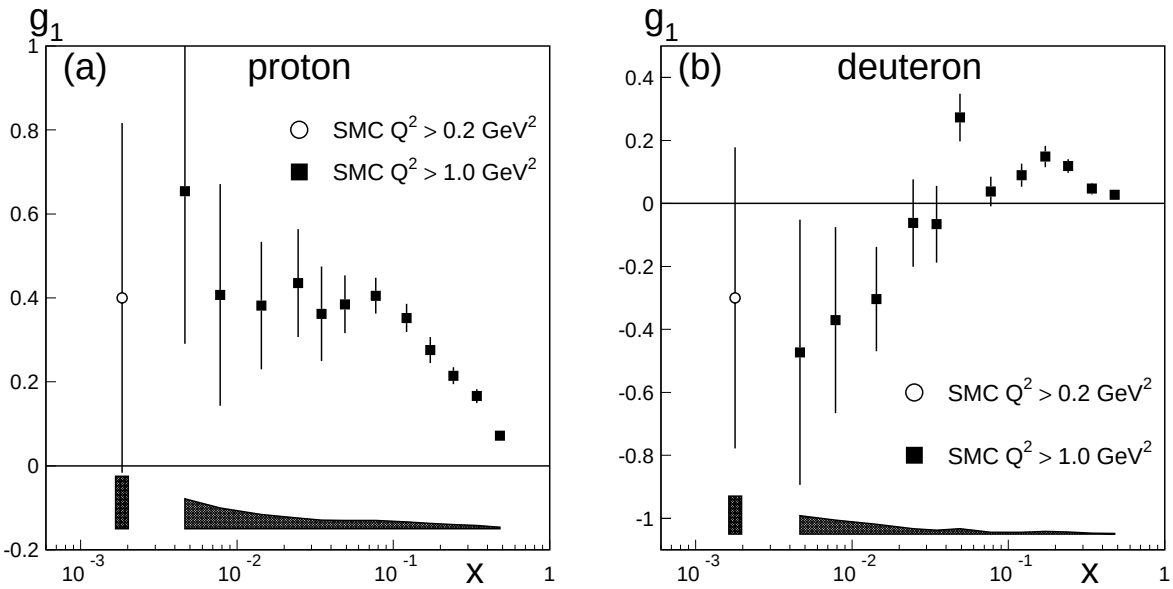

Figure 5.15: The optimal set of SMC results for g_1: (a) for proton and (b) for deuteron. The statistical errors are shown as error bars, while the shaded band below the data points indicates the systematic uncertainty. The $Q^2 > 0.2$ GeV^2 result was obtained by combining the three lowest A_1 bins.

x bin point was obtained by combining the data of the three lowest x bins of the A_1 results; it contains data with Q^2 values below 1 GeV^2. These low x data can be shown because a valid parametrization of F_2 for this region became available. Due to concerns of the applicability of the perturbative QCD at low Q^2, only data with $Q^2 > 1$ GeV^2 have been used in the QCD analysis described below. Figure 5.16 shows a compilation of almost all available world data on g_1 at the measured Q^2.

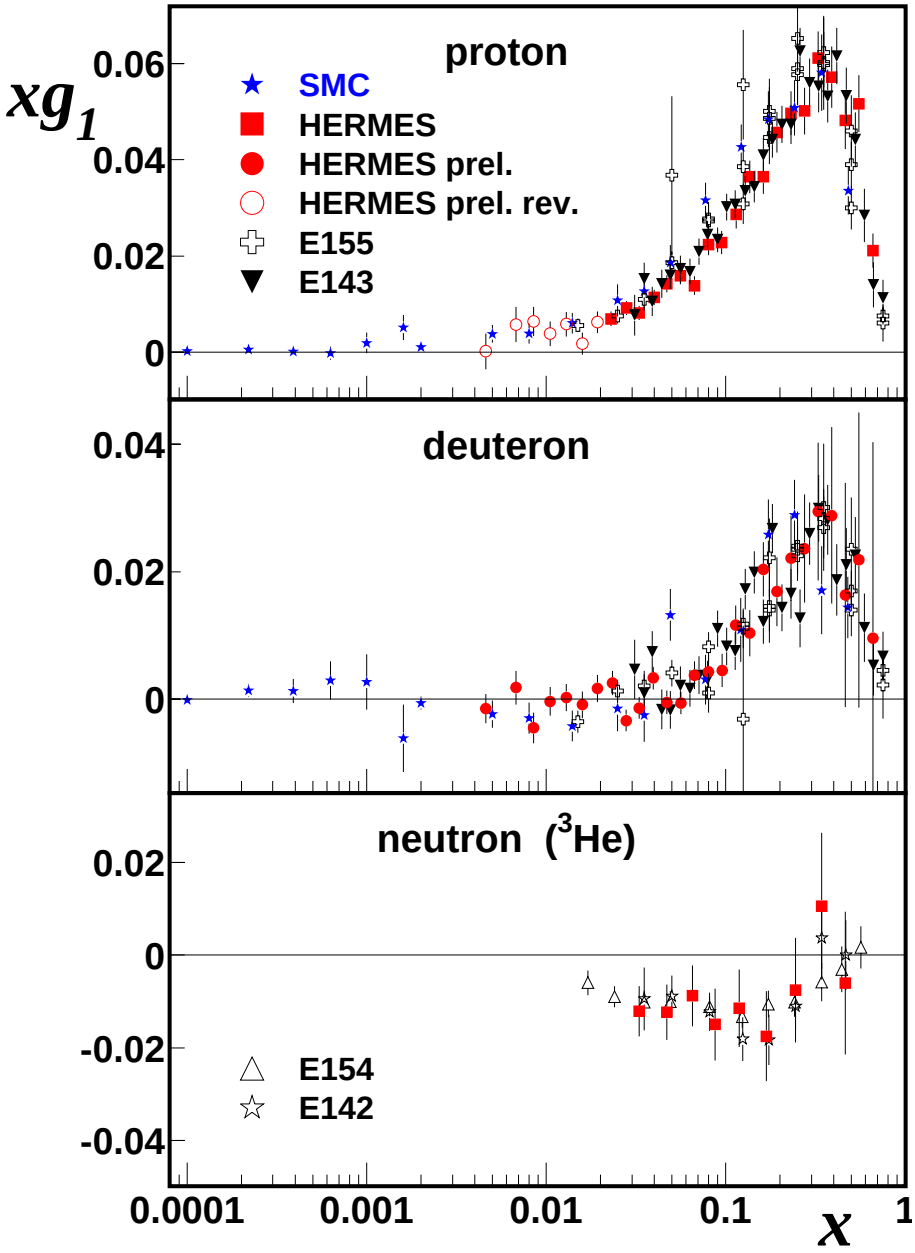

Figure 5.16: Compilation of (almost) all available world data on $xg_1(x, Q^2)$ (except for EMC) at the measured Q^2 (plot from [119]).

x Range	$\langle x \rangle$	$\langle Q^2 \rangle$ (GeV^2)	g_1^p	g_1^p (Q_0^2=10 GeV^2)
0.0008–0.003	0.002	0.5	0.49±0.42±0.13	
0.003–0.006	0.005	1.3	0.75±0.36±0.07	1.19±0.36±0.07±0.56
0.006–0.010	0.008	2.1	0.48±0.26±0.05	0.79±0.26±0.05±0.25
0.010–0.020	0.014	3.6	0.43±0.15±0.04	0.59±0.15±0.03±0.07
0.020–0.030	0.025	5.7	0.43±0.13±0.03	0.50±0.13±0.03±0.02
0.030–0.040	0.035	7.8	0.36±0.11±0.02	0.39±0.11±0.02±0.01
0.040–0.060	0.049	10.4	0.38±0.07±0.02	0.38±0.07±0.02±0.00
0.060–0.100	0.077	14.9	0.41±0.04±0.02	0.39±0.04±0.02±0.00
0.100–0.150	0.122	21.3	0.35±0.03±0.02	0.33±0.03±0.02±0.00
0.150–0.200	0.173	27.8	0.28±0.03±0.01	0.27±0.03±0.01±0.00
0.200–0.300	0.242	35.6	0.21±0.02±0.01	0.22±0.02±0.01±0.01
0.300–0.400	0.342	45.9	0.17±0.02±0.01	0.18±0.02±0.01±0.00
0.400–0.700	0.480	58.0	0.07±0.01±0.00	0.09±0.01±0.00±0.00

Table 5.9: The proton spin-dependent structure function g_1^p at the measured Q^2; and for $Q^2 > 1$ GeV^2, where the QCD evolution is applicable, evolved to $Q_0^2 = 10$ GeV^2. The first bin, which has $Q^2 > 0.2$ GeV^2, was obtained by combining the three lowest A_1 bins from Table 5.2. The first error is statistical and the second is systematic. In the last column the third error indicates the uncertainty in the QCD evolution.

x Range	$\langle x \rangle$	$\langle Q^2 \rangle$ (GeV^2)	$g_1^{\rm d}$	$g_1^{\rm d}$ (Q_0^2=10 GeV^2)
0.0008–0.003	0.002	0.5	$-0.30\pm0.48\pm0.12$	
0.003–0.006	0.005	1.3	$-0.47\pm0.42\pm0.06$	$-0.30\pm0.42\pm0.06\pm0.49$
0.006–0.010	0.008	2.1	$-0.37\pm0.30\pm0.04$	$-0.22\pm0.30\pm0.04\pm0.22$
0.010–0.020	0.014	3.5	$-0.30\pm0.17\pm0.03$	$-0.22\pm0.17\pm0.03\pm0.06$
0.020–0.030	0.025	5.5	$-0.06\pm0.14\pm0.02$	$-0.02\pm0.14\pm0.02\pm0.02$
0.030–0.040	0.035	7.5	$-0.07\pm0.12\pm0.01$	$-0.05\pm0.12\pm0.01\pm0.01$
0.040–0.060	0.049	10.0	$0.27\pm0.08\pm0.02$	$0.27\pm0.08\pm0.02\pm0.00$
0.060–0.100	0.077	14.4	$0.04\pm0.05\pm0.01$	$0.03\pm0.05\pm0.01\pm0.00$
0.100–0.150	0.121	20.6	$0.09\pm0.04\pm0.01$	$0.08\pm0.04\pm0.01\pm0.00$
0.150–0.200	0.172	26.8	$0.15\pm0.03\pm0.01$	$0.14\pm0.03\pm0.01\pm0.00$
0.200–0.300	0.241	34.3	$0.12\pm0.02\pm0.01$	$0.12\pm0.02\pm0.01\pm0.00$
0.300–0.400	0.342	43.9	$0.05\pm0.02\pm0.00$	$0.05\pm0.02\pm0.00\pm0.00$
0.400–0.700	0.479	54.8	$0.03\pm0.01\pm0.00$	$0.04\pm0.01\pm0.00\pm0.00$

Table 5.10: The deuteron spin-dependent structure function $g_1^{\rm d}$ at the measured Q^2; and for $Q^2 > 1$ GeV^2 evolved to $Q_0^2 = 10$ GeV^2. Otherwise, explanations as for Table 5.9.

5.5.4 QCD Evolution Analysis

The evaluation of the sum rules, like the Bjorken sum rule (section 1.7.1) requires the integration of g_1 over the entire x range of $0 < x < 1$ at a fixed value of Q^2. However, for the A_1 and g_1 measurements, only part of the x range is accessible; moreover, in the accessible range, each x bin covers a different Q^2 interval. Because of these reasons, a so-called QCD evolution analysis (section 1.6) is necessary. That allows to evolve the measured g_1 values to a common Q^2 and to extrapolate g_1 to the unmeasured regions (section 1.7.3). The basis of this evolution analysis are the DGLAP evolution equations [35] (Equations 1.53, 1.54, and 1.55), that allow the parton distribution functions to be evolved from the measured Q^2 to any other value of Q^2.

In order to perform the evolution using the DGLAP evolution equations, the polarized parton distributions need to be extracted from the experimental structure function data. The functional form of the polarized parton distributions has to account for both the low x and high x behaviors with a minimum number of free parameters. The following parametrization was used [50]

$$\Delta f(x, Q^2) = N(\alpha_f, \beta_f, a_f)\, \eta_f\, x^{\alpha_f}\, (1-x)^{\beta_f}\, (1 + \alpha_f x) \tag{5.48}$$

where $N(\alpha, \beta, a)$ is fixed by the normalization condition,

$$N(\alpha, \beta, a) \int_0^1 x^{\alpha}\, (1-x)^{\beta} (1 + \alpha x) = 1\ . \tag{5.49}$$

Δf denotes $\Delta\Sigma$, Δq_{NS} or Δg. With this normalization the parameters η_S, η_{NS} and η_g, are the first moments of the singlet quark, the non-singlet quark and the gluon distributions at the starting scale, respectively. As discussed in section 1.6, the spin-dependent structure function g_1 can be expressed in terms of the quark singlet and non-singlet and the gluon distributions (Equation 1.50).

The SMC proton and deuteron data of Tables 5.9 and 5.10, along with the proton and deuteron data of EMC [7] and E143 [106], and the neutron data of E142 [120], E154 [121], and HERMES [122] were used. The parameters of the parton distribution functions have been determined by a χ^2 minimization procedure. The initial parametrizations of Equation 5.48, at a starting Q^2 of 1 GeV^2, have been evolved to the measured Q^2 of each data point with the

DGLAP equations using an evolution program written by R. Ball *et al.* [123]. This program uses a method which solves the DGLAP equations in momentum space with the boundary condition of Equation 5.48 at an initial scale of $Q_i^2 = 1$ GeV^2. For each set of starting parameters η_f, α_f, β_f and a_f the following χ^2

$$\chi^2 = \Sigma_{i=1}^{n} \frac{[g_1^{calc}(x,Q^2) - g_1^{data}(x,Q^2)]^2}{[\delta_{stat} g_1^{data}(x,Q^2)]^2} \tag{5.50}$$

has been computed. The sum i is over the number of experimental data points (about 100), g_1^{calc} is the calculated g_1, g_1^{data} is the measured g_1, and δ_{stat} is the statistical error of the measured g_1. The χ^2 is minimized by varying the starting parameters η_f, α_f, β_f and a_f of the parton distributions (Equation 5.48) in order to obtain the best fit at the measured Q^2.

Not all of the parameters of Equation 5.48 are well constrained by the data; therefore some of them had to be fixed. The parameters β_g, which controls the behavior of the gluon distribution at large x, is fixed to 4 by the QCD sum rules [47]. The non-singlet η_{NS} terms are fixed by using the neutron and hyperon β decay constants and by assuming SU(3) flavor symmetry:

$$\eta_{NS}^{p,(n)} = +(-)\frac{3}{4}\frac{g_A}{g_V} + \frac{1}{4}a_8 \ , \tag{5.51}$$

where $|g_A/g_V| = F + D = 1.2601 \pm 0.0025$ [38] and $F/D = 0.575 \pm 0.016$ [124], with $\alpha_s(M_Z^2) = 0.118 \pm 0.003$ [38].

Figure 5.17 shows the polarized parton distributions obtained from this NLO pQCD analysis of the polarized structure function g_1 at $Q_i^2 = 1$ GeV^2 including their statistical uncertainties as obtained from this fit procedure. The values of the parameters at the same initial scales are summarized in [50].

The program of R. Ball *et al.* [123] was also used in order to evolve the data from the measured Q^2 to a fixed Q_0^2 of 5 GeV^2 and 10 GeV^2. In order to obtain g_1 at the desired fixed Q_0^2, the difference between the fit value at the measured Q^2 and at the fixed Q_0^2 is added to the g_1 at the measured Q^2 as

$$g_1(x,Q_0^2) = g_1(x,Q^2) + [g_1^{fit}(x,Q_0^2) - g_1^{fit}(x,Q^2)] \, . \tag{5.52}$$

The results of the fits to g_1 at $Q^2 = 5$ GeV^2 are shown in Figures 5.18, 5.19, and 5.20 for the proton, the deuteron and the neutron, respectively [50]. The

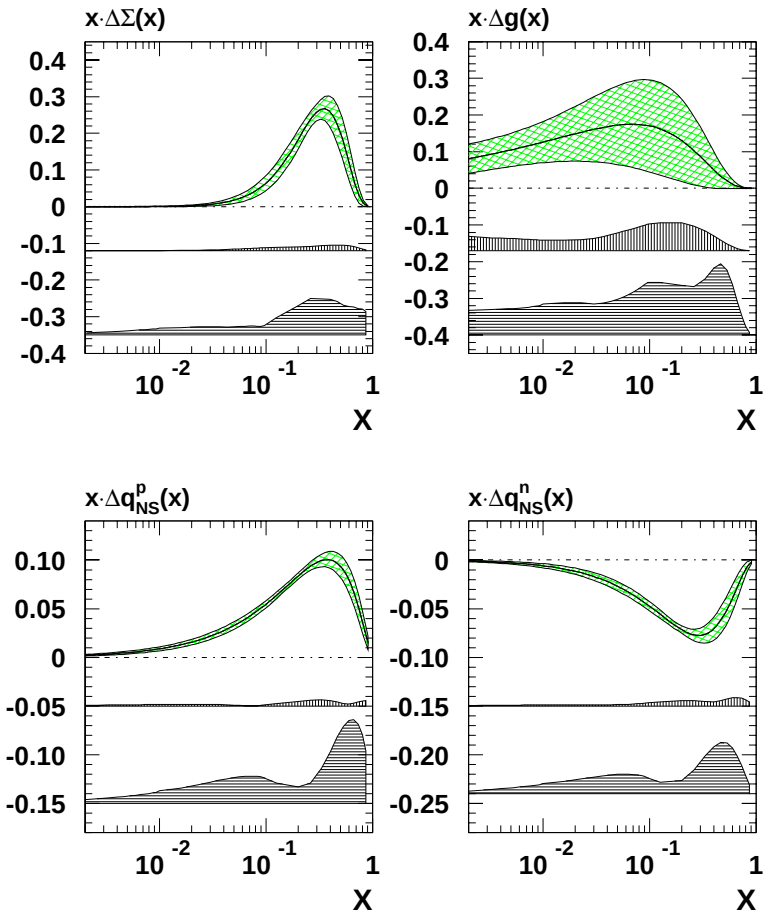

Figure 5.17: Polarized parton distribution functions determined from a pQCD analysis at $Q_i^2 = 1$ GeV^2. The crossed hatched bands represent their statistical uncertainty as obtained from the NLO QCD fit. The vertical and horizontal hatched bands represent the experimental and theoretical uncertainties.

data have also been evolved to the same $Q^2 = 5$ GeV^2, which is close to the avarage Q^2 of the world data set used for this analysis. The results of the g_1 evolved to $Q^2 = 10$ GeV^2 for the SMC data are shown in Tables 5.9 and 5.10.

The contributions to the uncertainty of g_1^{fit} consist of the uncertainties of the factorization and renormalization scales, the functional form chosen for the parton distributions, α_s, g_A and the quark mass thresholds.

Since this analysis has been completed, new data have become available at larger x than SMC [125] and new QCD analyses have been performed. The results of the most recent analysis of [126] for the proton are shown in Figure 5.21. The new data at large x, however, have little impact on the overall behavior of g_1 and

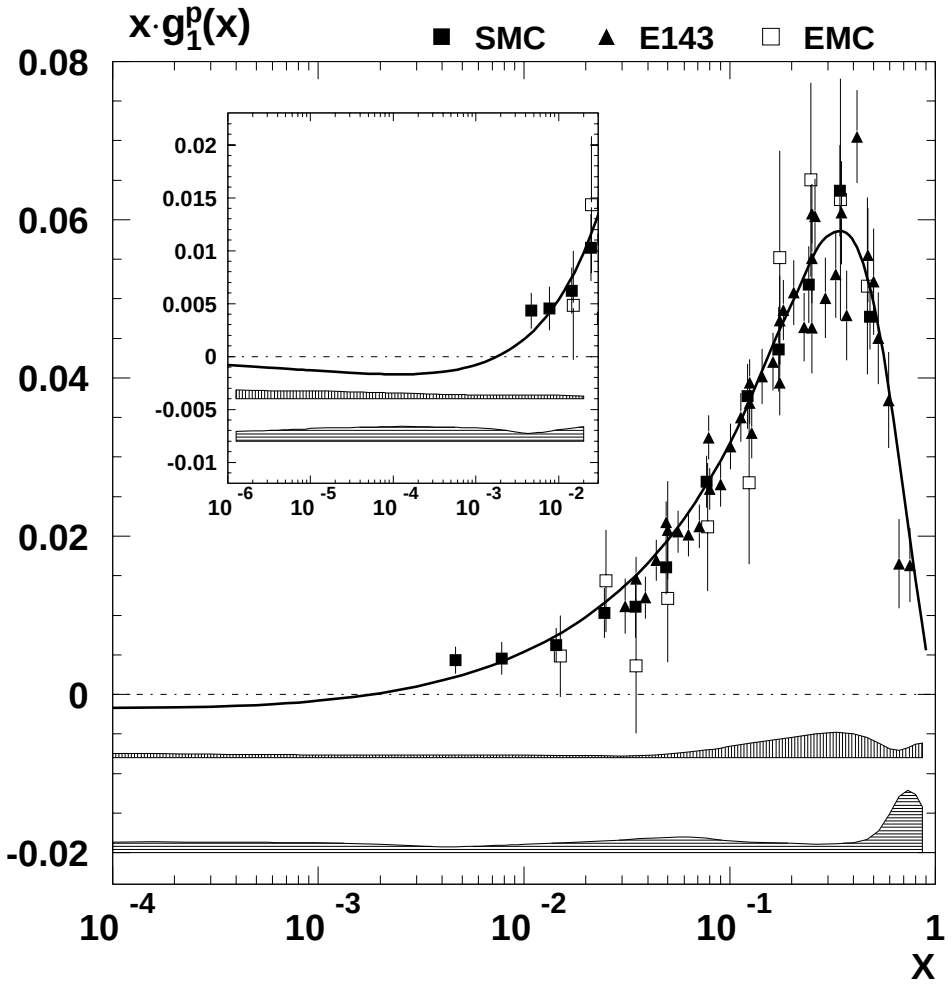

Figure 5.18: $x\,g_1^{\mathrm{p}}$ (proton) vs. x for the world data with the QCD fit at $Q^2 = 5$ GeV^2. The low x region is emphasized in the inset. The data points are shown with their statistical errors. The uncertainties of the fit due to experimental systematics and theoretical sources are shown by the vertically and horizontally hatched bands, respectively.

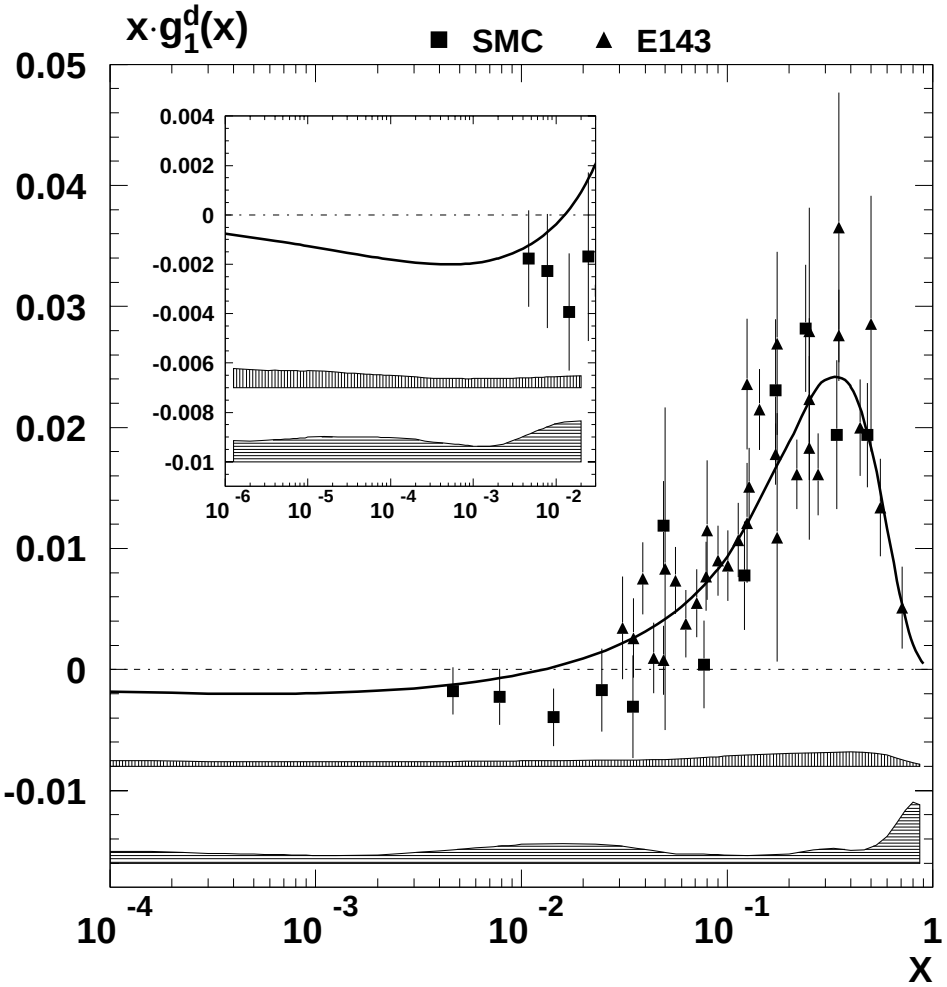

Figure 5.19: $x\,g_1^{\rm d}$ (deuteron) vs. x for the world data with the QCD fit at $Q^2 = 5$ GeV^2. The low x region is emphasized in the inset. The data points are shown with their statistical errors. The uncertainties of the fit due to experimental systematics and theoretical sources are shown by the vertically and horizontally hatched bands, respectively.

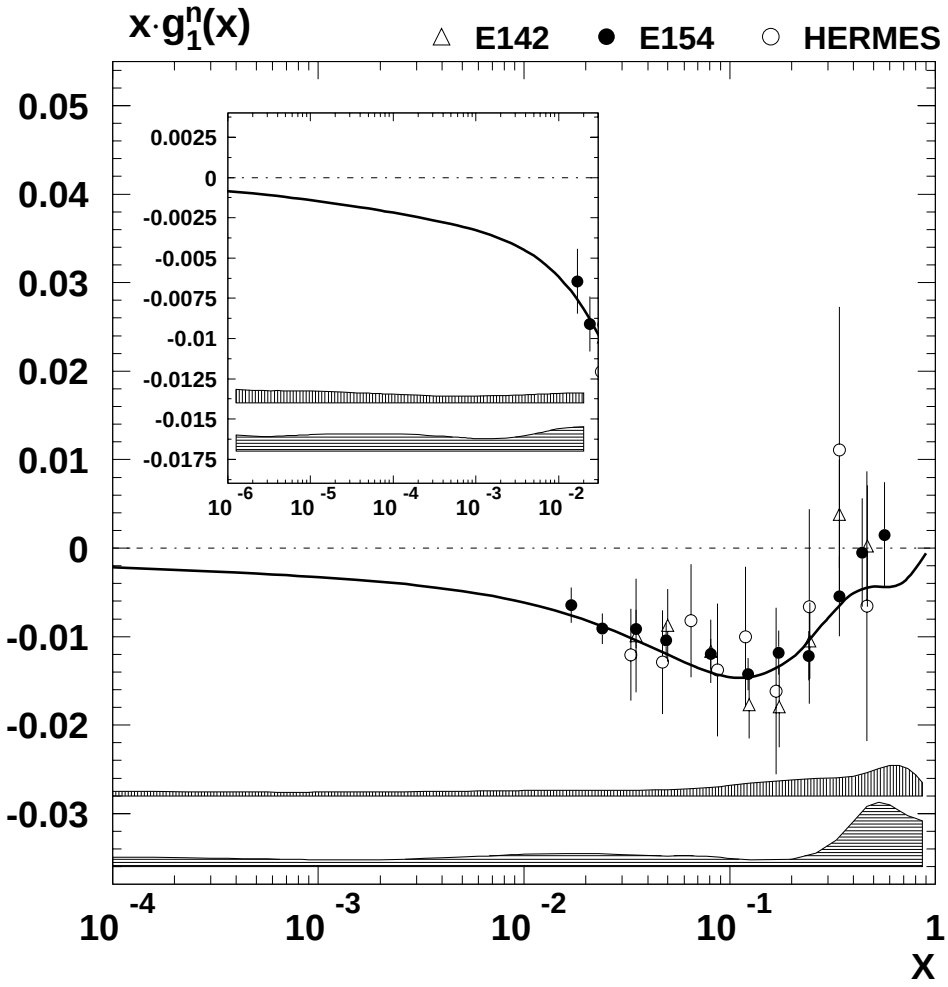

Figure 5.20: $x\,g_1^{\mathrm{n}}$ (neutron) vs. x for the world data with the QCD fit at $Q^2 = 5$ GeV^2. Only statistical errors are shown with the data points. The low x region is emphasized in the inset. The uncertainties in the fit due to experimental systematics and theoretical sources are shown by the vertically and horizontally hatched bands, respectively.

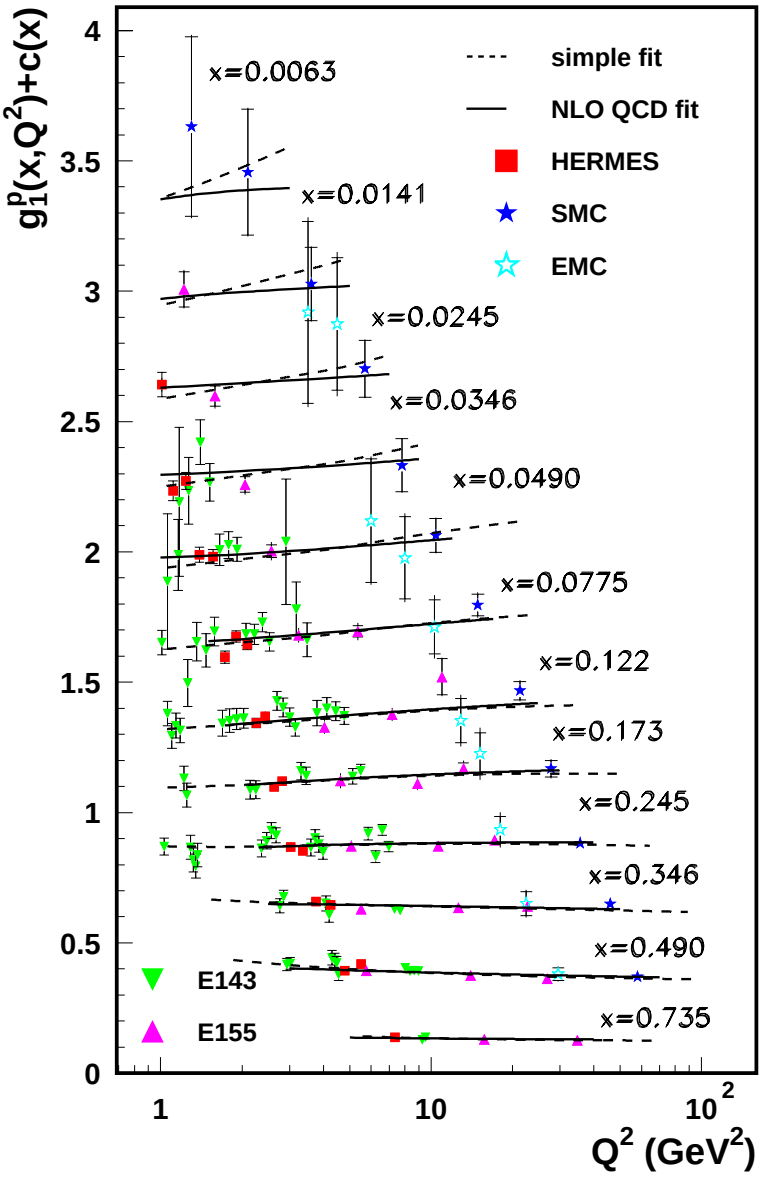

Figure 5.21: Q^2 dependence of $g_1^{\rm p}(x,Q^2)$ for the proton world data with $Q^2 > 1$ GeV^2. Also shown are the fit (dashed line) according to $A_1 = x^{0.7}(0.817 + 1.014x - 1.489x^2) \times (1 - 0.04/Q^2)$ [125] and a NLO pQCD fit (full line) of [126]. For better visibility each data set for a given $\langle x \rangle$ is shifted by a fixed value $c(x)$: starting from bottom +0, +0.3, +0.5, +0.7, +0.9, +1.1, +1.4, +1.7, +2.0, +2.3, +2.6, and +3.0.

do not change substantially the picture obtained in the SMC analysis [50].

5.6 The First Moments and the Sum Rules

The first moment of g_1, referred to as Γ_1, is the integral of g_1 at a fixed Q^2 over the entire x range, from 0 to 1:

$$\Gamma_1 = \int_0^1 g_1 dx \,. \tag{5.53}$$

In the measured range, $0.003 < x < 0.7$, $g_1(x, Q_0^2)$ is calculated from the NLO QCD analysis using Equation 5.52 for a fixed Q_0^2 of 10 GeV^2, which is close to the average Q^2 of the SMC data. These results are presented below

$$\int_{0.003}^{0.7} g_1^p(x, Q_0^2)\, dx = 0.131 \pm 0.005 \pm 0.006 \pm 0.004 \,, \tag{5.54}$$

$$\int_{0.003}^{0.7} g_1^d(x, Q_0^2)\, dx = 0.037 \pm 0.006 \pm 0.003 \pm 0.003 \,, \tag{5.55}$$

where the first uncertainty is statistical, the second systematic and the third one comes from the uncertainty in the Q^2 evolution. The total systematic error is obtained by adding the individual contributions, which are detailed in Table 5.11.

In addition to the systematic errors on A_1 propagated to g_1 and to the integral over the measured region, the contributions from the kinematical resolution and the error due to the approximations in the asymmetry evaluation procedure are also included.

The results for the first moments, which are the integrals taken over the full range, are

$$\Gamma_1^p(Q^2 = 10 \text{ GeV}^2) = \int_0^1 g_1^p(x, Q_0^2)\, dx = 0.120 \pm 0.005 \pm 0.006 \pm 0.014 \,, \tag{5.56}$$

$$\Gamma_1^d(Q^2 = 10 \text{ GeV}^2 = \int_0^1 g_1^d(x, Q_0^2)\, dx = 0.019 \pm 0.006 \pm 0.003 \pm 0.013 \,. \tag{5.57}$$

As far as the contributions from the unmeasured regions, the QCD fit is extended into these regions and the area under the curve is taken. The behavior of the QCD fits in these unmeasured regions can be seen in Figures 5.18, 5.19, and 5.20. The contribution to the error from the unmeasured regions is evaluated in the same way as for the measured region.

Source of the error	$\Delta\Gamma_1^{\mathrm{p}}$	$\Delta\Gamma_1^{\mathrm{d}}$
Target polarization	0.0037	0.0012
Beam polarization	0.0029	0.0008
Dilution factor	0.0027	0.0006
Uncertainty in F_2	0.0023	0.0010
Acceptance variation	0.0015	0.0014
Radiative corrections	0.0007	0.0008
Asymmetry evaluation	0.0006	0.0006
Neglect of A_2	0.0005	0.0006
Polarized background	0.0005	0.0004
Kinematical resolution	0.0003	0.0003
Momentum measurement	0.0003	0.0001
Uncertainty on R	0.0000	0.0000
Total systematic error	0.0062	0.0026
Evolution	0.0036	0.0027
Statistics	0.0052	0.0057

Table 5.11: The sources of uncertainties for the integrals of g_1^{p} and g_1^{d} in the measured region $0.003 < x < 0.7$.

5.6.1 The Ellis-Jaffe Sum Rule

The predictions of Ellis-Jaffe for the first moments were calculated, for a fixed Q^2 of 10 GeV^2, by using Equation 1.67:

$$\Gamma_1^p(Q^2 = 10 \text{ GeV}^2) = 0.170 \pm 0.005 \tag{5.58}$$

$$\Gamma_1^d(Q^2 = 10 \text{ GeV}^2) = 0.071 \pm 0.004\,. \tag{5.59}$$

The experimental value for Γ_1^p (Equations 5.56) disagrees with the Ellis-Jaffe prediction by almost 3 standard deviations, while the experimental value for Γ_1^d (Equations 5.57) also disagrees with the Ellis-Jaffe prediction by almost 4 standard deviations. In both cases the experimental values are smaller than the predictions. This fact further confirms that the quark singlet contribution to the nucleon spin $\Delta\Sigma$ is small.

In the Adler-Bardeen renormalization scheme [123, 18] the pQCD anlaysis gives

$$\Delta\Sigma(Q^2 = 1 \text{ GeV}^2) = 0.23 \pm 0.07(stat) \pm 0.19(syst)\,. \tag{5.60}$$

This value corresponds to about $\frac{1}{3}$ of the QPM expectation of $\Delta\Sigma = 0.58$ [42]. The large systematic unceratinty is due to the correlation (in this scheme) of this quantity with Δg and its uncertainty in the evaluation.

The same analysis gives for Δg

$$\Delta g(Q^2 = 1 \text{ GeV}^2) = 0.99 \, ^{+1.17}_{-0.31}(sta) \, ^{+0.42}_{-0.22}(sys) \, ^{+1.43}_{-0.45}(th) \, . \tag{5.61}$$

When evolved to $Q^2 = 5$ GeV^2 and $Q^2 = 10$ GeV^2, the values for Δg become 1.7 and 2.0, respectively. The large error reflects the fact, that the uncertainty on Δg from scaling violations is still too large to significantly constrain the gluon contribution to the nucleon spin.

5.6.2 The Bjorken Sum Rule

The Bjorken sum rule (Equation 1.65) relates the difference of Γ_1^p and Γ_1^n to the neutron β decay constant $|g_A/g_V|$. The conventional method of testing the Bjorken sum rule, which has been used in most experimental papers, is to evaluate the difference $\Gamma_1^p - \Gamma_1^n$ at a fixed Q^2 and to verify, if Equation 1.63 holds.

In order to reduce the number of free parameters, in the SMC NLO pQCD analysis, instead, $|g_A/g_V|$ has been fixed to its nominal value of 1.2601 ± 0.0025 [38]. This is equivalent to assume that the Bjorken sum rule is valid. In SMC pQCD analysis, the Bjorken sum rule has been tested by releasing this constraint in the pQCD analysis by making $|g_A/g_V|$ one of the free parameters to be fitted with the g_1 data. This is an alternative way to test this sum rule. The fit gave

$$\left|g_A/g_V\right| = 1.15 \, ^{+0.03}_{-0.03}(sta) \, ^{+0.07}_{-0.06}(sys) \, ^{+0.14}_{-0.04}(th) \, . \tag{5.62}$$

The value obtained here is consistent with the nominal value used above.

To evaluate the Bjorken sum rule this fitted value for $|g_A/g_V|$ and its uncertainty have been used in the pQCD analysis at $Q^2 = 5$ GeV^2. It has been obtained

$$\Gamma_1^p - \Gamma_1^n = 0.174 \, ^{+0.005}_{-0.005}(sta) \, ^{+0.011}_{-0.009}(sys) \, ^{+0.021}_{-0.006}(th) = 0.174 \, ^{+0.024}_{-0.012} \, , \tag{5.63}$$

which is in very good agreement with the theoretically calculated value of $\Gamma_1^p - \Gamma_1^n = 0.181 \pm 0.003$ [43] at the same Q^2 of 5 GeV^2. This result confirms the Bjorken sum rule to an accuracy of about 10 % (c.l. > 95 %).

Chapter 6

The ρ^0 Analysis

The main characteristic of the elastic ρ^0 production, $\mu p \to \mu' \rho^0 p'$, is that in the event, in addition to the scattered muon (Figure 2.1), there are only the two oppositely charged pion tracks coming from the $\rho^0 \to \pi^+\pi^-$ decay (B.R. $\sim$ 100 %). In order to fully reconstruct the exclusive process $\mu p \to \mu' \rho^0 p'$, all the tracks of the incoming and outgoing particles have to be reconstructed. In addition to the scattered muon μ', the recoiling nucleon and the two pions from the ρ^0 meson decay, there should be no other particles in the final state. The recoiling nucleon (or nucleus), however, is too slow and thus remains undetected in the SMC spectrometer. In the case of an *ideal* exclusive process, the kinematics of the event is fully constrained by the produced ρ^0 and by the incoming μ and the outgoing μ' tracks. Some particles produced with the ρ^0, however, do not enter the spectrometer acceptance and thus cannot be detected. For this reason, additional selection criteria are needed to remove the background arising from non-elastic processes.

6.1 The ρ^0 Sample

Event Selection

First, *good* μp scattering events have been selected on the basis of the scattered μ kinematics, which also defines the four-momentum and polarization of the virtual photon. The selection criteria applied are similar to the inclusive analysis

described in section 5.2:

a) $Q^2 > 0.01$ GeV^2;

b) muon scattering angle $\vartheta > 2$ mrad [1];

c) $y > 0.4$ so that the γ^* carries a large fraction of the incoming muon energy and to guarantee good acceptance for the ρ^0's;

d) $y < 0.9$ to reject large radiative events;

e) scattered muon momentum $p_{\mu'} > 19$ GeV/c ($p_{\mu'} > 10$ GeV/c for the 100 GeV beam) to assure good acceptance for the scattered μ in the trigger and in the muon section of the spectrometer, and to suppress muons coming from the decay of pions or kaons produced in the interaction;

f) incoming muon momentum p_μ between 170 GeV/c and 210 GeV/c (90 GeV/c < p_μ < 110 GeV/c for the 100 GeV beam);

g) muon interaction vertex within the target volume: the reconstructed primary vertex must lie within one of the two target halves, both longitudinally and radially;

h) good beam definition: the reconstructed incoming muon trajectories must pass through both target halves to ensure that both target halves see the same beam flux, so that the beam flux can be safely cancelled out when extracting the spin asymmetries.

Track Selection

Next, in order to isolate an elastic ρ^0 sample, three-track events have been selected requiring

i) only two hadron tracks of opposite charge fitted to the interaction vertex in addition to the scattered muon track;

[1] Selections **a)** and **b)** depend on the trigger type:
for T1 $Q^2 > 1.0$ GeV^2 and $\vartheta > 9$ mrad
for T2 and T14 $Q^2 > 0.2$ GeV^2 and $\vartheta > 2$ mrad
for T15 $Q^2 > 0.01$ GeV^2 and $\vartheta > 2$ mrad

j) minimum hadron momentum $p_{had} > 5$ GeV/c ($p_{had} > 3$ GeV/c for the 100 GeV beam) to assure good acceptance for the pions generated in the ρ^0 decay.

Each reconstructed hadron track has been assumed to be a pion, since there was no hadron identification in the spectrometer. The spectrometer, however, allowed the identification of electrons and muons (section 3.3.4). Electrons were removed with the help of the electromagnetic calorimeter. Muons were identified in the muon section of the spectrometer and, except for the scattered muon, were thus removed.

Interaction Vertex Determination

The primary interaction vertex is defined by the incident and the scattered muon tracks as the closest approach between the incoming muon (upstream of the target) and the scattered muon track (downstream of the target) reconstructed back to the target (section 4.1, Figures 4.2 and 4.3). Longitudinally, the vertex must be exactly within one of the two target halves and, radially, within 2.3 cm from the target axis, while the target holder had a radius of about 2.5 cm. Being a resonance, the ρ^0 decays where it has been produced. Therefore the two pions from the ρ^0 decay originate at the production vertex and can be fitted to the muon interaction vertex (vertex of Type 3). In this way the primary vertex, as well as all the track parameters, can be reconstructed with better precision. This vertex reconstruction procedure is especially relevant for small muon scattering angles, typically at low values of Q^2. The inclusion of the non-fitted tracks increases the amount of background without increasing appreciably the elastic ρ^0 sample. Therefore, only the fitted tracks have been used. In the following ρ^0 analysis, it has always been required that the two oppositely charged pion tracks have been fitted to the primary vertex.

Preliminary ρ^0 Sample

After all these selections, a *preliminary* ρ^0 sample has been obtained. Since the ρ^0 is a resonance, it can be shown only in the invariant mass distribution $m(\pi^+\pi^-)$. Figure 6.1 shows the invariant mass distribution $m(\pi^+\pi^-)$ with the event and

track selections discussed above [2]. The invariant mass $m(\pi^+\pi^-)$ is calculated using the 4-momentum vectors p_{π^+} and p_{π^-} of the two detected hadrons, assuming that they are pions:

$$m^2(\pi^+\pi^-) = (p_{\pi^+} + p_{\pi^-})^2 \,. \tag{6.1}$$

The ρ^0 peak is clearly visible in the invariant mass distribution, but it sits above a large continuum background, since also many non-exclusive events have passed these selections. This can happen if one ore more tracks are undetected in the event. As discussed in section 4.1, for $p_{had} < 5$ GeV/c most hadron tracks do not enter into the spectrometer acceptance and thus are not reconstructed. Also all neutral hadrons (i.e. neutrons and K^0's) and photons remain undetected, as well.

6.1.1 Isolation of the Exclusive Process

These relatively simple selections are not sufficient to isolate the exclusive process. In order to isolate a *pure* exclusive ρ^0 sample, additional selections on the final state kinematics are needed and have been implemented.

In the exclusive process, the produced ρ^0 takes essentially all of the virtual photon energy ν. This is true, in particular, at high energies, where the energy of the recoiling system is small with respect to the γ^* energy. Events with particles produced in addition to the two pions originating in the ρ^0 decay can then be excluded by demanding that the two pions take up all the energy lost by the muon in the interaction: [3]

$$E_\rho = E_{\pi^+} + E_{\pi^-} \simeq \nu \,. \tag{6.2}$$

Indeed conservation of energy gives:

$$E_\mu + E_{target} = E_{\mu'} + E_\rho + E_{target'} \tag{6.3}$$

and

$$E_\rho = \nu + \frac{\mid t \mid}{2M_p} \,. \tag{6.4}$$

[2]Where not indicated explicitly, all the plots are based on the 1995 data sample. For other data samples (years) similar plots have been obtained.

[3]For the notation and the definition of the variables see Table 2.1.

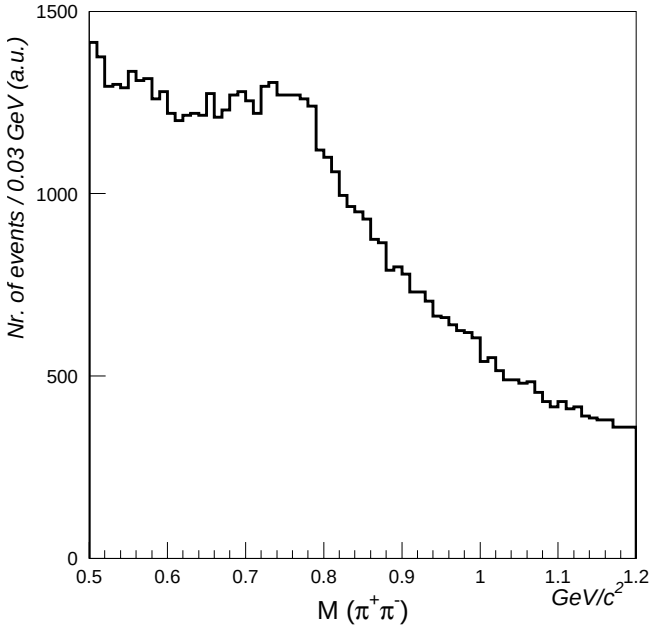

Figure 6.1: Invariant mass distribution $m(\pi^+\pi^-)$ after selections **a)** – **j)**.

The Mandelstam variable $t \equiv (p - p')^2$ is the 4-momentum squared transferred to the target. For the SMC kinematics the term $\frac{|t|}{2M_p}$, typically a fraction of a GeV, is negligible compared to the γ^* energy ν and $E_\rho \simeq \nu$. For an exclusive event, therefore, the energy fraction Z_{pair} of the pion pair

$$Z_{pair} \equiv \frac{E_{\pi^+} + E_{\pi^-}}{\nu} = \frac{E_\rho}{\nu} \quad \stackrel{exclusive}{\longrightarrow} \quad 1 \tag{6.5}$$

goes to 1 ($Z_{pair} \to 1$). The event is characterized as *exclusive* if $Z_{pair} = 1$. Figure 6.2 shows the Z_{pair} distribution after selections **a)** – **j)** in the ρ^0 mass window $0.62 < m(\pi^+\pi^-) < 1.07$ GeV/c^2. e^+e^- and K^+K^- pairs have also been rejected from this sample (cuts **m)** and **n)** introduced later).

The elastic peak is clearly visible around $Z_{pair} = 1$. The large tail extending to the left from the peak comes from the combinatorial background. The smearing of the elastic peak is due to the finite resolution in the reconstruction of the event, to secondary interactions, etc.

In principle, the cut $0.9 < Z_{pair} < 1.1$ is sufficiently good to remove most of the combinatorial background and to select the elastic process, as can be seen in Figure 6.6. For instance, the E665 experiment at Fermilab [71] used this method to select the elastic ρ^0 process.

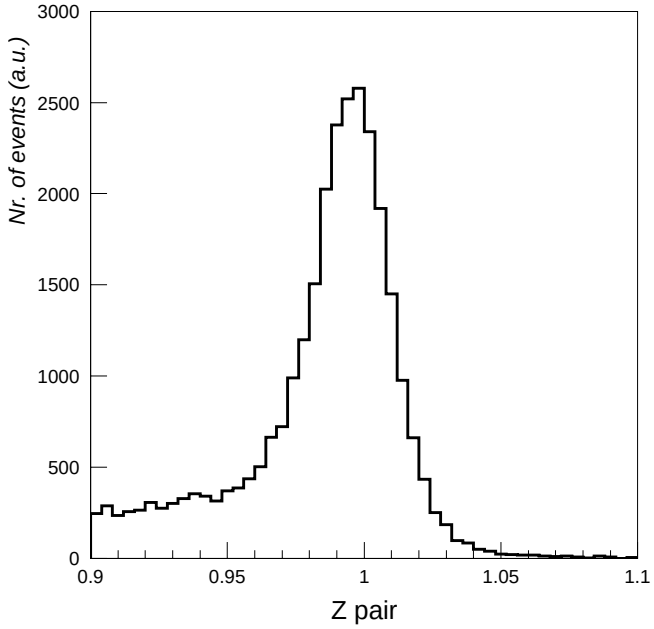

Figure 6.2: Z_{pair} distribution after selections. For this and the following 4 figures cuts **a)** – **j)** have been applied. The events have been selected in the ρ^0 mass window $0.62 < m(\pi^+\pi^-) < 1.07$ GeV/c^2. e^+e^- and K^+K^- pairs have also been rejected from this sample using cuts **m)** and **n)**.

Inelasticity

A detailed momentum – energy balance, which takes into account also the undetected recoiling system, is however much more preferable. For this purpose, the so-called inelasticity I, defined as

$$I = (M_X^2 - M_p^2)/W^2\,, \tag{6.6}$$

is used. It expresses the difference between the (calculated) missing invariant mass squared of the recoiling system M_X^2, and the invariant mass squared of the recoiling system M_p^2, assuming it is a proton, normalized to the total energy squared W^2 of the $\gamma^* - N$ system. M_X^2 is determined from the kinematics of the measured particles

$$M_X^2 = (p + q - v)^2\,, \tag{6.7}$$

where p, q and v are the 4-momenta of the target nuclon, the exchanged virtual photon and the produced ρ^0, respectively. By normalizing the momentum-energy

balance ($M_X^2 - M_p^2$) to W^2 ($W^2 \simeq 2M_p\nu$), an energy independent quantity is obtained, which can be interpreted as the energy fraction of the $\gamma^* - N$ system, which did not go into the elastic process $\gamma^* N \to \rho^0 N'$, i.e. the inelasticity. In the exclusive process, the unobserved recoiling system is indeed the target proton (or neutron) and $M_X = M_p$, which gives $I = 0$; while, for a non-elastic process, $M_X > M_p$ and $I > 0$.

Figure 6.3 shows the inelasticity distribution for the selected ρ^0 sample in the ρ^0 mass window $0.62 < m(\pi^+\pi^-) < 1.07$ GeV/c^2 after the suppression of the e^+e- and K^+K^- pairs. The peak centered around zero contains the elastic events above an inelastic background extending to the right. As can be seen, the elastic events are distributed symmetrically around $I = 0$, and the width of the elastic peak is essentially due to the measurement smearing:

- the momenta of the muon and of the pions are not measured exactly
- multiple scattering
- one or both pions can undergo secondary interactions, which change their 4-momenta.

The inelastic background starts at about $I = 0$ (the unphysical region $I < 0$ is not accessible except for the smearing of the measurement) and grows linearly with I. It is mainly due to the unobserved particles, such as slow hadrons, neutral hadrons and photons. Due to the finite resolution of the spectrometer, the unobserved particles cannot be resolved from the exclusive ρ^0 peak below and in the close vicinity of that peak.

The inelasticity distribution has been fitted with a gaussian, describing the elastic peak plus a straight line describing the background (Figure 6.3). The gaussian is peaked around zero, as expected, and its width $\delta I \simeq 0.014$ indicates the smearing of the measurement. The curve describing the background, when extrapolated below the elastic peak, points to zero at $I = 0$. This description, however, is not complete. The event abundance, on the right of the elastic peak, comes mainly from events where, in addition to the ρ^0, a relatively soft photon has been emitted by the incoming or scattered muon (radiative events). These radiative events contribute about 3 % to the exclusive process [127].

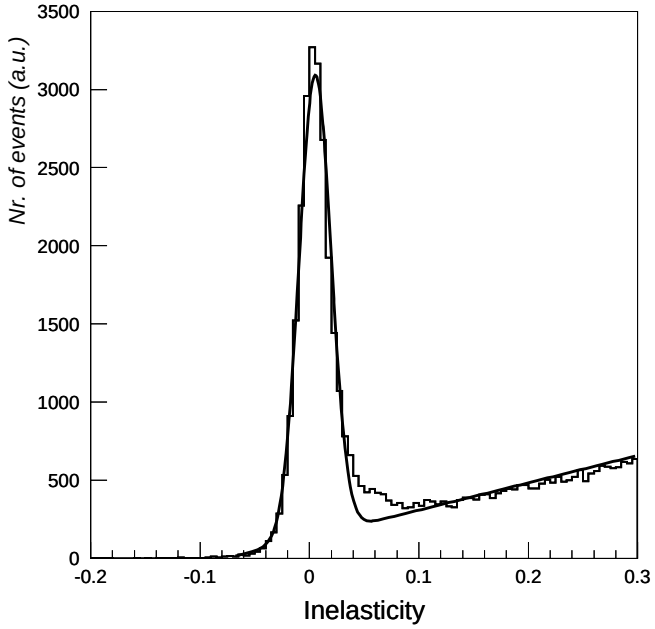

Figure 6.3: Inelasticity distribution after selections. The superimposed line represents a fit (gaussian + first order polynomial) to the inelasticity distribution. The excess of events for $0.05 < I < 0.1$ is mainly due to radiative events.

To select the elastic process, the following cut on the inelasticity has been imposed:

k) inelasticity cut: $-0.05 < I < 0.05$.

This inelasticity interval corresponds to about $\pm 3 \times \delta I$. The width of the selected inelasticity interval determines also the amount of background that enters in the elastic sample. A tighter cut could reduce this amount but would also reduce the number of elastic events, while a wider cut would not yield much more events but would introduce a larger background contamination. It turned out that $|I| < 0.05$ is a good compromise for maximizing the number of events, while keeping the background low. The inelasticity distribution obtained here (as well as the selected I interval) is about a factor two narrower compared to the one obtained by the NMC experiment [70] (NMC used $-0.1 < I < 0.08$). This is due mainly to the better track reconstruction in SMC compared to NMC. This also means that the amount of background in the SMC sample is smaller than in NMC in the same kinematical region.

Q^2 interval	deuteron (1995)		proton (1996)	
[GeV^2]	all p_T	$p_T > 0.09$ GeV^2	all p_T	$p_T > 0.09$ GeV^2
$0.01 - 0.2$	5.9 %	11.4 %	5.0 %	11.5 %
$0.2 - 0.6$	6.4 %	11.9 %	5.5 %	12.0 %
$0.6 - 1.0$	6.8 %	12.3 %	5.9 %	12.4 %
$1.0 - 2.0$	6.8 %	13.7 %	7.0 %	10.8 %
$2.0 - 4.0$	9.3 %	11.1 %	10.2 %	18.6 %
> 4.0	13.8 %	22.6 %	13.9 %	18.9 %

Table 6.1: Fraction of background (in %) in the elastic ρ^0 sample after all selections (cuts **a)** – **n)**).

For some parts of the analysis, as well as for cross checks, more restrictive background rejection cuts have been used. A background free sample, in principle, can be obtained for $I < 0$ at the price of loosing half of the events.

From fits like the one in Figure 6.3, the amount of the inelastic background has been estimated by extrapolating the line below the gaussian. The study of the amount of the background in the elastic region shows no significant nuclear dependence, a small Q^2 and W^2 dependence, and a slightly more pronounced dependence on the transverse momentum p_T^2 of the ρ^0. This p_T^2 dependence can be explained by a different behavior of the exclusive ρ^0 cross section off nuclei (section 7.1.1): at very low values of p_T^2 ($p_T^2 < 0.09$ GeV$^2/c^2$) the process is dominated by coherent scattering off different nuclei in the target with a very large cross section, while for larger values of p_T^2 ($p_T^2 > 0.09$ GeV$^2/c^2$) the process is essentially non-coherent with a much smaller cross section. The inelastic background, which also decreases exponentially with increasing p_T^2 (however with no change of the slope), does not exhibit such a peculiar behaviour and therefore the relative amount of the inelastic background for $p_T^2 < 0.09$ GeV$^2/c^2$ is smaller than for $p_T^2 > 0.09$ GeV$^2/c^2$. Table 6.1 summarizes the kinematical dependence of the fraction of the inelastic background in the selected exclusive ρ^0 sample.

The requirement on I is rather tight. It is not, however, sufficient to suppress inelastic contributions involving nucleon excitations due to the finite resolution of the measurement (the exclusive ρ^0 peak cannot be fully isolated).

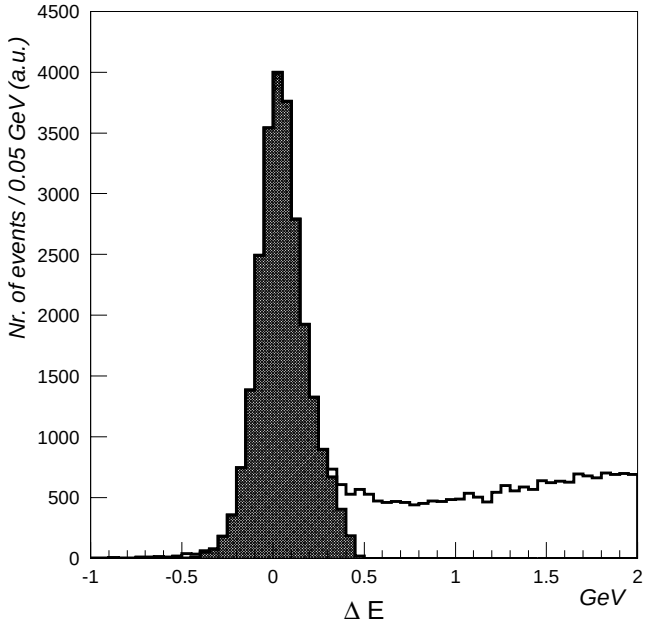

Figure 6.4: Missing energy ΔE distribution after selections. The shaded area shows the ΔE distribution restricted to $|I| < 0.05$.

Energy Balance

Other experiments use still another method [128]: they cut on the missing energy $\Delta E = (M_X^2 - M_p^2)/2M_p$. For large values of ν, $\Delta E \simeq I \cdot \nu$. Figure 6.4 shows the ΔE distribution for the selected event sample. As expected, the elastic peak is observed at $\Delta E = 0$ with the non-elastic background extending to the right of the peak ($\Delta E > 0$). The width of the ΔE distribution is about 140 MeV/c^2 (i.e. about the mass of the pion), which sets a limit on the selectivity of the elastic process that can be achieved. Basically, an event containing in addition to the ρ^0 a very slow pion will not be resolved from an elastic ρ^0 event. Although the momenta of each track are measured with a resolution of several GeV/c, the resolution on ΔE is not surprising, since the energy balance is basically performed in the transverse plane with respect to the virtual photon direction, where the transverse momenta are much smaller than the total momenta and therefore are measured much more precisely along with the corresponding angles.

The ΔE and I cuts are rather equivalent, as can be seen in Figure 6.4, where the shaded area represents the ΔE distribution restricted to the $|I| < 0.05$ interval. The cut $|\Delta E| < 0.5$ GeV corresponds roughly to the cut $|I| < 0.05$.

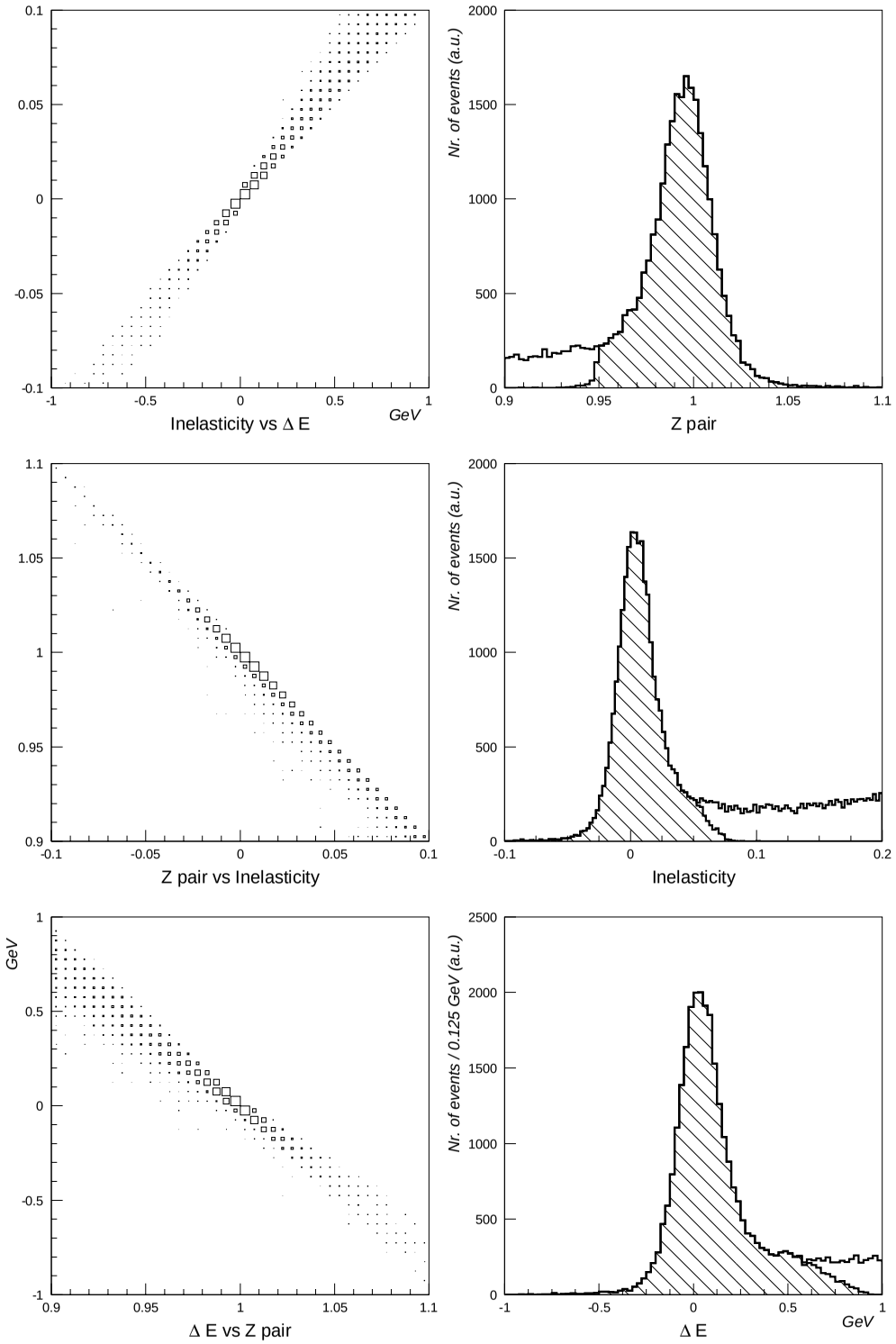

Figure 6.5: Comparison of various inelasticity cuts after selections. Left column: the three variables are plotted one against the others. Right column, from top: Z_{pair} distribution, also restricted to $|I| < 0.05$ (hatched area); inelasticisty distribution, also restricted to $|\Delta E| < 0.5$ GeV (hatched area); ΔE distribution, also restricted to $0.9 < Z_{pair} < 1.1$ (hatched area).

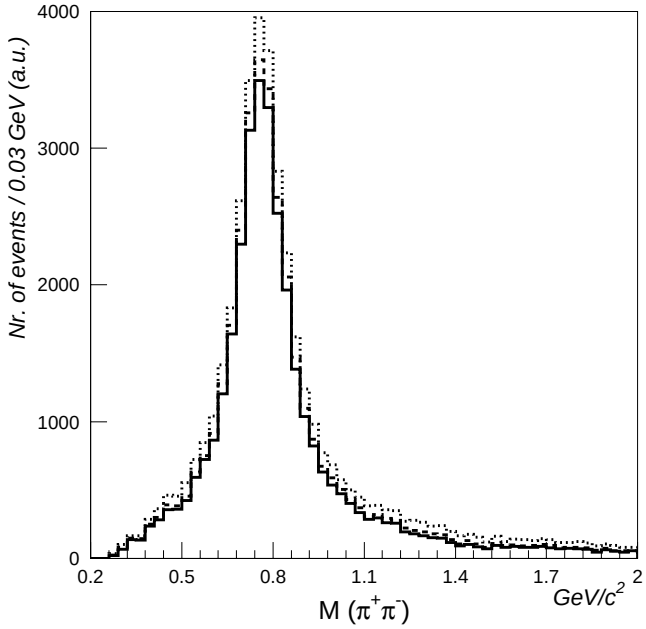

Figure 6.6: Invariant mass distributions $m(\pi^+\pi^-)$ for the three different inelasticity cuts after selections **a)** – **j)**: full line $|\Delta I| < 0.05$, dahsed line $|\Delta E| < 0.5$ GeV and dotted line $0.9 < Z_{pair} < 1.1$. Electron conversions and ϕ meson reflections have been already removed from this distribution.

Figures 6.5 and 6.6 compare the various inelasticity selections discussed above. As can be seen, all the three criteria discussed above, i.e. $0.9 < Z_{pair} < 1.1$, $|I| < 0.05$ and $|\Delta E| < 0.5$ GeV, are rather equivalent. The inelasticity cut (cut **k)**) has been preferred in this analysis, because it is an energy independent quantity and because it gives the strongest background rejection.

6.1.2 ρ^0 Mass Spectrum

Finally, events have been selected in the ρ^0 mass window:

l) ρ^0 mass window: $0.62\ \text{GeV}/c^2 < m(\pi^+\pi^-) < 1.07\ \text{GeV}/c^2$.

The selected ρ^0 mass window is asymmetric with respect to the ρ^0 resonance peak at 770 MeV/c^2 (see Figure 6.6); it extends to about 1 Γ to the left and to about 2 Γ to the right of the peak, where $\Gamma = 150$ MeV/c^2 is the width of the resonance. Different mass windows have also been considered.

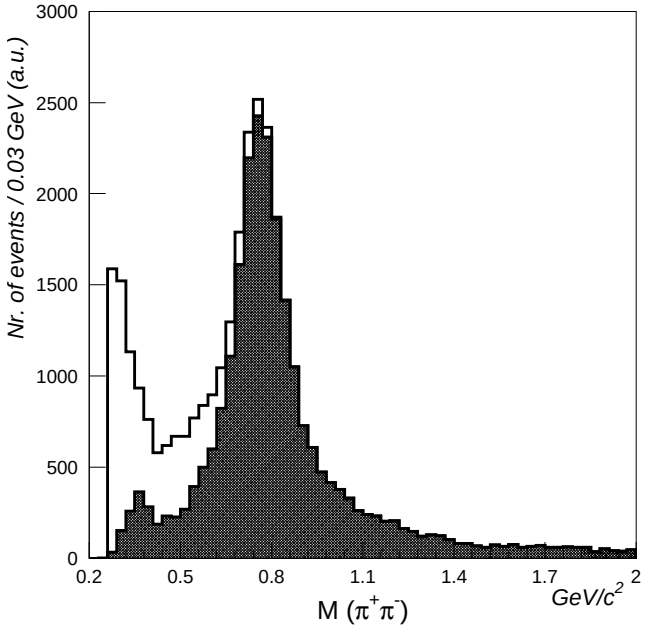

Figure 6.7: Invariant mass distributions $m(\pi^+\pi^-)$ after selections **a)** – **j)** including the inelasticity cut $|I| < 0.05$ (cut **k)**). The peak at about 0.3 GeV/c^2 is mainly due to the $\gamma \to e^+e^-$ conversions. The shaded area shows the $m(\pi^+\pi^-)$ distribution after the electron pair removal. The small bump in the distribution at about 0.4 GeV/c^2 is due to the $\phi \to K^+K^-$ meson reflections.

Figure 6.7 shows the invariant mass distribution $m(\pi^+\pi^-)$ after the inelasticity cut (cut **k)**). The ρ^0 resonance appears rather clean, except for the large peak on the left of the ρ^0 peak. The peak at about 0.3 GeV/c^2 is mainly due to the γ conversions ($\gamma \to e^+e^-$) and to the so-called ϕ meson reflections ($\phi \to K^+K^-$). Therefore, electron pairs from bremsstrahlung photons ($\gamma \to e^+e^-$ conversions) and kaon pairs from the ϕ meson reflections ($\phi \to K^+K^-$) have to be rejected from the sample. Note that the distribution starts at $2 \times m_\pi \sim 0.28$ GeV/c^2. These events are characterized by very small opening angles of the track pair.

Electron Removal

Radiative events with a γ converting into an e^+e^- pair ($\gamma \to e^+e^-$) can satisfy the above selections and still reproduce correctly the ρ^0 invariant mass, as well. They represent a background, which is not completely contained in the peak at

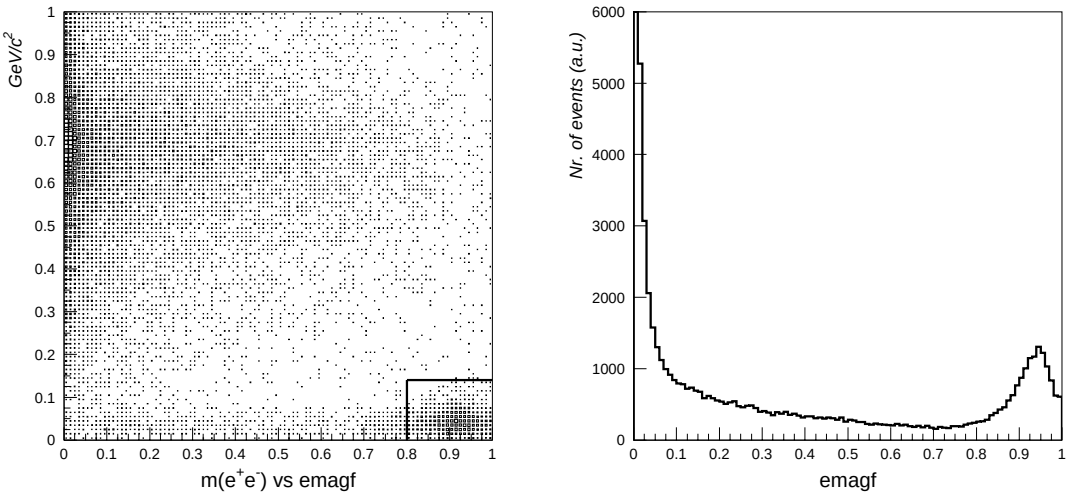

Figure 6.8: Left: $m(e^+e^-)$ distribution plotted against *emagf*. Events due to $\gamma \to e^+e^-$ conversions, are concentrated in the bottom right corner. The box indicates the exclusion region. Right: *emagf* distribution. The peak at *emagf* > 0.8 is due to electrons.

about 0.3 GeV/c^2 in the $m(\pi^+\pi^-)$ spectrum, but extends also into the ρ^0 mass window. Therefore they must be removed. Two different criteria based on

1. the H2 calorimeter
2. a cut on the $m^2(e^+e^-)$ invariant mass

have been combined and used to suppress the contamination of the ρ^0 sample from the electron pairs.

For each shower in the H2 calorimeter (section 3.3.4) associated with a selected track, the ratio

$$emagf = \frac{E_{em}}{E_{em} + E_{had}} \tag{6.8}$$

between the energy deposited in the electromagnetic part of H2 and the total energy deposited in the calorimeter was calculated. Figure 6.8 (right) shows the *emagf* distribution. The peak at *emagf* > 0.8 is generated by electrons, which deposit most of their energy in the electromagnetic part of the calorimeter.

For each selected event, the invariant mass $m(e^+e^-)$ was calculated by assigning to the 'hadron' tracks the electron mass. In Figure 6.8 $m(e^+e^-)$ is plotted against the *emagf* ratio. As can be seen, all the $\gamma \to e^+e^-$ conversions are concentrated at low values of the invariant mass $m(e^+e^-)$: $m^2(e^+e^-) < 0.02$ GeV$^2/c^4$.

This small value of $m(e^+e^-)$, as well as the fact that the γ conversions in the $m(\pi^+\pi^-)$ invariant mass distribution are concentrated at about 0.3 GeV/c^2, is due to the very small opening angle ϑ of the electron pair originating in the $\gamma \to e^+e^-$ conversion ($\vartheta \sim 1/\gamma$, in this expression γ is the Lorentz relativistic factor), to which corresponds a very small transverse momentum of the electrons with respect to the photon line of flight: in the case of a $\gamma \to e^+e^-$ conversion, the two pions masses adds and $m(\pi^+\pi^-) \sim 2m_\pi$.

To remove the electrons, a combination of both criteria has been imposed:

m) electron removal: the track was kept, if *emagf* < 0.8 for both tracks or $m^2(e^+e^-) > 0.02$ GeV$^2/c^4$ for each pair simultaneously, otherwise it was rejected.

The effect of the removal of the electron pairs on the $m(\pi^+\pi^-)$ invariant mass spectrum is shown in Figure 6.7 (dashed line). A detailed study of this cut has shown that the loss of good ρ^0 events is negligible and that the electron suppression efficiency is higher than 99 %. The background due to electron pairs is thus negligible.

ϕ Removal

As can be seen in Figure 6.9 (dashed line), there is still a smaller bump left centered around 0.4 GeV/c^2, which is due to the so-called $\phi \to K^+K^-$ meson reflections.

The ϕ meson reflection in the $m(\pi^+\pi^-)$ mass spectrum can be easily removed, thanks to the very narrow width of the ϕ resonance ($m_\phi = 1.020$ GeV/c^2, $\Gamma_\phi = 4.4$ MeV/c^2), by excluding events, which in the ϕ mass hypothesis (the hadron tracks are assumed to be kaons), reproduce correctly the invariant mass of the ϕ meson:

n) ϕ meson reflection removal: $1.010 \text{ GeV}/c^2 < m(K^+K^-) < 1.030 \text{ GeV}/c^2$.

Figure 6.9 (dotted line) shows also the $m(\pi^+\pi^-)$ spectrum after the ϕ reflection removal. As expected, the bump at $m(\pi^+\pi^-) \sim 0.4$ GeV/c^2 is substantially reduced and the spectrum above $m(\pi^+\pi^-) \sim 0.5$ GeV/c^2 is unaffected.

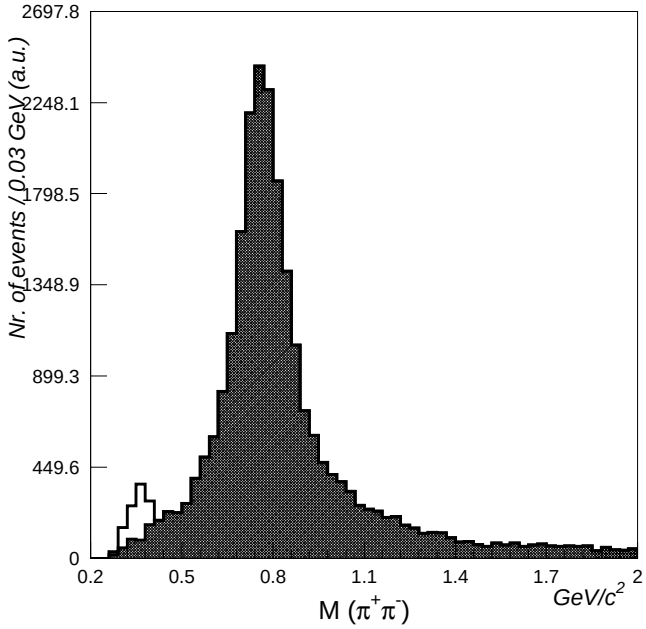

Figure 6.9: Invariant mass distributions $m(\pi^+\pi^-)$ after selections **a)** – **k)** and **m)**. The bump in the distribution at about 0.4 GeV/c^2 is due to the $\phi \to K^+K^-$ meson reflections. The shaded area shows the $m(\pi^+\pi^-)$ distribution after the removal of the ϕ reflection (cut **n)**).

6.1.3 The *final* ρ^0 Sample

Figure 6.10 shows the *final* $m(\pi^+\pi^-)$ invariant mass spectrum of the selected data sample with a clear and clean ρ^0 peak. The $m(\pi^+\pi^-)$ distribution has a long tail extending to the right of the peak ρ^0, which is not characteristic of a *pure* Breit-Wigner resonance line-shape [129]. This effect, as well as the various fits to the $m(\pi^+\pi^-)$ distribution, will be discussed in the next sections. All the selection criteria applied (cuts) are summarized in Table 6.2.

A Monte Carlo study of the exclusive ρ^0 production using the SMC apparatus, inclusive of the detector performance, has shown that the invariant mass distribution $m(\pi^+\pi^-)$ is not distorted by acceptance and reconstruction efficiency effects. This fact will allow to study the shape of the ρ^0 mass distribution without introducing acceptance and efficiency corrections.

The *final* ρ^0 sample consists of about $67,000$ ρ^0's produced on polarized proton (butanol and ammonia) targets and $47,000$ ρ^0's produced on polarized deuteron

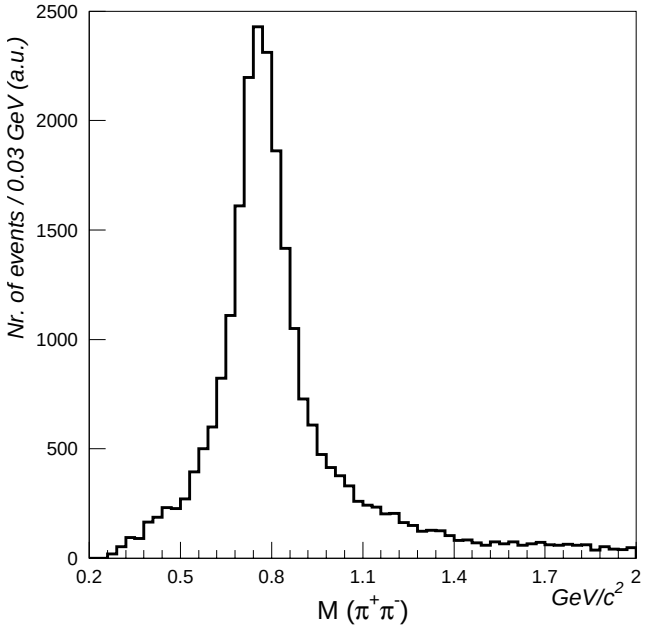

Figure 6.10: Final invariant mass distributions $m(\pi^+\pi^-)$ after all selections (cuts **a) – k)**, **m)**, **n)**).

(deuterated butanol) targets. For $p_T^2 > 0.09$ GeV$^2/c^4$, about $18,000$ ρ^0's on protons and about $13,000$ ρ^0's on deuterons are left. The final ρ^0 statistics is summarized in Table 6.3.

The kinematical region covered by this ρ^0 sample is shown in Figure 6.11 as a function of W, Q^2 and x, and is summarized here below:

- Q^2: $0.01 < Q^2 < 60$ GeV^2
- x: $5 \times 10^{-4} < x < 0.7$
- W^2: $140 < W^2 < 360$ GeV^2 .

The effect of the trigger acceptance on y, which propagates to W^2 through $W^2 \simeq 2M_p\nu = 2M_p y E_{beam}$, can be seen in Figure 6.11. This well justifies the cut $y > 0.4$, which given the beam energy of 190 GeV corresponds roughly to $W > 12$ GeV. In any case, events at low y have a bad depolarization factor and are thus not very interesting for the study of the spin-asymmetries. Also the shapes of the event distributions in the scattered plots are mainly due to the

trigger acceptance, while the kinematical bounds are set by the beam energy and the accepted γ^* energy interval (y interval).

	cut	description
a)	$Q^2 > 0.01$ GeV^2	minimum Q^2
b)	$\vartheta > 2$ mrad	min muon scattering angle
c)	$y > 0.4$	min γ^* energy fraction
d)	$y < 0.9$	max γ^* energy fraction
e)	$p_{\mu'} > 19$ GeV/c	min scattered μ momentum
f)	$170 < p_\mu < 210$ GeV/c	incoming μ momentum
g)		primary vertex within target volume
h)		good beam definition
i)		only 2 hadron tracks of opposite charge fitted to primary vertex
j)	$p_{had} > 5$ GeV/c	min hadron momentum
k)	$-0.05 < I < 0.05$	inelasticity cut
l)	$0.62 < m(\pi^+\pi^-) < 1.07$ GeV/c^2	ρ^0 mass window
m)	$m^2(e^+e^-) > 0.02$ GeV$^2/c^4$ *or* $emagf < 0.8$	electron removal
n)	$\lvert m(\pi^+\pi^-) - m_\phi \rvert > 10$ MeV/c^2	ϕ *reflection* removal

Table 6.2: List of all selection cuts used to isolate the elastic ρ^0 sample.

Year	Beam Energy [GeV]	Target Material	Polarization	Number of events ($\times 10^3$) all p_T^2	Number of events ($\times 10^3$) $p_T^2 > 0.09$ [GeV$^2/c^2$]
1992	100	Deut. Butanol: C_4D_9OD	0.2–0.4	5.8	1.6
1993	190	Butanol: C_4H_9OH	0.9	14.4	3.8
1994	190	Deut. Butanol: C_4D_9OD	0.5	14.4	3.9
1995	190	Deut. Butanol: C_4D_9OD	0.5	27.1	7.6
1996	190	Ammonia: NH_3	0.9	52.8	14.3
all				114.5	31.2

Table 6.3: The final ρ^0 sample statistics.

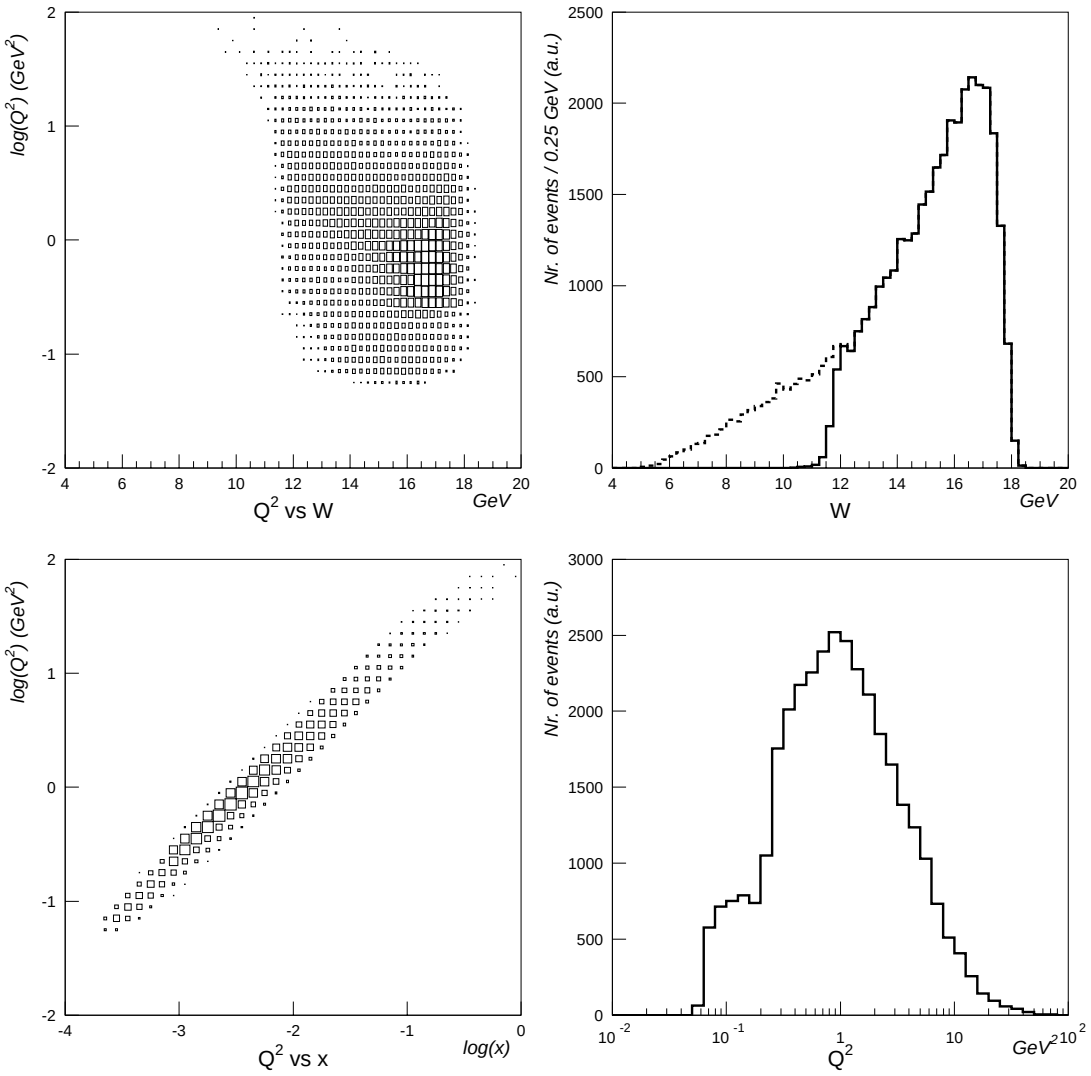

Figure 6.11: ρ^0 kinematics after all selections. Top: Q^2 vs. W and W distributions. The sharp cut in the left plot at $W \sim 12$ GeV is due to the $y > 0.4$ cut. For the dashed line of the W distribution on the right the cut on y, $y > 0.4$, has not been applied. Events with $W > 12$ GeV are not affected by the $y > 0.4$ cut. Bottom: Q^2 vs. x and Q^2 distributions. The apparently discontinous shape of the Q^2 distribution around 0.2 GeV^2 is due to the prescaling of T15 (see section 3.3.5) w.r.t. the other triggers.

6.2 The Shape of the Invariant Mass $m(\pi^+\pi^-)$

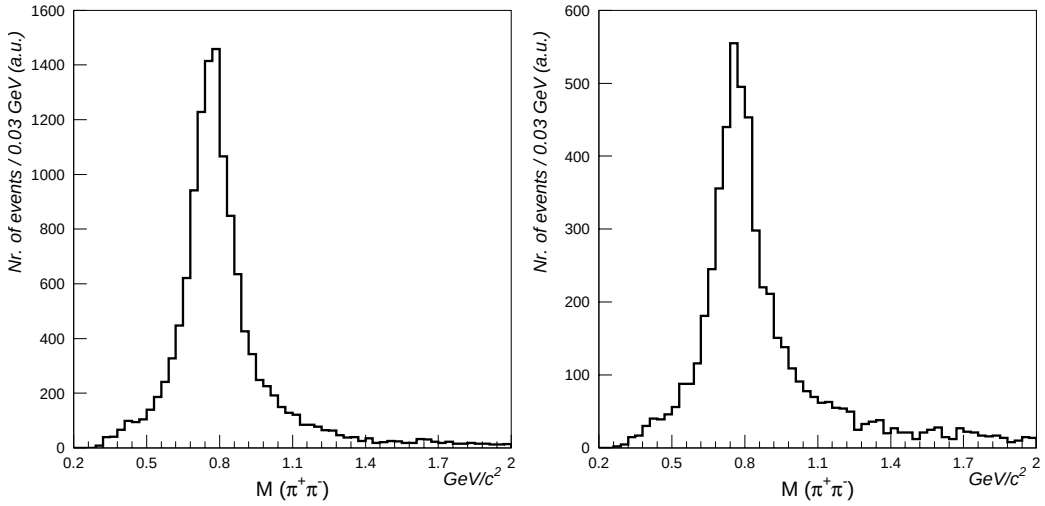

Figure 6.12: Invariant mass distributions $m(\pi^+\pi^-)$ after all selections, restricted to the inelasticity interval $-0.05 < I < 0$ for two separate p_T intervals: $p_T^2 < 0.09$ GeV$^2/c^2$ (left) and $p_T^2 > 0.09$ GeV$^2/c^2$ (right).

After having isolated the exclusive ρ^0 sample, it is important to verify that the characteristics of the reconstructed ρ^0 meson, like its mass and its width, reproduce the properties of the ρ^0 meson determined in other experiments [38]. Figure 6.12 shows the *final* invariant mass distribution $m(\pi^+\pi^-)$ for two separate p_T intervals: $p_T^2 < 0.09$ GeV$^2/c^2$ (coherent production) and $p_T^2 > 0.09$ GeV$^2/c^2$ (non-coherent production). The two distributions look quite similar. As discussed in the previous section, the invariant mass distribution $m(\pi^+\pi^-)$ is not affected visibly by acceptance and reconstruction efficiency effects. This allows to study $m(\pi^+\pi^-)$ without the introduction of these corrections.

For the analysis of the $m(\pi^+\pi^-)$ shape, data obtained on the deuteron (year 1995) and proton (year 1996) targets have been combined. The ρ^0's displayed in this section have been produced on targets consisting of a mixture of different nuclei: H, D, ^{3}He, ^{4}He, ^{12}C, ^{14}N and O.

To suppress almost completely the amount of the non-resonant and combinatorial background in the ρ^0 sample, the events have been selected in a tighter inelasticity interval,

$$-0.05 < I < 0 \ . \tag{6.9}$$

The statistics left is more than sufficient for the study of the shape of the invariant mass distribution $m(\pi^+\pi^-)$.

Breit-Wigner Line Shape

The simplest function describing the invariant mass distribution $m(\pi^+\pi^-)$ is the relativistic Breit-Wigner (BW) distribution for a spin-1 particle (p-wave) decaying into two spin-0 particles and it is given by [129]:

$$\frac{dN}{dm_{\pi\pi}} = \frac{m_{\pi\pi}\, m_\rho\, \Gamma(m_{\pi\pi})}{(m_{\pi\pi}^2 - m_\rho^2)^2 \,+\, m_\rho^2\, \Gamma^2(m_{\pi\pi})} \equiv BW_\rho(m_{\pi\pi})\,, \tag{6.10}$$

where $m_{\pi\pi}$ is the invariant mass of the pion pair, m_ρ is the invariant mass of the pion pair at the ρ^0 peak. The width $\Gamma(m_{\pi\pi})$ depends on the momentum of the two decay pions and is given by:

$$\Gamma(m_{\pi\pi}) = \Gamma_\rho \cdot \left(\frac{p^*}{p_0^*}\right)^3 \cdot \left(\frac{m_\rho}{m_{\pi\pi}}\right)\,. \tag{6.11}$$

$p^* = \sqrt{m_{\pi\pi}^2/4 - m_\pi^2}$ is the momentum of the pions in the $(\pi^+\pi^-)$ center of mass and $p_0^* = \sqrt{m_\rho^2/4 - m_\pi^2}$ is the same momentum for $m_{\pi\pi} = m_\rho$. Apart from a normalizaztion factor, m_ρ and Γ_ρ are the only free parameters of the BW distribution. The dependence on the width of the resonance on the momentum of the decay pions, $\Gamma = \Gamma(m_{\pi\pi})$ represents the main difference between the relativistic and the non relativistic BW distributions. The last multiplicative term in Equation 6.11, $\frac{m_\rho}{m_{\pi\pi}}$ can be interpreted as a spherical form factor of the distribution. In different parametrizations of Γ_ρ the $\frac{m_\rho}{m_{\pi\pi}}$ term has been replaced with a dipole type form factor $\frac{2}{1+(p^*/p_0^*)^2}$ [130]; otherwise it could be simply dropped.

Although the various sources of background have been carefully looked at and most of the non-resonant background has been removed, in particular with the tighter inelasticity cut $-0.05 < I < 0$, some background might still be present. For this reason, in the parametrization of the invariant mass distribution $m(\pi^+\pi^-)$ a function describing the background has been added to the BW distribution. The background has been described with a phase space function in terms of the two pion masses only with an exponential decrease at large values of $m_{\pi\pi}$:

$$f_{bg}\,(m_{\pi\pi} - 2m_\pi)^{a_1}\, \exp^{-a_2\, m_{\pi\pi}}\,, \tag{6.12}$$

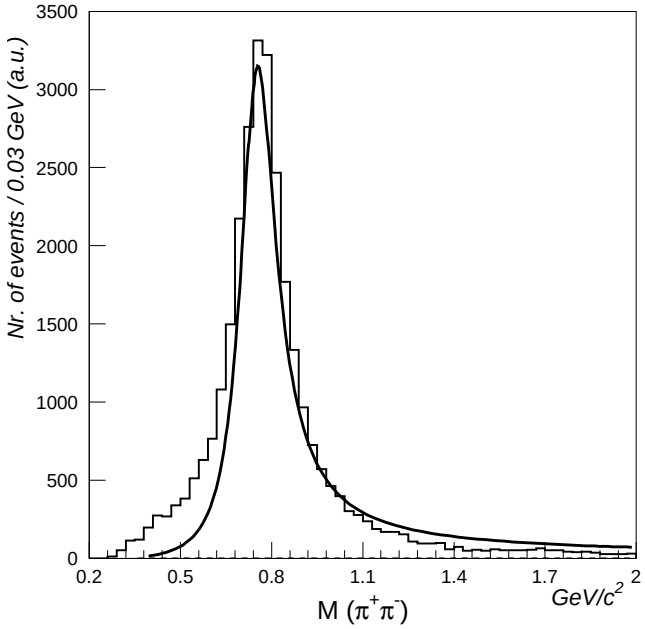

Figure 6.13: Invariant mass distributions $m(\pi^+\pi^-)$. The full line represents a fit to the distribution of a relativistic p-wave Breit-Wigner line shape with the superposition of a non resonant background.

where f_{bg}, a_1 and a_2 are three adjustable parameters with f_{bg} giving the background fraction.

Figure 6.13 shows the result of the fit to the invariant mass distributions $m(\pi^+\pi^-)$ of a relativistic p-wave BW distribution (Equation 6.10) with the superposition of a non resonant background (Equation 6.12):

$$\frac{dN}{dm_{\pi\pi}} = f_\rho \frac{m_{\pi\pi}\, m_\rho\, \Gamma(m_{\pi\pi})}{(m_{\pi\pi}^2 - m_\rho^2)^2 \,+\, m_\rho^2\, \Gamma^2(m_{\pi\pi})} \,+\, f_{bg}\,(m_{\pi\pi} - 2m_\pi)^{a_1}\, \exp^{-a_2\, m_{\pi\pi}} \quad . \tag{6.13}$$

The fit has been performed over the interval $0.4 < m(\pi^+\pi^-) < 2.0$ GeV/c^2. The $m(\pi^+\pi^-)$ distribution at the Q^2 values covered in this analysis, shows a distortion when compared to a relativistic BW function: an excess of events at low $m(\pi^+\pi^-)$ ($m(\pi^+\pi^-) \leq 0.77$ GeV/c^2) and a lack of events at high $m(\pi^+\pi^-)$ ($m(\pi^+\pi^-) \geq 0.77$ GeV/c^2) is observed; i.e. the $m(\pi^+\pi^-)$ distribution has a tail extending to the right of the ρ^0 peak, which is not characteristic of a *pure* Breit-Wigner resonance. This disagreement cannot be assigned simply to the background. This deformation of the $m(\pi^+\pi^-)$ distribution is a property of the

ρ^0 resonance and is referred to as *skewing*. The *skewing* of the ρ^0 mass distribution has been observed in the photo-production of ρ^0 mesons and in electro-production at low-medium Q^2, but it is not present at large values of Q^2 [131].

The ρ^0 invariant mass distribution, however, is well described by different phenomenological models, which have been proposed to account for the non-resonant background and the $\rho^0 - \omega$ interference. Non-resonant background is caused mainly by reactions which produce two oppositely charged pions without a vector meson being involved. The ω is a vector meson with the same quantum numbers as the ρ^0 (see section 2.5), similar mass ($m_\omega = 0.782$ GeV/c^2), which predominantly decays into $\pi^+\pi^-\pi^0$. About 2 % of ω's decay into $\pi^+\pi^-$ and interfere with the $\rho^0 \to \pi^+\pi^-$ decay amplitude resulting in the distortion of the ρ^0 line shape.

Ross-Stodolsky Model

In order to describe the distortion of the $m(\pi^+\pi^-)$ mass shape, **Ross and Stodolsky** have proposed the following parametrization [132]:

$$\frac{dN}{dm_{\pi\pi}} = f_\rho \, BW_\rho \cdot \left(\frac{m_\rho}{m_{\pi\pi}}\right)^n + f_{bg} \, (m_{\pi\pi} - 2m_\pi)^{a_1} \, e^{-a_2 m_{\pi\pi}} \, , \qquad (6.14)$$

where f_ρ and f_{bg} are normalization constants and the term $(\frac{m_\rho}{m_{\pi\pi}})^n$ accounts for the *skewing* of the ρ^0 mass distribution. n is called the skewing factor. It also represents an additional degree of freedom in the parametrization of the mass distribution. The second term represents the background superimposed to the elastic events, in which the virtual photon dissociates into an ensemble of particles among them only two charged particles of opposite charge are detected. The background parametrization is identical to the one adopted before, when describing the $m(\pi^+\pi^-)$ distribution with a BW function (Equation 6.12). f_{bg}, a_1 and a_2 are constants which have to be adjusted. Although this parametrization is not based on a dynamical model, it is suitable to describe the data.

Figure 6.14 shows the result of a fit to the $m(\pi^+\pi^-)$ distribution according to the Ross-Stodolsky model. The fit has been performed over the interval $0.4 < m(\pi^+\pi^-) < 1.6$ GeV/c^2. As can be seen, the agreement is much better compared to the BW fit shown in Figure 6.13. The value obtained for the mass of the

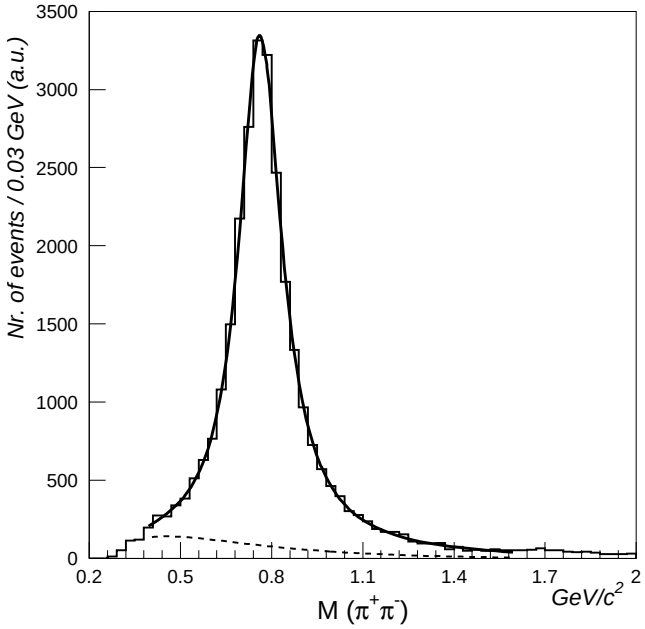

Figure 6.14: Ross-Stodolsky model fit to the invariant mass distributions $m(\pi^+\pi^-)$. The dashed line describes the non-resonant background.

resonance is $m_\rho = 780 \pm 2$ MeV/c^2, which is in fair agreement with the value reported by the Particle Data Group (PDG) [38] of $m_\rho = 769.3 \pm 0.8$ MeV/c^2. The width $\Gamma_\rho = 180 \pm 3$ MeV/c^2, instead, is quite larger compared to the PDG value of $\Gamma_\rho = 150.2 \pm 0.8$ MeV/c^2. The PDG values, however, refer to ρ^0's produced off a hydrogen target (i.e. protons), while in this experiment a target consisting of several different nuclei has been used and the ρ^0's have been produced off a mixture of different nuclei. Such a value for Γ_ρ has been already reported by the E665 experiment at Fermilab [133], which studied the exclusive ρ^0 production using a nitrogen target.

The broadening of the ρ^0 mass distribution might be attributed to nuclear effects, in which the ρ^0 is produced inside a nucleus and also decays inside the nucleus. Before emerging from the nucleus, the decay pions undergo multiple elastic scatterings with the nucleons inside the nucleus. As a result their momenta are smeared w.r.t. to the original directions leading to the broadening of the ρ^0 distribution, which corresponds to a larger value for Γ_ρ.

The value of the skewing factor, integrated over the whole Q^2 range is $n = 2.06 \pm 0.09$. The estimated contribution from the background (f_{bg}) is small,

corresponding to a few % of the events. If the background term f_{bg} is not included in the fit, the values obtained for m_ρ, Γ_ρ, and n are the same.

Söding Model

In addition to the resonant production of ρ^0 mesons **Söding** [134] also considers a non-resonant $\pi^+\pi^-$ production (known as the Drell-Hiida-Deck background), which occurs without involving the production of a ρ^0 vector meson (Figure 6.15).

In this model, the distortion of the invariant mass distribution $m(\pi^+\pi^-)$ is due to the interference between the resonant $\rho^0 \to \pi^+\pi^-$ and the non-resonant amplitude. Söding has proposed the following parametrization [134]:

$$\frac{dN}{dm_{\pi\pi}} = \left| \mathrm{A}\,\frac{\sqrt{m_{\pi\pi} m_\rho \Gamma(\pi\pi)}}{(m_{\pi\pi}^2 - m_\rho^2) + i m_\rho \Gamma_(\pi\pi)} + \mathrm{B} \right|^2 + \mathrm{C} + \mathrm{D}\, m_{\pi\pi}\ , \tag{6.15}$$

where B represents the real non-resonant background amplitude, which does not depend on $m_{\pi\pi}$. The two last terms (C and D) represent a common background, which could be also expressed with Equation 6.12.

After some algebra Equation 6.15 becomes

$$\frac{dN}{dm_{\pi\pi}} = f_\rho BW_\rho(m_{\pi\pi}) + f_I I(m_{\pi\pi}) + f_{NR}\,, \tag{6.16}$$

with

$$I(m_{\pi\pi}) = \frac{m_\rho^2 - m_{\pi\pi}^2}{(m_{\pi\pi}^2 - m_\rho^2)^2 + m_\rho^2 \Gamma^2(\pi\pi)} \tag{6.17}$$

showing explicitely the various contributions from the resonant BW (f_ρ), the interference (f_I), and the non-resonant background (f_{NR}). Because of the uncertainty on the phase between the resonant and non-resonant amplitudes, no

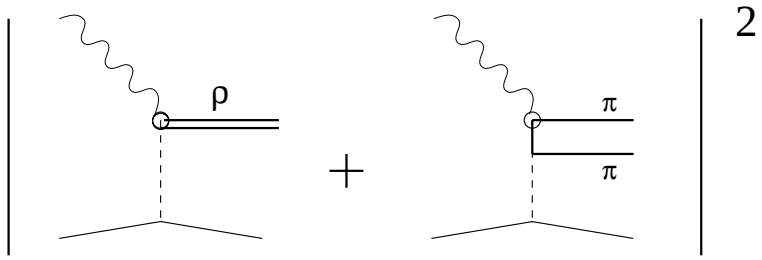

Figure 6.15: Resonant ρ^0 production: resonant pion ($\pi^+\pi^-$) pair (left) and non-resonant pion ($\pi^+\pi^-$) pair production (right).

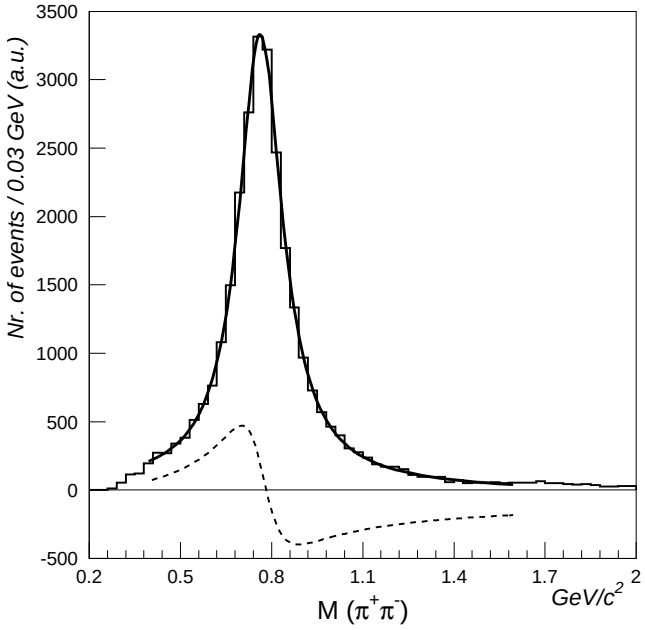

Figure 6.16: Söding model fit to the invariant mass distribution $m(\pi^+\pi^-)$; full line: all the components, dotted line: interference term between the resonant and non-resonant amplitudes.

constraints can be imposed on the relative normalization of the interference f_I and non-resonant f_{NR} terms. The ratio f_I/f_ρ can be interpreted as a deformation parameter.

In Figure 6.16 a fit to the invariant mass distribution $m(\pi^+\pi^-)$ is performed according to the Söding model (Equation 6.15). The fit has been performed over the interval $0.4 < m(\pi^+\pi^-) < 1.6$ GeV/c^2. As can be seen, the quality of this fit is similar to the Ross-Stodolsky model fit (Figure 6.14). The values obtained for m_ρ and Γ_ρ are similar and compatible with the previous fit, with $m_\rho = 781 \pm 2$ MeV/c^2 and $\Gamma_\rho = 182 \pm 3$ MeV/c^2. For the ratio f_I/f_ρ a value of 0.25 ± 0.05 has been obtained.

Chapter 7

Exclusive ρ^0 Spin-Asymmetries

In this chapter the cross section spin-asymmetries $A_{LL}^{lN\to\rho^0 l'N}$ for the exclusive lepto-production of the ρ^0 meson will be presented. Their kinematical dependence will be addressed in detail. The exclusive ρ^0 physics spin-asymmetries are extracted from the spin-sorted counting rates in a way similar to the inclusive ones. Data were taken with polarized proton (butanol and ammonia) and deuteron (deuterated butanol) targets.

The spin dependence of the exclusive ρ^0 production has been studied for the first time by the Spin Muon Collaboration over a broad Q^2 range from the photoproduction limit at very low Q^2 to the deep inelastic regime at medium-high Q^2. This measurement will add more insight into the ρ^0 production mechanism, as well as into its spin dependence. It might also allow to deduce some spin properties of the hadronic character of the photon at low Q^2. Given the energy of the polarized muon beam of 190 GeV, the cross section spin-asymmetries are determined around $\langle W\rangle \sim 15.5$ GeV, where at lower values of Q^2 the unpolarized cross section data are interpreted in terms of a *soft* Pomeron exchange. This study can also bring direct information on the spin dependence in diffractive processes.

7.1 Asymmetry Extraction

The exclusive ρ^0 events have been selected according to the criteria discussed in the previous chapter (Tables 6.2 and 6.3). The ρ^0 spin-asymmetries $A_{LL}^{lN\to\rho^0 l'N}$ are extracted from the spin-sorted counting rates in a way similar to the inclusive

ones. The asymmetry extraction method, discussed in section 5.1 for the inclusive analysis, also applies to the analysis of the ρ^0 data, and the asymmetry extraction proceeds in a similar way.

The cross section spin-asymmetry for the exclusive ρ^0 lepto-production $A_{LL}^{lN\to\rho^0 l'N}$, where both the beam and the target are longitudinally polarized, is given by:

$$A_{LL}^{lN\to\rho^0 l'N} = \frac{\Delta\sigma_{||}^{lN\to\rho^0 l'N}}{\overline{\sigma}^{lN\to\rho^0 l'N}} = \frac{\sigma^{\rightleftarrows} - \sigma^{\rightrightarrows}}{\sigma^{\rightleftarrows} + \sigma^{\rightrightarrows}} = \frac{-1}{fP_b\langle P_t\rangle}\frac{1}{2}\left[\left(\frac{N^{\rightleftarrows} - N^{\rightrightarrows}}{N^{\rightleftarrows} + N^{\rightrightarrows}}\right) - \left(\frac{N^{\rightleftarrows} - N^{\rightrightarrows}}{N^{\rightleftarrows} + N^{\rightrightarrows}}\right)'\right] . \tag{7.1}$$

In this expression N (N') is the number of reconstructed events before (after) the target polarization rotation. The indices $\rightleftarrows$ and $\rightrightarrows$ refer to the relative orientation of the muon and proton (or deuteron) spins. P_t and P_b are the target and beam polarizations, respectively. f is the dilution factor, which gives the fraction of polarized nucleons to the total nucleons in the target weighed by the corresponding exclusive cross sections. This expression for $A_{LL}^{lN\to\rho^0 l'N}$ is identical to Equation 5.13 for the inclusive A_{LL}.

In this analysis the number of events (Table 6.3) is typically a factor 10^3 smaller than in the case of the inclusive analysis with only few events selected per run. The data grouping of the events originating from the oppositely polarized target cells for different orientations of the target magnetic field, therefore, is more delicate than in the case of the inclusive analysis. With much less events per full or half configuration the asymmetries might become unstable and vary significantly from configuration to configuration. See section 5.1.2 for the definition of the various configurations. To prevent such fluctuations, more events per configuration are needed. This can be achieved by adding several runs together over periods of time of stable spectrometer operation, without loosing the intrinsic bias-cancelling properties of the inclusive analysis. For this reason, the exclusive ρ^0 spin-asymmetries have been extracted using the **sum** and the **persum** configurations, instead of the **full** or the **half** configurations.

As it has been the case for the inclusive analysis, f and P_b depend on the event kinematics. In order to take into account these variations, each event is weighed with its corresponding fP_b factor (see section 5.1.1) and Equation 7.1

can be rewritten as

$$A_{LL}^{lN\to\rho^0 l'N} = \frac{-1}{\langle P_t\rangle}\frac{1}{2}\left[\frac{\sum_u (fP_b)_u - \sum_d (fP_b)_d}{\sum_u (fP_b)_u + \sum_d (fP_b)_d} - \frac{\sum_u (fP_b)'_u - \sum_d (fP_b)'_d}{\sum_u (fP_b)'_u + \sum_d (fP_b)'_d}\right] , \quad (7.2)$$

where the sums run over the number of selected events for each target cell, gathered over several polarization reversals (sum and persum configurations), for the target magnetic field pointing in the direction of the incident beam (no $'$) and in the opposite direction ($'$). This expression for $A_{LL}^{lN\to\rho^0 l'N}$ is almost identical to Equation 5.16. In this case the longitudinal muon–nucleon cross section spin-asymmetries are extracted instead of the one-photon exchange spin-asymmetries and, therefore, the depolarization factor D does not enter in this expression.

7.1.1 Coherent and Non-Coherent ρ^0 Production

As already discussed, two different regimes compete in the case of the exclusive ρ^0 production off nuclei: the coherent and the non-coherent production. The coherent production dominates at low p_T, typically for $p_T < 300$ MeV/c [62].

In the case of coherent production the nucleus reacts as a whole and the ρ^0 scatters elastically off a uniform nuclear field generated by the various nucleons inside the nucleus. For larger values of p_T, the scattering is non-coherent, i.e. the ρ^0 scatters elastically off one of the various nucleons in the nucleus. Consequently the nucleus is excited to a higher mass state and decays, or breaks up immediately. The interacting nucleon, however, remains in its ground state.

The transition between the two regimes occurs around a p_T of 300 MeV/c ($p_T^2 \simeq 0.1$ GeV$^2/c^2$) for the light nuclei, like carbon or nitrogen. The p_T value for which this transition occurs, depends on the atomic number A: the larger the A, the smaller the p_T. This can be easily understood if a wavelength is associated to the 4-momentum transfer $t \simeq -p_T^2$. As long as this wavelength is bigger or comparable to the size of the nucleus, the various nucleons inside the nucleus cannot be resolved and the production is coherent. The two sets of ρ^0 events corresponding to these two regimes are treated separately.

Figure 7.1 shows the p_T^2 (i.e. $\sim -t$) distribution for the selected ρ^0's, uncorrected for acceptance and efficiency losses. The distribution is fitted with two exponential functions, $A\exp(-Bp_T^2)$, with different slopes for $p_T^2 < 0.09$ GeV$^2/c^2$

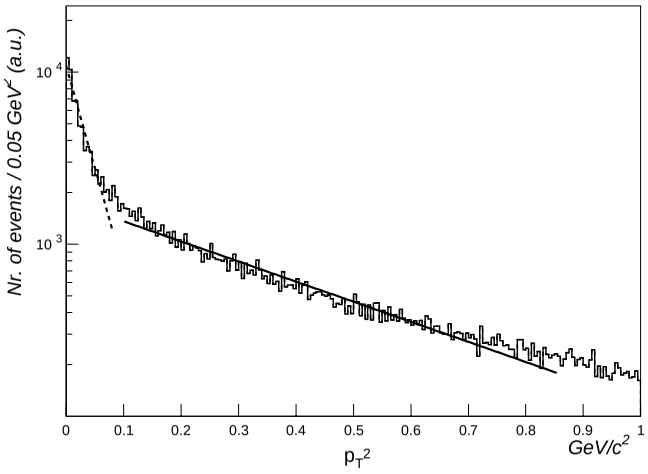

Figure 7.1: Exclusive ρ^0 transverse momentum p_T^2. Note the change of the slope of the distribution around $p_T^2 \simeq 0.1$ GeV$^2/c^2$, which indicates the transition from the coherent (dashed l.) to the non-coherent (full l.) production regime.

(dashed line) and $p_T^2 > 0.09$ GeV$^2/c^2$ (full line). For this qualitative discussion the uncorrected p_T^2 distribution describes sufficiently well the p_T^2 dependence of the exclusive ρ^0 cross section. At low p_T^2 the slope is much steeper than at large p_T^2. As it has been already pointed out in chapter 2, the slope can be related to the radius of the nucleus from which the ρ^0 scatters off elastically. The steeper slope at low p_T^2 indicates that the radius of the object from which the ρ^0 scatters off is larger than the radius of the nucleon (larger p_T^2). Indeed, at low p_T^2 the ρ^0 scatters elastically off the whole nucleus, while at larger p_T^2 th ρ^0 scatters (quasi-)elastically off the individual nucleons inside the nucleus.

7.1.2 The Dilution Factor for the Exclusive ρ^0 Production

The spin-asymmetry originates from scattering off polarized protons or deuterons in the target material and the ρ^0's produced off unpolarized nuclei represent a background, which leads to the dilution of the spin-asymmetry. This dilution effect is properly accounted for by the dilution factor f, which measures the ratio of polarizable nucleons to the total number of nucleons in the target material weighed by the corresponding cross sections:

$$f = \frac{n_{p,d}\,\sigma_{p,d}}{n_{p,d}\,\sigma_{p,d} + \sum_A (n_A \sigma_A)} \,. \tag{7.3}$$

n is the number of the various nuclei present in the target material and the σ_A's are the unpolarized cross sections for the exclusive ρ^0 lepto-production off these nuclei.

Since these cross sections depend on the event kinematics, and they might exhibit a different $A-$dependence as a function of Q^2, W^2 and p_T^2, the dilution factor will also depend on the event kinematics and $f = f(Q^2, W^2, p_T^2)$. In the W region covered by this experiment, the exclusive ρ^0 cross section varies very slowly with the energy W. Therefore it can be safely assumed that f does not depend on W. From the hadronic interactions it appears that there is no strong $A-$dependence for p_T^2, which suggests that also in lepto-production this could be the case, in particular at lower Q^2's, where the photon behaves as a hadron. On the other hand, as discussed above, two different production regimes compete at low and at high p_T^2. Therefore f will be treated for $p_T^2 < 0.09$ GeV$^2/c^2$ and $p_T^2 > 0.09$ GeV$^2/c^2$ differently. As Q^2 increases, the per-nucleon cross section $\sigma_A/A\sigma_p$ increases in both the coherent and non-coherent cases, indicating that a significant Q^2 dependence will remain in f.

Contrary to the inclusive cross sections, very few cross section data are available for the exclusive lepto-production of ρ^0 off nuclei. Most data come from the E665 [133] and NMC [70] experiments. Exclusive ρ^0 production off nuclei has been extensively studied in photo-production at low photon beam energies [56]. Figure 7.2 shows a compilation of all available cross section data in the kinematical range of this experiment as a function of Q^2 in the non-coherent region, i.e. for $p_T^2 > 0.1$ GeV$^2/c^2$. The data have been fitted with

$$\sigma_A(Q^2) = \sigma_p \cdot A^{\alpha(Q^2)} \tag{7.4}$$

with

$$\alpha(Q^2) = 1 - \frac{1}{3} e^{-Q^2/Q_0^2} , \tag{7.5}$$

which implies that for $Q^2 \to 0$, $\alpha = \frac{2}{3}$ (black disk limit) and that for $Q^2 \to \infty$, $\alpha \to 1$ (QCD limit) [135]. This fit gave $Q_0^2 = 9 \pm 3$ GeV^2. In the coherent region a similar fit gave $Q_0^2 = 1.8 \pm 0.8$ GeV^2. The contribution of non-coherent events for $p_T^2 < 0.1$ GeV^2 is almost negligible compared to the coherent events. The uncertainty on Q_0^2 and on the functional form adopted lead to a rather large

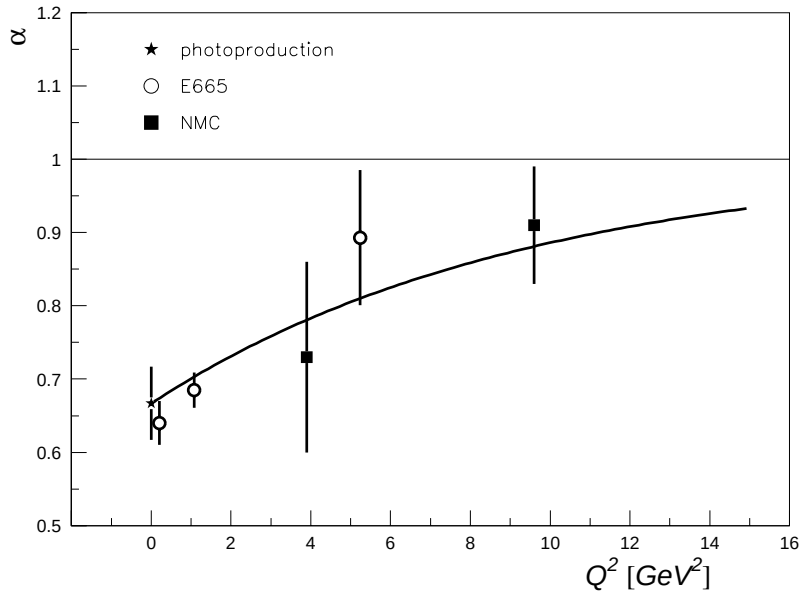

Figure 7.2: $A-$dependence of the exclusive ρ^0 cross sections off nuclei as a function of Q^2 in the non-coherent region of $p_T^2 > 0.1$ GeV^2. Plotted is the $\alpha(Q^2)$ parameter defined in Equation 7.4. The line is a fit to the data according to Equation 7.5. The data are from [133] (E665) and [70] (NMC).

error on the dilution factor f which propagates through to the $A_{LL}^{lN\to\rho^0 l'N}$ spin-asymmetry (section 7.3.2).

In the case of the exclusive ρ^0 production, there are no big contributions from the radiative events (see section 5.3), i.e. a ρ^0 accompanied by a γ emitted by the incident or scattered muon, since the kinematical constraints (inelasticity or ΔE cut) would not be satisfied if the ρ^0 is not carrying all the energy apparently lost by the interacting muon. The radiative contribution has been estimated to be less than 3 % of the total cross section in [127]. As it was discussed in the previous chapter, in the inelasticity plot (Figure 6.6) there is evidence for a 1 % to 2 % contamination of the elastic sample from these radiative events. This contribution can be further suppressed by tightening the inelasticity cut (cut **k**)). In any case, the fraction of radiative events in the selected ρ^0 sample is smaller than the fraction of non-exclusive background events. Given the statistical precision reachable with the present event sample, the corrections would be very small compared to the statistical uncertainties and to the other errors and can therefore be safely left out.

7.2 $A_{LL}^{lN\to\rho^0 l'N}$ Results

7.2.1 Q^2 Dependence

Figure 7.3 shows the exclusive ρ^0 lepto-production spin-asymmetries $A_{LL}^{lN\to\rho^0 l'N}$ for the proton and the deuteron as a function of Q^2 for all p_T's integrated over the whole W range ($\langle W\rangle \simeq 15.5$ GeV). In Figure 7.4 the same data are shown for $p_T^2 > 0.09$ GeV$^2/c^2$, in order to study these spin-asymmetries also in the non-coherent production regime. These $A_{LL}^{lN\to\rho^0 l'N}$ results are also summarized in Table 7.1, where both the statistical and the systematic errors are reported.

The spin-asymmetries for the proton and the deuteron can be combined under the assumption that the ρ^0 production in the W range of this experiment is dominated by the two gluon exchange process and that the gluons are polarized in the same way in the proton and in the deuteron. Indeed, given the Q^2 and W^2 ranges of this analysis, most events come from the low x region (Figure 6.11), where gluons dominate over quarks. If the production is dominated by the quark exchange process, which is the case at low W, then it would not be possible to combine the proton and the deuteron data by adding the two event samples as done in Figure 7.3.

The data show no significant spin dependence neither for the proton nor for the deuteron. Within the measurement errors, each data point is compatible with zero. The data points also fluctuate around zero, which indicates that even by adding several Q^2 bins to increase the statistics of few data points, the asymmetry results will still be compatible with zero.

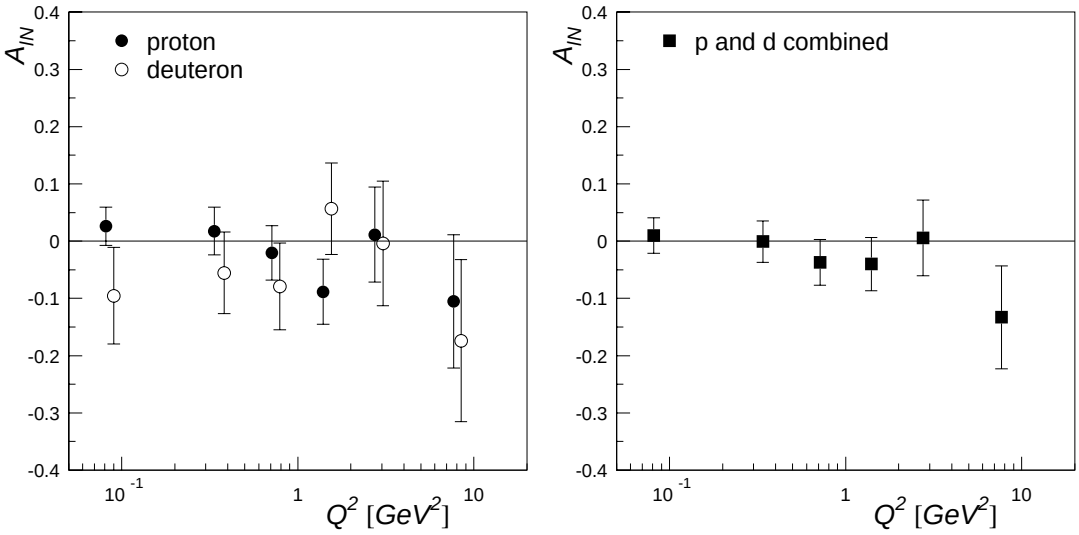

Figure 7.3: $A_{LL}^{lN\to\rho^0 l' N}$ for proton and deuteron as a function of Q^2. The displayed errors are statistical only.

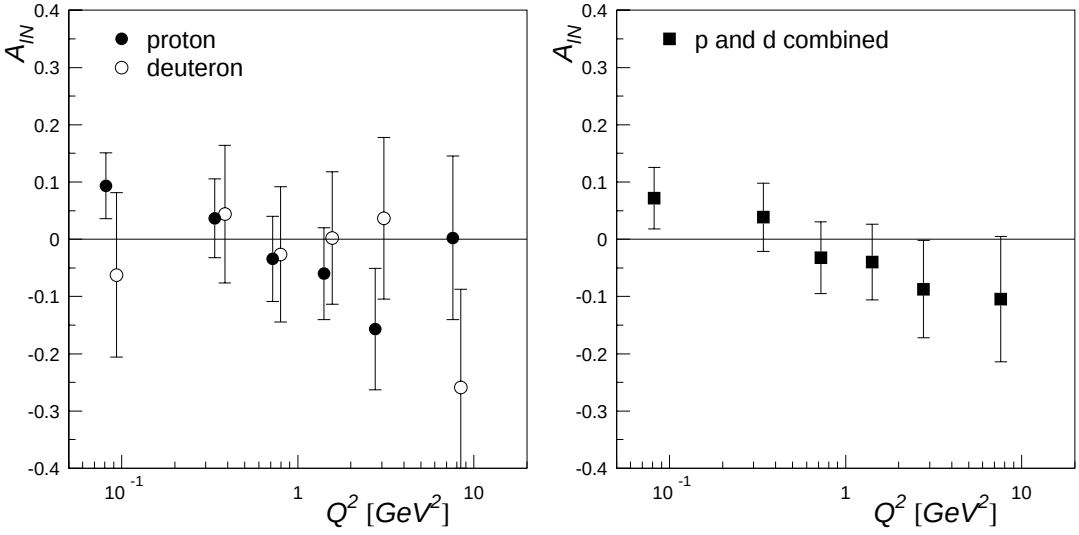

Figure 7.4: $A_{LL}^{lN\to\rho^0 l' N}$ for proton and deuteron as a function of Q^2 for $p_T^2 > 0.09$ GeV$^2/c^4$. The displayed errors are statistical only.

	Q^2 (GeV^2)	$\langle Q^2\rangle$ (GeV^2)	$\langle W^2\rangle$ (GeV^2)	$A_{LL}^{lN\to\rho^0 l' N}$ all p_T	$A_{LL}^{lN\to\rho^0 l' N}$ $p_T^2 > 0.09$ GeV$^2/c^2$
p	$0.01-0.2$	0.1	235	$0.026 \pm 0.033 \pm 0.005 \pm 0.037$	$0.093 \pm 0.056 \pm 0.014 \pm 0.039$
	$0.2-0.5$	0.3	241	$0.018 \pm 0.041 \pm 0.004 \pm 0.037$	$0.037 \pm 0.069 \pm 0.005 \pm 0.037$
	$0.5-1.0$	0.7	234	$-0.021 \pm 0.047 \pm 0.004 \pm 0.037$	$-0.035 \pm 0.074 \pm 0.005 \pm 0.037$
	$1.0-2.0$	1.4	218	$-0.089 \pm 0.057 \pm 0.018 \pm 0.037$	$-0.060 \pm 0.080 \pm 0.009 \pm 0.038$
	$2.0-4.0$	2.7	208	$0.011 \pm 0.083 \pm 0.002 \pm 0.037$	$-0.16 \pm 0.11 \pm 0.02 \pm 0.04$
	>4.0	7.7	201	$-0.11 \pm 0.12 \pm 0.02 \pm 0.04$	$0.0 \pm 0.14 \pm 0.0 \pm 0.04$
d	$0.01-0.2$	0.1	234	$-0.095 \pm 0.084 \pm 0.019 \pm 0.037$	$-0.06 \pm 0.14 \pm 0.01 \pm 0.04$
	$0.2-0.5$	0.3	259	$-0.055 \pm 0.071 \pm 0.011 \pm 0.037$	$0.04 \pm 0.12 \pm 0.01 \pm 0.04$
	$0.5-1.0$	0.7	248	$-0.079 \pm 0.076 \pm 0.016 \pm 0.037$	$-0.03 \pm 0.12 \pm 0.01 \pm 0.04$
	$1.0-2.0$	1.4	197	$0.057 \pm 0.080 \pm 0.011 \pm 0.037$	$0.0 \pm 0.11 \pm 0.0 \pm 0.04$
	$2.0-4.0$	2.8	183	$0.0 \pm 0.11 \pm 0.0 \pm 0.04$	$0.04 \pm 0.14 \pm 0.01 \pm 0.04$
	>4.0	7.7	189	$-0.17 \pm 0.14 \pm 0.03 \pm 0.04$	$-0.26 \pm 0.17 \pm 0.04 \pm 0.07$
p + d	$0.01-0.2$	0.1	235	$0.010 \pm 0.031 \pm 0.002 \pm 0.037$	$0.072 \pm 0.053 \pm 0.011 \pm 0.038$
	$0.2-0.5$	0.3	245	$0.001 \pm 0.036 \pm 0.0 \pm 0.037$	$0.038 \pm 0.060 \pm 0.006 \pm 0.037$
	$0.5-1.0$	0.7	238	$-0.037 \pm 0.040 \pm 0.007 \pm 0.037$	$-0.032 \pm 0.063 \pm 0.005 \pm 0.037$
	$1.0-2.0$	1.4	211	$-0.040 \pm 0.046 \pm 0.008 \pm 0.037$	$-0.040 \pm 0.066 \pm 0.006 \pm 0.037$
	$2.0-4.0$	2.7	198	$0.006 \pm 0.066 \pm 0.001 \pm 0.037$	$-0.087 \pm 0.085 \pm 0.013 \pm 0.039$
	>4.0	7.7	196	$-0.133 \pm 0.090 \pm 0.027 \pm 0.041$	$-0.10 \pm 0.11 \pm 0.02 \pm 0.04$

Table 7.1: $A_{LL}^{lN\to\rho^0 l' N}$ results for proton and deuteron as a function of Q^2 for all p_T's and $p_T^2 > 0.09$ GeV$^2/c^2$. The first error is statistical and the last two systematic. The first systematic error represents the scale uncertainty of the asymmetry result, while the second one the additive part of the systematic error, which is almost equal for all kinematical bins.

7.2.2 W^2 Dependence

Figures 7.5 and 7.6 show the $A_{LL}^{lN\to\rho^0 l' N}$ spin-asymmetries as a function of W^2 for two different p_T^2 intervals integrated over the whole Q^2 range. These $A_{LL}^{lN\to\rho^0 l' N}$ results are also summarized in Table 7.2 along with the corresponding statistical and systematic errors.

As discussed before in chapter 2, $x = \frac{Q^2}{2M_p\nu}$ is a property of the exchanged virtual photon γ^*, which is identified within the QPM with the momentum fraction of the proton carried by the struck parton. The QPM model, however, does not apply to the exclusive processes; the variable x, therefore, cannot be directly related to the interacting proton. The variable W^2 instead, which measures the energy of the final hadronic system, appears to be more directly connected to the interaction dynamics. The connection between Q^2, W^2 and x is straightforward: $x = \frac{Q^2}{Q^2 + W^2}$. Hence W^2 is used as the second independent kinematical variable to describe the virtual photon vertex instead of x.

The $A_{LL}^{lN\to\rho^0 l' N}$ spin-asymmetries have also been studied as a function of Q^2 and W^2 simultaneously. Figure 7.7 shows the $A_{LL}^{lN\to\rho^0 l' N}$ results for the proton and the deuteron as a function of Q^2 for two separate W intervals: $W > 15.5$ GeV and $W < 15.5$ GeV. In Figure 7.8 the same data are shown for $p_T^2 > 0.09$ GeV$^2/c^2$. Figure 7.9 shows the same asymmetries once the proton and the deuteron data have been combined.

Also in this case, when the $A_{LL}^{lN\to\rho^0 l' N}$ spin-asymmetries are plotted as a function of W^2 no appreciable spin-effects are observed. A mild trend is observed in Figure 7.5, where the spin-asymmetries increase from slightly negative values at lower W^2 to zero with increasing W^2.

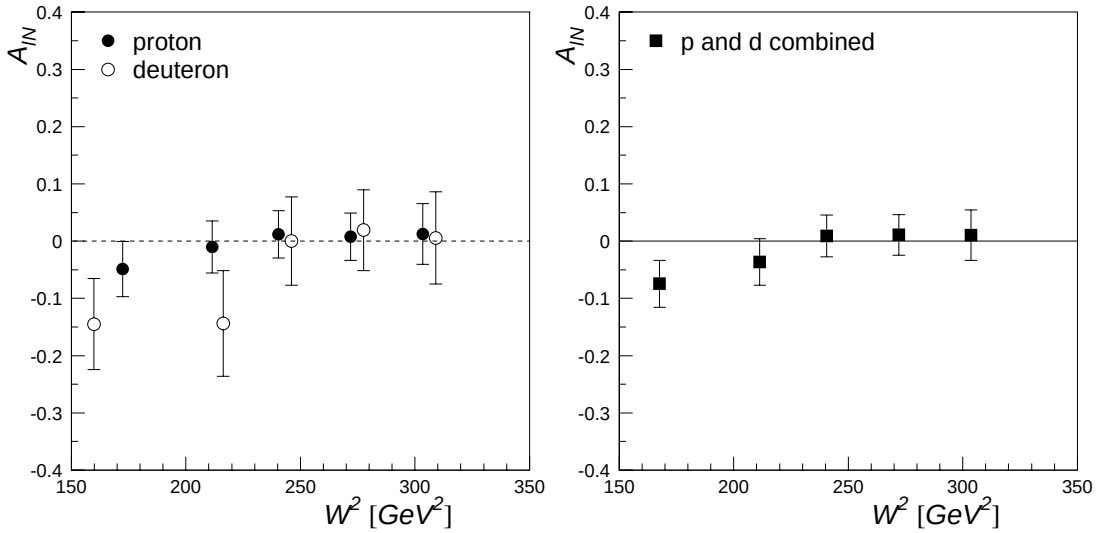

Figure 7.5: $A_{LL}^{lN\to\rho^0 l'N}$ for proton and deuteron as a function of W^2. The displayed errors are statistical only.

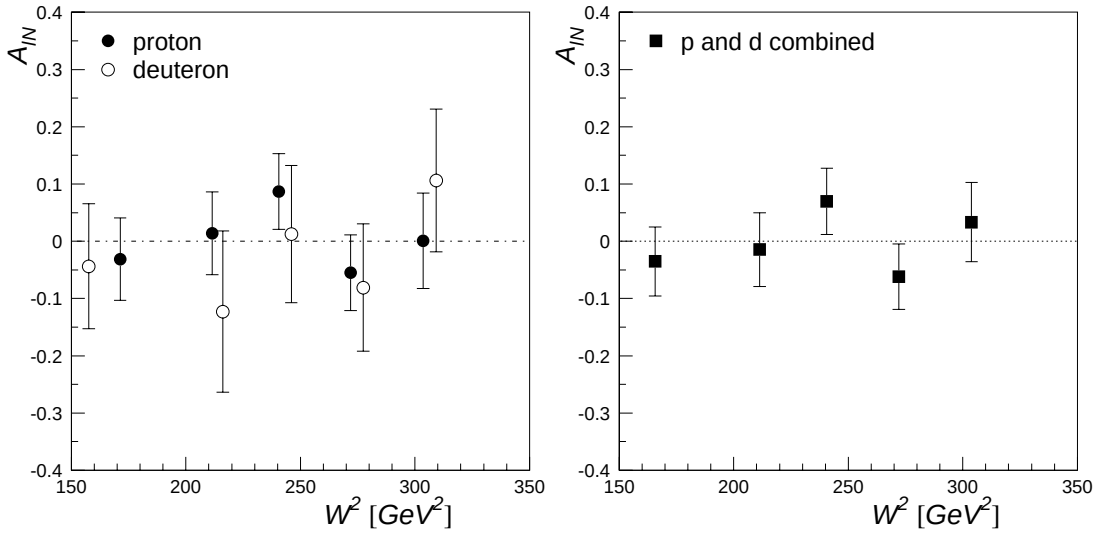

Figure 7.6: $A_{LL}^{lN\to\rho^0 l'N}$ for proton and deuteron as a function of W^2 for $p_T^2 > 0.09$ GeV$^2/c^2$. The displayed errors are statistical only.

	W (GeV)	$\langle W^2 \rangle$ (GeV^2)	$\langle Q^2 \rangle$ (GeV^2)	$A_{LL}^{lN \to \rho^0 l' N}$ all p_T	$p_T^2 > 0.09$ GeV$^2/c^2$
p	< 14	172	1.6	$-0.049 \pm 0.048 \pm 0.010 \pm 0.037$	$-0.031 \pm 0.072 \pm 0.005 \pm 0.037$
	$14-15$	211	0.7	$-0.010 \pm 0.045 \pm 0.002 \pm 0.037$	$0.014 \pm 0.072 \pm 0.002 \pm 0.037$
	$15-16$	240	0.6	$0.011 \pm 0.041 \pm 0.002 \pm 0.037$	$0.087 \pm 0.066 \pm 0.013 \pm 0.039$
	$16-17$	272	0.6	$0.008 \pm 0.041 \pm 0.002 \pm 0.037$	$-0.055 \pm 0.066 \pm 0.008 \pm 0.038$
	> 17	303	0.7	$0.012 \pm 0.053 \pm 0.002 \pm 0.037$	$0.001 \pm 0.083 \pm 0.0 \pm 0.037$
d	< 14	154	2.6	$-0.145 \pm 0.079 \pm 0.029 \pm 0.039$	$-0.04 \pm 0.11 \pm 0.01 \pm 0.04$
	$14-15$	211	1.3	$-0.144 \pm 0.092 \pm 0.029 \pm 0.039$	$-0.12 \pm 0.14 \pm 0.02 \pm 0.04$
	$15-16$	241	1.0	$0.0 \pm 0.077 \pm 0.0 \pm 0.037$	$0.01 \pm 0.12 \pm 0.01 \pm 0.04$
	$16-17$	272	0.9	$0.019 \pm 0.070 \pm 0.004 \pm 0.037$	$-0.08 \pm 0.11 \pm 0.01 \pm 0.04$
	> 17	304	0.9	$0.005 \pm 0.080 \pm 0.001 \pm 0.037$	$0.11 \pm 0.12 \pm 0.02 \pm 0.04$
$p+d$	< 14	168	1.8	$-0.074 \pm 0.041 \pm 0.015 \pm 0.038$	$-0.035 \pm 0.060 \pm 0.005 \pm 0.037$
	$14-15$	211	0.8	$-0.036 \pm 0.041 \pm 0.007 \pm 0.037$	$-0.015 \pm 0.064 \pm 0.002 \pm 0.037$
	$15-16$	241	0.7	$0.009 \pm 0.036 \pm 0.002 \pm 0.037$	$0.070 \pm 0.058 \pm 0.011 \pm 0.038$
	$16-17$	272	0.7	$0.011 \pm 0.036 \pm 0.002 \pm 0.037$	$-0.062 \pm 0.057 \pm 0.009 \pm 0.038$
	> 17	304	0.8	$0.010 \pm 0.044 \pm 0.002 \pm 0.037$	$0.033 \pm 0.069 \pm 0.005 \pm 0.037$

Table 7.2: $A_{LL}^{lN \to \rho^0 l' N}$ results for proton and deuteron as a function of W^2 for all p_T's and $p_T^2 > 0.09$ GeV$^2/c^2$. The first error is statistical and the last two systematic. The first systematic error represents the scale uncertainty of the asymmetry result, while the second one the additive part of the systematic error. The $\langle Q^2 \rangle$ of the deuteron data is slightly higher than the $\langle Q^2 \rangle$ of the proton data, because more data with the low-Q^2 triggers were taken with proton targets.

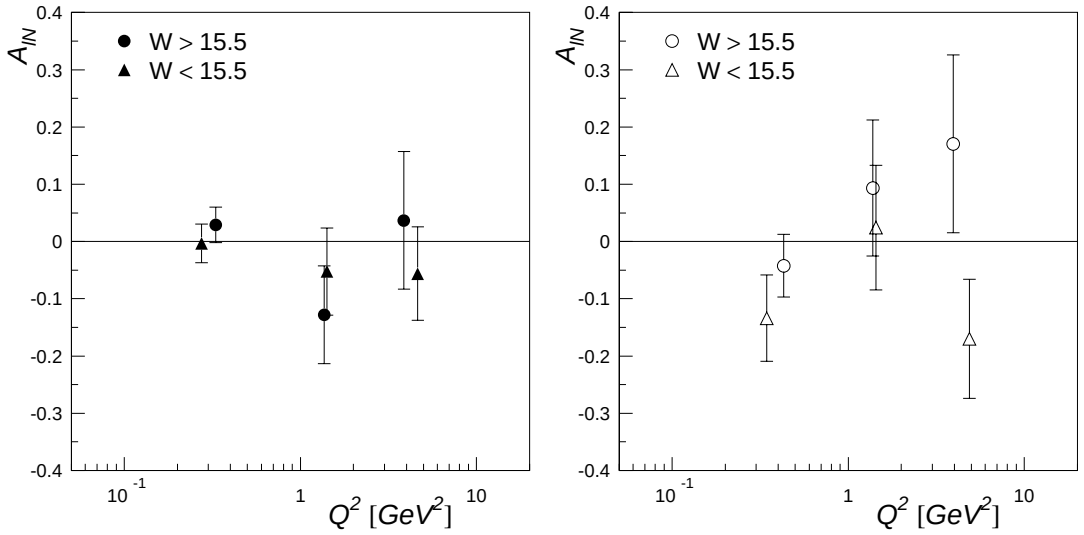

Figure 7.7: $A_{LL}^{lN\to\rho^0 l' N}$ for proton (left) and deuteron (right) as a function of Q^2 for two W^2 intervals ($W > 15.5$ GeV and $W < 15.5$ GeV). The displayed errors are statistical only.

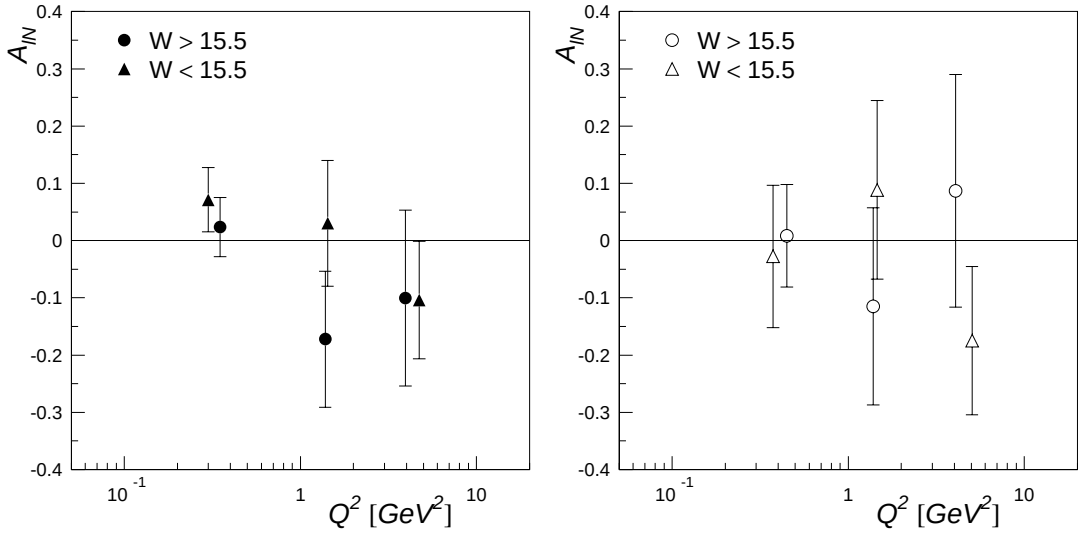

Figure 7.8: $A_{LL}^{lN\to\rho^0 l' N}$ for proton (left) and deuteron (right) as a function of Q^2 for two W^2 intervals ($W > 15.5$ GeV and $W < 15.5$ GeV) and $p_T^2 > 0.09$ GeV$^2/c^2$. The displayed errors are statistical only.

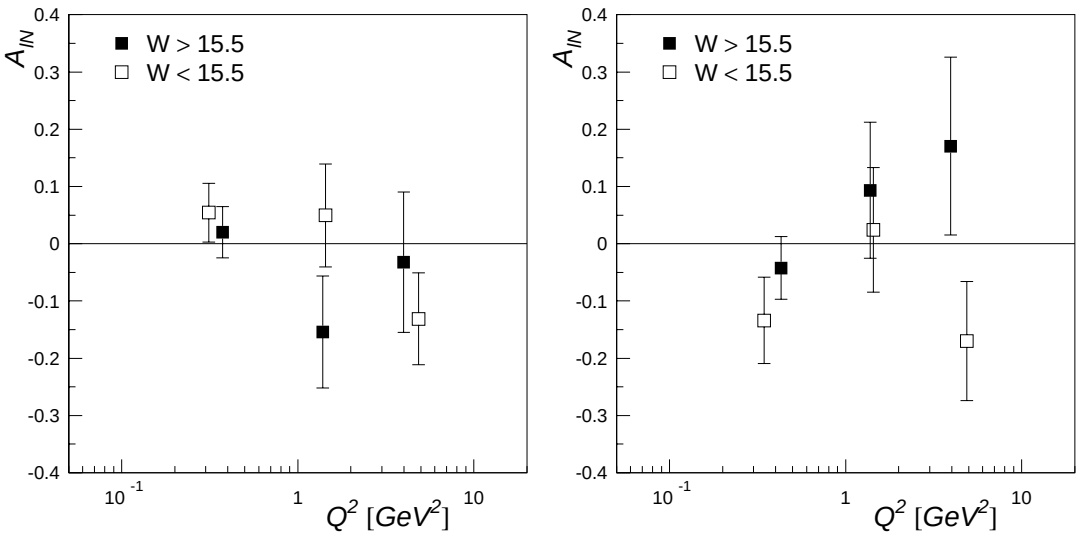

Figure 7.9: $A_{LL}^{lN\to\rho^0 l' N}$ for proton and deuteron combined as a function of Q^2 and W^2 ($W > 15.5$ GeV and $W < 15.5$ GeV) for all p_T's (left) and $p_T^2 > 0.09$ GeV$^2/c^2$ (right). The displayed errors are statistical only.

7.2.3 p_T^2 Dependence

The exclusive ρ^0 production depends also on the 4-momentum transfer t between the target nucleon and the recoiling nucleon in addition to Q^2 and W^2. The exclusive ρ^0 production muon–nucleon spin-asymmetries have also been studied as a function of $p_T^2 \simeq -t$. Figures 7.10, 7.11, and 7.12 show $A_{LL}^{lN\to\rho^0 l'N}$ as a function of Q^2 and its dependence on p_T^2 for the proton and the deuteron separately and combined.

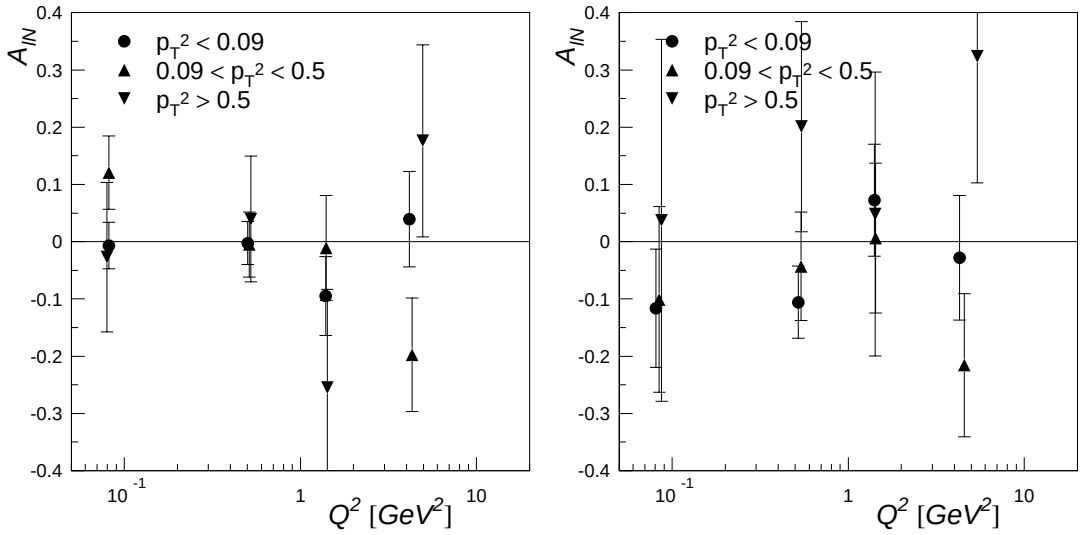

Figure 7.10: $A_{LL}^{lN\to\rho^0 l'N}$ as a function of Q^2 for three p_T^2 intervals of $p_T^2 < 0.09$, $0.09 < p_T^2 < 0.5$, and $p_T^2 < 0.5$ GeV$^2/c^2$ for proton (left) and deuteron (right). The displayed errors are statistical only.

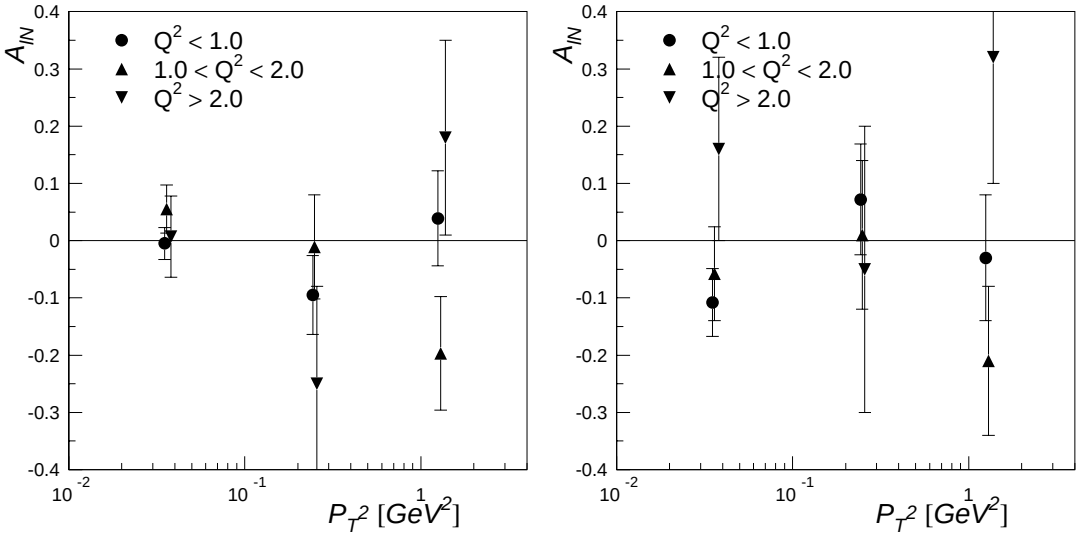

Figure 7.11: $A_{LL}^{lN\to\rho^0 l' N}$ as a function of p_T^2 for three Q^2 intervals for proton (left) and deuteron (right). The displayed errors are statistical only.

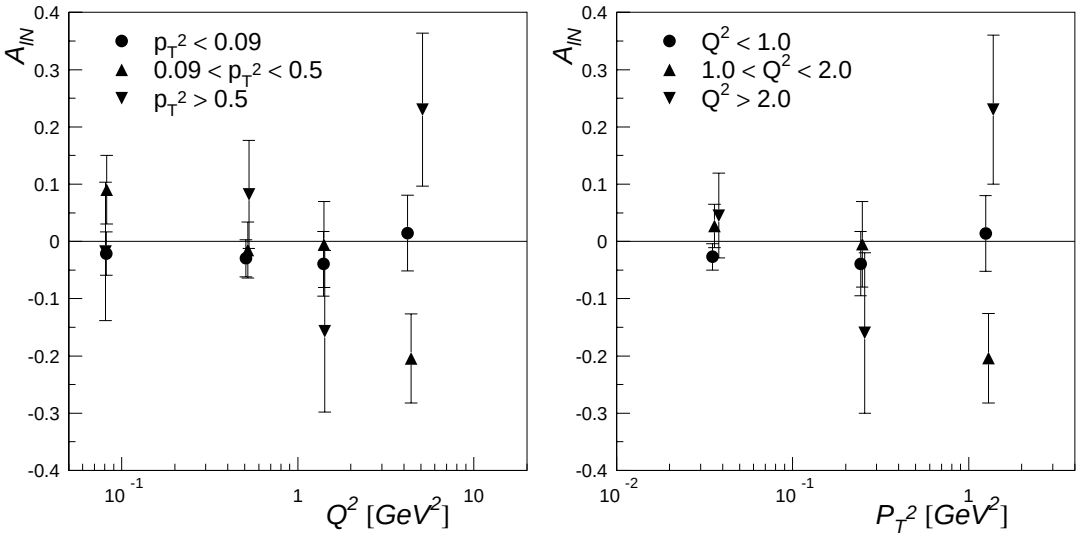

Figure 7.12: $A_{LL}^{lN\to\rho^0 l' N}$ for proton and deuteron combined as a function of Q^2 for three p_T^2 intervals (left) and as a function of p_T^2 for three Q^2 intervals (right). The displayed errors are statistical only.

7.2.4 $\cos\vartheta^*$ Dependence

The ρ^0 muon–nucleon production spin-asymmetries $A_{LL}^{lN\to\rho^0 l' N}$ have also been studied as a function of the polar angle ϑ of the decay π^+ in the ρ^0 c.m.s. For $|\cos\vartheta| < 0.5$ ($|\cos\vartheta| > 0.5$) the ρ^0's are predominantly transversely (longitudinally) polarized. Figure 7.13 shows $A_{LL}^{lN\to\rho^0 l' N}$ as a function of Q^2 for $|\cos\vartheta| > 0.5$ and $|\cos\vartheta| < 0.5$ for the proton and the deuteron separately. In Figures 7.14 the same data are shown for $p_T^2 > 0.09\ \mathrm{GeV}^2/c^2$. Figure 7.15 shows these asymmetries after the proton and the deuteron data have been combined.

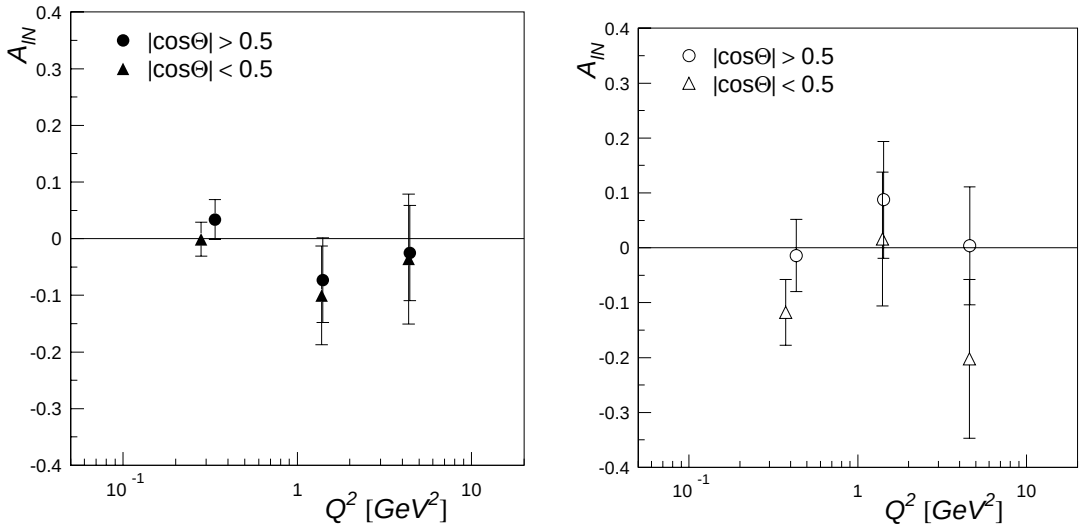

Figure 7.13: $A_{LL}^{lN\to\rho^0 l' N}$ for $|\cos\vartheta| > 0.5$ and $|\cos\vartheta| < 0.5$ for proton (left) and deuteron (right). The displayed errors are statistical only.

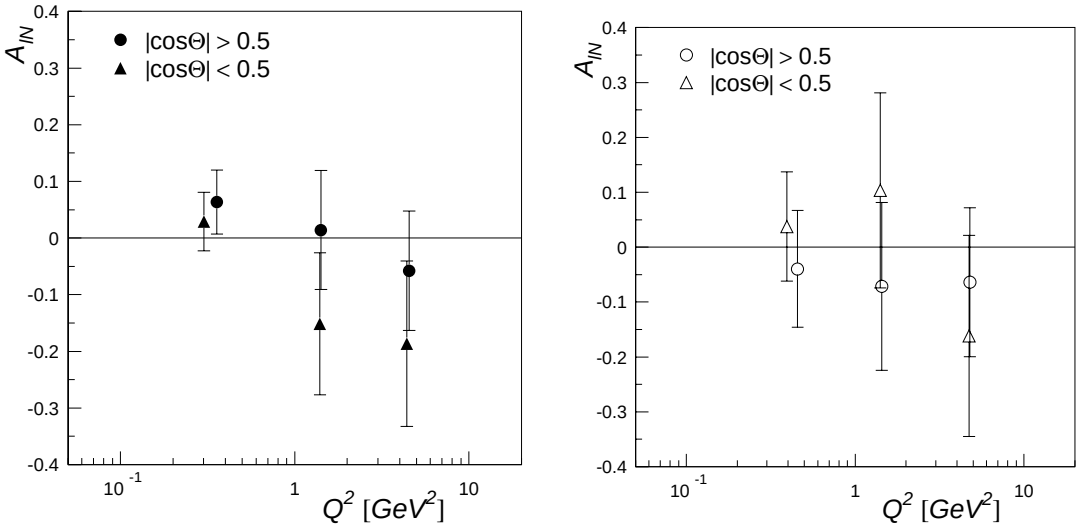

Figure 7.14: $A_{LL}^{lN\to\rho^0 l' N}$ for $|\cos\vartheta| > 0.5$ and $|\cos\vartheta| < 0.5$ for proton (left) and deuteron (right) for $p_T^2 > 0.09$ GeV$^2/c^2$. The displayed errors are statistical only.

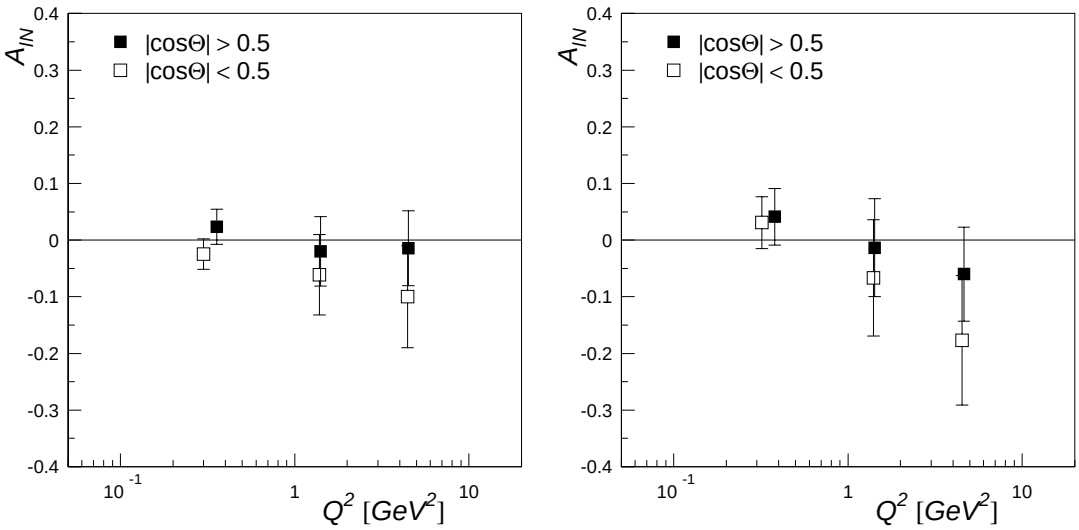

Figure 7.15: $A_{LL}^{lN\to\rho^0 l' N}$ for proton and deuteron combined for all p_T's (left) and $p_T^2 > 0.09$ GeV$^2/c^2$ (right). The displayed errors are statistical only.

7.3 Systematic Studies

7.3.1 Consistency Checks

A number of consistency checks has been performed in order to verify that no unwanted effects have been introduced in the $A_{LL}^{lN\to\rho^0 l'N}$ spin-asymmetry results presented in the previous section. These studies include the time stability of the asymmetries, the selection criteria of the ρ^0 sample, the false asymmetries, etc.

Figure 7.16 shows the $A_{LL}^{lN\to\rho^0 l'N}$ asymmetry, evaluated period by period, as a function of Q^2 for the 1995 deuteron data. As it can be observed, the data for each Q^2 bin are consistent among themselves and the differences can be attributed to statistical fluctuations. This result supports the conclusion, that there are no time dependences in the asymmetry results. Similar plots have been also obtained as a function of different kinematical variables and for the other years of data taking. In all cases the data divided period by period are statistically consistent among themselves.

To study the stability of the asymmetry results under the selection criteria of the ρ^0 sample, different selections for the ρ^0 have been compared, among which:

- different inelasticity intervals;
- addition of the so-called close tracks;
- different mass intervals;
- vertex of Type 3 and vertex of Type 1.

As illustrated in Figure 7.17 for some of the tests, for the proton and the deuteron data separately, the results are compatible between themselves and the differences are typically much smaller than the statistical errors. This supports the fact that the asymmetry results are almost insensitive to the selection criteria adopted and that they are stable in the selected intervals.

As another check of systematic effects, the false asymmetries, which by construction should lead to asymmetries consistent with zero, have been computed accordingly to the same procedure as for the inclusive data. For the details on the definition and evaluation of the false asymmetries see section 5.1.3. As can

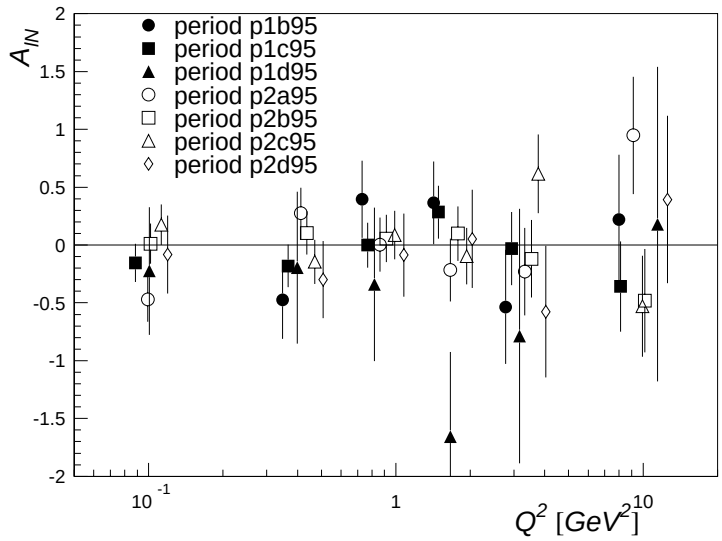

Figure 7.16: $A_{LL}^{lN\to\rho^0 l' N}$, period by period, as a function of Q^2 for the 1995 deuteron data. The errors are statistical only.

be seen in Figure 7.18 the false asymmetries are indeed compatible with zero (in this plot the asymmetry scale has been expanded by a factor of 10 compared to the other asymmetry plots).

Another source of concern is the level of inelastic background in the exclusive ρ^0 sample (see Table 6.3). Figure 7.19 shows $A_{LL}^{lN\to\rho^0 l' N}$ in the inelasticity interval of $0.05 < I < 0.20$ as a function of Q^2. This inelasticity region, on the right of the elastic peak, contains mainly non-elastic events, in which a slow, non detected particle has been produced in addition to the ρ^0. As can be observed in Figure 7.19, the asymmetries are consistent with zero within the statistical precision, supporting the assumption that the background events have no spin dependence.

7.3.2 Systematic Uncertainties

The two main sources of systematic uncertainties are:

1. the fraction of non-elastic background events in the exclusive ρ^0 sample: it is about 5 % at low Q^2 and increases with Q^2 up to about 10 % (see Table 6.1);

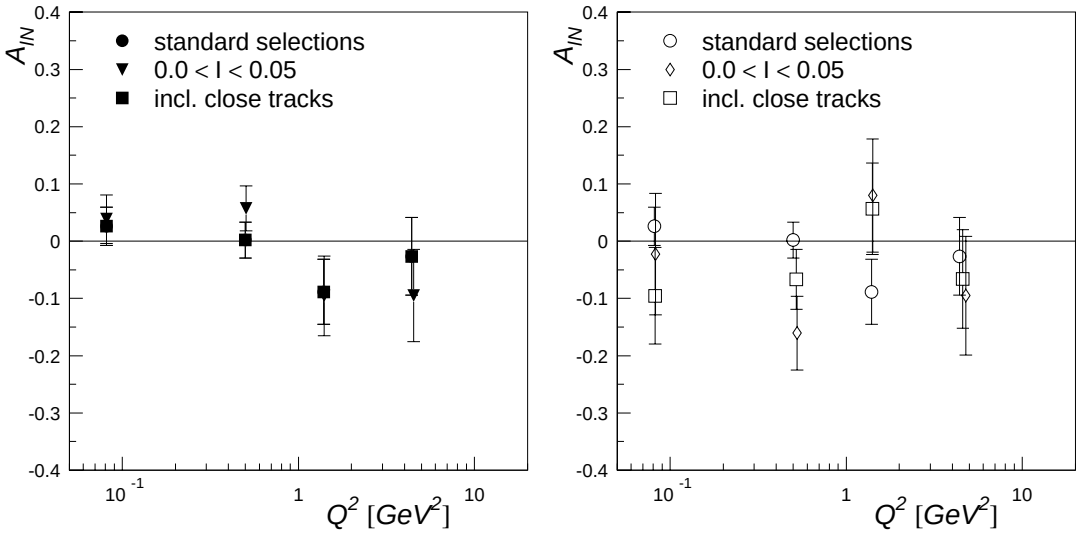

Figure 7.17: $A_{LL}^{lN\to\rho^0 l' N}$ for different ρ^0 selections: standard selections, different I intervals, addition of the close tracks for proton (left) and deuteron (right). The errors are statistical only.

2. the uncertainty on the dilution factor coming from the poor knowledge of the A-dependence of the cross section $\sigma_A(Q^2, p_T^2)$.

The other major sources of systematic errors are:

- beam polarization;
- target polarization;
- false asymmetries;
- selection criteria.

The systematic uncertainties can be grouped into two classes: scale erros and additive errors. The scale errors are multiplicative quantities, which change the scale of the asymmetry but not its *significance*: if σ is the statistical error on the asymmetry A, then the ratio $\frac{A}{\sigma}$ (i.e. significance) will not be affected by a change of the scale. This is of particular relevance, for instance when searching for non-zero spin effects, like in the case of the exclusive ρ^0 production, or when simply trying to assess the sign of the spin-asymmetry. The uncertainties on the dilution factor, the beam polarization and the target polarization belong to the class of scale errors. These two classes of errors will be kept separated.

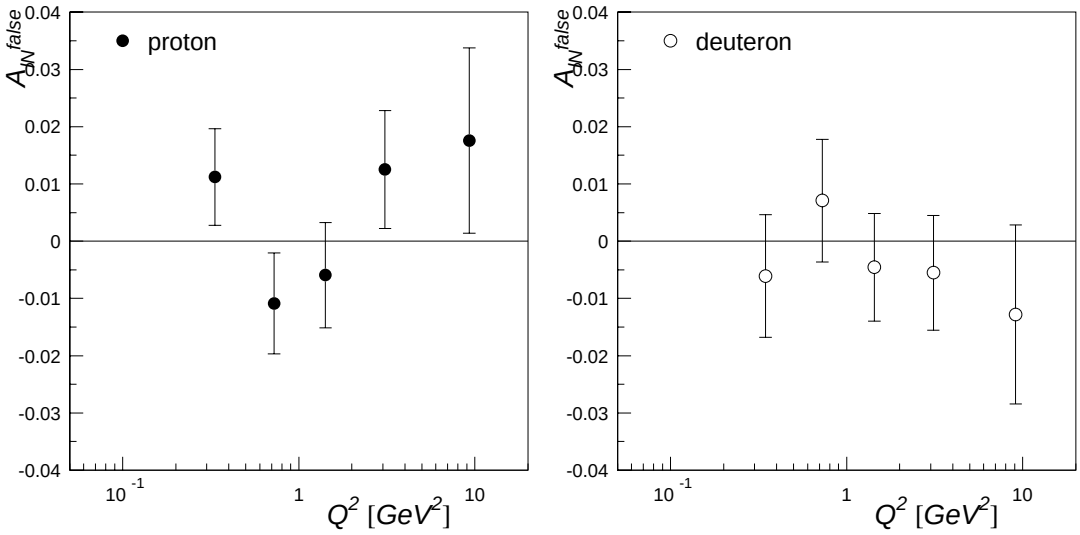

Figure 7.18: $A_{LL}^{lN\to\rho^0 l' N}$ false asymmetries for proton (left) and deuteron (right). Note the vertical scale, which is expanded by a factor of 10 compared to the scale used for the other asymmetry plots. The errors are statistical only.

The Inelastic Background

In the presence of background, the measured spin-asymmetry A^{meas} differs from the physics spin-asymmetry A by

$$A^{meas} = A - \Big[A - A^{Bkg}\Big] \times R\,, \tag{7.6}$$

where A^{Bkg} is the spin-asymmetry of the background events and R is the fraction of background events to total events: $R = N_{Bkg}/(N_{Sig} + N_{Bkg})$ with N_{Sig} the number of exclusive ρ^0 events and N_{Bkg} the number of non-elastic events in the ρ^0 sample. If $A^{Bkg} = A$, then the physics asymmetry and the measured asymmetry coincide and the background has no effect on the extracted result. If $A^{Bkg} = 0$, the net effect is the dilution of the physics asymmetry by the factor $(1 - R)$. In practice the second case is more probable. In general some corrections to the measured asymmetry are applied in order to extract the physics asymmetry.

The contamination of the exclusive ρ^0 sample by non-elastic events is summarized in Table 6.1. The background effects have been studied with different inelasticity cuts around the selected $-0.05 < I < 0.05$ interval and no appreciable effects beyond the statistical fluctuations have been observed. As shown in Figure 7.19, the background asymmetry has been found to be compatible with zero.

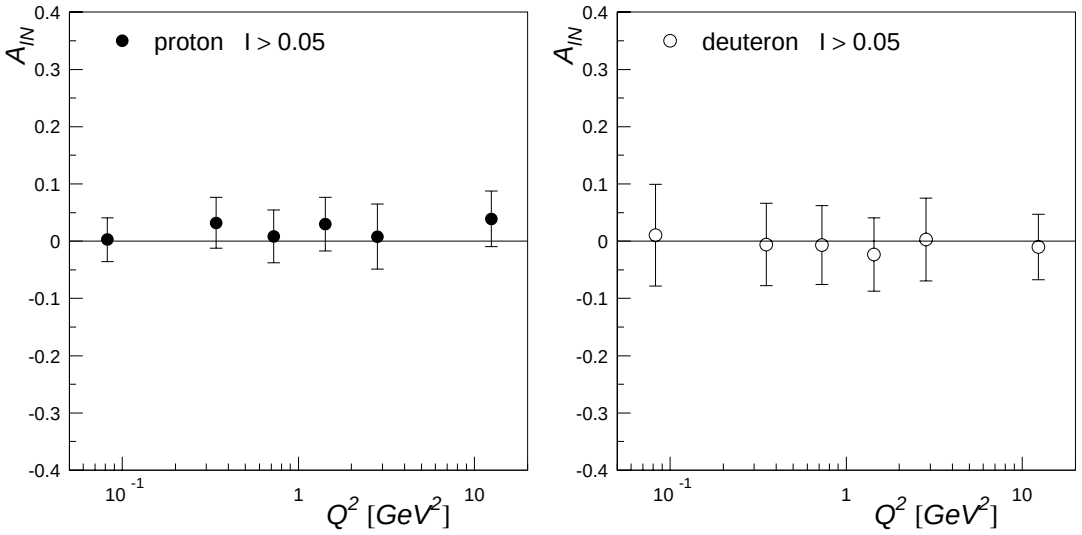

Figure 7.19: $A_{LL}^{lN\to\rho^0 l' N}$ for $0.05 < I < 0.20$ for proton (left) and deuteron (right). The errors are statistical only.

Based on this observation it has been assumed that also in the $-0.05 < I < 0.05$ interval the background asymmetry is zero as for $I > 0.05$. Therefore, in the case of this analysis, the non-elastic background represents a dilution of the physics asymmetry only. This dilution effect depends on the event kinematics (Q^2 and p_T^2). Given the smallness of the effect, it has been included in the systematic error bin by bin rather than correcting the measured asymmetry for the dilution due to the background and (R can be found in Table 6.1)

$$\delta A_{LL}^{Bkg} = R\,|A_{LL}| \quad \text{with} \quad \delta A_{LL}^{Bkg} < 0.02\,. \tag{7.7}$$

A different approach to the background issue would have been to first group all the ρ^0 events according to the relative orientations of the beam and target polarizations, then subtract the number of background events from the number of the selected ρ^0 events for the two data sets separately, and finally calculate the spin-asymmetries. Given the limited statistics of the whole sample, however, all the data should have been combined in order to perform the background subtraction. In this case all the advantages of the bias-cancelling inherent in the data grouping over short time periods would have been lost, leading to the appearance of large false asymmetries. For this analysis it turned out that the first approach leads to smaller systematic uncertainties.

Uncertainty on f

The uncertainty on the dilution factor f is due to the poor knowledge of the A-dependence of the cross section for exclusive ρ^0 production off nuclei $\sigma_A(Q^2, p_T^2)$. This uncertainty has been estimated by varying the functional form and fit parameters to the existing exclusive ρ^0 cross section data (section 7.1.2 and Figure 7.2). This study has given $\frac{\Delta f}{f} \leq 0.19$ for all p_T^2 and $\frac{\Delta f}{f} \leq 0.14$ for $p_T^2 > 0.09$ GeV^2 (non-coherent production). The uncertainty on f propagates to the systematic uncertainty on $A_{LL}^{lN \to \rho^0 l' N}$ as

$$\delta A_{LL}^{f} = \left(\frac{\delta f}{f}\right) |A_{LL}| \;\leq\; \begin{matrix} 0.19 \\ 0.14 \end{matrix} \times |A_{LL}| \;\begin{matrix} \mathrm{all} p_T^2 \\ \mathrm{non-coherent} \end{matrix} . \tag{7.8}$$

Uncertainty on P_b and P_t

These systematic uncertainties are the same as for the inclusive analysis. The error on the beam polarization $\frac{\delta P_b}{P_b}$ is reported in Table 3.1 and it propagates to A_{LL} as

$$\delta A_{LL}^{P_b} = \left(\frac{\delta P_b}{P_b}\right) |A_{LL}| = 0.019 \times |A_{LL}| . \tag{7.9}$$

The uncertainties on the target polarization $\frac{\delta P_t}{P_t}$ are summarized in Table 3.3 and

$$\delta A_{LL}^{P_t} = \left(\frac{\delta P_t}{P_t}\right) |A_{LL}| = \begin{matrix} 0.028 \\ 0.037 \end{matrix} \times |A_{LL}| \;\begin{matrix} \mathrm{proton} \\ \mathrm{deuteron} \end{matrix} . \tag{7.10}$$

False Asymmetries

Rather than correcting the data for the false asymmetries, they have been included in the systematic error. Also, a common value for all kinematical bins has been assumed. The absolute value of the maximum deviation from zero (Figure 7.18) has been assumed as an estimate of the systematic error on A_{LL} and

$$\delta A_{LL}^{false} = 0.017 \tag{7.11}$$

for all kinematical bins.

ρ^0 Selection Criteria

As an estimate of the systematic error due to the different selection criteria, the average of the absolute values of the maximum deviations of the asymmetry values from the asymmetries obtained with the standard ρ^0 selection (Figure 7.17) has been assumed:

$$\delta A_{LL}^{sel} = 0.033\,. \tag{7.12}$$

This value has been applied to all kinematical bins.

The various systematic errors derived in this section are assumed to be uncorrelated and are added in quadrature. The scale erros have been kept separated from the other errors and

$$\delta A_{LL}^{scale} = 0.20 \times |A_{LL}| \qquad \text{all } p_T^2 \tag{7.13}$$

$$\delta A_{LL}^{scale} = 0.15 \times |A_{LL}| \qquad p_T^2 > 0.09 \text{ GeV}^2/c^2\,. \tag{7.14}$$

In this analysis the systematic error due to the background contamination behaves as a multiplicative error, diluting the physics asymmetry. It has been included, however, with the additive errors. For most of the kinematical bins, the additive systematic errors turned out to be the same and equal to $\delta A_{LL}^{add} = 0.037$.

The systematic uncertainties are summarized in Tables 7.1 and 7.2 as a function of Q^2 and W^2. As it can be observed, these errors are typically much smaller than the statistical ones. This is due to the fact, that the available statistic for this analysis was not that large; compared to the inclusive analysis, the statistic available for the ρ^0 analysis is about 10^3 times smaller. The role of the systematic uncertainties, therefore, is much less relevant than for the inclusive case; **the measurement of $A_{LL}^{lN\to\rho^0 l'N}$ is dominated by statistics**. For this reason the systematic erros have been shown only in the Tables 7.1 and 7.2 and have not been included in the $A_{LL}^{lN\to\rho^0 l'N}$ asymmetry plots.

Chapter 8

Conclusions and Outlook

This thesis presents a study of the exclusive ρ^0 production in polarized lepton–nucleon scattering within the Spin Muon Collaboration (SMC) at CERN. The data cover a very broad range in Q^2 from the photo-production limit ($Q^2 > 0.01$ GeV^2) to the DIS regime at medium W ($\langle W^2 \rangle \sim 240$ GeV^2), where the ρ^0 production is believed to be mediated by the Pomeron exchange. This kinematical region corresponds to the regime transition between the short distance QCD, where perturbative calculations are valid, and long distance QCD, which is not yet calculable. At this stage, the interpretation of these data can only be phenomenological. However, ultimately, the partially successful phenomenology of the Regge and the VMD models is hoped to be interpreted in terms of QCD, the strong interaction.

The selection of the exclusive ρ^0 sample from the recorded lepton–nucleon data has been studied very carefully. The $m(\pi^+\pi^-)$ distribution shows a deviation from the resonance shape as described by a relativistic p-wave Breit-Wigner, consistent with previous observations. This distortion of the ρ^0 mass shape is well described by the Ross-Stodolsky and Söding models in terms of the interference between the resonant and non-resonant $\pi^+\pi^-$ production.

The cross section spin-asymmetry $A_{LL}^{lN \to \rho^0 l' N}$ has been studied as a function of several kinematical variables, Q^2 and W^2, p_T^2 and $\cos\vartheta^*$. Given the relatively low statistics of the exclusvie ρ^0 data sample, the asymmetry results are dominated by statistical uncertainties and not by systematic ones. In order to increase the statistical precision of the measurement, the data obtained from proton and

deuteron targets have been combined. It has been assumed that the exclusive ρ^0 production in the kinematical range of this experiment is dominated by the two gluon exchange process within the pQCD models and that the Pomeron coupling to protons and neutrons is the same in the non-perturbative models.

Within the statistical precision of this measurement, no spin dependence has been observed in the exclusive ρ^0 lepto-production off polarized protons nor off polarized deuterons. These results, however, do not exclude a spin dependence at the level of a few %. Combining proton and deuteron data, a value of -0.005 ± 0.020 for $A_{LL}^{lN\to\rho^0 l'N}$ is obtained for $Q^2 < 1$ GeV^2 and a value of 0.041 ± 0.035 for $Q^2 > 1$ GeV^2. For $p_T^2 > 0.09$ GeV$^2/c^2$ in the non-coherent production regime $A_{LL}^{lN\to\rho^0 l'N} = 0.032 \pm 0.034$ for $Q^2 < 1$ GeV^2 and $A_{LL}^{lN\to\rho^0 l'N} = -0.065 \pm 0.047$ for $Q^2 > 1$ GeV^2. The measured asymmetries indeed show a very mild trend to decrease from zero to negative values with increasing Q^2. They also show a trend to increase from negative values to zero with increasing W.

In contrast to DIS, the theoretical understanding of longitudinal double spin asymmetries in exclusive vector meson production is limited. Also the unpolarized case is still poorly understood. Models of vector meson production based on Regge theory suggest no spin dependence, since the exchanged object is the spin-0 Pomeron [137]. Some model approaches predict non-zero spin effects for diffractive processes in the Regge limit of $s \to \infty$ and $|t|/s \to 0$. In these models a spin-flip term is added to the proton–Pomeron vertex [138]. This means that the Pomeron might not conserve the helicity in the $s-$channel. This conclusion is especially important for the diffractive scattering of polarized particles, where the complicated spin structure and coupling of the Pomeron should be manifest. Evidence for a helicity flip amplitude corresponding to the production of longitudinally polarized ρ^0's by transversely polarized virtual photons comes from the study of the azimuthal distribution of exclusively produced ρ^0 around the virtual photon axis (i.e. of the angular distribution between the lepton scattering plane and the ρ^0 production plane) [139]. This effect is quantified with the ρ^0 density matrix element r_{00}^5, which measures the ratio of the spin-flip amplitude to the spin-non-flip amplitudes in exclusive ρ^0 production.

A first theoretical study of the longitudinal double spin asymmetries based on the off-diagonal generalized VMD model suggested that these asymmetries might

be twice as large as the corresponding inclusive ones [136]. In pQCD the exclusive process at medium-large W is described in terms of the exchange of a pair of gluons, thus a spin-asymmetry might result from the polarization of gluons Δg inside the polarized nucleon [140]. This possibility has stimulated an interesting debate, whether the hard exclusive lepto-production of vector mesons in polarized scattering could be used as a tool to study the polarized gluon distribution Δg. In particular it has been suggested that the double spin asymmetry for the hard exclusive J/Ψ production might be directly proportional to Δg: $A_{LL} = 2\Delta g/g$. In principle, this model can also be extended to the exclusive ρ^0 production at large Q^2 as in the unpolarized case. This approach, however, is quite problematic, since the spin-asymmetry for the hard exclusvie J/Ψ production vanishes at the twist-2 level and because the spin-flip transition amplitude between the hard photon and the J/Ψ is also suppressed [141]. The relativistic corrections to the J/Ψ wave function depend on Δg but the predicted analyzing power is very small.

A study of the double spin asymmetries in exclusive vector meson electro-production, similar to SMC, has been performed by the HERMES experiment at DESY [11] with a much lower beam energy compared to SMC. The HERMES data cover a considerably lower range in W ($\langle W^2 \rangle \sim 24$ GeV^2), where the ρ^0 production is expected to be dominated by Reggeon exchanges. HERMES observed a positive asymmetry at a 2 σ level, with no evident kinematical dependence. HERMES reported the one-photon exchange asymmetries, which are obtained from $A_{LL}^{lN \to \rho^0 l' N}$ after accounting for the exchanged virtual photon polarization. From the reported values ($A_1 \approx 0.24 \pm 0.11$) and the corresponding event kinematics, the HERMES $A_{LL}^{lN \to \rho^0 l' N}$ asymmetries are about (10 ± 5) %, still well compatible with this measurement.

A data sample at least 10 times larger and a several times more precise measurement are required to study and understand this very interesting aspect of diffraction. Such data might soon come from the COMPASS experiment at CERN [142], which has recently started to take data.

The main objective of the Spin Muon Collaboration has been the study of the internal spin structure of the nucleon. SMC measured the spin dependent structure functions for the proton g_1^p and for the deuteron g_1^d by deep inelastic scattering of a polarized muon beam off polarized proton and deuteron targets.

SMC was created in 1988 to confirm the results obtained by the European Muon Collaboration (EMC) on the nucleon spin that led to the so-called *spin crisis*. EMC found that in DIS of high energy muons on polarized protons the quark spin contribution $\Delta\Sigma$ to the proton spin was unexpectedly small, even compatible with zero.

SMC measured the proton structure function g_1^p in a wider kinematical range ($1 \leq Q^2 \leq 60$ GeV^2 and $0.003 \leq x \leq 0.7$) with a better accuracy (smaller statistical and systematical errors) than previous experiments. The statistical errors could be reduced not only because of a bigger amount of data taken, but mainly because of the high target polarization, which was achieved by applying frequency modulated microwaves. The polarization was stable throughout the whole data taking, with a fast build-up. The systematic error could also be significantly reduced thanks to the stability of the detectors acceptances and by the frequent reversals of the target polarization direction with almost no loss of polarization. These remarks also apply to the exclusive ρ^0 analysis.

This thesis also contains the complete data set of the inclusive SMC analysis of the virtual photon absorption cross section asymmetries for the proton A_1^p and the deuteron A_1^d. For small x the asymmety A_1 is close to zero and for large x the asymmetry approaches unity, which is in qualitative agreement with the expectation for the valence quark contribution at large x. Within the experimental errors, the measured asymmetries do not depend on Q^2. In the overlapping kinematical range the SMC results are in agreement with other experiments. These asymmetries were used together with the spin independent structure function F_2 and the ratio R to obtain the spin dependent structure functions g_1^p and g_1^d. The resulting values of g_1^p are found to be positive in the measured kinematical range of the experiment. The values for g_1^d are smaller and also positive except for $0.003 < x < 0.04$, where they become negative. The statistical uncertainty of g_1 is dominant at small x; at medium and large x the statistical and systematic uncertainties contribute almost equally.

In order to compare the SMC results to the theoretical predictions expressed by the spin sum rules, the first moments $\Gamma_1 = \int_0^1 g_1(x)dx$ of the spin-dependent structure functions at a fixed Q^2 have been derived. Assuming that A_1 scales, i.e. that A_1 does not depend on Q^2, the integral of g_1^p, in the region $0.01 < x < 0.7$,

amounts to 0.125 ± 0.008, which confirms the EMC findings of 0.120 ± 0.013. The spin dependent structure functions had to be evolved from the measured Q^2 to a fixed Q^2. This was done by performing a next-to-leading order QCD analysis of the world spin dependent structure function data.

The Ellis-Jaffe sum rule was found to be badly violated by the SMC data both for the proton and the neutron. The Bjorken sum rule was tested by leaving $|g_a/g_v|$ as a free parameter in the QCD fit. An agreement with the theoretical prediction at the level of 10 % has been found. In previous tests of the Bjorken sum rule, the difference of Γ_1^p and Γ_1^n was compared to the predictions of the Bjorken sum rule using the published value of $|g_a/g_v|$. In this procedure it is indirectly assumed that the Bjorken sum rule is valid, since the QCD fitting procedure for determining Γ_1^p and Γ_1^n uses the published value of $|g_a/g_v|$. On the other hand by leaving $|g_a/g_v|$ as a free parameter in the QCD anlaysis, the verification of the Bjorken sum rule, with an accuracy of 10%, means that there is nothing fundamentally wrong with QCD.

The results obtained for the axial charges from Γ_1^p and Γ_1^n at $Q_0^2 = 10$ GeV^2 are consistent among themselves with $a_0 = 0.27 \pm 0.09$ and $a_s = -0.11 \pm 0.03$. The charge a_0 gives the overall fraction of the proton spin that is carried by quarks, while a_s gives the contribution of the strange sea quarks. The smallness of a_0 can be understood by assuming a large positive gluon polarization Δg, which affects the measured a_0 through the axial anomaly (a low order virtual photon–gluon interaction). In order to restore the quark spin contribution to its nominal value of 0.6–0.7, Δg should be approximately $1 - 2\hbar$, which appears to be a reasonable value.

The main goals of the recent experiments have been achieved by now. Further progress in the understanding of the nucleon's spin structure requires a direct measurement of the gluon polarization Δg, by studying the spin-dependent aspects of QCD processed induced by gluons. Several new experiments with the main goal of determining Δg have just started to collect data.

The COMPASS experiment at CERN [142] has started to take data this summer. COMPASS is a fixed target experiment similar to SMC, but with a much larger acceptance and full identification of hadrons. COMPASS will measure $\Delta g/g$ in the kinematical range $0.07 < x_g < 0.4$, with the projected precision of

$\Delta g/g = 0.11$ via open charm production using a longitudinally polarized muon beam and a polarized target. The charm quarks will be tagged by their fragmentation into D mesons and the subsequent decay into kaon-pion pairs. COMPASS will also access Δg via the measurement of correlated high$-p_T$ hadron pairs [144] with a projected precision of $\Delta g/g = 0.05$ in several x_g bins. The COMPASS experiment will also provide high statistics data for g_1, semi-inclusive muon scattering, and for the twist-2 nucleon structure function h_1 referred to as transversity.

PHENIX and STAR are two major experiments at RHIC in Brookhaven. RHIC is the first polarized proton–proton collider ever built [143]. Polarized protons are provided by a powerful polarized H^- source and could be accelarated to high energies and stored in RHIC with the use of *siberian snakes*, a set of helicoidal magnets used to prevent the protons from loosing their polarization. Collisions of polarized protons have been seen for the first time in December 2001.

The RHIC experiments PHENIX and STAR will determine $\Delta g/g$ in the kinematical range $0.03 < x_g < 0.3$ from direct-photon and di-jet production in polarized proton–proton collisions. In these processes the measured asymmetries involve two polarized parton distribution functions, for instance $\Delta g(x)$ and $\Delta q(x)$, where the quark polarizations $\Delta q(x)$ must come from other experiments. Neglecting the uncertainty in $\Delta q(x)$, a precision of the order $\Delta g/g = 0.05$ is projected over this x_g range.

Bibliography

[1] L.D. Landau and E.M. Lifshitz, *Quantum Mechanics* (Pergamon 1977).

[2] R. Taylor, Rev. Mod. Phys. **63** (1991) 573;
H. Kendall, Rev. Mod. Phys. **63** (1991) 597;
J. Friedman, Rev. Mod. Phys. **63** (1991) 615.

[3] R.P. Feynman, Phys. Rev. Lett. **23** (1969) 1415;
J.D. Bjorken and E.A. Paschos, Phys. Rev. **185** (1969) 1975.

[4] M. Gell-Mann, Phys. Lett. **8** (1964) 214;
G. Zweig, CERN Preprint TH401 (1964), TH412 (1964), unpublished.

[5] J.D. Bjorken, Phys. Rev. **179** (1969) 1547.

[6] V.W. Hughes and J. Kuti, Ann. Rev. Nucl. Part. Sci. **33** (1983) 611;
SLAC E80 Collaboration, M.J. Alguard *et al.*, Phys Rev. Lett. **37** (1976) 1261; Phys. Rev. Lett. **41** (1978) 70,
SLAC E130 Collaboration, G. Baum *et al.*, Phys. Rev. Lett. **51** (1983) 1135.

[7] EMC Collaboration, J. Ashman *et al.*, Phys. Lett. B **206** (1988) 364; Nucl. Phys. B **328** (1989) 1.

[8] V.W. Hughes *et al.* , Phys. Lett. B **212** (1988) 511.

[9] SMC Collaboration, *Measurement of the spin dependent structure function of neutron and proton*, proposal NA47 CERN/SPSC 88-47 (SPSC/P242).

[10] A. Tripet, for the SMC Collaboration, *DIS99*, Nucl. Phys. B **79** (Proc. Suppl.) (1999) 529.

[11] F. Meissner, for the HERMES Collaboration, *DIS99*, Nucl. Phys. B **79** (Proc. Suppl.) (1999) 532;
HERMES Collaboartion, A. Airapetian *et al.*, Phys. Lett. B **513** (2001) 301.

[12] M.L. Good and W.D. Walker, Phys. Rev. **120** (1960) 1857.

[13] F. Halzen and A.D. Martin, *Quarks and Leptons* (Wiley & Sons 1984).

[14] M.E. Peskin and D.V. Schroeder, *An Introduction to Quantum Field Theory* (Addison Wesley 1995).

[15] M. Anselmino, A. Efremov, and E. Leader, Phys. Rep. **261** (1995) 1.

[16] B. Lampe and E. Reya, Phys. Rep. **332** (2000) 1.

[17] R.L. Jaffe, in *The Spin Structure of the Nucleon*, Eds. B. Frois *et al.*, Erice, Italy, August 1995 (World Scientific 1997)

[18] E. Leader and E. Predazzi, *An Introduction to Gauge Theories and Modern Particle Physiscs* (Cambridge 1996).

[19] W. Greiner and A. Schäfer, *Quantum Chromodynamics* (Springer 1995).

[20] P. Renton, *Electroweak Interactions* (Cambridge 1990).

[21] E. Leader, *Spin in Particle Physics* (Cambridge 2002).

[22] K.G. Wilson, *Phys. Rev.* **179** (1969) 1499.

[23] L.N. Hand, Phys. Rev. **129** (1963) 1834.

[24] R.L. Jaffe, Comm. Nucl. Part. Phys. **19** (1990) 239.

[25] P. Hoodbhoy, R.L. Jaffe, and A. Manohar, Nucl. Phys. B **312** (1989) 571;
R.L. Jaffe and A. Manohar, Nucl. Phys. B **321** (1989) 343.

[26] H. Khan and P. Hoodbhoy, Phys. Lett. B **185** (1993) 181.

[27] M.G. Doncel and E. de Rafael, Nuovo Cim. A **4** (1971) 363;
P. Gnadig and F. Niedermayer, Nucl. Phys. B **55** (1973) 612.

[28] J. Soffer and O.V. Teryaev, Phys. Lett. B **490** (2000) 106.

[29] SMC Collaboration, D. Adams *et al.*, Phys. Lett. B **336**, (1994) 125.

[30] SMC Collaboration, D. Adams *et al.*, Phys. Lett. B **396** (1997) 338.

[31] SLAC E143 Collaboration, K. Abe *et al.*, Phys. Rev. Lett. **76** (1996) 587.

[32] W. Buck and F. Gross, Phys. Rev. D **20** (1979) 2361;
M.Z. Zuilhof and J.A. Tjon, Phys. Rev. C **22** (1980) 2369;
M. Lacombe *et al.*, Phys. Rev. C **21** (1980) 861.

[33] C.G. Callan and D.J. Gross, Phys. Rev. Lett. **22** (1969) 156.

[34] G. Altarelli, Phys. Rep. **81** (1982) 1.

[35] G. Altarelli and G. Parisi, Nucl Phys. B **126** (1977) 298;
V.N. Gribov and L.N. Lipatov, Sov. J. Nucl. Phys. **15** (1972) 438 and 675;
Yu.L. Dokshitzer, Sov. Phys. JTEP **46** (1977) 641.

[36] E.B. Zijlstra and W.L. Neerven, Nucl. Phys. B **417** (1994) 61.

[37] W. Vogelsang, Phys. Rev. D **54** (1996) 2023.

[38] Particle Data Group, D.E. Groom *et al.*, Eur. Phys. J. C **15** (2000) 1.

[39] J. Kodaira *et al.*, Phys. Rev. D **20** (1979) 627;
J. Kodaira *et al.*, Nucl. Phys. B **159** (1979) 99.

[40] G. Altarelli and G.G. Ross, Phys. Lett. B **212** (1988) 391;
A.V. Efremov and O.V. Teryaev, Phys. Lett. B **200** (1987) 363;
R.D. Carlitz, J.C. Collins and A.H. Mueller, Phys. Lett. B **214** (1988) 229.

[41] J.D. Bjorken, Phys. Rev. **148** (1966) 1467; Phys. Rev. D **1** (1970) 1376.

[42] J. Ellis and R. L. Jaffe, Phys. Rev. D **9** (1974) 1444.

[43] S.A. Larin *et al.*, Phys. Rev. Lett. **66** (1991) 862;
S.A. Larin and J.A.M. Vermaseren, Phys. Lett. B **259**, (1991) 345.

[44] A.L. Kataev and V.V. Starshenko, Mod. Phys. Lett. A **10** (1995) 235.

[45] S.A. Larin, Phys. Lett. B **334** (1994) 192.

[46] A.L. Kataev, Phys. Rev. D **50** (1995) R5469.

[47] S.J. Brodsky, M. Burkardt and I. Schmidt, Nucl. Phys. B **441** (1995) 197.

[48] R.L. Heimann, Nucl. Phys. B **64** (1973) 429;
J. Ellis and M. Karliner, Phys. Lett. B **213** (1988) 73.

[49] R.D. Ball, S. Forte and G. Ridolfi, Nucl. Phys. B **444** (1995) 287; Nucl. Phys. B **449** (1995) 680.

[50] SMC Collaboration, B. Adeva *et al.*, Phys. Rev. D **58** (1998) 112002.

[51] M.L. Perl, *High Energy Hadron Physics* (Wiley & Sons 1974).

[52] P.D.B. Collins, *Regge Theory and High Energy Physics* (Cambridge 1977).

[53] J.R. Forshaw and D.A. Ross, *Quantum Chromodynamics and the Pomeron* (Cambridge 1997).

[54] V. Barone and E. Predazzi, *High Energy Particle Diffraction* (Springer 2002).

[55] A. Hebecker, Phys. Rep. **331** (2000) 1.

[56] T.H Bauer, R.D. Spital and D.R. Yennie, Rev. Mod. Phys. **50** (1978) 261.

[57] J.A. Crittenden, *Exclusive Production of Neutral Vector Mesons at the Electron-Proton Collider HERA*, Springer Tracts in Mod. Phys. **140** (1997).

[58] R. Hagedorn, *Relativistic Kinematics* (Benjamin / Cummings 1963).

[59] I.Y. Pomeranchuk, Sov. Phys. JETP **7** (1958) 499;
V.N. Gribov, JETP Lett. **41** (1961) 667.

[60] F.E. Close and G.A. Schuler, Phys. Lett. B **464** (1999) 279.

[61] K. Schilling, P. Seyboth and G. Wolf, Nucl. Phys. B **15** (1970) 397;
K. Schilling and G. Wolf, Nucl. Phys. B **61** (1973) 381.

[62] V.N. Gribov, Sov. Phys. JETP **30** (1970) 709.

[63] J.C. Collins, L. Frankfurt and M. Strikman, Phys. Rev. D **56** (1997) 2982.

[64] Durham cross sections database:
`http://durpdg.dur.ac.uk/hepdata/reac.html`.

[65] L.P.A. Haakman *et al.*, Phys. Lett. B **365** (1996) 411.

[66] F.E. Low, Phys. Rev. D **12** (1975) 163.

[67] S. Nussinov, Phys. Rev. Lett. **34** (1975) 1286.

[68] G.A. Schuler and T. Sjostrand, Phys. Lett. B **300** (1993) 169; Nucl. Phys. B **407** (1993) 539.

[69] J.J. Sakurai, Ann. Phys. **11** (1960) 1; Phys. Rev. Lett. **22** (1969) 981.

[70] NMC Collaboration, M. Arneodo *et al.*, Nucl. Phys. B **429** (1994) 503.

[71] E665 Collaboration, M.R. Adams *et al.*, Z. Phys. C **74** (1997) 237.

[72] ZEUS Collaboration, J. Breitweg *et al.*, Eur. Phys. J. C **6** (1997) 603.

[73] H1 Collaboration, S. Aid *et al.*, Nucl. Phys. B **463** (1996) 3.

[74] H1 Collaboration, S. Aid *et al.*, Nucl. Phys. B **468** (1996) 3.

[75] J.J. Sakurai and D. Schildknecht, Phys. Lett. B **40** (1972) 121;
B. Gorczyca and D. Schildknecht, Phys. Lett. B **47** (1973) 71.

[76] T. Regge, Nuovo Cim. **14** (1959) 951; Nuovo Cim. **18** (1960) 947.

[77] B. Badelek *et al.*, Rev. Mod. Phys. **64** (1992) 927.

[78] G.F.P. Chew and S.C. Frautschi, Phys. Rev. Lett. **7** (1961) 394; Phys. Rev. Lett. **8** (1962) 41.

[79] A. Donnachie and P.V. Landshoff, Phys. Lett. B **296** (1992) 227.

[80] ZEUS Collaboration, M. Derrich *et al.*, Phys. Lett. B **350** (1995) 120;
H1 Collaboration, S. Aid *et al.*, Nucl. Phys. B **472** (1996) 3.

[81] S.J. Brodsky *et al.*, Phys. Rev. D **50** (1994) 3134.

[82] M.G. Ryskin, Z. Phys. C **57** (1993) 89;
M.G. Ryskin *et al.*, Z. Phys. C **76** (1997) 231.

[83] L. Frankfurt, W. Koepf and M. Strikman, Phys. Rev. D **54** (1996) 3194.

[84] A.D. Martin, M.G. Ryskin, and T. Teubner, Phys. Rev. D **55** (1997) 4329.

[85] N. Doble *et al.*, Nucl. Instr. Meth. A **343** (1994) 351.

[86] E. Wigner, Rev. Mod. Phys. **29** (1957) 255.

[87] K.L. Brown *et al.*, *TRANSPORT*, CERN Yellow Report 80-04 (1980).

[88] SMC Collaboration, B. Adeva *et al.*, Nucl. Instr. Meth. A **343** (1994) 363.

[89] SMC Collaboration, D. Adams *et al.*, Nucl. Instr. Meth. A **443** (2000) 1.

[90] L. Michel, Proc. Phys. Soc. A **63** (1950) 514.

[91] D. Bardin and L. Kalinovskaya, DESY-97-230 (1997), hep-ph/9712310;
see also A.M. Bincer, Phys. Rev. **107** (1957) 1437.

[92] N. de Botton *et al.*, IEEE Transactions on Magnetics **30** (1994) 2447.

[93] T.O. Niinikoski, Nucl. Instr. Meth. A **192** (1982) 151.

[94] S.C. Brown *et al.*, in 4^{th} *International Workshop on Polarized Target Materials and Techniques*, Ed. W. Meyer, Bad Honnef, Germany, 1984.

[95] EMC Collaboration, O.C. Allkofer *et al.*, Nucl. Instr. Meth. A **179** (1981) 445.

[96] SMC Collaboration, D. Adams *et al.*, Nucl. Instr. Meth. A **435** (1999) 354.

[97] A. Steinmetz, Ph. D. Thesis, Universität Mainz (1996).

[98] G. Bardin *et al.*, SMC internal report, SMC/92/12 (1992), unpublished.

[99] A. Tripet, SMC Internal Report, SMC/96/01 (1996), unpublished.

[100] N. Hayashi *et al.* SMC Internal Report, SMC/95/20 (1995), unpublished.

[101] T. Pussieux, Ph. D. Thesis, Université de Paris Sud (1994).

[102] S. Bueltmann *et al.*, Nucl. Inst. Meth. A **356** (1995) 102.

[103] A.A. Akhundov *et al.*, Sov. J. Nucl. Phys. **26** (1977) 660; **44** (1986) 988; D. Bardin and N.M. Shumeiko, Sov. J. Nucl. Phys. **29** (1979) 449.

[104] T.V. Kukhto and N.M. Shumeiko, Nucl. Phys. B **219** (1983) 412; I.V. Akushevich and N.M. Shumeiko, J. Phys. G **20** (1994) 513.

[105] SMC Collaboration, B. Adeva *et al.*, Phys. Rev. D **58** (1998) 112001.

[106] SLAC E143 Collaboration, K. Abe *et al.*, Phys. Rev. Lett. **74** (1995) 346; Phys. Rev. Lett. **75** (1995) 25.

[107] NMC Collaboration, P. Amaudruz *et al.*, Nucl. Phys. B **371** (1992) 3.

[108] A. Bravar, K. Kurek and R. Windmolders, Comp. Phys. Comm. **105** (1997) 42.

[109] SMC Collaboration, B. Adeva *et al.*, Nucl. Instr. Meth. A **419**, (1998) 60.

[110] BCDMS Collaboration, A.C. Benvenuti *et al.*, Phys. Lett. B **233**, (1989) 485.

[111] FNAL E665 Collaboration, M.R. Adams *et al.*, Phys. Rev. D **54**, (1996) 3006.

[112] L.W. Whitlow *et al.*, Phys. Lett. B **282** (1992) 475.

[113] H1 Collaboration, S. Aid *et al.*, Nucl. Phys. B **470** (1996) 3.

[114] ZEUS Collaboration, M. Derrick *et al.*, Z. Phys. C **72** (1996) 399.

[115] T. Cuhadar, Ph. D. Thesis, Free Univeristy of Amsterdam (1998).

[116] NMC Collaboration, M. Arneodo *et al.*, Nucl. Phys. B **483** (1997) 3.

[117] L.W. Whitlow *et al.*, Phys. Lett. B **250** (1990) 193.

[118] NMC Collaboration M. Arneodo *et al.*, Nucl. Phys. B **487** (1997) 3.

[119] U. Stösslein, hep-ex/0201036 (2002).

[120] SLAC E142 Collaboration, P. Anthony *et al.*, Phys. Rev. D **54** (1996) 6620.

[121] SLAC E154 Collaboration, K. Abe *et al.*, Phys. Rev. Lett. **79** (1997) 26.

[122] HERMES Collaboration, K. Ackerstaff *et al.*, Phys. Lett. B **404** (1997) 383.

[123] R.D. Ball, S. Forte and G. Ridolfi, Phys. Lett. B **378** (1996) 255.

[124] F.E. Close and R.G. Roberts, Phys. Lett. B **316** (1993) 165.

[125] SLAC E155 Collaboration, P. Anthony *et al.*, Phys. Lett. B **493** (2000) 19.

[126] J. Blümlein and H. Böttcher, Nucl. Phys. B **636** (2002) 225.

[127] K. Kurek, hep-ph/9606240; Z. Phys. C **63** (1994) 561.

[128] HERMES Collaboration, A. Airapetian *et al.*, Eur. Phys. J. C **17** (2000) 389.

[129] J.D. Jackson, Nuovo Cim. **34** (1964) 1644.

[130] G. Kramer and J.L. Uretsky, Phys. Rev. **181** (1969) 1918.

[131] H1 Collaboration, C. Adloff *et al.*, Eur. Phys. J. C **13** (2000) 371.

[132] M. Ross and L. Stodolsky, Phys. Rev. **149** (1996) 1172.

[133] FNAL E665 Collaboration, M.R. Adams *et al.*, Phys. Rev. Lett. **74** (1995) 1525.

[134] P. Söding, Phys. Lett. **19** (1965) 702.

[135] S.J. Brodsky and A.H. Mueller, Phys. Lett. B **206** (1988) 685.

[136] H. Fraas, Nucl. Phys. B **113** (1976) 532.

[137] S.I. Manayenkov, hep-ph/9903405.

[138] C. Burrely, J. Soffer and T.T. Wu, Phys. Rev. D **19** (1979) 3249;
S Goloskokov, S.P. Kuleshov and O.V. Selyugin, Z. Phys. C **50** (1991) 455.

[139] ZEUS Collaboration, J. Breitweg *et al.*, Eur. Phys. J C **12** (2000) 393;
H1 Collaboration, C. Adloff *et al.*, Eur. Phys. J. C **13** (2000) 371.

[140] M.G. Ryskin, Phys. Lett. B **403** (1997) 335; hep-ph/9706505 (1997).

[141] M. Vänttinen and L. Mankiewicz, Phys. Lett. B **434** (1998) 141; Phys. Lett. B **440** (1998) 157.

[142] *COMPASS* Proposal, CERN/SPSLC 96-14, SPSC/P297, March 1996; http://axhyp1.cern.ch/compass/.

[143] G. Bunce *et al.*, Ann. Rev. Nucl. Part. Sci. **50** (2000) 525.

[144] A. Bravar, D. von Harrach and A. Kotzinian, Phys. Lett. B **421** (1998) 349.

Acknowledgments

I would like to express my gratitude to my advisor, Prof. Günter Baum, for his understanding and support at crucial moments, and for his careful reading of this thesis.

I am particularly grateful to Dr. Alessandro Bravar who proposed me to study the exclusive ρ^0 production as my own thesis subject in addition to the SMC inclusive results I had already dealt with. His advice and guidance were welcome.

I would like to thank all the members of SMC, and in particular the spokesman Prof. Vernon Hughes and the various contactmen: Dr. Gerhardd K. Mallot, Dr. Alain Magnon, Dr. Jean-Marc Le Goff and Prof. Roland Windmolders.

Dr. Nicolo de Groot and Prof. Arnold Staude for having given me the opportunity to begin to work on the SMC experiment.

As analysis coordinators, Dr. Ulrich Stiegler, Dr. Jean-Marc Le Goff and Dr. Ewa Rondio for having contributed to this thesis by guiding the inclusive analysis group through interesting analysis meetings.

Dr. Jörg Pretz, Dr. Axel Steinmetz, Dr. Brian Derro, Dr. Akio Ogawa and Dr. Rainer Gehring for all their useful explanations and friendship.

It has been a great pleasure to work with my colleagues Dr. Stephen Bültmann, Dr. Tülay Çuhadar, Dr. Hubert Gilly, Dr. Joanna Kiryluk, Dr. Yoshiyuki Miyachi, Dr. Gaby Rädel, Dr. Ernst P. Sichtermann, as well as with many others which are not mentioned here.

Dr. Maarten Litmaath for supplying the disk space that was needed for the exclusive ρ^0 analysis. He always kept the SMC cluster running even after he moved to FERMILAB. Un grand merci aussi à Pierre Roth qui a secondé Maarten.

Je tiens aussi à remercier Yolande Camp d'avoir organisé les données et d'avoir été une très grande amie. Sans Lynn Veronneau, Annamaria Galbiati-Steinmetz

et Carnita Hervet-Segui, l'aspect administratif de SMC aurait été monotone.

Un grand merci aussi à M. Boileau pour les supports techniques des cours.

I would like to thank all the members of the CERN choir, in particular its director Mr. Gonzalo Martinez, its president Mr. Baudouin Bleus and his wife Christine, as well as Mrs. Françoise Lutz and Mrs. Baglin.

Je tiens à remercier ma prof. de danses contemporaine et classique Mme Blandine Girard à Versonnex dans le cadre de la MJC (Maison des Jeunes et de la Culture) de Gex.

Mon prof. de flûte M. Eric Weber, mon prof. de piano M. Emile Willemin, ainsi que ma prof. de danse classique Mme Marina Grandjean-Hartmann ont fait preuve d'une compréhension particulière: grâce à leurs "cours du samedi" à Neuchâtel j'ai pu me "ressourcer" et par là-même mener à bien mon doctorat tout en conservant des activités vitales pour mon équilibre physique et psychique.

Ma prof. de flûte actuelle Mme Eliane-Aita Decosterd ainsi que mon prof. de danse classique M. Michael Hartmann ont contribué à me redonner de l'énergie spécialement durant les derniers mois.

Des remerciements bien mérités à Christiane Ehrenreich-Forster pour la relecture attentive de cette thèse: même si tout ce qui se rapportait à la physique était incompréhensible pour elle, elle n'a jamais renoncé à m'aider.

Cette thèse a pu être menée à bien grâce à la bienveillance de mon oncle François Orlando et de la famille Bongiovanni.

L'amitié dont ont fait preuve mes amies Marianne Clottu Balegamire et Evelyne Habegger-Dürig m'a permis de ne pas "étouffer" sous ma thèse.

Finalement, j'aimerais remercier tout particulièrement mes parents, Anne-Marie et Jean-Pierre, pour leurs encouragements et leur soutien tout au long de mes études.